Local Positive Velocity Feedback for the Movement Control of Elastic Joints in Closed Kinematic Chains:

A modelling and simulation study of a 2DoF arm and a 3DoF insect leg

Dissertation zur Erlangung
des Akademischen Grades des Doktors der Naturwissenschaften

vorgelegt von

Axel Schneider

Betreuer:

Josef Schmitz

Universität Bielefeld
Fakultät für Biologie
Universitätsstr. 25
33615 Bielefeld

Juli, 2006

Versicherung der Autorenschaft

Ich versichere, dass ich die vorliegende Dissertation selbständig verfasst und keine anderen als die angegebenen Quellen und Hilfsmittel verwendet habe. Alle Stellen, die dem Sinn nach anderen Werken entnommen sind, habe ich in jedem einzelnen Fall unter genauer Angabe der Quelle deutlich als Zitat kenntlich gemacht.

Bielefeld, 28.07.2006 Axel Schneider

Christine und Simon

Danksagung

Ich danke Josef Schmitz und Holk Cruse für die andauernde Unterstützung während meiner Zeit in der Abteilung Biologische Kybernetik. Sie wurden nie müde mit mir zu diskutieren, um meinen"biologischen Horizont" zu erweitern. Gleichzeitig waren sie auch immer bereit, sich auf meine Sicht der Dinge einzulassen.
Meinen Kollegen, aus denen im Laufe der Zeit auch Freunde wurden, danke ich für viele fruchtbare und auch unterhaltsame Diskussionen. In einer so netten Umgebung habe ich bisher selten gearbeitet.
Besonders bedanken möchte ich mich auch bei meiner Frau Christine für ihre Geduld, ihr Verständnis und ihre Liebe und bei meinem Sohn Simon, der noch zu jung ist, um zu verstehen warum Papa oft so spät nach Hause kommt.
Diese Arbeit wurde durch die DFG (Graduiertenkolleg *Strukturbildungsprozesse*, Bielefeld und CR 58/10-1) und durch die EU (EU-IST Programm, SPARK Projekt) unterstützt.

Bielefeld, Juli 2006 Axel Schneider

Zusammenfassung

In der Beinbewegungssteuerung von laufenden Tieren (z.B. in unserem Modellsystem, der indischen Stabheuschrecke *Carausius morosus*) unterscheidet man Stemm- und Schwingbewegungen. Während einer Schwingbewegung hat das schwingende Bein keinerlei Objektkontakt, da es vom Boden abgehoben duch die Luft nach vorne geführt wird. Das Bein kann als offene kinematische Kette betrachtet und jedes Gelenk der Kette frei bewegt werden. Während der Stemmbewegung haben alle beteiligten Beine Bodenkontakt und bilden somit geschlossene kinematische Ketten. Die Gelenkwinkel derjenigen Beine, die an diesen geschlossenen kinematischen Ketten beteiligt sind, sind nicht mehr frei wählbar. Eine beliebige Einzelbewegung eines Gelenks führt zu Verspannungen in den kinematischen Ketten, die nur durch die aktive (entspannende) Bewegung anderer Gelenke aufgelöst werden können. Ähnliche Probleme treten auch bei Bewegungen mit Armen und Händen auf, wenn diese Manipulationsaufgaben mit Objektkontakt ausführen (z.B. beim Öffnen einer Tür durch einen Menschen). Aufgabenstellungen dieser Art werden in der Robotik unter dem Begriff "compliant motion tasks" zusammengefasst. Beispiele hierfür sind Kontaktschweißen, kooperative Manipulation von Objekten durch mehrere Roboter, Pick-and-Place Aufgaben bei Montagerobotern und, wie erwähnt, auch Stemmbewegungen bei Laufmaschinen. Klassische Lösungsansätze für diese Art von Problemen basieren auf dem "hybrid control" Ansatz von Raibert & Craig (Raibert and Craig, 1981, Trans. of the ASME, 102: 126-133) oder auf dem"impedance control" Ansatz von Hogan (Hogan, 1985, ASME J. Dynam. Syst., Meas., Contr., 107: 1-23). Für die Ansteuerung einer sechsbeinigen Laufmaschine mit insgesamt 18 Gelenken müssen dafür die entsprechenden kinematischen und dynamischen Gleichungen bekannt sein und in jedem Regleraufruf neu berechnet werden. Es scheint unwahrscheinlich, dass Tiere diese Berechnungen explizit durchführen. Cruse und Mitarbeiter (Cruse et al., 1995, Advances in Artificial Life, 668-678) schlugen vor, dass Insekten diese Aufgabe unter Ausnutzung der in der Literatur vielfach beschriebenen Reflexumkehr (auch Unterstützungsreflex) bewältigen (siehe z.B. Bässler, 1976, Biol. Cybernetics 24: 47-49). Bei der Reflexumkehr unterstützt ein Regelmechanismus, der im ruhenden Tier für die Beibehaltung einer Gelenksposition bei äußeren Störungen sorgt, im aktiven Tier eine passive Bewegung und verstärkt diese aktiv. Nimmt man nun im stemmenden Tier eine aktive Bewegung eines Gelenks an, so wirkt sich diese mechanisch vermittelt über die geschlossenen Ketten auf alle anderen Gelenke aus. Der Unterstützungsreflex in den anderen Gelenken führt dazu, dass diese die angeregte Bewegung mitmachen und verstärken. Das Ergebnis ist eine koordinierte Stemmbewegung, die von den lokal geregelten Gelenken gemeinsam ausgeführt wird, obwohl diese nicht neuronal miteinander kommunizieren und keine zentrale Instanz einen vorausberechneten Bewegungsplan ausgibt. In der vorliegenden Arbeit wird diese Hypothese aufgegriffen und quantitativ überprüft. Es werden verschiedene elastische Gelenkmodelle entwickelt, die als Grundlage

für die Implementierung eines Unterstützungsreflex dienen. Der Unterstützungsreflex als solcher wird in Form von Lokaler Positiver Geschwindigkeitsrückkopplung (Local Positive Velocity Feedback, LPVF) hergeleitet und seine Funktionsfähigkeit mit einem Standardtest, dem einarmigen Kurbeln getestet. Die wichtigste Eigenschaft, nämlich die Fähigkeit verschiedene Gelenke ohne direkte Kommunikation zu koordinieren, wird damit nachgewiesen. In einem weiteren Schritt wird gezeigt, dass eine Erweiterung des Ansatzes durch Einführung einer Leistungssteuerung dazu führt, dass die Koordinationsfähigkeit selbst dann erhalten bleibt, wenn eine stemmende Gliedmaße große Kräfte, z.B. gegen eine äußere Trägheitskraft, aufbringen muss. Das Regelungskonzept wird auf einer dynamischen Einbeinsimulation getestet, die Funktionsfähigkeit demonstriert und mit den biologischen Daten von aktivierten Tieren verglichen. In einem letzten Schritt wird der LPVF-Regler mit einem Stehregler kombiniert. Der entstandene Gesamtregler erklärt biologische Befunde aus der Lauf- und aus der Stehdomäne.

Contents

Chapter 1

Introduction

Animals and humans have evolved arms and legs to interact with their environment. The word "interaction" stands for a variety of complex manipulations of objects or for moving the own body by - relative to the body fixed coordinate system - pushing away from other objects. The latter also embraces the whole field of locomotion. For instance, the stance phase of walking can be regarded as pushing away the substrate backwards to propel the body forward. The consistency of the substrate may not always be rigid; in fact it ranges from desert sand over craggy ground to branches and leaves. Thus, walking takes place under various conditions.

Another aspect, beside the substrate, is the different morphologies different walkers bring along to cope with the task of moving in complex environments. A varying number of legs, provided with varying gripping devices and sensors, support bodies of different weights, sizes and shapes.

Facing this high level of complexity, it is appropriate to go into more detail and pose the question: How might biological systems control walking? A divide and conquer approach could be formulated as follows: *"How can the task of walking be divided into smaller tasks that can be solved separately"*? In order to find subtasks, the single step cycle of a leg can be divided into a *swing phase* without ground contact and a *stance phase* with ground contact. Thus, the swing and stance phase of different legs need to be coordinated. This is referred to as the *inter-leg coordination* (Roggendorf, 2005; Dürr et al., 2004; Porta and Celaya, 2001; Cruse et al., 1998a). Besides that, a walker needs a mechanism that coordinates the joint movements within a leg during stance or swing. This is termed the *inter-joint coordination*, accordingly.

During swing, the leg has no contact with other objects as long as it does not collide with an obstacle or touches the ground. This also means that each joint angle in the swinging leg can be changed independently without large tensions in the leg structure.

During stance, all participating legs touch the ground and build mechanical loops. These loops constrain the freedom of movement of single joints. Only coordinated movements of all joints in a suitable manner lead to a forward movement of the body with a minimum of inner forces. Therefore, the stance phase enforces a coupling of those leg joints the legs of which have ground

contact. Suitable joint movements in this case require a high level of inter-joint and inter-leg coordination. At a first glance this seems to be possible only with one central controller that controls all joints.

Walking legs moving as part of closed mechanical loops are a special case. Biological arms and legs just like their technical pendants can be subsumed under the concept of *kinematic chains*, a concatenation of segments and joints. According to the connotation above, it can be distinguished between *open* (free moving) and *closed* (mechanically constrained) kinematic chains. Mechanically constrained movements are called *compliant motions*. Examples for tasks that require compliant motions are the stance phase of a walking cycle, but also turning a crank with a planar manipulator, window cleaning, cooperative manipulation of objects by several agents (robots), object insertion in automation and many more (see e.g. Bruyninckx and De Schutter, 1996).
This thesis shows that it is possible to control the joints of a closed kinematic chain with local joint controllers. These local controllers do not use information on the kinematic chain, the task and the movement of other joints. The desired movement of the closed kinematic chain is an emergent property of the interplay between the local controllers. Local joint controllers developed in this work use positive feedback of the joint velocity and the bending information of their elastic joints in order to decide about the joint movement in the next moment. This control strategy is referred to as ***L**ocal **P**ositive **V**elocity **F**eedback* (LPVF). A prerequisite for the use of Local Positive Velocity Feedback is the existence of elasticity (passive compliance) in the joints. The idea of using a positive feedback strategy to solve a compliant motion task is biologically inspired. This chapter provides an introduction to:

- systems and signals as a prerequisite for control systems (Sect. 1.1),
- open and closed loop systems (Sect. 1.2),
- a differentiation between positive and negative feedback (Sect. 1.3),
- examples for positive feedback in technical systems (Sect. 1.4) and
- examples for positive feedback in biological systems (Sect. 1.5).

Chapter 2 provides a detailed derivation of LPVF control of elastic joints. It shows that this control strategy is able to coordinate the joints of a planar manipulator in a crank turning task. In Chapter 3, the control approach is extended in order to maintain the coordination ability even when disturbed by additional external forces that act on the kinematic chain. This, for example, is the case if a heavy load is attached to the crank via a string and the manipulator has to winch up the weight under LPVF control. The extension is termed *Local Positive Velocity Feedback with power controlled relaxation*. It will be distinguished between a switched and a continuous LPVF version. Chapter 4 analyzes the implementation of passive elastic joints and shows the applicability of LPVF

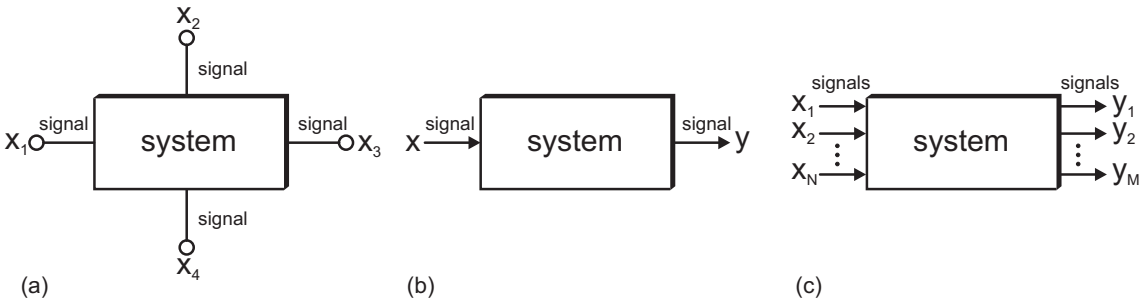

Figure 1.1: Graphical representation of systems. (a) A general system without declaration of signal direction. (b) A SISO (Single Input, Single Output) and a MIMO (Multiple Input, Multiple Output) system (c).

on walking in a 3-*Degree of Freedom* (DoF) test leg. Chapter 5 combines the LPVF approach with a negative feedback controller that regulates the behavior of a standing leg. The resulting universal controller therefore covers the two most important situation of a leg with ground contact. This work finishes with a discussion of the results and an outlook in Chapter 6.

1.1 Systems and Signals

The introduction of feedback into a system requires to consider the tools and concepts that are necessary in order to handle complex systems. The basis for this was laid in the forties and fifties of the last century when *general systems theory* was founded by the Austrian biologist Ludwig von Bertalanffy, the English psychiatrist William Ross Ashby and others (Bertalanffy, 1968). Systems theory deals with the interaction of *systems* as a whole. A system is composed of subunits which interact with each other in such a way that, from a superordinate point of view, their cooperative function serves the same objective. This cooperation distinguishes a system from other systems and its environment. An applied definition is given by Girod: "*A system is the abstraction of a process or object that puts a number of signals into some relationship*" (Girod et al., 2001, p. 6). Practically, a system can be regarded to be a black box that communicates or interacts with other systems in its environment via *signals*. Following another definition by Girod, "*a signal is a function or sequence of values that represents information*" (Girod et al., 2001, p. 3). A signal can be any variable and measurable quantity. It can be one-dimensional or multi-dimensional, (time-, amplitude-) continuous or (time-, amplitude-) discrete, real- or complex-valued and may contain information about deterministic or stochastic processes. Figure 1.1(a) shows a system that relates different signals without any particular function or direction. In most of the cases signals are directed and can thus be called *inputs* or *outputs* of a system [Fig. 1.1(b) and (c)]. Figure 1.1(b) depicts a system with one input and one output. Such systems are called *SISO* systems (***S**ingle **I**nput, **S**ingle **O**utput*). Figure 1.1(c) shows a system with N inputs and M outputs. These systems are called *MIMO* systems (***M**ultiple **I**nput, **M**ultiple **O**utput*), accordingly. Moreover,

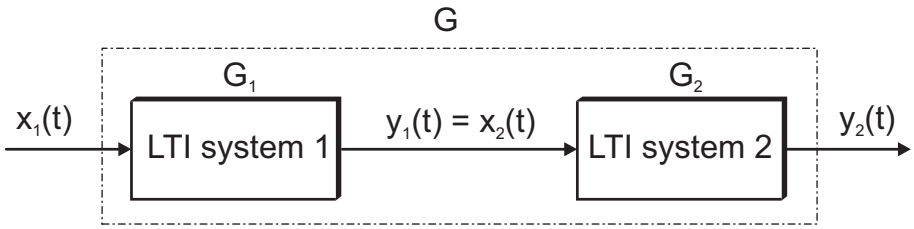

Figure 1.2: Block diagram of a concatenation of two systems H_1 and H_2.

hybrid systems like SIMO or MISO exist. The single joint controllers which are developed in this work, are considered to be SISO systems.

A special case in systems theory is the theory of *linear, time-invariant* (LTI) systems. A system is called linear if the superposition principle applies. Girod defines the superposition principle as follows: "*If the response of a system to a linear combination of input signals always consists of the corresponding combination of the individual output signals, then for this system the superposition principle applies*" (Girod et al., 2001, p. 8). A time-invariant system is "*a system that responds to a delayed input signal with a correspondingly delayed output signal*" (Girod et al., 2001, p. 9). The theoretical tool set for LTI systems can also be applied to non-linear systems if those systems can be linearized for small signal amplitudes.

Perhaps the most important achievement of systems theory is the abstraction of processes in a way that the system model does not need to be concerned with the details of the actual system components but rather uses a (simplified) mathematical description instead. Real physical components are replaced by their ideal equivalents. If, for example, a basin is filled with water or a capacitor is loaded with an electrical current, the level of water or voltage is the integral of the amount of water or charge per time divided by the base area or the capacitor. The key concept or ideal equivalent here is the integrator function. In that way, processes from different domains like engineering, biology, physics, chemistry and even from humanities and social sciences can be analyzed with the same set of tools. A consequence of this is that solutions, that already exist in one discipline, can be transferred to another discipline via the common language of systems theory.

Models from systems theory are commonly represented by their *linear differential equations* if the system is analyzed in the *time domain*. The models are represented by the *Laplace transforms* of these equations if they are analyzed in the *frequency domain*. They are visualized by *block diagrams* in which the whole system model (including any subsystems) with all signal pathways is shown. A simple example for the concatenation of two systems is shown in Fig. 1.2. Given a SISO system with an input and an output signal, the system model itself represents the relationship between

the output signal and the input signal. This relationship is called the *transfer function* G. It is defined as

$$G = \frac{\text{input signal}}{\text{output signal}} = \frac{y}{x}.$$

If a system contains for example a concatenation of subsystems, as shown in Fig. 1.2, it is desirable to feed a signal x_1 into the first system and multiply it with the first transfer function G_1 to get the intermediate output y_1. The signal y_1 in turn serves as an input for the next subsystem G_2 and so on. Each block can be treated separately. The relationships between the input and the output of an LTI system is generally described by the following linear differential equation in the time domain

$$\begin{aligned} a_m y^{(m)}(t) + \cdots + a_2 \ddot{y}(t) + a_1 \dot{y}(t) + a_0 y(t) &= b_n x^{(n)}(t) + \cdots + b_2 \ddot{x}(t) + b_1 \dot{x}(t) + b_0 x(t) \\ &\quad \text{with } y^{(m)} = \frac{d^m y}{dt^m}. \end{aligned} \tag{1.1}$$

In (1.1) it is not possible to separate the variables to obtain an y/x-relationship of a transfer function because also the derivatives appear in the differential equation. In order to inspect a concatenation of systems and to set up transfer functions, the Laplace transformation is used. A Laplace transformation of a linear differential equation represents a functional description of the equation in the frequency or Laplace domain. The Laplace transform uses damped oscillations of the form $x = e^{j\omega t} \cdot e^{-\sigma t}$, similar to the Fourier transform which uses complex oscillations $x = e^{j\omega t}$. In the Laplace transformation the frequency variable $s = j\omega + \sigma$ is introduced. The Laplace transformation of the linear differential equation results in:

$$\begin{aligned} a_m s^m Y(s) + \cdots + a_2 s^2 Y(s) + a_1 s Y(s) + a_0 Y(s) &= b_n s^n X(s) + \cdots + b_2 s^2 X(s) + b_1 s X(s) + \\ &\quad b_0 X(s) \\ Y(s)\left(a_m s^m + \cdots + a_2 s^2 + a_1 s + a_0\right) &= X(s)\left(b_n s^n + \cdots + b_2 s^2 + b_1 s + b_0\right), \\ &\quad \text{(and initial conditions).} \end{aligned}$$

The derivative operation in the time domain changes into a multiplication with the variable s in the Laplace domain, the n^{th}-derivative changes into a multiplication with s^n. The Laplace transform of other operations can be found in transformation tables in books on control theory or systems theory, for example in Girod et al., 2001, p. 561. The differential equation is converted into an algebraic equation. Therefore, in the Laplace domain it is possible to separate the variables and to set up a transfer function, accordingly:

$$G(s) = \frac{Y(s)}{X(s)} = \frac{\left(b_n s^n + \cdots + b_2 s^2 + b_1 s + b_0\right)}{\left(a_m s^m + \cdots + a_2 s^2 + a_1 s + a_0\right)}.$$

The transfer function G of the complete system in Fig.1.2 can be calculated as the product of the single transfer functions $G_1(s)$ and $G_2(s)$.

1.2 Open-loop and closed-loop systems and cybernetics

In the last section some basic aspects of systems theory were introduced. The concepts of systems, signals and block diagrams permit the construction of concatenated systems or networks of subsystems. In this section the concept of *feedback* and the principle of *open-* and *closed-loop* (control) systems is introduced.

1.2.1 Open-loop systems

Simple technical appliances are often feed-forward or open-loop controlled. This means that a control instance sends a signal to a goal system which changes its state accordingly. The sender of the signal does not monitor whether its command changed the state of the system as expected. There is no *feedback* in the system. For example, if there is a light switch outside a room. A person using the switch does not know whether the light is on or not. Another example is a room ventilator that is constructed to rotate with only a few different velocities. Once a velocity is set via the built in switch, the ventilator rotates with some velocity which however is neither measured nor controlled. A disturbance, like a blown bulb in the first example or an air draft in the room in the second example, is not compensated.

Also in biological systems open-loop control can be found. *Mantis* have specialized forelegs to catch their prey. The velocity of the catching movement is too high to make any corrections during the movement. Once it is started, the leg movement has to be finished without any neural feedback (Hassenstein, 1966, pp. 664-666). Also in human movement it has been shown that so called *explosive movements* like throwing, kicking and jumping have such short movement times that the latencies of neural feedback loops are long in comparison (Soest and Bobbert, 1993). For example the execution time of Muhammad Ali's left jab lies in the range of 40 ms (Schmidt, 1982). This means, that at least some of the signals controlling these movements must be executed without feedback.

1.2.2 Closed-loop systems

Technical systems are often supposed to be influenced in a way that certain parameters of the system show a desired behavior. A *controller* is introduced in order to regulate the behavior of the goal system (also called the *plant*). The general setup of a closed-loop control system is depicted in Fig. 1.3. The aim of the controller is to keep the state of the plant within a certain parameter range by continuously measuring the plant output (*controlled variable*) which represents the actual state of the plant, and compare it with the *command variable* (also: *reference signal* r or *setpoint*). The comparative value is then used to change the controlled variable in such a way that it converges towards the reference.

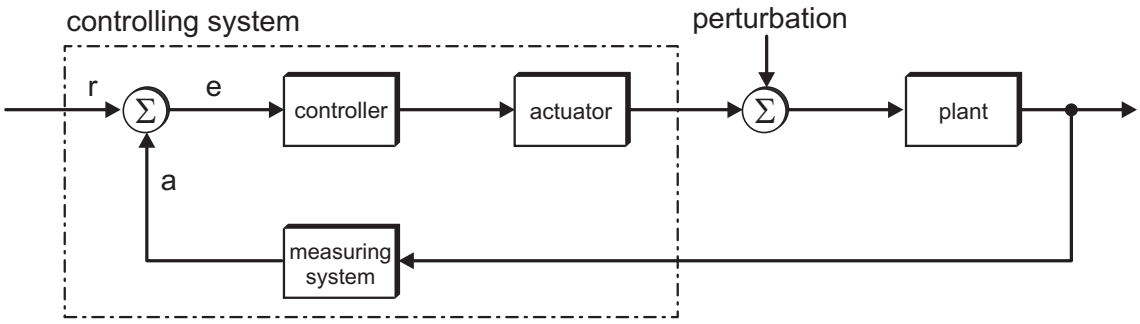

Figure 1.3: Closed-loop control system with a desired reference value r as input and the actual value a as a feedback signal from the measuring device which measures the output of the plant. Variables r and a are compared which results in an error signal e that is fed into the actual controller.

There are many historical examples for feedback controllers in technical systems. An important and well known example is the steam engine. Steam devices were already known in ancient Greece. The first modern steam engines were invented in the 17^{th} century by Edward Somerset, 2nd Marquess of Worcester, Denis Papin, Gottfried Leibniz and Samuel Morland, to name a few. At the beginning of the 18^{th} century Thomas Newcomen invented steam engines that were suitable for industrial use. In the late 18^{th} century James Watt applied important improvements to the Newcomen type engines which led to a drastic increase of efficiency. This resulted in the general acceptance of steam engines in industry. For industrial applications using steam engines it is important that the engine speed is kept constant even under different loading conditions. For this purpose a *governor* was used. A governor is a device that measures and controls the velocity of a machine. James Watt introduced the centrifugal governor for steam engines in 1788. Figure 1.4(a) shows a centrifugal governor (Routledge, 1900). The function principle is as follows: Two weights are mounted on spring-loaded arms that are connected to a central axis. This axis is connected to the rotating output shaft of the steam engine. If the engine velocity increases, the weights lift the arms. This in turn leads to linear movement which is transferred via a lever to a valve which is closed. The result is a decreasing engine velocity because the valve controls the amount of steam that is brought to the steam engine. If the engine velocity decreases, the weights move downwards and open the valve. The engine velocity increases. The operations, described above, enable the governor to keep the steam engine at an almost constant velocity by means of *proportional* control. At this point, if the actions that the governor takes on the valve are too vigorous, the process starts to oscillate. Therefore, it is important to find a suitable description of the dynamics of a feedback system in order to figure out under which circumstances such a system is unstable. The first significant publication on such feedback mechanisms, according to Wiener, 1948, p. 19, was published by Maxwell, 1868.

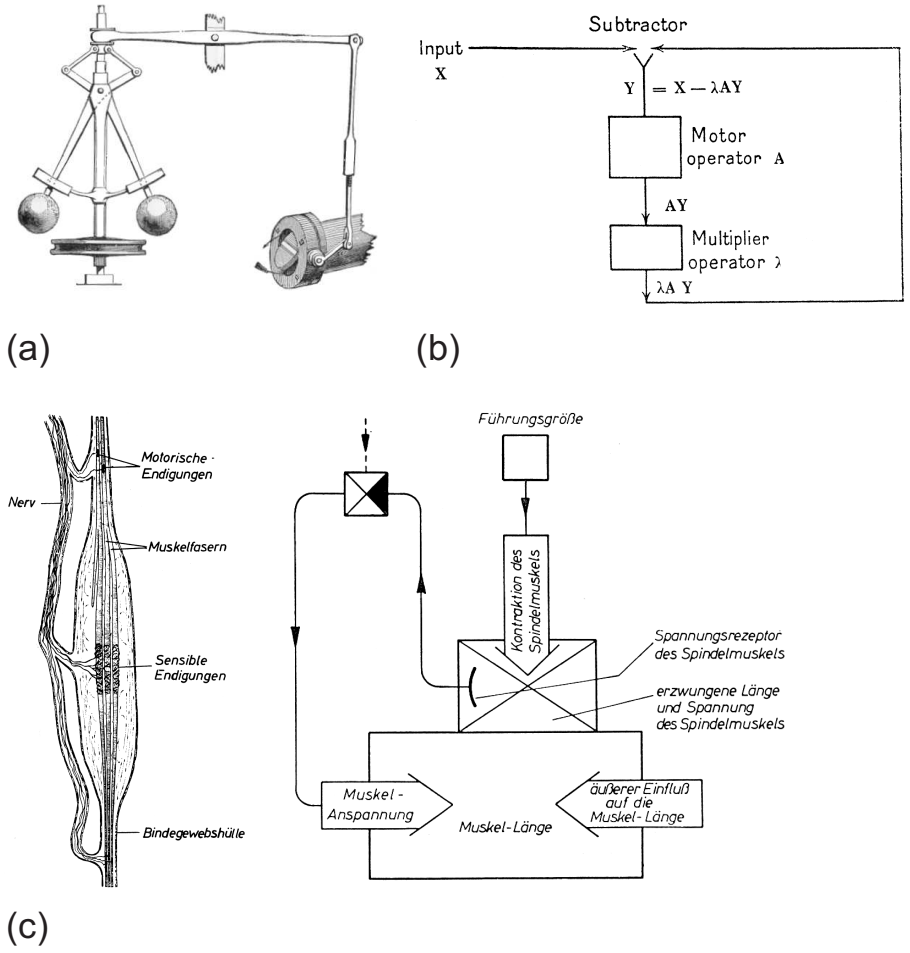

Figure 1.4: (a) The centrifugal governor of a steam engine adopted from Routledge, 1900. (b) A control flowchart of a system with feedback drawn by Wiener, 1948, p. 121. (c) Longitudinal section of a muscle spindle and the block diagram of the muscle spindle control circuit as found in Hassenstein, 1966, p. 677.

1.2.3 Cybernetics

In the forties of last century, Norbert Wiener and Arturo Rosenblueth became aware that the class of problems concerned with communication-, control- and systems theory and statistical mechanics are essentially the same in biological and technical systems. Since the existing terminology in the different disciplines was heavily biased, Rosenblueth and Wiener decided in summer of 1947 to call the entire field of control and communication theory, be it for biology or for engineering, *Cybernetics* (Wiener, 1948, p. 19). The name stems from the Greek word "kybernetes" which means steersman or governor. Feedback is a leading concept in the whole theory of cybernetics. Figure 1.4(b) shows a control flowchart of a system with feedback taken from Wiener (Wiener, 1948, p. 121). The input X is the reference value and the output λAY from the feedback loop is subtracted in order to obtain the input to the motor operator A. Wiener used this flowchart to discuss the stability of the system in dependence on the factor λ.

Figure 1.4(c) shows a biological closed-loop control circuit consisting of a muscle spindle and the reflex circuit that controls the muscle length (Hassenstein, 1966, p. 677). This circuit could also be described by means of Wiener's flowchart in Fig. 1.4(b). Muscle spindles are embedded in the skeletal muscles tissue (also: *extrafusal muscle fibres*) of vertebrates. The spindles are firmly connected to the muscle tissue and are passively shortened and lengthened whenever the muscle fibres contract or relax. Muscle spindles are very weak muscle fibres themselves (also: *intrafusal muscles fibres*) and their level of contraction is controlled by signals from the spinal cord via γ-motoneurons. At the same time, muscle spindles are able to measure their own length. If a muscle spindle is activated, it contracts. This contraction leads to an afferent signal (Ia afferent) that travels to the spinal cord where it activates the α-motoneurons of the muscle. This in turn leads to a contraction of the muscle which results in a relaxation of the muscle spindle until the spindle has reached its original length. This mechanism allows the control of muscle length by "setting" the contraction of the muscle spindles. As it is already shown in Fig. 1.4(b), closed-loop control relies on negative feedback. The actual output of a system is subtracted [see "subtractor" in Fig. 1.4(b)] from the reference input. In the muscle spindle reflex circuit this subtraction is yielded mechanically since a contraction of the muscle leads to a relaxation of the muscle spindles.

1.3 Negative versus positive feedback

The introduction of feedback into a system implies that a recurrent connection is established. This increases the ability of the system to develop a dynamic behavior that can still be stable but also may get unstable, oscillating or even chaotic. Feedback is generally divided into *negative* and *positive* feedback. There are several possible definitions for negative feedback in a system:

1. The feedback in a system is called negative feedback if the algebraic sign in the loop is changed.

2. The feedback in a system is called negative feedback if the part of the output signal which is fed back reverses the direction of change of the output signal.

Usually, negative feedback is used in control systems in order to *stabilize* the output of a plant (see item 2). In contrast, positive feedback is defined as follows:

1. The feedback in a system is called positive feedback if the algebraic sign in the loop does not change. DeAngelis formulated it as follows: *"A feedback loop is positive if the product of all signs in the loop is positive"* (DeAngelis et al., 1986, p. 9).

2. The feedback in a system is called positive feedback if the part of the output signal which is fed back changes the output signal even more in the same direction as the input.

The general idea of positive feedback is that it *destabilizes* the output (see item 2). As it will be shown later, this destabilization may lead to behaviors like output saturation, oscillations with

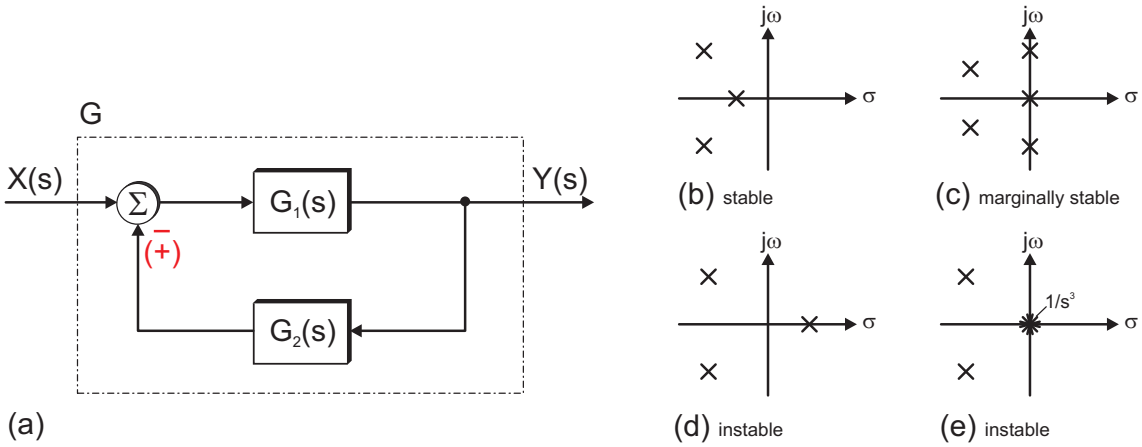

Figure 1.5: (a) Two systems $G_1(s)$ and $G_2(s)$ configured as a feedback circuit. The Σ sign represents the comparator. The minus sign represents negative feedback, the plus sign positive feedback. Examples for the location of the complex-valued poles (imaginary part plotted over the real part, poles represented by crosses) of a stable system (b), a marginally stable system (c) and instable systems (d) and (e).

increasing amplitude but also to the self-enhancement of a process. This emphasizes that the expressions *positive* or *negative* in terms of feedback do not mean that some result is wanted or unwanted.

The first definition for negative and positive feedback, respectively, is based on the appearance of the system in a block diagram. The second definition focusses on the effect negative or positive feedback might have in a system. But, as shown below, the effect in terms of behavior and stability is a matter of the overall transfer function, the phase shift and the gain in the loop. The example of the steam engine regulated by a governor has shown that a negative feedback system can be destabilized and brought to oscillations. Likewise, a positive feedback system can be stable in the sense that the output is bounded or damped as it will be shown in the positive position feedback example in Sect. 1.4.4.

Therefore, this thesis relies on the first definition for negative or positive feedback which only considers the change of the algebraic sign. The actual behavior and the stability of the system have to be analyzed with the appropriate methods.

Figure 1.5(a) shows a simplified sketch of a system G that consists of a system $G_1(s)$ in the forward path and a system $G_2(s)$ in the feedback path. If $G_2(s)$ represents a device that measures the output $Y(s)$ of the system $G(s)$ and feeds it back to the input without a large phase shift (first-order system) or a large amplification, the negative sign in the summation Σ (comparator) indicates a negative feedback. The positive sign indicates a positive feedback characteristic according to the first definition in the list above.

For LTI systems, stability can be examined with the closed-loop transfer function of the system. For the system in Fig. 1.5(a) it is set up by calculating the output $Y(s)$ of the feedback system based on the input $X(s)$:

$$\begin{aligned} Y(s) &= G_1(s) \cdot [X(s) \mp G_2(s)Y(s)] \\ &= G_1(s)X(s) \mp G_1(s)G_2(s)Y(s) \\ Y(s)\,[1 \pm G_1(s)G_2(s)] &= G_1(s)X(s). \end{aligned}$$

The closed-loop transfer function $G(s)$ can be written as

$$G(s) = \frac{Y(s)}{X(s)} = \frac{G_1(s)}{1 \pm G_1(s)G_2(s)} = \frac{\text{Numerator(s)}}{\text{Denominator(s)}} = \frac{N(s)}{D(s)}.$$

The stability of a rational LTI system $G(s)$ can be examined by exciting the system with a pulse at the input. The output is called *pulse response*. If the pulse response is bounded after having given a bounded input, the system is said to be *BIBO*- (Bounded Input/ Bounded Output) stable. According to the behavior of the pulse response the following definitions for stability (of LTI systems) have been formulated (Unbehauen, 1997, pp. 163-165):

- **Asymptotically stable system**: *If the pulse response converges to zero with increasing time t, the system is asymptotically stable.* This also means that all poles of the transfer function have strictly negative real parts [Fig. 1.5(b)].
- **Marginally stable system**: *If the pulse response stays below or converges to a finite value (system output is bounded), the system is marginally stable.* This means that no pole of the transfer function has a positive real part and there is at least one single pole on the imaginary axis. Multiple poles on the imaginary axis are not allowed [Fig. 1.5(c)].
- **Unstable system**: *If the pulse response is infinite the system is called unstable.* This is the case if there is at least one pole with positive real part [Fig. 1.5(d)] or at least one multiple pole on the imaginary axis [Fig. 1.5(e)].

The stability definitions above are specified in the time domain and also in the Laplace domain (pole location of the closed-loop transfer function). The poles of an LTI system are the zeros of the denominator polynomial $D(s)$ of the transfer function $G(s)$. The task of finding zeros of a given polynomial function in a closed form is only possible up to the third degree. For higher degrees the search for zeros is an iterative procedure which can easily be solved using computer algorithms (Press et al., 1992). If stability of a higher-order system has to be evaluated without a computer, a set of different criteria exist that have been formulated in literature (Lutz and Wendt, 2003). These criteria are based on the estimation of the localization of the poles of the transfer function without explicitly calculating them.

One criterion which is used for the analysis of stability in LTI systems is the *Nyquist* criterion. It makes assumptions about the open-loop behavior of a feedback system from which can be derived whether the closed-loop system is stable or not. There are two important aspects which have to be considered in order to achieve a stable system:

- The open-loop gain must be smaller than one.
- The open-loop phase shift must be different from $(n \cdot 2\pi)$ ("out of phase") with an appropriate phase margin (= distance to the critical phase value). In negative feedback there is already an immanent phase lag of $-\pi$. Therefore, the critical phase shift is $-\pi$. In positive feedback the critical phase shift is 0.

For systems which have a Bode plot with a more complex shape, more elaborate rules apply (Cruse, 1996, pp. 59-64).
If the open-loop gain is equal to or larger than one and the phase shift is $n \cdot 2\pi$, the system oscillates [*Barkhausen* criterion, Barkhausen, 1932, named after the German physicist Heinrich Barkhausen (1881-1956)].
Similar assumptions can be made for time discrete systems like those which are described in Chapters 2, 3 and 4.

1.4 Positive feedback in technical systems

In the preceding sections some general aspects on systems and feedback have been discussed. This work focuses on Local Positive Velocity Feedback (LPVF) for the generation of movements in closed kinematic chains. The purpose of this and the next section is to embed LPVF into examples of positive feedback systems known from engineering and biology.

1.4.1 Exhaust gas turbocharger

At the beginning of the last century, the Swiss engineer Alfred Büchi found that combustion engines have a bad efficiency because two third of the engine's energy is lost with the hot exhaust gas. In order to improve the efficiency, he invented the *exhaust gas turbocharger*. A sketch of it is shown in Fig. 1.6(a). The hot exhaust gas drives the wheel of a turbine which is mounted on the same shaft like the wheel of a compressor. This compressor compresses the intake air of the engine above atmospheric pressure. The intake air is cooled down and finally enters the combustion chambers of the engine's cylinders. The increase of the pressure increases the effective oxygen mass during combustion and as a result increases the engine power. Alfred Büchi filed the patent for the turbocharger in 1905 (Büchi, 1953; Büchi, 1922). Figure 1.6(b) depicts a simplified block diagram of the exhaust gas turbocharger. The three outputs of the combustion engine are first the angular velocity ω of the crankshaft, second the torque τ of the crankshaft and third the pressure and

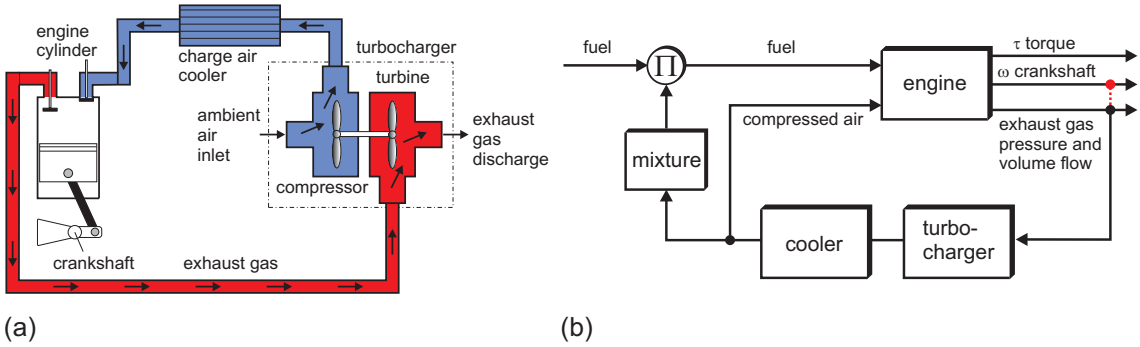

Figure 1.6: (a) Scheme of a closed-loop system consisting of an exhaust gas turbocharger, a charge air cooler and an engine cylinder. (b) Simplified block diagram of turbocharging.

volume flow of the exhaust gas. The product of torque and angular velocity is the mechanical power of the engine. Heat power is dissipated via the hot exhaust gas. In the case of the exhaust gas turbocharger, the exhaust gas drives the turbine of the turbocharger and in the case of the so called *supercharger* the turbine is connected directly to the crankshaft (represented by the short dashed line on the right side of the figure). The compressed air is cooled down in the charge air cooler. The cooling process is important in order to increase the density of the compressed air and to reduce the exhaust gas temperature. The positive feedback loop is closed when the compressed air enters the combustion chamber. Because of the increased level of oxygen mass, the amount of fuel that is brought to the combustion chamber has to be increased, too, in order to maintain the desired air to fuel ratio.

The positive feedback effect in this case is bounded by nonlinearities in the process. In ventilators, compressors and pumps the driving torque increases with the square of the number of revolutions; the mechanical power consumption increases even with the third power of the number of revolutions. This results in an effect that is called the turbine backpressure.

1.4.2 Schmitt trigger and relaxation oscillator

Positive feedback can be a source of instability which is not desired in most technical applications. However, there are also technical applications in which instability is a useful effect. This section introduces a special kind of a comparator with hysteresis which is called the *Schmitt trigger* which is based on positive feedback. It can be used as a comparator and, if equipped with an RC network, as a relaxation oscillator.

Figure 1.7(a) shows the circuit diagram of a Schmitt trigger that inverts the input signal. It consists of an operational amplifier that amplifies the difference voltage between its positive (V_p) and its negative (V_n) terminal with an infinite ("very high") gain. The positive feedback loop consists of the resistor network R_1 and R_2. Supposed the resistor R_1 is zero and the input voltage V_n is a bit smaller than $V_p = V_{\text{out}}$ then the output voltage V_{out} is positive. Feeding back this positive voltage

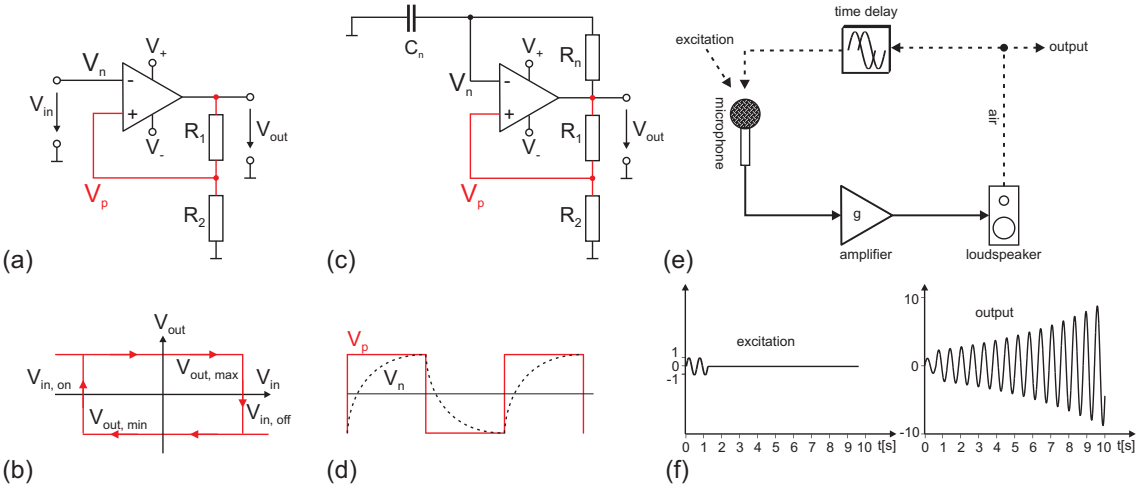

Figure 1.7: (a) Schmitt trigger with (b) hysteresis. (c) Relaxation oscillator with (d) voltage diagram. The voltage V_p at the positive terminal and V_n (dashed line) at the negative terminal of the operational amplifier are shown. (e) Audio feedback loop and (f) plots of the input excitation and output response plotted over time.

to the positive input V_p of the operational amplifier will result in full positive output saturation. In general, if the negative input V_n is smaller than V_p, the output saturates at $V_{\text{out, max}}$. If the negative input V_n is bigger than V_p, the output saturates at $V_{\text{out, min}}$. The output therefore has two stable states represented by the output voltage. If the input voltage crosses one state, the system's output voltage changes to the other. To get another change of the state, the input has to change to the new state and cross it. This behavior is known as *hysteresis* and is shown in Fig. 1.7(b). The hysteresis level for switching from low to high ($V_{\text{in, on}}$) and the hysteresis level for switching from high to low ($V_{\text{in, off}}$) can be chosen with the resistors R_1 and R_2:

$$V_{\text{in, on}} = \frac{R_2}{R_1 + R_2} \cdot V_{\text{out, min}}; \quad V_{\text{in, off}} = \frac{R_2}{R_1 + R_2} \cdot V_{\text{out, max}}.$$

The Schmitt trigger can be regarded as a kind of first-order system in which positive feedback leads to saturation.

Systems that oscillate are at least second-order systems. This means, that they have at least two energy storages. Oscillators are *harmonic*, if they oscillate sinusoidally or they can be of the *relaxation* type that does not oscillate sinusoidally. The electronic relaxation oscillator in Fig. 1.7(c) is derived from the Schmitt trigger in Fig. 1.7(a). The input is now driven by the RC network consisting of R_n and C_n. This network provides a delayed negative feedback which - together with the immediate positive feedback of the Schmitt trigger circuit - results in an oscillation as shown in Fig. 1.7(d). If the voltage V_{out} saturates positively, the capacitor C_n is charged until V_n is higher than V_p which drives the output into negative saturation. This in turn reverses the charging process of the capacitor. The voltage V_n is decreased as long as it is higher than V_p. If it falls below V_p, the whole process starts again.

1.4.3 Audio and video feedback

A common example for positive feedback is audio feedback, sketched in Fig. 1.7(e). This kind of feedback occurs if an acoustic sensor, for example a microphone or a guitar pickup, is placed in front of an acoustic effector like a loudspeaker. The sound emitted by the loudspeaker enters the microphone with a certain delay and is amplified by an audio amplifier that in turn is connected to the loudspeaker. The signal circles in the loop. If the Barkhausen criterion is met, the system oscillates with a high-pitched tone. Already a short excitation, as depicted on the left side of Fig. 1.7(f), is sufficient to excite the output which then oscillates with an increasing amplitude as shown on the right side of the same figure. This effect is also called the *Larsen* effect, named after the Danish physicist Søren Larsen (1871-1957). Although audio feedback is usually unwanted, famous electric guitar players like Pete Townshend (The Who) and Jimi Hendrix used this feedback as a special audio effect.

Video or optical feedback is equivalent to audio feedback. It occurs if an optical sensor, like a video camera, is placed in front of an optical effector, for example a television set. The monitor image is captured by the camera and projected on the monitor. This leads to a closed-loop with a very fast positive feedback accompanied by interference artifacts. A similar effect occurs if two mirrors are placed opposite of each other.

1.4.4 Positive Position Feedback

In mechanical engineering a special kind of positive feedback which is called ***P**ositive **P**osition **F**eedback* (PPF) is used for vibration suppression in large space structures (Goh and Caughey, 1985). A PPF controller is a second-order low-pass filter that rolls off quickly at high frequencies which is the source of its high selectivity. The function principle of PPF is based on that of the tuned mass damper. Bell and Kashani showed that PPF is able to damp a particular mode or even a cluster of modes of vibration in a rectangular flexible plate (Bell and Kashani, 1995). Figure 1.8 displays some details about the application of PPF control in vibration damping of a rectangular steel plate. Figure 1.8(a) shows the setup consisting of a thin metal plate that is fixed at two sides. The plate can be actuated at two points with piezoelectric actuators. Two piezoelectric strain sensors are mounted very close to the actuators.

Figure 1.8(b) depicts the block diagram of the controlled plate. The plant box has two inputs representing the actuators and two outputs representing the two strain sensors. The strain sensors measure the oscillation of the plate and feed the signals into the PPF controllers $H_1(s)$ and $H_2(s)$. The outputs of the PPF controllers are fed back positively into the inputs of the collocated actuators. w is the disturbance input that is used in order to excite the plate via one of the piezoelectric actuators. Figure 1.8(c) shows the frequency response function (FRF) of the actuated plate (y_1/w). One of the controller is tuned to 44 Hz and the other to 133 Hz. If the system is operated open loop, the plate shows different modes of vibration indicated by the black arrows. In the closed loop

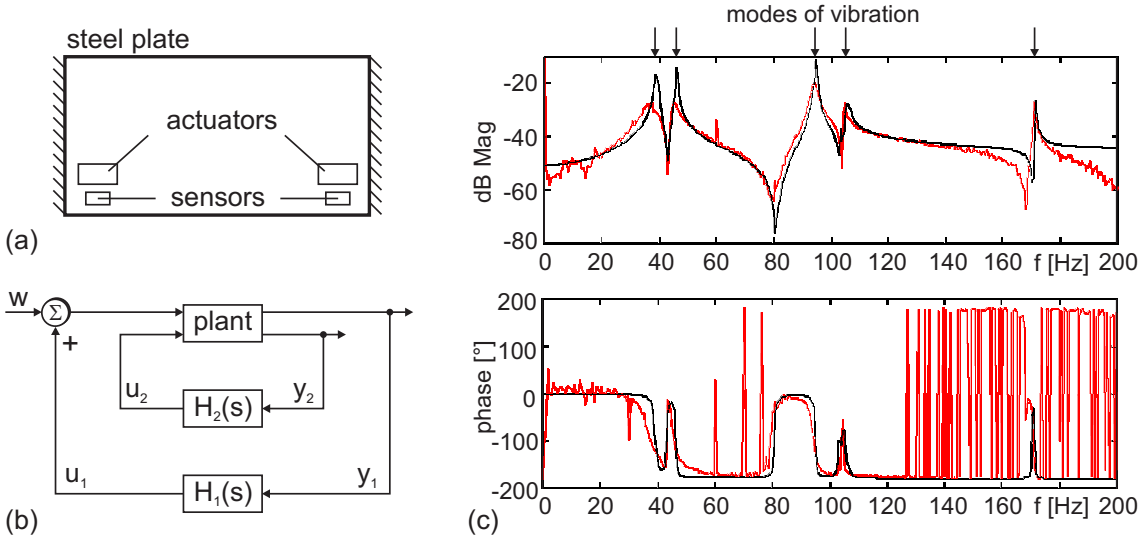

Figure 1.8: (a) Thin steel plate 28.5 x 38.5 cm with two piezoelectric actuators and two piezoelectric strain sensors. (b) Two PPF controllers (second-order low-pass filters $H_1(s)$ and $H_2(s)$) that act on the plant (steel plate). (c) Frequency response function (FRF) of the open loop (black) and closed loop (red) system. (Adopted from Bell and Kashani, 1995)

operation the PPF controllers are able to damp the vibrations of the first five modes of vibration (red lines) effectively.
This example shows that, according to the algebraic sign definition of positive feedback introduced in Sect. 1.3, PPF control is positive feedback although it exhibits a stabilizing effect.

There are also further enhancements of PPF. Fanson and Caughey used PPF in vibration suppression of cantilever beams (Fanson and Caughey, 1990). Song and co-workers performed robustness studies on PPF control and discussed different behaviors of the controlled structure that are called *active stiffness*, *active flexibility* and *active damping* (Song et al., 2001). Rew and co-workers introduced an adjustable version of PPF called adaptive PPF which is based on adaptive signal processing for real-time frequency estimation (Rew et al., 2002).

A control strategy that is closely related to PPF is called *Delayed Positive Feedback* (Abdallah et al., 1993). Delayed Positive Feedback stabilizes oscillatory systems by feeding back a delayed copy of the position output. Baz and Poh introduced *Optimal Modal Positive Position Feedback* (OMPPF) also closely related to PPF (Baz and Poh, 1996). OMPPF represents a positive position feedback via a tunable first-order filter whose parameters are set by means of an optimal control approach.

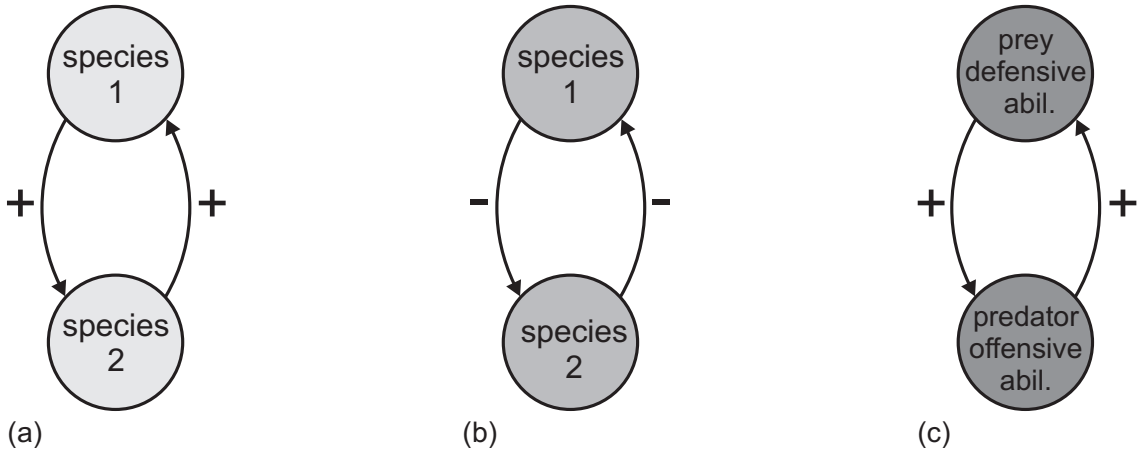

Figure 1.9: Block diagrams of (a) a two-species mutualism, (b) a two-species competition and (c) co-evolution of defensive and offensive skills. (Adopted from DeAngelis et al., 1986, p. 9)

1.5 Positive feedback in biological systems

Nature itself has evolved positive feedback strategies in order to preserve and accelerate processes ranging from the cellular up to the macroscopic level. In this section only a few of a large number of examples will be introduced to show how powerful this principle can be to generate structures in natural systems.

1.5.1 Positive feedback in ecological systems

Positive feedback in ecological systems can be observed in the interaction of two populations of the same or different species.

The first principle is that of *mutualism*. A loose definition is given by DeAngelis and co-authors (DeAngelis et al., 1986, p. 99). They state that mutualism "*is the interaction between two populations that results in a net benefit for one or both populations*". This can also be defined as a reciprocal exchange of benefits between the two populations. Figure 1.9(a) depicts the block diagram of a mutualistic system of two species. An increase of species A either in population numbers or in biomass causes an increase in species B. The same holds the other way round resulting in a closed loop which exhibits a positive feedback. Mutualism spans a wide variety of possible dependencies ranging from *obligate*, where neither species can survive without the other, over *facultative*, where interactions take place via various dependencies to *indirect* mutualism, where the species do not interact with each other directly but benefit from each other via a mediative agent. Indirect mutualism generates beneficial effects for example from so called *enemies' enemies* relationships. That means if a species A is a competitor of species B and species B is a competitor of species C, than the net interaction between A and C may be (indirect) mutualistic ("my enemy's enemy might be my friend"). There are also other examples for indirect mutualism like *friends' friends*

relationships and *protection without interaction*. These examples can be found in the review of Boucher et al., 1982 or in DeAngelis et al., 1986, pp. 101-103.
An example for obligate mutualism are lichens. Lichens are symbiotic associations of a fungus and an algae. The fungus provides suitable physical conditions for the growth of the algae and the algae provides the food for the fungus (DeAngelis et al., 1986, p. 101).
The relationship of sea anemones and anemone fish (clownfish) is an example for a facultative mutualism. The anemone fish is covered with a mucus which allows it to stay within the sea anemone's stinging and toxic tentacles. The sea anemone offers protection to and at the same time receives food scraps from the anemone fish (DeAngelis et al., 1986, p. 102).
One key question in mutualistic systems is under which conditions interactions become mutualistic or parasitic (Hoeksema and Bruna, 2000).

The second principle is that of *competition* between two populations A and B [Fig. 1.9(b)]. The first point to notice in the figure is that the arrows which indicate interaction, are marked with a negative sign indicating a negative effect. If the negative effect that population A has on population B increases, for example owing to an increase of aggressive behavior, then the size of population B will be decreased. This results in a decrease of the negative effect that population B has on population 1 which in turn increases population A. Two negative effects in the loop result in a net positive feedback effect. This is because the number of negative signs is even [1] (see Sect. 1.3, first definition in the positive feedback list).
These two examples involve mutual reinforcement of the populations or biomass. However, there are also other ecological variables that exhibit mutual reinforcement. For example in the *co-evolution* of defensive and offensive abilities in predator-prey systems (DeAngelis et al., 1986, pp. 9-10). On a short timescale (several years), a system of predators and their prey is characterized by negative feedback. If a growing predator population decimates the prey population, the decreasing food supply also decimates the number of predators. However, on an evolutionary timescale certain features exhibit a positive feedback relationship [Figure 1.9(c)]. If the prey evolves better defense abilities, the predator also has to improve its offensive abilities during evolution to keep up with its prey. There is a positive feedback relationship between these two parameters, although the relationship between the two populations might be characterized by negative feedback.

1.5.2 Positive feedback in the behavior of social insects

Social insects like ants, termites, bees and wasps collectively achieve remarkable goals as a group although the individual animals exhibit only simple behaviors. A principle which underlies these achievements is called *stigmergy*. Grassé derived the word stigmergy from the Greek roots "stigma"

[1] The algebraic sign in the loop does not change if there is any number of positive signs but an even number of negative signs.

(outstanding sign) and "ergon" (work) (Grassé, 1959). He formed this expression during studies of termite building behavior in order to define the "incitement of work by the result of work". This means that a behavior of an agent is triggered by an environmental change caused by the previous behavior of the same or other agents. This may result in a self-enhancement of a behavior which indicates positive feedback (also: *autocatalysis, facilitation*).

Termites (e.g. *Macrotermes*) impregnate soil pallets with a pheromone and build pillars with it (Bonabeau et al., 1997; Grassé, 1959). This is done collectively in two phases. In the first, non-coordinated phase the pellets are deposited randomly on the ground. Other termites are attracted by the odor which increases the probability of depositing more pallets close to the same spot. If one of the deposit heaps by chance reaches a critical size, the second, coordinated phase is introduced which is characterized by the emergence of pillars. The process is self-preserving (autocatalytic) since the accumulation of building material increases the pheromone level which in turn encourages more termites to unload their pallets on the pillar. If two pillars are adjacent, there is also pheromone floating from one to the other which leads to a bias in the building procedure and the pillars incline towards each other. This building behavior results in the formation of arches.

Another important example for stigmergy is the trail recruitment in the exploratory pattern of ants. Deneubourg and co-workers showed that the Argentine ant *Iridomyrmex humilis* exhibits an exceptional behavior to explore unknown terrains collectively (Deneubourg et al., 1993). It marks its way with trail pheromone nearly all the time. First the area in front of the nest is explored randomly. As the exploratory group advances further into unknown areas, a pheromone trail extends from the exploration front to the nest and the number of explorers grows because this pheromone does not only guide but also recruit nestmates to participate in the exploration (Van Vorhis Key and Baker, 1986).

To make the ants choose a certain trail out of two possibilities, Deneubourg an co-workers introduced a bridge with two equal branches as a path element from the nest to an arena to be explored (Deneubourg et al., 1993). Figure 1.10(a) displays a sketch of the bridge. Figure 1.10(b) shows the number of ants which use the upper or the lower branch of the bridge plotted over time. In the beginning the ants choose their path randomly (fifty-fifty chance). However, later nearly all ants have decided to use the same branch of the bridge [the upper one in Fig. 1.10(b)]. The reason for that is the positive feedback effect of the trail pheromone. When, by chance, one branch is visited more often than the other one, more ants are attracted to this branch because of the higher pheromone level. The positive feedback principle is the same as in the termite nest building example but in this example the choice of a certain route is consolidated.

Beckers, Deneubourg and Goss could show that ants are able to select the shortest path between the nest and the food source (Beckers et al., 1992). If there exist multiple paths from a nest to a food source, the non-linear dependence of successful trail following on the pheromone concentration favors the consolidation of already strong trails. Strong trails retain ants and reduce the number

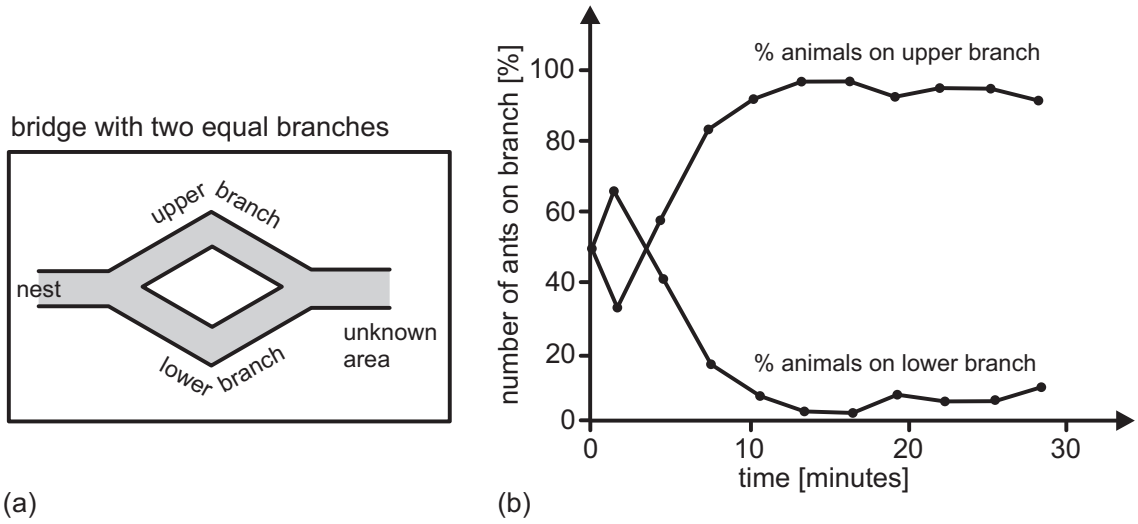

Figure 1.10: (a) Bridge with two equal branches leading from the nest to an unexplored area. (b) Percentage of usage of the upper branch and the lower branch of the bridge. Positive feedback effect leads to break of symmetry and the preference of one branch. (Adopted from Deneubourg et al., 1993)

of available ants for other paths. Evaporation and pheromone breakdown reduces the level of pheromone on all trails. As a result a single trail becomes dominant. This trail represents in many cases a very good choice in terms of path length and quality of the food source (number of visits) that can be reached via this path. The positive feedback (stigmergy) is counterbalanced by a negative feedback (pheromone evaporation and breakdown). Usually, this process relaxes in an optimum. Thus, positive feedback in social insects, as shown in this ant example, helps to find optimal solutions. This observation inspired the application of positive feedback based search strategies like *ACO* (Ant Colony Optimization) for example to find solutions for the *Travelling Salesman Problem* (a review can be found in Dorigo et al., 1991).

The principle of stigmergy helps to coordinate the gathering of corpses in ant colonies (Beckers et al., 1994; Deneubourg et al., 1990). If there are dead nestmates, other ants carry these corpses away and drop them after a while preferably near another corpse. Therefore, the dead ants are put in small clusters. After some time the amount of clusters decreases and bigger clusters are formed until there is only one or two clusters left. Again, the amount of corpses (environmental change) leads to an increase of the number of new corpses unloaded at the same spot (triggering of a behavior).

1.5.3 Positive feedback in the motor system of animals

Positive and negative feedback is also used when the position of a limb has to be controlled. In general, the control loops of joints in a standing animal are assumed to utilize negative feedback in order to maintain the position of the limb, even when exposed to external forces. For legged organisms the control of posture is important to guarantee a static stability during locomotion.

Therefore, even when resting, legged animals try to maintain a preferred species-dependent posture by using negative feedback control loops (Prochazka, 1989; Bässler, 1983; Wendler, 1964).

One might conclude that this holds also for the moving animal. Different studies in legged locomotion suggest that the sign of a reflex elicited by a given sensory input depends on the task or the state of the animal. When moving (animal in an active state), the reaction to sensory signals might also depend on the phase of the limb movement, i.e. stance or swing phase.

Burrows and Pflüger, 1988 reported that even in a standing locust a positive feedback loop (also termed *reflex reversal*) is employed in the preparation of a kicking movement. Two campaniform sensilla (CS), which play a crucial role in this loop, are situated on the anterior and posterior side of the proximal tibia of a locust hindleg. These CS monitor strains in the tibial cuticle (Delcomyn, 1991; Zill and Moran, 1981; Pringle, 1938). If the tibia is moved actively or passively, theses sensors do not show activity unless the leg encounters a resistance. The primary afferents of the two CS project - most probably monosynaptically - onto FETi and fast flexor motoneurons. In preparation of a kick, when the femur-tibia joint is maximally flexed, the CS spike at a high frequency and depolarize extensor and flexor motoneurons which in turn also spike and increase the co-contraction of tibial muscles. This results in an increased tension of the muscles and provides for a powerful thrusting movement.

If the tibial extension movement is obstructed in a walking locust, the two CS are also activated above threshold and in turn enhance extensor activity that increases the force generation.

In technical terms, this loop can be described as a positive feedback loop in which increased cuticular strain leads to increased muscle contraction, leading to further increased cuticular strain. Incorporated are threshold and saturation characteristics which ensure that the working range of this system is limited and which prevent damage to the joint.

An example for state dependent positive feedback in the locomotion system of mammals is given by the halfcenter oscillator (Brown, 1911). It describes the neural correlate of the rhythmic motor pattern generation in a joint driven by antagonistic muscles. The general setup is depicted in Fig. 1.11(a). Brown's halfcenter oscillator consists of two interneurons which are biased with a tonic activation that represents the state of the animal. The two interneurons inhibit each other via high-pass filters (HPF) that represent the fatigue of the inhibitory synapses. If the animal is in an active state (bias high), one interneuron by chance exhibits a slightly higher activation and starts inhibiting the second interneuron. Due to the recurrent connection this interneuron inhibits the first interneuron less thus allowing for increased activity of the latter and so on. However, as the inhibition is high-pass filtered, it decays over time. This increases the activation level of the second interneuron until it is higher than its spike threshold. The second interneuron becomes active and inhibits the first. In this case the inhibition of the first interneuron decays over time owing to the second high-pass filter. The occurring oscillation is caused by the red feedback loop in

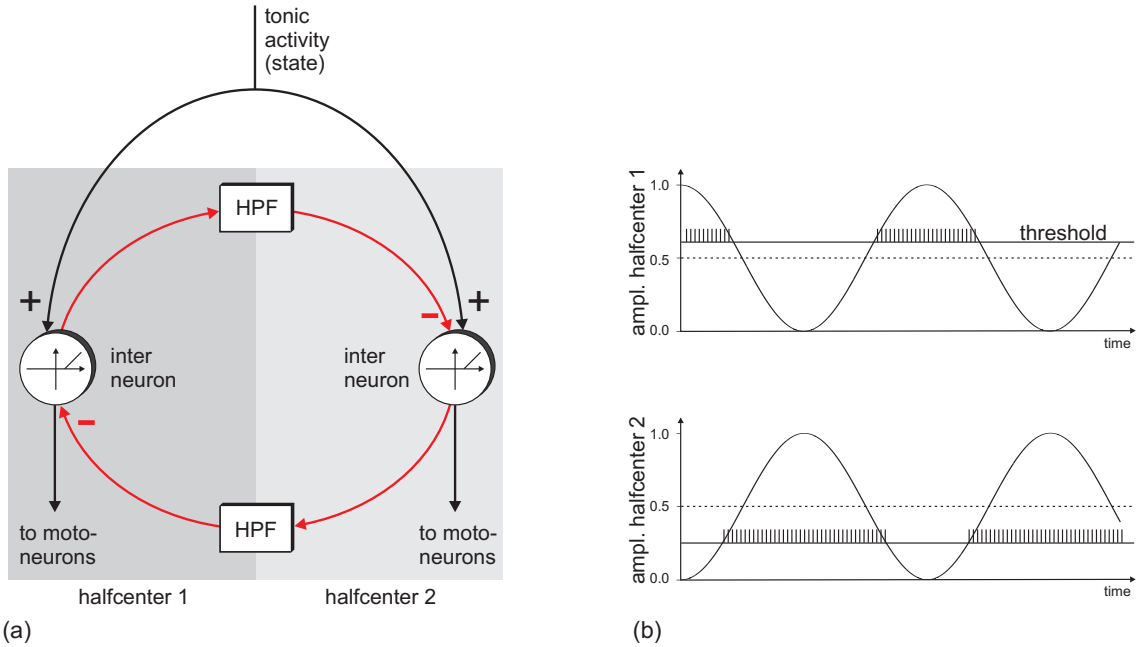

Figure 1.11: (a) Brown Halfcenter oscillator. (b) Output of the two halfcenters. When the activity is higher than a threshold, the simulated interneurons start spiking.

Fig. 1.11(a). Note, that the number of negative signs in the feedback loop is even which indicates a positive feedback. The oscillator is active only if the animal is activated. The same model was used by Wilson, 1961 to analyze the generation of the motor output pattern in flying locusts. The function principle is similar to the relaxation oscillator introduced in Sect. 1.4.2. Figure 1.11(b) shows the two outputs of the halfcenter oscillator. The sine waves indicate the membrane potential of the two centers. The spikes represent the output of the interneurons.

Zill showed that during periods of active searching movements of a locust leg (*Schistocerca gregaria*), the tibial flexor motoneurons fired phasically in response to joint movements in any direction (Zill, 1985). The tibial extensor motoneurons were always inhibited. This is not a complete reflex reversal but characterizes a more complex alteration of the reflex which also cannot be explained by the classical negative feedback (also termed *resistance reflex*).

Reflex reversals due to changes in the activation state of an animal were shown for several species and sensory-motor pathways.

Forssberg and co-workers reported a phase dependent reflex reversal in spinalized, walking cats (Forssberg et al., 1975). Application of even a modest tactile stimulus to the dorsum of a hind leg during the swing phase leads to an enhanced flexion of all leg joints in order to overcome the perceived obstacle. However, a tactile stimulation of the dorsum during stance increases the activation of the extensors which accelerates the stance movement.

Vedel found reflex reversals in the antennal motor system of the rock lobster (Vedel, 1980). The rock lobster antennae consists of four joints and four segments. The movements of the two most distal joints are monitored by one proprioceptor, the chordotonal organ. In the quiescent animal resistance reflexes occur in these two joints whenever the angular position of the joints is changed by an imposed movement. These resistance reflexes involve both extensor and flexor motoneurons. In the activated animal an assistance reflex (reflex reversal) in the distal joints can be induced by joint stimulation. This assistance reflex mainly involves extensor motoneurons.

DiCaprio and Clarac demonstrated that a passive movement of the basal (thoracic-coxal) leg joint of the shore crab *Carcinus maenas* leads to a resistance reflex but can also change into an assistance reflex depending on the activation state of the animal (DiCaprio and Clarac, 1981).

Similar results have been obtained by Skorupski and Sillar for the crayfish *Pacifastacus leniusculus* (Skorupski and Sillar, 1986). Both negative and positive feedback is mediated by the thoraco-coxal muscle receptor organ in dependance of the central excitation (state) of the animal.

For the Indian stick insect *Carausius morosus*, several studies (Schmitz et al., 1995; Bässler and Büschges, 1990; Bässler, 1988; Bässler, 1976) showed that a reflex reversal from negative to positive feedback exists in the femur-tibia joint of the activated animal. During resting, passive flexion of the femur-tibia joint exerts a stretch on the femoral chordotonal organ (fCO) via the apodeme that connects the fCO to the proximal part of the tibia. The fCO activates fast extensor tibiae (FETi) and slow extensor tibiae (SETi) neurons via monosynaptic and polysynaptic pathways which in turn extend the tibia. Similar pathways exist for a passive extension and flexor motoneurons (Bässler, 1983; Bässler, 1972). This corresponds to a negative feedback.

In the case of reflex reversal, instead of correcting for the enforced deviation, the control loop even enhances the disturbance by activation of the agonistic and inhibition of the antagonistic muscles. Thus, a positive feedback is observed.

What might be the biological sense of this positive feedback? Cruse put forward the hypothesis that exploiting positive feedback in the joint control loops might drastically decrease the calculatory effort necessary to generate a coordinated movement of all joints that are part of closed kinematic chains, provided that an animal had its legs on the ground at the beginning of a stance phase and moved one joint actively (Cruse et al., 1995). Then, due to the mechanical coupling via the substrate, all other joints adjust to this active movement passively owing to elastic properties of muscles and tendons. The deviation of the joint from its former posture is monitored by means of proprioceptors in each joint. If reflex reversal is present, each joint amplifies the small passive movement which it measured. As a result the whole animal performs a coordinated stance movement. Instead of calculating joint movements for all legs in the stance phase explicitly, the animal might use such a distributed control strategy in the form of local positive displacement feedback (Dürr et al., 2004).

These examples give rise to the assumption that during the stance phase of a walking arthropod positive feedback might play an important role in the execution of the overall stance movement. The work presented here interprets the reflex reversal as a positive displacement (velocity) feedback on the single joint level. In the following chapters a model named Local Positive Velocity Feedback (LPVF) is derived that is inspired by the principle of reflex reversal. It enables motion control of closed kinematic chains like legs during stance movement. This novel control approach is tested on a planar manipulator turning an unloaded and loaded crank which is a standard benchmark for generating movements in closed kinematic chains (Bruyninckx and De Schutter, 1996). The new controllers are integrated in the joints of a 3DoF test leg to generate stance trajectories in a walking leg. Finally, a self-regulating negative feedback joint controller for standing was combined with the LPVF controller for walking. The resulting general joint controller covers different situations in which a leg is part of a closed kinematic chain.

Chapter 2

Generation of coordinated movements in a chain of elastic joints with LPVF

Starting from studies which revealed that positive feedback is found in the control system for walking in arthropods, we have constructed a new positive-feedback-driven joint that can be used for solving compliant motion tasks. We propose two different joint constructions each of which shows passive compliance. Based on these joints three different *Local Positive Velocity Feedback (LPVF)* controllers are introduced and their properties are analyzed in the context of motion generation in closed kinematic chains. The third circuit named *undelayed dLPVF* is used for the control of a compliant planar manipulator which turns a crank. Our concept is of a highly decentralized nature and follows the idea of embodiment. In this case it means that a process which is controlled by LPVF controllers reveals its nature when the controllers interact with this process.

2.1 Introduction

Whenever systems with multi-joint limbs have to perform a movement while they are part of a closed kinematic chain, plain trajectory control is not sufficient. Trajectory control cannot prevent the participating joints from generating undesired tensions since joint torques are not considered by the controller. Plain force control on the other hand can resolve the problem of undesired tensions, but it provides no means of trajectory generation. Such tasks in which the motion of the endpoint of a limb is constrained - because of contact with another object - are combined in the superordinate concept of *compliant motion*. Compliant motions occur for example when a single limb is turning a crank, when two robot arms handle a workpiece cooperatively or when a walking machine touches

the ground with its feet during the stance phase. Classical engineering solutions for these tasks use a combination of both trajectory and force control. Structurally, these mixed approaches follow either *hybrid control* (Raibert and Craig, 1981) or *impedance control* (Hogan, 1985). In both cases calculations for direct and inverse kinematics as well as dynamics are necessary. These calculations have to be performed while taking into account optimality criteria concerning force distribution and the prevention of shearing stress. However, this procedure requires exact knowledge of the body geometry. Moreover, the geometry has to stay invariant for a given computation. Especially in systems with a high number of DOFs (*degrees of freedom*) such as a walking machine with many legs, these calculations require a considerable amount of computational power. In this chapter it is shown how to accomplish a compliant motion task by combining two bio-inspired approaches. The first approach is a concept from structural bionics which makes use of serial elasticities in biological actuators (muscles). The second approach is adopted from neuro-bionics, namely the occurrence of positive feedback in the neural control of insect joints. The combination of both solves compliant motion tasks without knowledge of the kinematics nor the dynamics of the system.
In the following these two biological foundations are described in detail. Their technical implementation in the form of elastic joints and different positive feedback controllers are shown and the theoretical details of the LPVF controllers are described. As a benchmark we equip a two joint planar manipulator with elastic joints and each of the joints with a LPVF controller and let this arm turn a crank. Finally, simulation and experimental results for the crank-turning task and the efficiency and stability of the system are discussed. The control approach is compared with classical control approaches.

2.2 The biological principle of compliant motions

How does nature solve compliant motion tasks? In order to answer this question we have a closer look at the stance phase of a leg during its walking cycle. Figure 2.1 shows an insect in two different postures while the foot positions are the same. Between the posture on the left side and the posture on the right side the insect has generated coordinated stance trajectories with all six legs in order to shift the body forward. Therefore the situation depicted in Fig. 2.1 can be regarded as two different snapshots of one ongoing stance movement during walking. However, it is conceivable that the animal does not generate the stance trajectory for every single leg through explicit calculation of the kinematic chains. Could the animal solve this task in a different way? The answer is yes.

Bässler and Schmitz found that in the activated stick insect *Carausius morosus* positive feedback (in some publications also termed *reflex reversal*) occurs in different joints during a stance phase, which could be used to actively continue the stance movement (Bässler, 1976; Schmitz et al., 1995). According to this biological evidence, Cruse and co-workers postulated that positive feedback in the body-coxa ("hip") and femur-tibia ("knee") joint is sufficient to produce realistic stance phases in

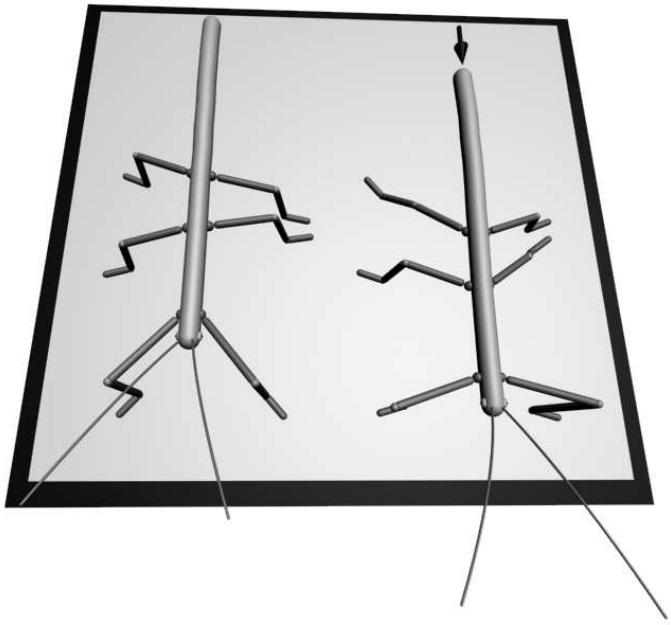

Figure 2.1: An insect in two different body postures while the foot contact positions are the same.

a six-legged robot (Cruse et al., 1995; Kindermann, 2002). An important prerequisite for positive feedback to work is the existence of the elastic components in the muscles and tendons actuating a joint.

These elastic properties add inaccuracy to a system, but also perform a lot of useful functions especially in walking and running. For example, they can save and store energy and when used in compliant foot plates they can moderate impact forces of feet touching the ground (Alexander, 1990). In order to understand how positive feedback makes use of the elastic properties of joints one has to go back to Fig. 2.1 and interpret the situation depicted differently. The configuration on the left side consists of closed kinematic chains only. No joint can be moved actively without affecting all other joints. On the right side of Fig. 2.1 the stick insect has still the same foot contact points as on the left side. But in this case its body is exposed to an external force that pushes it forward (indicated by the black arrow). The elastic properties of the joints allow the body to adopt the new posture according to its interaction with the environment without any explicit kinematics calculation or active movement of its actuators. The new posture is taken in following the physical principle of minimum potential energy (Mussa Ivaldi et al., 1988). In other terms, the compliant joints give way passively to an external force. If feedback controllers in the joints observed the amount of bending that occurred they would ultimately know how to generate the same movement actively in order to maintain the motion that was imposed on the system. To put it another way, the controllers positively feed back the effective joint velocities into the joint actuators in order to keep up the overall motion.

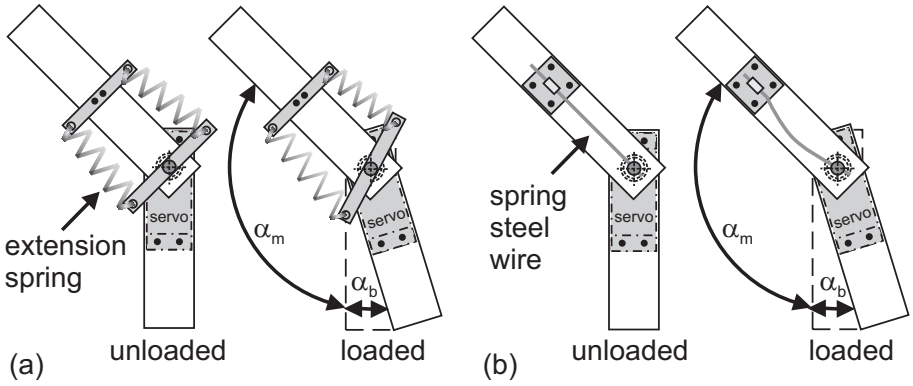

Figure 2.2: Two constructions for a mechanical joint with passive compliance.

This consideration allows a decentralised control strategy for the joints since the coordination is reached mechanically. Instead of an external force, a joint itself can perform an active movement and all the other joints follow passively within the range of their elastic boundaries. This novel decentralised control strategy is termed *Local Positive Velocity Feedback* or *LPVF* control and will be explained in more detail in the next section.

2.3 Implementation of the biological idea

As pointed out before, passive compliance is a key feature of every joint controlled by LPVF. Thus we developed two alternative types of compliant joints by introducing serial elasticities into joints driven by servo motors. Figure 2.2 illustrates how these two versions work.

Figure 2.2(a) shows the joint construction with extension springs in an unloaded and loaded condition, respectively. A servo motor is mounted on the lower of the two segments, which are linked together by a ball-bearing connection. The motor shaft protrudes through the bearing and meets a bracket which is attached to the motor shaft's head. This bracket is connected to a counter bracket on the upper segment by two extension springs. If one of the two segments is fixed, a rotation of the motor shaft results in a rotation of the free segment. However, if the shaft is at a standstill, the extension springs allow a passive bending of the joint by outer torques. Because of their antagonistic arrangement, the extension springs can be mounted in a pre-stretched state. Thus they can respond with a distinct restoring force even to small deflections.

Figure 2.2b displays the second design again in an unloaded and a loaded state. Instead of two extension springs a single spring steel wire takes over the role of the elastic element. The second design is less space-consuming and can therefore be used in joints close to the body.

Both designs roughly approximate a biological joint with elastic properties as found in its actuating muscles and tendons. Apart from the sensor for the motor shaft angle (α_m), the compliant joint is equipped with a linear hall sensor and a permanent magnet, which together work as an angle transducer in order to measure the angle of bending (α_b). The overall angle of the joint (α_j) is

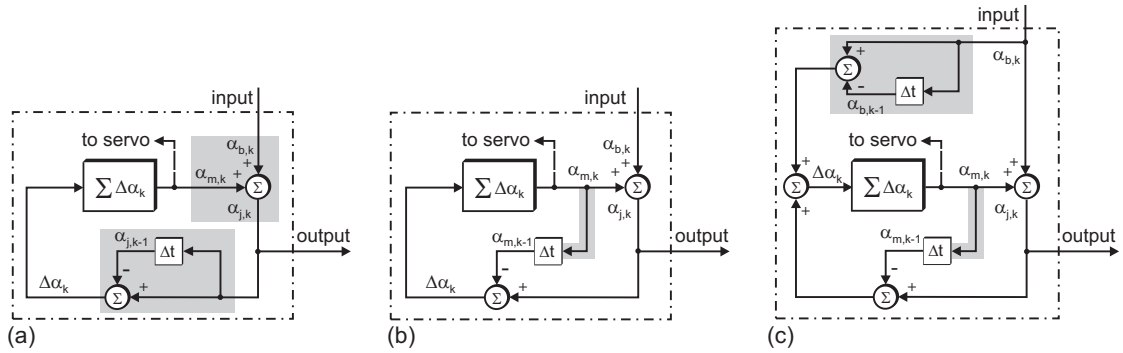

Figure 2.3: Diagrams for three different discrete local positive velocity feedback (dLPVF) circuits.

the sum of the motor angle and the bending angle ($\alpha_j = \alpha_m + \alpha_b$) at any time. Starting from this expression for the joint angle, we can construct a basic LPVF controller [Fig. 2.3(a)]. The light gray box in the upper part of the scheme marks the angular relationship just derived. The angular position α_m of the integrator output (motor signal) is corrected by the measured bending angle α_b of the actuated compliant joint in order to get the real joint angle α_j. This value in turn is differentiated (light gray box in the lower part of the scheme) to gain the current angular velocity measure $\Delta\alpha$ for the joint. This signal in turn is positively fed back into the input of the integrator, which closes the positive feedback loop. There is strong biological evidence for the existence of this integrator in the motor control system of walking insects. In biological systems muscles are driven by spike trains generated by their motor neurons. It has been observed in insect walking that the mean spike frequencies of motor neurons appear to be proportional to the angular velocity of the appendant joint (Tryba and Ritzmann, 2000). Thus muscles can be regarded as integrators that convert input signals proportional to joint velocities into current angular positions of the attached joints. In our case we use an integrator that sums up the angular velocity signal in order to get the new angular position of the joint. The new motor position α_m is the input signal for the position-controlled servo motor situated in the compliant joint.

According to the aforementioned principle, three LPVF controllers with different behaviors are derived in Sect. 2.3.1 - 2.3.3. In order to obtain control algorithms, we describe the LPVF controllers in the discrete time domain ($\mathcal{Z}$-domain) first and term them *dLPVF* controllers.

2.3.1 dLPVF controller I

The control principle - already explained on the basis of the circuit diagram in Fig. 2.3(a) - will now be formulated mathematically and its behavior will be inspected in more detail.

Because of the decentralised control principle (one dLPVF controller for each joint), the dLPVF controller in Fig. 2.3(a) can be regarded as a SISO (Single Input Single Output) controller. The

measured bending α_b is the input and the joint angle α_j is the output. Based on that, the system equations are as follows:

$$\begin{aligned} \alpha_{m,k} &= \alpha_{m,k-1} + \Delta\alpha_{k-1} && \text{(2.1a)} \\ \alpha_{j,k} &= \alpha_{m,k} + \alpha_{b,k} \Leftrightarrow \alpha_{m,k} = \alpha_{j,k} - \alpha_{b,k} && \text{(2.1b)} \\ \Delta\alpha_k &= \alpha_{j,k} - \alpha_{j,k-1}. && \text{(2.1c)} \end{aligned}$$

From these three system equations the discrete transfer function for the circuit in Fig. 2.3(a) can be derived. Inserting (2.1c) in (2.1a) yields

$$\alpha_{m,k} = \alpha_{m,k-1} + \alpha_{j,k-1} - \alpha_{j,k-2}. \tag{2.2}$$

By replacing $\alpha_{m,k}$ and $\alpha_{m,k-1}$ in (2.2) by the right hand side of (2.1b) we get

$$\alpha_{j,k} = 2\alpha_{j,k-1} - \alpha_{j,k-2} + \alpha_{b,k} - \alpha_{b,k-1}. \tag{2.3}$$

The $\mathcal{Z}$-transform of (2.3) is

$$\begin{aligned} &\alpha_j = 2\alpha_j z^{-1} - \alpha_j z^{-2} + \alpha_b - \alpha_b z^{-1} \\ &\Leftrightarrow \alpha_j \left(1 - 2z^{-1} + z^{-2}\right) = \alpha_b \left(1 - z^{-1}\right). \end{aligned} \tag{2.4}$$

Using (2.4), the discrete transfer function $G(z)$ reads as follows:

$$G(z) = \frac{\alpha_j(z)}{\alpha_b(z)} = \frac{z^2 - z}{z^2 - 2z + 1} = \frac{z^2 - z}{(z-1)^2}. \tag{2.5}$$

This transfer function relates the behavior of the joint to the bending it is exposed to.
In Sect. 2.2 it was pointed out that the joint has to maintain its angular velocity even when the bending signal has vanished ($\alpha_b = 0$) in order to convert the passive into an active motion. The dLPVF controller with active position compliance introduced here does not fulfil this requirement. We will show that the angular velocity of the joint is solely determined by the bending signal α_b. Actually this means that the joint is moving faster when the bending is bigger. But when the bending is 0, it returns to its former angular velocity.
We insert (2.1b) in (2.1c), use (2.1a) to eliminate $\Delta\alpha_{k-1}$ and receive

$$\begin{aligned} \Delta\alpha_k - \Delta\alpha_{k-1} &= \alpha_{b,k} - \alpha_{b,k-1} \\ \Leftrightarrow \Delta^2\alpha_k &= \Delta\alpha_{b,k} \\ \Leftrightarrow \ddot{\alpha}_k &= \dot{\alpha}_{b,k}. \end{aligned} \tag{2.6}$$

The left side of (2.6) is the angular acceleration of the joint which is equal to the velocity of the bending signal. Or, by integrating this we get

$$\dot{\alpha}_k + \dot{\alpha}_0 = \alpha_{b,k}. \tag{2.7}$$

Equation (2.7) means that the angular velocity of the joint is equal to the actual bending signal (apart from a constant initial angular velocity $\dot{\alpha}_0$). The joint immediately returns to the initial

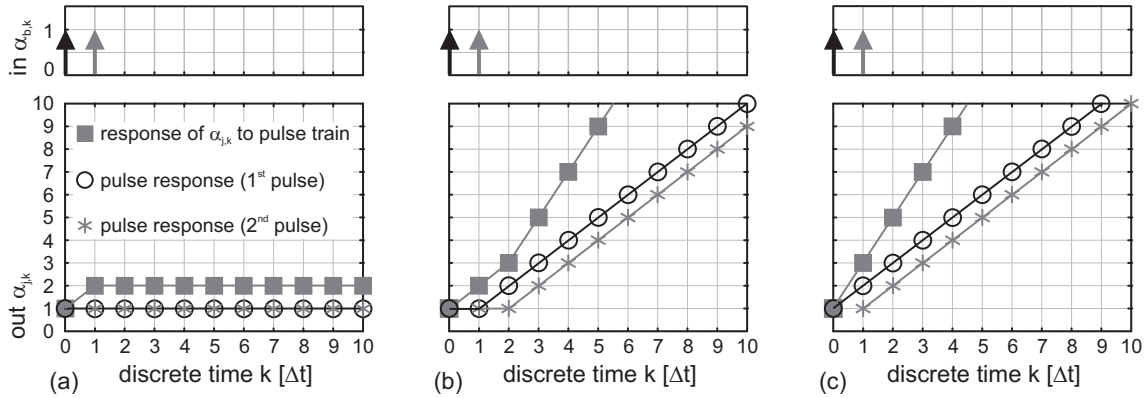

Figure 2.4: Pulse responses and responses to square pulses of length $2\Delta t$ for the three circuits shown in Fig. 2.3(a)-(c), respectively.

angular velocity at the end of the external excitation. Thus the joint cannot preserve the new angular velocity without bending. This can also be seen in the pulse response shown in Fig. 2.4(a). A single bending pulse at its input shifts the joint ahead one step. In a closed kinematic chain this leads to the resolution of the bending situation. A second pulse just shifts the joint ahead another step but the velocity remains zero afterwards. Thus we call this behavior active position compliance and hence the controller a *dLPVF controller with active position compliance*.

2.3.2 dLPVF controller II

The examination of the circuit in Fig. 2.3(a) shows that we have to introduce some changes in order to reach different levels of joint velocity which outlast an external excitation. A way to gain this is to exclude the bending portion of the joint angle from the discrete derivative [Fig. 2.3(b)]. Accordingly, the system equations in (2.8a) to (2.8c) look as follows:

$$\alpha_{m,k} = \alpha_{m,k-1} + \Delta\alpha_{k-1} \tag{2.8a}$$

$$\alpha_{j,k} = \alpha_{m,k} + \alpha_{b,k} \Leftrightarrow \alpha_{m,k} = \alpha_{j,k} - \alpha_{b,k} \tag{2.8b}$$

$$\Delta\alpha_k = \alpha_{j,k} - \alpha_{m,k-1}. \tag{2.8c}$$

In order to get the discrete transfer function for the circuit in Fig. 2.3(b) we perform the same steps as in Sect. 2.3.1

$$G(z) = \frac{\alpha_j(z)}{\alpha_b(z)} = \frac{z^2 - z + 1}{z^2 - 2z + 1} = \frac{z^2 - z + 1}{(z-1)^2}. \tag{2.9}$$

The implications of this equation for the behavior of the system are discussed in the following.

As opposed to the circuit that is represented by transfer function (2.5) this version of the dLPVF control fulfills the postulated requirement from Sect. 2.2. This means that after the application of a bending force the joint moves on with the velocity that was reached towards the end of the

bending period. The joint has adopted the angular velocity of the passive movement. We can show this by inserting (2.8b) in (2.8c)

$$\Delta\alpha_k = \alpha_{m,k} + \alpha_{b,k} - \alpha_{m,k-1}. \tag{2.10}$$

Again we can derive from (2.8a) that $\Delta\alpha_{k-1} = \alpha_{m,k} - \alpha_{m,k-1}$. If we use this in (2.10) we get

$$\begin{aligned} \Delta\alpha_k - \Delta\alpha_{k-1} &= \alpha_{b,k} \\ \Leftrightarrow \Delta^2\alpha_k &= \alpha_{b,k} \\ \Leftrightarrow \ddot{\alpha}_k &= \alpha_{b,k}. \end{aligned} \tag{2.11}$$

Thus the angular acceleration of the joint is determined by the actual bending signal. The absence of the bending therefore only means that the system is not accelerated any further. In turn this is significant for the desired function because the joint velocity is maintained.
If we take a closer look at the pulse response of this circuit [Fig. 2.4(b)], we can see that the response of the joint to a pulse at time $k\Delta t = 0$ (upper panel, black arrow) appears at the output with a time delay (lower panel, black line, circles). The same is valid for a second pulse at $k\Delta t = 1$. The superposition of both responses leads to the angular position curve depicted by the gray squares in Fig. 2.4(b). The final joint velocity, which has to be 2 after two pulses, is only reached at $k\Delta t = 3$, one time step after the last pulse. A time delay indicates that the active joint always reacts too late or, in other words, it drags behind the passive bending that it should adapt to. This in turn means that a coordination between the participating joints cannot emerge. This has been confirmed by experiments in a closed kinematic chain, like in the crank experiment (see Sect. 2.4). Based on this, we formulate a second basic requirement for the LPVF approach: An LPVF controller has to adapt to the bending signal at its input immediately (without any time delay). Since the dLPVF controller II [Fig. 2.3(b) and 2.4(b)] shows such a time delay, we call it *dLPVF controller with delayed active velocity compliance.*

2.3.3 dLPVF controller III

In order to eliminate the delay shown by controller II, this circuit is further modified by adding the bending velocity to the joint actuator velocity $\Delta\alpha_k$. Figure 2.3(c) shows the new circuit. We set up the system equations for the new controller as follows:

$$\alpha_{m,k} = \alpha_{m,k-1} + \Delta\alpha_{k-1} \tag{2.12a}$$

$$\alpha_{j,k} = \alpha_{m,k} + \alpha_{b,k} \Leftrightarrow \alpha_{m,k} = \alpha_{j,k} - \alpha_{b,k} \tag{2.12b}$$

$$\Delta\alpha_k = \alpha_{j,k} - \alpha_{m,k-1} + \alpha_{b,k} - \alpha_{b,k-1}. \tag{2.12c}$$

Following the same strategy as in Sect. 2.3.1, we can derive the discrete transfer function $G(z)$ for the circuit in Fig. 2.3(c)

$$G(z) = \frac{\alpha_j(z)}{\alpha_b(z)} = \frac{z^2}{z^2 - 2z + 1} = \frac{z^2}{(z-1)^2}. \tag{2.13}$$

The circuit change has led to a simpler transfer function. We expand the transfer function (2.13) into partial fractions

$$G_p(z) = \frac{z}{z-1} + \frac{z}{(z-1)^2}. \tag{2.14}$$

The first term of (2.14) represents a unit step function, the second term a unit ramp function. The superposition of both results in the pulse response is depicted in Fig. 2.4(c). Circles show the response for the pulse at $k\Delta t = 0$ and stars the response for the pulse at $k\Delta t = 1$.
It is now clear that the dLPVF circuit from Fig. 2.3(c) transfers the passive joint bending into an active movement without a time delay, which means, that it meets both requirements mentioned above. By inserting (2.12b) in (2.12c), we derive the angular acceleration of the joint

$$\Delta\alpha_k = \alpha_{m,k} + 2\alpha_{b,k} - \alpha_{m,k-1} - \alpha_{b,k-1}. \tag{2.15}$$

By using (2.12a) we replace $\alpha_{m,k}$ and $\alpha_{m,k-1}$ in (2.15) by $\Delta\alpha_{k-1}$

$$\begin{aligned} \Delta\alpha_k - \Delta\alpha_{k-1} &= 2\alpha_{b,k} - \alpha_{b,k-1} \\ \Leftrightarrow \Delta^2\alpha_k &= \alpha_{b,k} + \Delta\alpha_{b,k} \\ \Leftrightarrow \ddot{\alpha}_k &= \alpha_{b,k} + \dot{\alpha}_{b,k}. \end{aligned} \tag{2.16}$$

The angular acceleration of the joint actuator in (2.16) is the same as in (2.11) except for the fact that in addition to the bending angle the angular velocity of the bending signal is included. As a result, the time delay in the pulse response observed in Fig. 2.4(b) is eliminated in Fig. 2.4(c) by using the dLPVF controller III. For this reason we call this controller *dLPVF controller with undelayed active velocity compliance.*

2.3.4 Simplification of the dLPVF controller III

A closer inspection of equation (2.12c) shows that it can be rearranged by replacing $\alpha_{m,k-1}+\alpha_{b,k-1}$ with $\alpha_{j,k-1}$ (according to (2.12b)). The result is the following:

$$\begin{aligned} \underbrace{\Delta\alpha_k}_{\text{actuator vel.}} &= \alpha_{j,k} - \alpha_{j,k-1} + \alpha_{b,k} \\ &= \underbrace{\Delta\alpha_{j,k}}_{\text{joint vel.}} + \underbrace{\alpha_{b,k}}_{\text{bending}}. \end{aligned} \tag{2.17}$$

Equation (2.17) allows a different interpretation of the undelayed dLPVF controller. The desired angular velocity of the joint actuator is the difference between the actual angle of the joint α_j at this time step and the time step before. This reflects the effective movement of the joint despite the fact that a bending occurred. The aim of the positive feedback control is to program the velocity of the actuator for the next time step in such a way that it produces the same angular displacement as in the last time step. In order to generate that effective movement, the bending has to be resolved

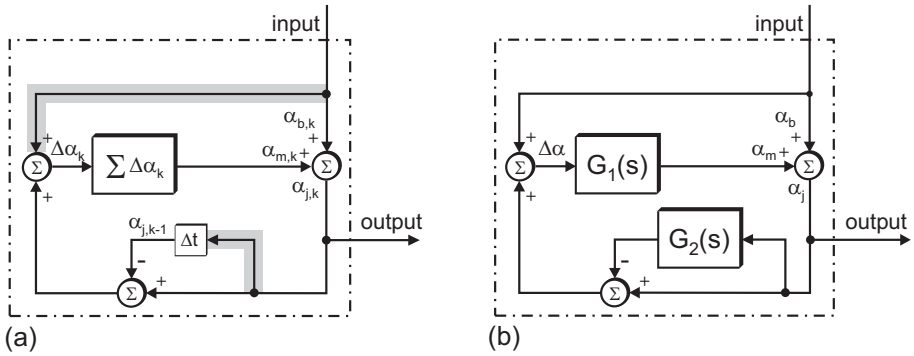

Figure 2.5: Simplification of the undelayed local positive velocity feedback circuit (dLPVF controller III) and its time-continuous equivalent.

additionally. This is reflected by the summand $\alpha_{b,k}$ in (2.17). According to this rearrangement we can sketch the circuit diagram differently [Fig. 2.5(a)]. Note that this circuit equals that shown in Fig. 2.3(c). At the same time it is closely related to the initial idea [Fig. 2.3(a)].

2.3.5 Actuator and joint velocity of the dLPVF controller III

Up to now, the system has been regarded as a SISO-system with the bending signal as its input and the joint angle as its output. We want to derive an expression for the angular velocity of the actuator $\Delta\alpha_k$ and an expression for the angular velocity of the joint $\Delta\alpha_{j,k} = \alpha_{j,k} - \alpha_{j,k-1}$ to compare both. This is instructive because it shows what the joint actuator has to do to adapt the movement of the joint smoothly to the bending signal.

To arrive at an expression for the angular velocity of the actuator, we can simply add up all accelerations $\Delta^2\alpha_k$ from $k = 0$ up to $k = K$, which means to integrate (2.16)

$$\Delta\alpha_K = \sum_{n=0}^{K} \alpha_{b,n} + \alpha_{b,K}. \tag{2.18}$$

From (2.17) we know the relationship between the angular velocities of the actuator and the joint. Using this in (2.18) results in

$$\Delta\alpha_{j,K} = \sum_{n=0}^{K} \alpha_{b,n}. \tag{2.19}$$

If we compare (2.19) with (2.18) we can see that the velocity of the actuator $\Delta\alpha_k$ and the velocity of the joint $\Delta\alpha_{j,k}$ is the same except for the fact that the actuator has to have twice the acceleration in those time steps in which bending occurs. This is easy to understand since the actuator has to move with the same velocity as the joint and additionally compensate for the bending. The cumulative velocity after two pulses is shown in Fig. 2.4(c) (squares). After one pulse at the input the overall velocity of the joint is immediately 1, after two pulses it is 2 and so on. So there is no delay in the cumulative velocity either.

2.3.6 The continuous equivalent for the dLPVF controller III

Now that the simplest dLPVF-circuit that satisfies our needs has been found, a continuous equivalent of that circuit needs to be determined. The continuous description is useful for the comparison with biological findings in the future because it is closer to the conventional biological representation. We chose the forward rectangular rule $z = sT + 1$, which results from a rectangular approximation of an integrator in control theory, for converting the transfer function from the $\mathcal{Z}$-domain to the $\mathcal{L}$-domain. The capital T denotes the sample time of the discrete system. If we insert this expression into the transfer function of (2.13), we get the following transfer function:

$$G(s) = \frac{\alpha_j(s)}{\alpha_b(s)} = \frac{s^2 + \frac{2}{T}s + \frac{1}{T^2}}{s^2}. \tag{2.20}$$

For this transfer function a corresponding circuit has to be found. Thus we try to maintain the same structure as in Fig. 2.5(a) in the $\mathcal{L}$-domain. This is shown in Fig. 2.5(b). We set up the characteristic equations to find the transfer function

$$\alpha_m = G_1(s)\Delta\alpha \tag{2.21a}$$

$$\alpha_j = \alpha_m + \alpha_b \Leftrightarrow \alpha_m = \alpha_j - \alpha_b \tag{2.21b}$$

$$\Delta\alpha = \alpha_j - G_2(s)\alpha_j + \alpha_b. \tag{2.21c}$$

By applying steps analog to those in Sect. 2.3.1, we get the continuous transfer function

$$G(s) = \frac{\alpha_j(s)}{\alpha_b(s)} = \frac{1 + G_1(s)}{1 - G_1(s) + G_1(s)G_2(s)}. \tag{2.22}$$

We now assume that $G_1(s)$ is an integrator and that $G_2(s)$ is a first-order low pass filter

$$G_1(s) = 1/(sT_i)$$
$$G_2(s) = k_{lp}/(1 + sT_{lp})$$

Based on this assumption, we arrive at the following transfer function:

$$G(s) = \frac{\alpha_j(s)}{\alpha_b(s)} = \frac{s^2 + s\frac{(T_i+T_{lp})}{T_iT_{lp}} + \frac{1}{T_iT_{lp}}}{s^2 + s\frac{(T_i-T_{lp})}{T_iT_{lp}} + \frac{k_{lp}-1}{T_iT_{lp}}}. \tag{2.23}$$

The comparison of the coefficients of (2.23) with the coefficients of (2.20) results in $T_i = T_{lp} = T$ and $k_{lp} = 1$. Using these assumptions, the time-continuous version of the LPVF controller is obtained and termed *cLPVF*.

2.4 Turning a crank

LPVF controllers implement the idea of decentral control. Each actuated joint in a kinematic chain uses its own dLPVF (or cLPVF) controller. The coordination results from the mechanical coupling only while joint bending mediates the coupling information. For the evaluation of the

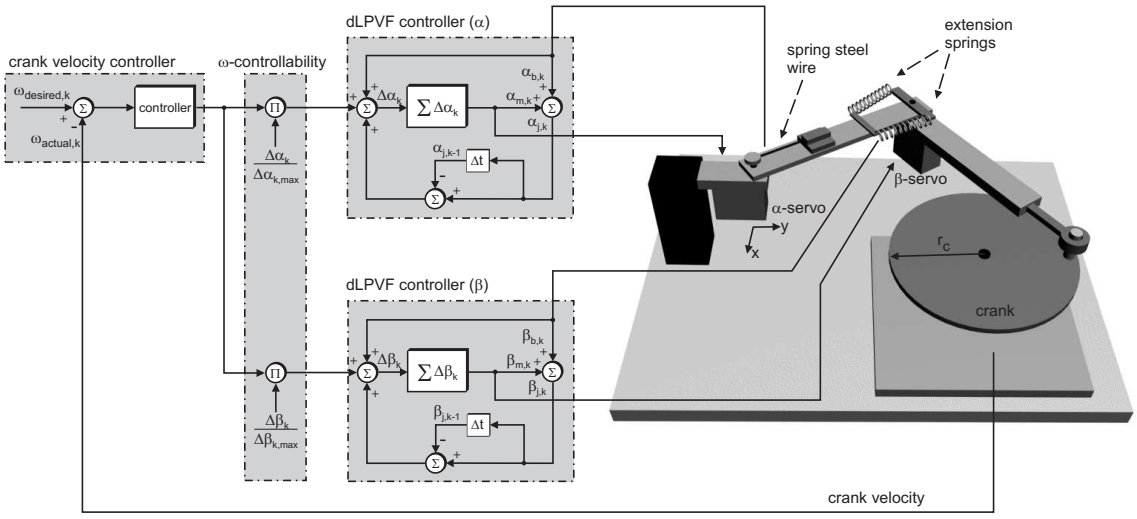

Figure 2.6: Scheme of the decentral control circuit for the crank turning task performed by a two joint planar manipulator.

control scheme a two joint compliant planar manipulator is used for crank turning as shown on the right side of Fig. 2.6. Crank turning was chosen as an example because it is a standard benchmark for compliant motion tasks. The planar manipulator has two joints (α, β) and two segments ($l_1 = 197\,\text{mm}$, $l_2 = 174\,\text{mm}$). The gripper ($l_g = 50\,\text{mm}$) at the end of the second segment is attached to the handle of a crank (radius: $r_c = 80\,\text{mm}$) which is pivoted with low friction. The base of the crank [default crank position: $x_c = 77\,\text{mm}$, $y_c = 197\,\text{mm}$, see Fig. 2.9(a)] is attached to the same base as the manipulator itself. Therefore this setup can be regarded as being a closed kinematic chain. It represents a simple case in which coordination between the two joints is needed for the generation of a cyclic movement. The following section addresses the question how such decentral controllers can in turn be controlled by a superordinated task controller. After that we discuss results from a kinematics and a dynamics simulation of this task and finally the real robot experiment.

2.4.1 Velocity control of a two joint planar manipulator

In crank turning, the global control variable for an ongoing cranking movement is the rotation velocity ω_k of the crank. The question arises how a superordinated crank velocity controller and the decentral joint controllers can be combined. A possible solution is shown in Fig. 2.6. The system consists of a negative feedback crank velocity controller (in our case a simple p-controller) depicted on the left side of Fig. 2.6 and of two dLPVF controllers (centre part of Fig. 2.6), one for each joint α and β. An additional input is added to the joint actuator velocity $\Delta\alpha_k$ of the dLPVF controllers. This input can be used to manipulate the angular velocity of the joint. The controller output variable of the velocity controller cannot be fed into the new input of the dLPVF circuit directly because it exclusively contains information on the overall velocity of the manipulator

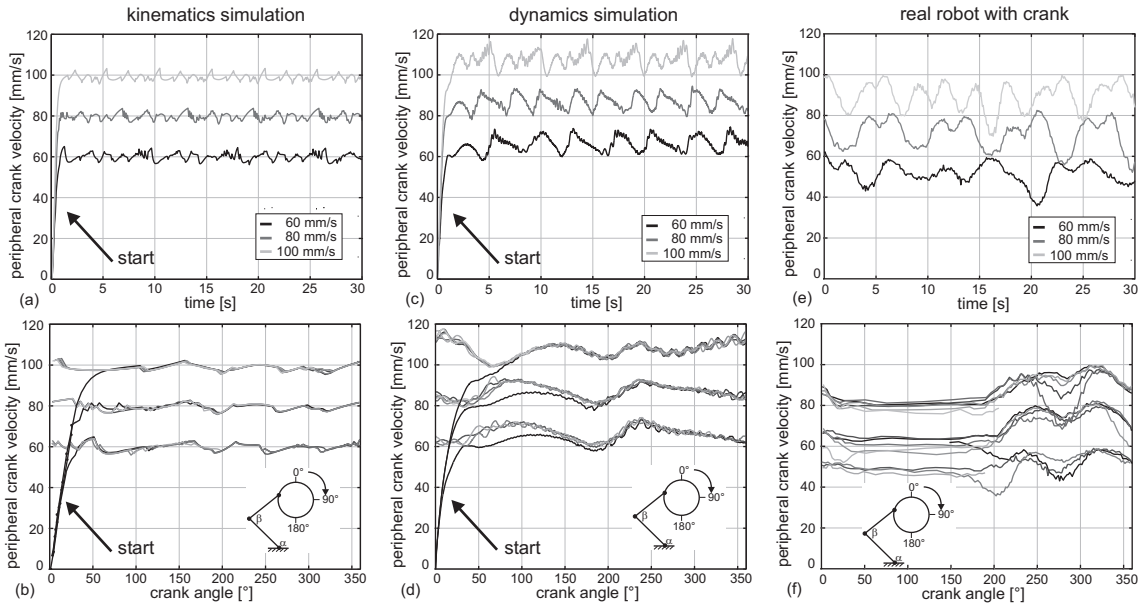

Figure 2.7: Tangential crank velocities plotted over time and over crank angle, respectively.

gripper during task execution. Therefore, the output of the velocity controller is used only as a quality measure that indicates the velocity performance of the manipulator. In order to mediate between the output of the crank velocity controller (global information) and the input of the LPVF circuit (local information), we introduce the ω-*controllability* measure, which is dependent on the angular velocity of the joint

$$\omega_{cont,\alpha} = \frac{\Delta\alpha_k}{\Delta\alpha_{max}}, \quad \omega_{cont,\beta} = \frac{\Delta\beta_k}{\Delta\beta_{max}}. \tag{2.24}$$

These measures are depicted in the long rectangular box in Fig. 2.6. The ω-controllability of a LPVF controlled joint is 0 when the course of the joint angle reaches an extremum during its movement. In this case the direction of joint rotation changes from clockwise to counterclockwise or vice versa, which means that the joint's share of the overall manipulator motion is small in this specific posture. When the joint's share of the overall velocity of the manipulator is high, the joint also moves with a considerable amount of its own maximum angular velocity. In turn this means that its ω-controllability is high. The ω-controllability is used for scaling the crank velocity controller output. With this method, the velocity controller's central information content is transformed into decentral information which can be fed into the joint controllers.

2.4.2 Kinematics simulation

In a first step we created a kinematics simulation of the crank turning task. Starting from the angular motor positions (α_m, β_m) of the dLPVF controller, the gripper position of the planar manipulator is calculated with the forward kinematics as if there were no elastic elements. If the position of the gripper lied outside the crank perimeter, we projected it back on the crank

orthogonally and calculated the corresponding posture with the inverse kinematics. The differences between the resulting joint angles (α_j, β_j) and the angular motor positions equal the bending angles (α_b, β_b) in the given time step.

The cranking experiment in the kinematics simulation was started by initialising the planar manipulator in a posture in which its gripper holds the handle of the crank in a 0° crank orientation [see Fig. 2.7(b) small sketch]. Then the system was excited by adding a small offset to the angular positions of both servo motors which shifted the gripper position in the intended direction of rotation. As a result, the manipulator started to turn the crank with the desired velocity (60 mm/s, 80 mm/s and 100 mm/s) and kept on cranking after the initial starting pulse was switched off at the end of the first controller iteration. Figure 2.7(a) depicts the time course of the peripheral crank velocities in a 30 s time interval. Figure 2.7(b) shows the same data plotted over the crank angle of 360°. The arm performed several rotations. Every new rotation is indicated by another shade of gray. During this simulation the desired velocities were adopted with the following accuracies. For $\omega_{desired} = 60\,\text{mm/s}$ the result was $\bar{\omega}_{actual} = 59.84 \pm 1.77\,\text{mm/s}$ (mean value ±1 standard deviation). For $\omega_{desired} = 80\,\text{mm/s}$ the mean actual velocity was $\bar{\omega}_{actual} = 79.57 \pm 1.71\,\text{mm/s}$ and for $\omega_{desired} = 100\,\text{mm/s}$ the mean output was $\bar{\omega}_{actual} = 98.71 \pm 1.47\,\text{mm/s}$. The desired velocities are reached with a good accuracy ($0.3 - 1.3\%$ mean deviation) because there are is inertia which pulls the system away from its movement state.

2.4.3 Dynamics simulation

In a second step, a dynamics simulation of the complete setup was developed. This was necessary because it was not clear from the beginning if very low damped second-order systems like our elastic joints would generate destructive oscillatory behavior under the control of the dLPVF controllers. For this purpose we had a closer look at our real robot arm, measuring details like the viscous friction of the joint bearings, the spring constants of the extension springs, the damping, the characteristics of the joint actuators (two Multiplex position-controlled servo motors) and the masses and lengths of the arm segments and the crank. We used Simulink 6 and SimMechanics 2.2 (The MathWorks Inc., 3 Apple Hill Drive, Natick, MA, USA) in order to implement a modular dynamics simulation. In the course of the implementation, single elements were designed like the Multiplex servos including their cascade position controller, the electrical and mechanical properties of the motor itself and the mechanical properties of the gear box. These elements were calibrated with the measured characteristics. Moreover, the elastic joints were implemented as modules. Their setup was chosen 1:1 according to Fig. 2.2. The crank was designed as a single module according to the real crank as used in the robotic experiment. Finally, the whole cranking setup was assembled in the computer with these modules and the dLPVF control algorithm was implemented as a Simulink S-function.

The outline of the cranking experiment in the dynamics simulation was basically the same as in Sect. 2.4.2. The manipulator was again initialised in a position in which the crank angle was 0°. All controller parameters remained the same. The system however was started by applying a small torque to the rotational joint of the crank disc for 0.3 seconds. After a short transient phase, the planar manipulator turned the crank with the desired velocity. Figure 2.7c and 2.7d display the results for the crank velocity plotted over time and over crank angle, respectively. It can be seen that the deviations from the desired velocity of the crank are stronger than in the kinematics simulation ($\bar{\omega}_{actual} = 65.38 \pm 3.59\,\mathrm{mm/s}$, $\bar{\omega}_{actual} = 86.20 \pm 3.60\,\mathrm{mm/s}$ and $\bar{\omega}_{actual} = 107.35 \pm 3.95\,\mathrm{mm/s}$). The mean deviation from the desired velocity lies between 7.4 and 9.0%. This increased value is due to the fact that in the dynamics simulation the inertia of the bodies involved try to keep up their states of motion. Also, the influence of the crank mass on the manipulator changes in different postures during cranking. In order to cope with this problem, one would have to find a dynamic control strategy for the velocity controller, which currently is not the main concern here. If the velocity controller is switched off completely, the manipulator performs cranking movements with a natural velocity of about 225 mm/s.

2.4.4 Real robot experiment

In a final step, the control architecture was implemented in a real robot (custom-made manipulator with Multiplex servos). Again the experimental outline remained the same. After initialisation of the arm in the same posture as in the simulations, the system was excited manually by applying a weak push to the crank handle. The robot turned the crank in the desired direction, as shown in Fig. 2.7(e) and 2.7(f). Furthermore, the desired velocities were adopted, albeit with slightly higher deviations than forecasted by the dynamics simulation [Fig. 2.7(c) and 2.7(d)]. The velocities observed were $\bar{\omega}_{actual} = 51.61 \pm 5.11\,\mathrm{mm/s}$, $\bar{\omega}_{actual} = 70.95 \pm 7.14\,\mathrm{mm/s}$ and $\bar{\omega}_{actual} = 89.56 \pm 6.68\,\mathrm{mm/s}$. The mean deviations fluctuate between 10.4 and 14.0%. In this case, the whole course of the diagram is shifted to lower velocities since the friction effects in the real system seemed to be higher than modelled in the dynamics simulation. Recapitulating one can assume that the control deviations can be further minimized if a more sophisticated control scheme for the velocity controller is used.

2.5 Efficiency and Stability

So far the decentral approach, when applied to the joints of an elastic planar manipulator, has proven to accomplish the compliant motion task of turning a crank. Important questions are then how efficiently the task is executed and how sensible the overall system reacts on variations of the physical and control parameters. Figure 2.8 gives an answer to the first question. It visualises the different bending angles that emerge during the cranking process in the dynamics simulation. On

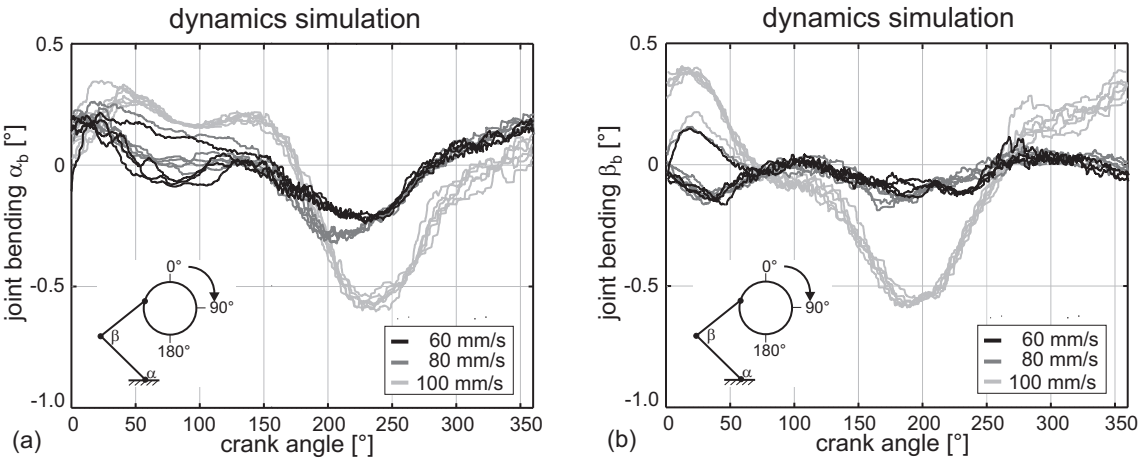

Figure 2.8: Bending of the α-joint (a) and β-joint (b) during consecutive crank rotations in the dynamics simulation.

the one hand the concept of LPVF is dependent on the occurrence of bending in the joint as a controller input. Assuming that our elastic joints have a linear relationship between bending angle and torque, it follows, on the other hand, that too much bending increases the torque and thus the energy consumption and the mechanical stress of the system. Therefore the amount of bending needed for the successful performance of the task is a quality measure for our decentral control approach. The bending values for both joints increase with the desired cranking velocity. In the range of velocities tested (60 to 100 mm/s), the bending of both joints lies in the interval from $0.4°$ to $-0.6°$. These are very good values if one considers that the position accuracy of the real servos used lies in the range of $\pm 0.5°$.

Figure 2.9 illustrates the cranking behavior when the position of the crank centre is changed in the dynamics simulation. Figure 2.9a shows the overall operating range of the planar manipulator, which covers the sectors A to D less the black centre at position $(0, 0)$. Geometrically possible positions for the crank centre are those areas in which the arm does not leave its operating range during a crank rotation. This is the case in sectors B and C but not in the hatched sectors A and D. The crank centre was shifted outwards from the innermost position in sector B on a straight line to the outermost position in sector C in 10 steps. This procedure was repeated for line angles from $0°$ to $180°$ in $10°$ steps. These 190 experiments are indicated by the black dots in Fig. 2.9(a). For each experiment the average peripheral crank velocity was determined. The desired crank velocity was $80\,mm/s$ and all other parameters remained as before. Figure 2.9(b) shows all cross sections along all 19 lines plotted on top of each other. In about 85% of the possible crank positions the controllers kept up the desired velocity of the crank [gray part of sector C in Fig. 2.9(a)].

For further proof of the system's stability the crank centre was put back to its default position [see Fig. 2.9(a)] and four tests were carried out with the dynamics simulation. The desired crank velocity was set to 80 mm/s and all other parameters were kept as in Sect. 2.4.3.

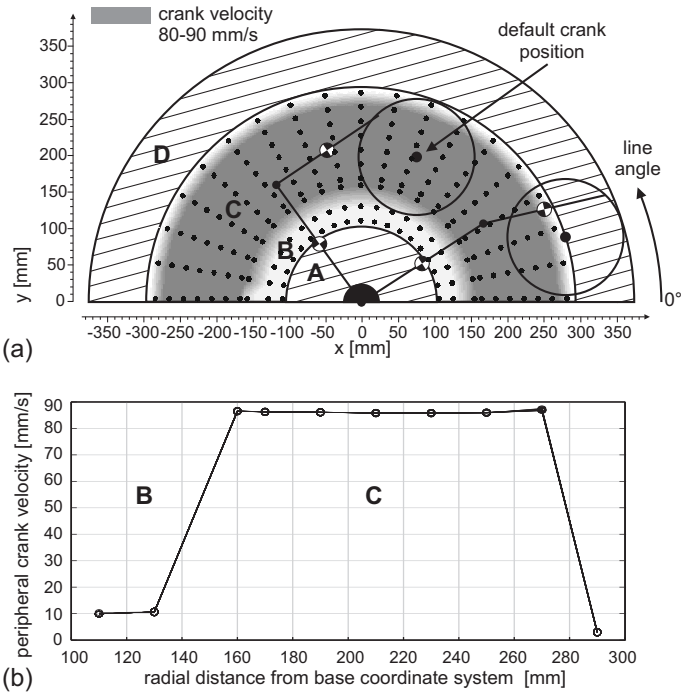

Figure 2.9: Crank performance for different crank positions in the dynamics simulation.

In the first test the crank radius was varied and the crank velocity observed. The default radius was 80 mm. A variation of ±50% ($r_c = 40...160$ mm) led to an actual peripheral crank velocity of $\bar{\omega}_{actual} = 85.04 \pm 2.35$ mm/s (mean value ±1 standard deviation).

In the second test the spring constant of both joints was varied. The default spring constant in both joints was $k_{\alpha,\beta} = 9.4$ Nm/rad. Again a variation of ±50% ($k_{\alpha,\beta} = 4.7 \ldots 14.1$ Nm/rad) resulted in an actual crank velocity of $\bar{\omega}_{actual} = 85.30 \pm 3.68$ mm/s.

In the third test the sample time was varied. The default sample time was $T_s = 0.08$ s. A variation of the sample time of ±20% ($T_s = 0.064 \ldots 0.096$ s) generated an actual crank velocity of $\bar{\omega}_{actual} = 86.26 \pm 3.69$ mm/s.

In the last test the P-value of the central velocity controller was varied [see Fig. 2.6]. The default P-value was $k_P = 0.06$. The maximum value was $k_P = 0.095$. A reduction of k_P led to a growing crank velocity. A value of $k_p = 0$ is equivalent to a free (uncontrolled) cranking with the two decentral dLPVF controllers. The process fell into its natural state, which is characterized by a cranking velocity of about 225 mm/s.

Outside the ranges discussed the system's performance degraded quickly. However, the task was accomplished successfully within a broad range of the parameters investigated, which demonstrates the benefits of our decentral control approach.

2.6 Discussion

With LPVF a novel alternative to classical strategies for solving compliant motion tasks is introduced. In technical applications using robots, compliant motion problems appear in different forms. Tasks in which robots have contact to objects tend to close the kinematic chain (base⇒robot⇒object⇒base). Important examples are assembly tasks (part mating, peg-in-hole problems), contact welding (following a surface) or cooperative manipulation with more than one robot (Yoshikawa and Zheng, 1990; Al-Jarrah et al., 1995; Al-Jarrah and Zheng, 1998). Legged locomotion also belongs into this group of tasks at least during stance phases (Kumar and Waldron, 1988; Kumar and Waldron, 1990; Gorinevsky and Schneider, 1990; Klein and Kittivatcharapong, 1990). Mason formulated the *Compliant Frame Formalism* or *Task Frame Formalism* to provide a specification tool for such problems (Mason, 1981). Most of the commonly used control strategies for compliant motions either follow the *hybrid control* approach (Raibert and Craig, 1981) or the *impedance control* approach (Hogan, 1985). In contrast to these control strategies, LPVF has a simple structure, it neither relies on an invariant and known geometry nor on the dynamics of the controlled process. As opposed to most of the hybrid control or impedance control algorithms, it has a decentral character meaning that every joint is controlled by its own LPVF controller. Coordination of the different joints is achieved through their mechanical interaction. A further advantage is the use of local sensor information coming from the close vicinity of the joint itself. Compared to LPVF controllers, central controllers have to cope with the problem of noise-induced errors on long information pathways as they rely on joint angle information of all distant joints. Thus the transfer of information via the mechanics of the animal or robot body and its immanent encoding in the local bending signal is a clear advantage of LPVF. As a consequence a system controlled by LPVF is error-tolerant since it is insensitive to mechanical changes for example due to plastic (permanent) deflection.

The idea of using serial elasticities in order to generate structural (passive) compliance is not new. Möhl used serial elastic elements for the construction of a composite drive which combines powerful operation and accuracy in a flexible robot arm (Möhl, 2003). An important feature of the composite drive is that the robotic system obtains tolerance against positioning errors. But positioning errors expose themselves through bending right in the moment they occur. The slightest bending signal causes the LPVF controller to take action and thus prevent position errors actively. This behavior is important especially for safety reasons. Berns, Kerscher and co-workers used fluidic muscles in order to drive the six-legged walking machines AirBug and AirInsect (Berns et al., 2001; Kerscher et al., 2004). Fluidic muscles are a good combination of actuator and elastic element. However, the combination of springs and electrical motors seems to be less complicated to control. At least the control of the electrical motors is a well understood task. Another design which makes use of passive compliance is implemented in RHex, a hexapod robot (Saranli et al., 2001). RHex has six actuators, one motor per hip. Its six compliant legs are brought to coordinated rotations

which let the robot traverse even rough terrain. The elasticity of the legs enables the robot to keep ground contact for all legs in their stance phase. As in our case the passive interaction with (objects in) the environment forces the system into a suitable state for the current situation. The LPVF approach goes one crucial step further by using the information of this passive process (bending) to actively resolve the situation (relaxation) and to extract the velocity of the motion.

Positive feedback in technical applications is often considered to be an unwanted side effect, but there are some examples in which positive feedback plays a crucial role. Positive position feedback (PPF) and active positive position feedback (APPF) is used for vibration suppression in flexible systems (Fanson and Caughey, 1990; Song et al., 2001; Rew et al., 2002). In rehabilitation engineering positive feedback is used in the form of patient-driven motion reinforcement (PDMR) by applying functional electrical stimulation of muscles (Riener et al., 2000). An inverse dynamic model predicts the stimulation pattern required to maintain the movement as it was initiated by the patient. This follows a similar fundamental idea as LPVF. PDMR, however, is a central rather than a decentral approach which requires complete knowledge of the inverse dynamics.

If LPVF is used for the generation of stance trajectories in walking, additional force control is desirable. Prochazka and co-workers gave indications on how this can be achieved (Prochazka et al., 1997a; Prochazka et al., 1997b). They found that positive force feedback appears in the feline locomotor control. Under certain circumstances positive force feedback reduces the sensitivity of the controlled extremities to perturbations and contributes to load compensation.

2.7 Conclusion

This chapter has shown that the compliant motion task of turning a crank can be solved by the novel decentral LPVF controller approach. Although the cranking process needs a high level of coordination between the participating joints, the joints are controlled independently. If information on the overall process parameters (like the crank velocity in the cranking example) is available, it can be used to alter the behavior of the single joints by the ω-controllability. The same system may be used to generate useful stance trajectories in a multi-legged robot during walking (see Chapter 4).

Chapter 3

Generation of large forces with Power Controlled LPVF

We introduce a new local joint controller for winching up heavy loads attached to a crank which is operated by a compliant manipulator. Recent studies on the local control of elastic joints in closed kinematic chains have revealed that *Local Positive Velocity Feedback (LPVF)* controllers coordinate several mechanically coupled joints of an elastic manipulator which has to solve a compliant motion task like cranking. Each controller measures the joint velocity and feeds it back positively into the joint actuator to maintain the joint velocity. Concurrently, joint bending due to the movement constraint of the tool is being relaxed by an active joint movement. Therefore, an LPVF controlled manipulator can follow an arbitrary contour. However, in the loaded case each bending of a joint consists of two parts, one is due to the deviation of the manipulator endpoint from the contour (which has to be relaxed) and the other is due to the load that has to be moved (which must not be relaxed). We propose *Power Controlled Relaxation LPVF* as a crucial extension of LPVF that restores the contour following ability and enables the manipulator to perform mechanical work (for example winching up heavy weights) even under the circumstances described above.

3.1 Introduction

Manipulators which are in contact with other objects while they accomplish a task can only perform constrained movements along the edge of the object. The *task frame formalism* (Mason, 1981), in which a coordinate frame is constructed at the endpoint of the manipulator, helps to distinguish a tangential and a normal direction of the contour for a given contact. The coordinate frame is moved together with the endpoint of the manipulator and is always oriented such that its axes represent the free and constrained degrees of freedom at the contact point separately. Tasks exist, in which the movement of the manipulator along the normal is only constrained in the approaching

direction because this movement would ultimately result in the penetration of the object. However, a movement away from the object would be possible. Examples of such a kind of compliant motions are *contact welding, surface inspection, seating and turning a bolt, sliding, pushing, leveling, and insertion or removal of a pin.* The situation becomes more difficult if disconnecting the manipulator from the object is impossible; this means that both approaching and departing movements along the contact normal are blocked. An example is *crank turning* which is the focus of this chapter. There are classical solutions for these tasks which are often based on *hybrid* (Raibert and Craig, 1981) or *impedance* (Hogan, 1985) control using central controllers based on global knowledge.

It has already been shown that *Local Positive Velocity Feedback* (LPVF) used for the control of elastic joints can solve compliant motion tasks without knowledge of either the construction of the limb the joint is part of or the overall (compliant motion) task that has to be accomplished (Schneider et al., 2005a). An LPVF joint controller determines the current velocity of its corresponding elastic joint and feeds it back positively into the joint actuator. With this strategy a joint in motion is maintaining its velocity. At the same time the LPVF controller measures the local bending of the elastic joint and superimposes a movement onto the positive feedback motor command which relaxes this bending. A multi-joint limb equipped with LPVF controllers exhibits a contour following ability in a compliant motion task using a local strategy only.

This chapter deals with a crucial extension of the LPVF control strategy which enables contour following of an LPVF controlled limb even if the local joint bending signal is superimposed by additional bending due to a large counter force acting on the manipulator endpoint along the contour. This could be, for example, large friction or heavy payloads which have to be moved by the limb.

We chose crank turning, a standard benchmark for compliant motion, as a test environment and increased the degree of difficulty by loading the crank with several extra weights on a string that have to be winched up by the planar manipulator operating the system (section 3.2). However, this control strategy could easily be adopted for other compliant motion tasks like walking of a multi-legged robot.

In Sect. 3.3 the original LPVF control strategy (LPVF with power controlled relaxation) is extended so that the controlled manipulator is enabled to winch up arbitrary weights and still manage tracking of the crank contour without any global knowledge. This approach will be compared with a hybrid control strategy that is based on LPVF, but uses global knowledge in order to cancel out the normal forces at the crank handle. The new extension of LPVF works more efficiently than the hybrid control strategy with respect to the torque effort in the joints. It is still possible to control the overall velocity of the cranking process with a central velocity controller that communicates with the local joint controllers. Finally, the choice of an appropriate spring constant for the elastic joints is discussed (Sect. 3.4).

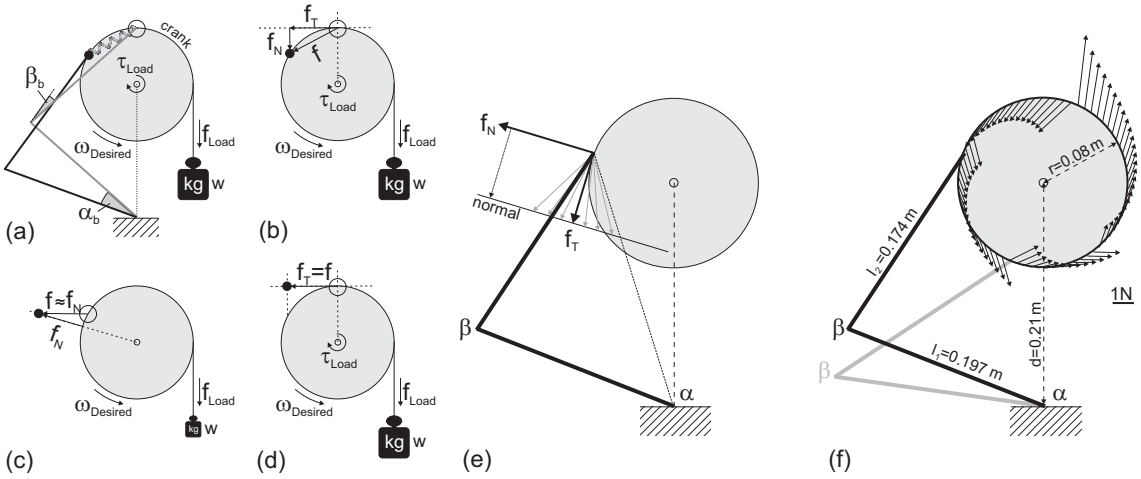

Figure 3.1: Task description of the loaded crank situation.

3.2 Task formulation

The task is to winch up a load with an elastic manipulator while retaining the decentral control strategy. Figure 3.1(a) shows a simplified sketch of the loaded crank situation (see Fig. 3.2 for the setup used). A weight w is attached to the crank (gray disc) via a string. The weight exerts a force $\vec{f}_{\text{Load}}$ on the crank perimeter which leads to a torque $\vec{\tau}_{\text{Load}}$ acting on the crank pivot. First, we assume a planar manipulator (black lines) with inelastic joints α and β whose gripper is attached to the handle of the crank (black dot). This manipulator generates the counter torque and thus balances the crank system. The weight is kept in an equilibrium position.

The black inelastic manipulator is a construct that represents a posture due to the motor angles (α_m and β_m) and is used here for explanation purposes only. It shows how an arm without elastic joints would react on the motor commands sent by the local LPVF controllers. We thus call this inelastic arm the *virtual manipulator*.

In the case of elastic joints, joint angles can be split into two parts, the motor angle and the bending angle ($\alpha_j = \alpha_m + \alpha_b$, $\beta_j = \beta_m + \beta_b$). The elastic manipulator (gray lines) and its tool (small open circle) adopt a new equilibrium posture because the elastic elements in the joints have to be stretched until they generate enough joint torque to balance the overall system again. The respective bending angles (α_b, β_b) are depicted in Fig. 3.1(a). It is important to mention that LPVF controllers require elastic joints (Schneider et al., 2005a). Therefore, the gray elastic manipulator is the actual manipulator used in the present study.

For a given posture, the system can be simplified by introducing an extension spring that connects the endpoint of the virtual manipulator (black) and the elastic joint manipulator (gray). This connection represents the force $\vec{f}$ which the manipulator exerts on the handle. This force can be split up into a force $\vec{f}_T$ tangential to the contour and a force $\vec{f}_N$ normal to the contour [Fig. 3.1(b)]. The tangential force component is necessary to lift the weight. If we neglect the mass of the crank

and of the manipulator, the crank is accelerated for $\vec{f}_T > \vec{f}_{\text{Load}}$ and is decelerated for $\vec{f}_T < \vec{f}_{\text{Load}}$. Here, we want to distinguish two important situations: First, winching up only a small weight and second winching up arbitrary weights by only generating tangential forces. In the former case the coordination task is almost not disturbed by superimposed bending due to a load [Fig. 3.1(c)]. If only a small weight is attached to the crank, also the corresponding tangential force $\vec{f}_T$ becomes very small. In this case it is sensible to assume that the overall force $\vec{f}$ consists of the normal force $\vec{f}_N$ only. The normal force is due to motor commands that try to move the manipulator away from the contour and therefore result in unnecessary bending in the elastic joints which can be relaxed completely. This is the situation which LPVF has coped with so far (Schneider et al., 2005a). The joint velocity was fed back positively and at the same time the complete bending was relaxed which resulted in perfect contour tracking without any global knowledge of the system's kinematics. But this strategy can only be applied if the joint movement in each step is larger than the relaxation.

The second case is depicted in Fig. 3.1(d). To winch up an arbitrary weight, only tangential forces are needed. Thus, it seems desirable to send only those motor commands to the two elastic joints that satisfy this condition. This solution is only possible with some global knowledge of the setup. In terms of the force exerted on the handle of the crank this strategy seems to be optimal as it generates the smallest possible force that solves the task.

But there is a further aspect to be considered. Is generating tangential forces also optimal in the sense of a minimal joint torque generation? Figure 3.1(e) shows that for a given tangential force it is possible to choose an arbitrary normal force which is led into the structure but does not lead to a movement of the manipulator. The joint torques can be calculated from the overall force with the help of the manipulator Jacobian:

$$\vec{\tau}_{\text{joint}} = J^T(\vec{q}, \vec{l})\vec{f}_{\text{handle}} \tag{3.1}$$

with $\vec{\tau}_{\text{joint}} = [\tau_\alpha, \tau_\beta]^T$, $\vec{q} = [\alpha_j, \beta_j]^T$ being the joint angles and $\vec{l} = [l_1, l_2]^T$ the segment lengths of the manipulator. We use the L^1 norm of the torque vector as a cost function that measures how much mechanical energy is fed into the manipulator. If there is no weight attached to the crank, the lowest value of $|\vec{\tau}|_1$ is achieved for $\vec{f} = \vec{f}_T = \vec{f}_N = 0$, which was to be expected intuitively. But the situation changes if a weight is attached to the crank as can be exemplified by an experiment in which the crank undergoes one full rotation in 1° steps. At each angular crank position the manipulator Jacobian is determined, a fixed tangential force of $|\vec{f}_T| = 1\,\text{N}$ applied and the normal force $|\vec{f}_N| = d|\vec{f}_T|, d = -10 \ldots 10$ varied. For each different position of the crank handle Fig. 3.1(f) shows those hand force vectors $\vec{f}$ whose torque vector cost function $|\vec{\tau}|_1$ was minimal in the experiment. It can be seen that the best choice for the hand force vector to minimize the joint torques almost always differs from the tangential force.

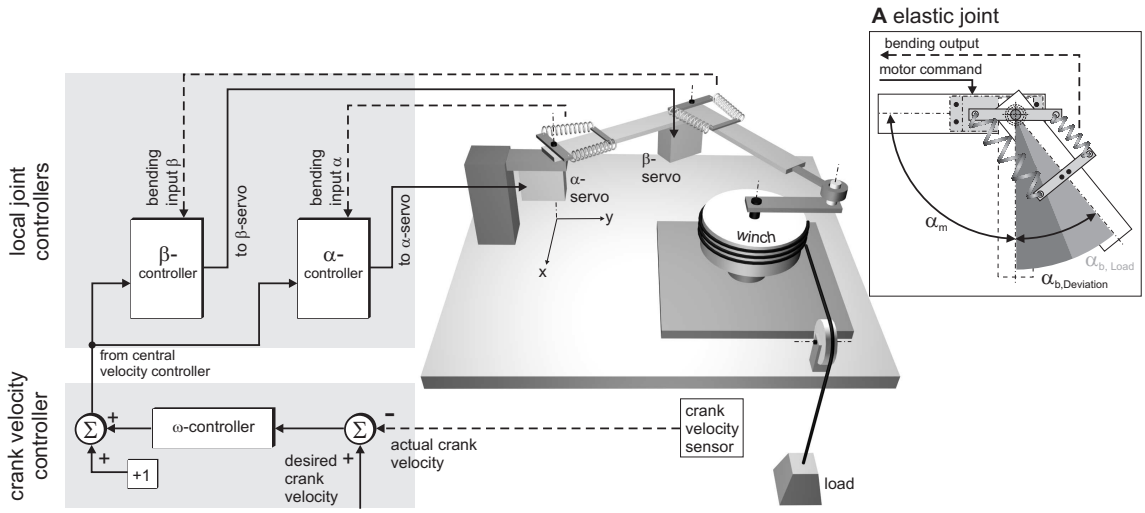

Figure 3.2: The overall setup of the loaded crank experiment. Inset A shows the bending situation in the elastic joint.

3.3 Local versus central control approaches

In order to compare central and local approaches we used the setup shown in Fig. 3.2. The endpoint of the manipulator is connected to the handle of a crank. This results in one rotational degree of freedom, and a changing translatory degree of freedom in tangential direction to the crank perimeter. A movement along the normal direction with respect to the contour results in a cross force which in turn produces bending in the elastic manipulator joints (α_b, β_b).

As long as the winch carries no load, the bending in both elastic joints is a result of the cross force that appears if the manipulator shows the tendency to leave the contour during the cranking movement. A local relaxation mechanism, such as the basic LPVF joint controller, could resolve the local bending completely. However, if a weight is attached to the winch it produces a tangential force at the crank handle which in turn results in an additional bending portion in the elastic joints. This situation is depicted in inset A of Fig. 3.2. The overall bending angle of one joint in this case consists of two portions: $\alpha_b = \alpha_{b,\text{Deviation}} + \alpha_{b,\text{Load}}$ and $\beta_b = \beta_{b,\text{Deviation}} + \beta_{b,\text{Load}}$. The bending angle is a scalar value and it seems to be impossible to separate the two angular parts "hidden" in this value only based on local joint information. However, in sections 3.3.2 to 3.3.4 we will derive LPVF-based joint controllers, which are able to solve this task using local information only.

The elastic joint shown in inset A of Fig. 3.2 is equipped with a servo motor and a serial elastic element (formed by two extension springs) (Schneider et al., 2005a; Schneider et al., 2006a). This joint possesses one single input which is the control signal for the servo motor and one single output which delivers the current bending angle of the joint. Each elastic joint of the manipulator is controlled by its own joint controller (α- and β-controller, respectively (Fig. 3.2)). This controller possesses one single input which is the bending signal from the corresponding joint and one single output which is the next angular servo motor position.

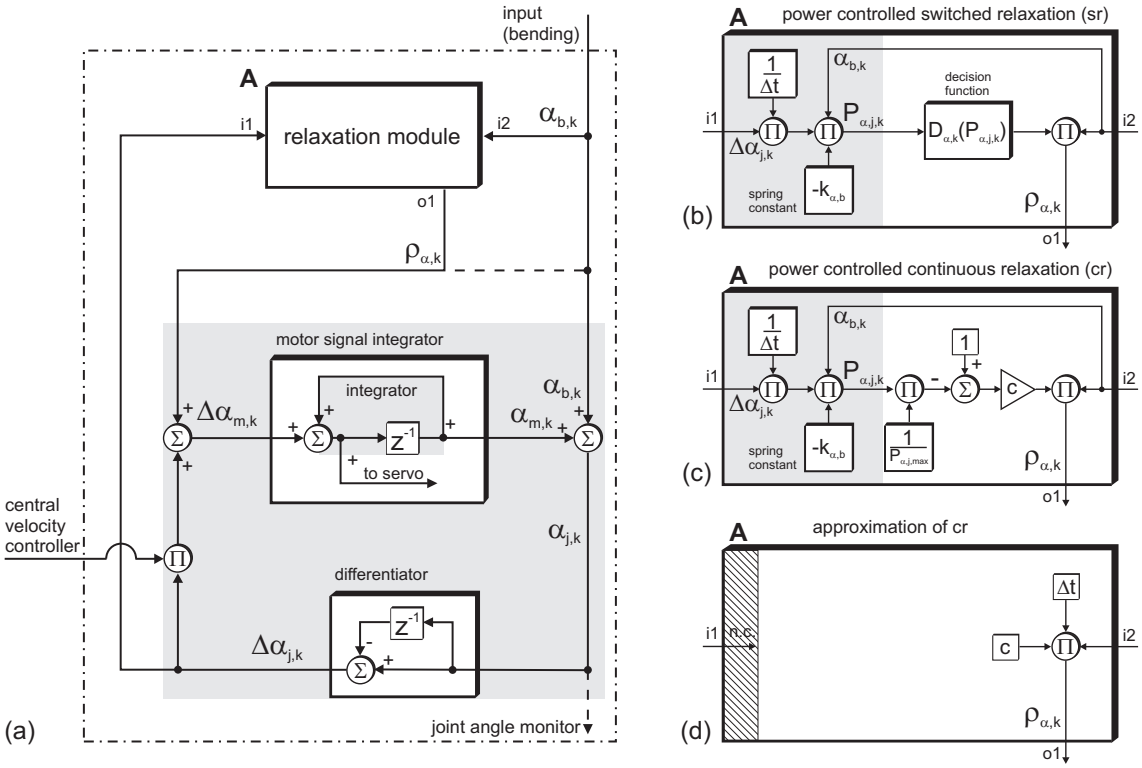

Figure 3.3: Local Positive Velocity Feedback with relaxation module A (a) and different local implementations of the module (b-d).

In the lower left gray box of Fig. 3.2 an additional crank velocity controller (ω-controller) is depicted, which calculates the deviation of the actual crank velocity ω_a from the desired value ω_d. The ω-controller generates global information at its output which has no meaning for the local controllers per se since they have no knowledge about the task. By adding 1 to the output of the ω-controller it can be used to scale the feedback gain of the Local Positive Velocity Feedback [see product on the left side of Fig. 3.3(a)].

3.3.1 The basic LPVF circuit

Local Positive Velocity Feedback control is a basic control strategy that serves as a foundation for all following controllers in this study. Figure 3.3(a) shows the content of the α- and β-controller boxes as introduced in Fig. 3.2. The basic LPVF circuit is shaded in gray. The summation (Σ-sign) on the right side of the gray area represents the calculation of the true joint angle $\alpha_{j,k}$ from the current angular motor position $\alpha_{m,k}$ and the bending input $\alpha_{b,k}$ in time step k. Thus, this part of the circuit reflects the function of the corresponding elastic joint as shown in inset A of Fig. 3.2. The actual joint angle $\alpha_{j,k}$ is fed into a discrete differentiator to obtain the current joint velocity $\Delta\alpha_{j,k}$. It has to be emphasized that this value shows the effective movement of the joint independent of the motor movement. If, for example, the manipulator tool had no degree of freedom left, i.e. if it was fixed completely, the motor movement and the resulting change of bending cancelled each

other out. The net joint movement would be zero. Therefore, it can be argued that the joint velocity $\Delta\alpha_{j,k}$ contains information about how much movement can be generated effectively by the joint drive in the constrained situation given. By positively feeding back the velocity signal $\Delta\alpha_{m,k}$ into the motor signal integrator, the next desired angular position of the servo motor is determined.

This LPVF strategy ensures that the next motor movement adapts to the unknown mechanical constraints of the manipulator in the current posture independent of how unappropriate the last motor command might have been. As a consequence, the concerted movements of all joints result in a manipulator movement tangential to the restricting crank contour without a central instance that coordinates the joints.

As the tangential movement does not lead to a perfect contour following (the arm tends to leave the crank perimeter), the elastic joints accumulate more and more bending. In addition to positively feeding back the joint velocity $\Delta\alpha_{j,k}$, the accumulated joint bending is relaxed by adding a relaxation signal $\rho_{\alpha,k}$ in order to get the next motor step $\Delta\alpha_{m,k}$ [see sum at the input of the motor signal integrator in Fig. 3.3(a)]. In the unloaded case, the bending value $\alpha_{b,k}$ can be chosen as a relaxation signal [see dashed line in Fig. 3.3(a)]. As discussed above, this simple relaxation strategy is not sufficient if the manipulator has to shift a considerable weight. In this case the relaxation signal $\rho_{\alpha,k}$ is generated by a relaxation module A as depicted in the upper part of Fig. 3.3(a).

The system equations for the basic LPVF circuit in Fig. 3.3(a) are the following:

$$\alpha_{m,k} = \alpha_{m,k-1} + \Delta\alpha_{m,k-1} \tag{3.2a}$$

$$\alpha_{j,k} = \alpha_{m,k} + \alpha_{b,k} \tag{3.2b}$$

$$\Delta\alpha_{m,k} = \Delta\alpha_{j,k} + \rho_{\alpha,k} \tag{3.2c}$$

$$\Delta\alpha_{j,k} = \alpha_{j,k} - \alpha_{j,k-1}. \tag{3.2d}$$

Equation (3.2a) describes the motor integrator, (3.2b) is the equation of the elastic joint, (3.2c) describes the input of the motor integrator consisting of the actual local velocity feedback of the joint (3.2d) and the output of the relaxation module $\rho_{\alpha,k}$.

The value of the angular joint velocity in the current time step can be determined by inserting (3.2b) in (3.2d) and using (3.2a) to merge the appearing motor expressions:

$$\begin{aligned} \Delta\alpha_{j,k} &= \alpha_{m,k} + \alpha_{b,k} - \alpha_{m,k-1} - \alpha_{b,k-1} \\ &= \Delta\alpha_{m,k-1} + \Delta\alpha_{b,k}. \end{aligned} \tag{3.3}$$

Replacing the motor expression $\Delta\alpha_{m,k-1}$ in (3.3) by (3.2c) results in:

$$\Delta\alpha_{j,k} = \Delta\alpha_{j,k-1} + \rho_{\alpha,k-1} + \Delta\alpha_{b,k}. \tag{3.4}$$

Reorganization of (3.4) determines the angular acceleration of the joint:

$$\begin{aligned} \Delta\alpha_{j,k} - \Delta\alpha_{j,k-1} &= \rho_{\alpha,k-1} + \Delta\alpha_{b,k} \\ \Leftrightarrow \Delta^2\alpha_{j,k} &= \rho_{\alpha,k-1} + \Delta\alpha_{b,k}. \end{aligned} \tag{3.5}$$

Finally, the expression for the angular joint velocity is obtained by integration of (3.5):

$$\Delta\alpha_{j,K} = \underbrace{\text{const} + \sum_{n=0}^{K-1} \rho_{\alpha,n}}_{\text{base angular velocity}} + \alpha_{b,K} \tag{3.6}$$

The joint velocity depends on the sum of all former outputs $\rho_{\alpha,n}$ of the relaxation module that have occurred up to the last but one time step plus a constant. The bending $\alpha_{b,K}$ in the current time step K modulates that value. Therefore, the current velocity of the joint is a deviation of a base angular velocity which is represented by the chosen relaxation strategy. In sections 3.3.2 to 3.3.5 four different LPVF-based joint controllers with different relaxation strategies are described. In the results (Sect. 3.4) their abilities to solve the problem will be tested and compared.

3.3.2 LPVF with Power Controlled Switched Relaxation

If no weight is attached to the crank, the joint bending signal $\alpha_{b,k}$ can be chosen as a relaxation signal [see dashed line in Fig. 3.3(a)], which results in a perfect contour following behavior of the manipulator (Schneider et al., 2005a). Yet, in the loaded case the attached weight superimposes a load- and posture-dependent bending on the elastic joint. The weight would be lowered instead of winched up if the above strategy was still applied because the entire bending was relaxed.
In order to gain control over the bending dependent relaxation, a relaxation module as depicted in Fig. 3.3(b) is introduced in the joint controller of Fig. 3.3(a). The input i2 represents the bending signal $\alpha_{b,k}$. It is multiplied by the decision function $D_{\alpha,k}$. Thus, the decision function works like a switch that connects through the bending $\alpha_{b,k}$ as a relaxation signal $\rho_{\alpha,k}$. The switch is closed if $D_{\alpha,j,k} = 1$ and it is opened if $D_{\alpha,j,k} = 0$. The decision function is based on the mechanical power which is generated in the elastic joint:

$$D_{\alpha,j,k}(P) = \begin{cases} 1 & : \text{ if } P_{\alpha,j,k} < 0 \\ 0 & : \text{ if } P_{\alpha,j,k} \geq 0 \end{cases} . \tag{3.7}$$

The mechanical joint power is the product of the angular joint velocity and the joint torque and can thus be calculated as:

$$P_{\alpha,j,k} = \frac{\Delta\alpha_{j,k}}{\Delta t}\tau_{\alpha,k} = -\frac{\Delta\alpha_{j,k}}{\Delta t}k_{\alpha,b}(\alpha_{j,k} - \alpha_{m,k}), \tag{3.8}$$

with $\tau_{\alpha,k}$ being the joint torque, Δt the sample time and $k_{\alpha,b}$ the spring constant of the joint.
The calculation of (3.8) is depicted in the gray area on the left side of Fig. 3.3(b). The input i1 represents the joint velocity $\Delta\alpha_{j,k}$. The joint velocity is divided by the sample time Δt in order to get a value which is independent of the sample time. The bending signal $\alpha_{b,k}$ is multiplied by the spring constant $k_{\alpha,b}$ of the elastic joint, which results in the current joint torque. The product of joint torque and joint velocity is the mechanical power $P_{\alpha,j,k}$, which is fed into the decision function.

If the mechanical power is positive, the actuator and the joint movement have the same direction. This indicates that the joint actuator is in traction mode, which in turn means that the overall task of winching up a weight benefits from the joint movement (switch opened, no relaxation).
If the mechanical power is negative, the actuator and the joint movement have opposite directions. This is an indicator for the joint actuator being in coasting mode, which means that other joints in the closed kinematic chain enforce the observed joint movement. In this case the overall task does not benefit from the motor action of the joint. The joint bending can be relaxed (switch closed).
If both joints of the planar manipulator in Fig. 3.2 are equipped with LPVF controllers, which use Power Controlled Switched Relaxation, the manipulator is able to winch up a weight.

3.3.3 LPVF with Power Controlled Continuous Relaxation

The switched relaxation strategy which was introduced in section 3.3.2 is based on a discrete "yes" or "no" decision which results in abrupt behaviors of the corresponding joint. In this section, a continuous relaxation strategy is derived in order to achieve a smooth relaxation. This strategy already relaxes parts of the bending, when the joint still generates positive mechanical power. Fig. 3.3(c) depicts the Power Controlled Continuous Relaxation controller. As in Fig. 3.3(b), the gray area in Fig. 3.3(c) indicates the calculation of the current mechanical joint power $P_{\alpha,j,k}$. While operating, each joint controller stores the maximum mechanical joint power $P_{\alpha,j,\max}$ which has been generated so far. $P_{\alpha,j,\max}$ is used to normalize the mechanical joint power in order to gain a measure that attains values between zero and one for control purposes. The normalized power is subtracted from one and multiplied by a relaxation factor c. The relaxation output $\rho_{\alpha,k}$ [Fig. 3.3(a), o1] can be written as:

$$\rho_{\alpha,k} = \left(1 - \frac{P_{\alpha,j,k}}{P_{\alpha,j,\max}}\right) c\, \alpha_{b,k} \tag{3.9}$$

If the mechanical joint power is large (near 1), the input i2 ($\alpha_{b,k}$) is multiplied by a small number. The relaxation output and thus the relaxation effect is very small. For low mechanical power (near 0) the input i2 ($\alpha_{b,k}$) is multiplied by a large number which is equivalent to a large relaxation output and to a large relaxation effect.
In contrast to the switched relaxation version (section 3.3.2), the continuous relaxation influences the behavior of the local joint all the time. The differences between the two versions concerning hand force and joint torque generation will be discussed in the results.

3.3.4 Approximation of Power Controlled Continuous Relaxation

The idea of Power Controlled Continuous Relaxation can be further simplified. By inserting the mechanical joint power (3.8) into the relaxation output function (3.9) we get the following expression:

$$\rho_{\alpha,k} = c\, \alpha_{b,k} + c\, k_{\text{aux}}\, \alpha_{b,k}^2\, (\alpha_{j,k} - \alpha_{j,k-1}) \tag{3.10}$$

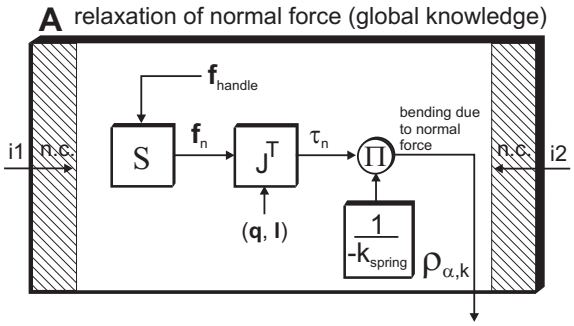

Figure 3.4: Normal Force Relaxation Controller using global information.

with $k_{\text{aux}} = k_{\alpha,b}/(\Delta t\, P_{\alpha,j,\max})$. Assuming that the bending angles are very small we omit the second summand of (3.10) because of the quadratic bending term and obtain:

$$\rho_{\alpha,k} = c\,\alpha_{b,k}. \tag{3.11}$$

According to (3.11), it is possible to use a relaxation module as depicted in Fig. 3.3(d). In section 3.4 we will show that this simple solution also works but that the joint torque generation of this system is higher compared to that of a manipulator with Power Controlled Continuous Relaxation controllers.

3.3.5 LPVF with Normal Force Relaxation

Finally, we introduce a joint controller based on the LPVF strategy for the maintenance of the joint velocity. However, in this case global information is used additionally to generate only those joint movements, which lead to tangential forces at the crank handle. The relaxation module can be seen in Fig. 3.4. The tool force $\vec{f}_{\text{handle}}$ is measured and the normal force $\vec{f}_N$ is separated by a selection matrix S. In the static case the joint torques of a given manipulator (segment lengths $\vec{l}$) in a certain posture (joint angles $\vec{q}$) can be calculated from the hand force by using the transposed manipulator Jacobian (3.1). If only the undesired normal force $\vec{f}_N$ is inserted into (3.1) we get the share τ_n of the joint torque which caused the normal force. Dividing τ_n by the spring constant k_{spring} results in the bending angle of the joint which is responsible for the normal force in the given posture. This bending angle can be used as the relaxation signal $\rho_{\alpha,k}$. The local inputs i1 and i2 are not connected. If each elastic joint in the kinematic chain is controlled by this controller, the normal force at the tool vanishes.

3.4 Simulation results

The four different joint controllers introduced in section 3.3 were tested in a dynamics simulation of the loaded crank setup as shown in Fig. 3.2. The results of the simulations are discussed with

respect to the different forces generated at the crank handle and with respect to different torques generated during operation. For our local approach (LPVF with Power Controlled Continuous Relaxation) it is shown that it winches up weights with different desired cranking velocities.

3.4.1 Dynamics simulation

The dynamics simulation of the setup in Fig. 3.2 was implemented in Simulink 6.1 and SimMechanics 2.2.1 (The MathWorks Inc., Natick, MA). In the simulation we neglected the masses of the manipulator segments and of the crank. The mass of the weight was $m_{\text{load}} = 0.1\,\text{kg}$, the segment lengths $l = [0.197, 0.174]^T\,\text{m}$, the crank radius $r_{\text{crank}} = 0.08\,\text{m}$ and the position of the crank $x_c = [0, 0.21]^T\,\text{m}$ in accordance with Schneider et al., 2005a.

Starting from the joint bending angles and the joint torques respectively, the hand force can be calculated with:

$$\vec{f}_{\text{handle}} = J^{-T}(\vec{q}, \vec{l})\,\vec{\tau}. \tag{3.12}$$

The hand force is then projected onto the tangent of the crank contour which yields the tangential force $\vec{f}_T$ that acts on the weight to be lifted. The difference between the tangential force f_T and the gravitational force $m_{\text{load}}\,g$ accelerates the weight upwards. The translational movement of the weight corresponds to a rotational movement of the crank. This means that the handle of the crank adopts a new angular position. Based on the new handle position, a new posture of the manipulator can be calculated using inverse kinematics. The difference of the new posture and the old posture causes new bending angles in the joints. These are fed into the corresponding joint controllers, which calculate the next motor commands. We assume that the motors adopt the shaft angles within one time step. At this point the simulation cycle starts again. The sample time of the simulation was $\Delta t = 0.1\,\text{ms}$.

The simulation is started by adding a displacement to the initial arm posture in the desired direction of cranking for a few time steps (here: $10\Delta t$).

3.4.2 Forces and relaxation signals

The four columns in Fig. 3.5 show force generation and relaxation data of the four joint controllers. Fig. 3.5 (upper row) shows the hand force vectors $\vec{f}_{\text{handle}}$ plotted in 5°-steps and Fig. 3.5 (lower row) the relaxation signal $\rho_{\alpha,k}$ in black and $\rho_{\beta,k}$ in gray for the four different joint controller types introduced in section 3.3. The relaxation signals are plotted over the crank circle perimeter which serves as the coordinate axis for the crank angle. Since $\rho_{\beta,k}$ (gray) is plotted on top of $\rho_{\alpha,k}$ (black) the gray areas sometimes overlap the black areas. In those cases the courses of the black curves are indicated by a black line. Positive values lie outside and negative values inside the circle. For clarity's sake, the crank perimeter is marked by light gray dots. Within the circles representing the crank perimeter the crank angles for extreme manipulator joint angles (*joint reversals*) are plotted

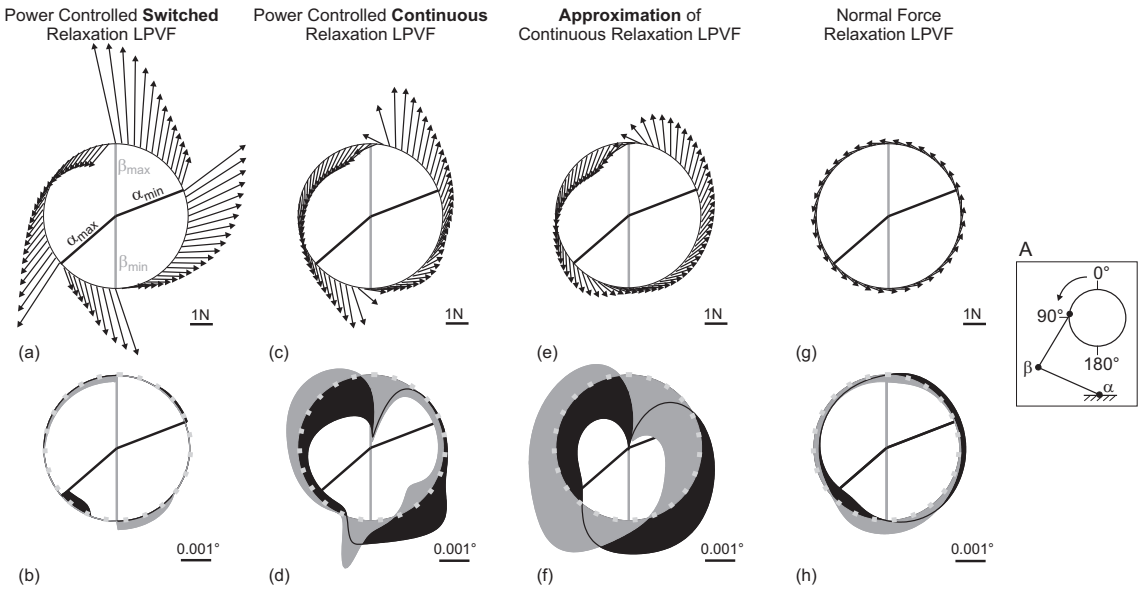

Figure 3.5: Forces (upper row) and relaxation signals (lower row) for four different joint controllers.

in black for the α-joint ($\alpha_{\min}$ and $\alpha_{\max}$) and in gray for the β-joint ($\beta_{\min}$ and $\beta_{\max}$). The direction of rotation for winching up the weight is counterclockwise as indicated in inset A of Fig. 3.5.

Fig. 3.5(a) shows the forces at the crank handle for LPVF Power Controlled Switched Relaxation. For crank angles from 0° until the maximum of the α-joint the normal part of the hand force vector grows. For $\alpha_{j,k} = \alpha_{\max}$ the mechanical joint power according to (3.8) becomes negative because the joint velocity changes its direction. Fig. 3.5(b) shows that the α-relaxation begins at the $\alpha_{\max}$-angle. Notice that the relaxation action for the α-joint does not guarantee that the mechanical joint power of the joint becomes positive immediately. In fact the relaxation signal is switched on for a cranking movement of about 20°. Although the relaxation is switched on discretely by the decision function (3.7), it is not a singular event. The same behavior can be observed for the other three extreme joint angles at $\beta_{\min}, \beta_{\max}$ and $\alpha_{\min}$.

Fig. 3.5(c) shows the hand forces for LPVF with Power Controlled Continuous Relaxation. Since the relaxation signal is present all the time, the hand force vectors tend to be smaller during the whole crank rotation. Fig. 3.5(d) shows the corresponding relaxation signals. Clearly, $\rho_{\alpha,k}$ (black) has the largest impact between the extreme values ($\alpha_{\min}$, $\alpha_{\max}$) of the corresponding α-joint. $\rho_{\beta,k}$ (gray) has peaks in the vicinity of the extreme values ($\beta_{\min}$, $\beta_{\max}$) of the β-joint.

Fig. 3.5(e) depicts the course of the hand force vector for the Approximation of the Power Controlled Continuous Relaxation. Compared to Fig. 3.5(c) the absolute values of the hand forces in Fig. 3.5(e) are smaller. This is because of the larger relaxation signals $\rho_{\alpha,k}$ (black) and $\rho_{\beta,k}$ (gray), which are shown in Fig. 3.5(f). Even though this seems to be an advantage for this approximated version, it will be shown in section 3.4.3 that the approximated version has higher joint torque costs than LPVF with Power Controlled Continuous Relaxation.

Finally, Fig. 3.5(g) displays the course of the hand force vector for the LPVF controller which uses global information in order to prevent normal forces at the crank handle (Normal Force Relaxation). As expected, only tangential forces of approximately 1 N for lifting the 0.1 kg weight are generated. The corresponding relaxation signals in Fig. 3.5(h) show lower activity than Power Controlled Continuous Relaxation LPVF controllers and their approximated version in Fig. 3.5(d,f).

In summary, the data show that the Normal Force Relaxation LPVF is optimal with respect to the absolute values of the hand forces that are produced. The controllers using LPVF only generate larger hand forces with large normal force portions. In section 3.4.3 it will be shown that Power Controlled Continuous Relaxation LPVF and its approximation, in addition to their advantage of being local solutions, are also better than the central Normal Force Relaxation approach with respect to the absolute amount of torque generated by the joints.

3.4.3 Joint torque dissipation

The amount of torque is a measure for the energy consumption of the manipulator. If the same task of winching up a certain weight can be accomplished with lower amounts of joint torque, the efficiency of the system is higher. The following cost function describes the joint torque consumption of the elastic manipulator:

$$\tau_{\text{abs}} = |\tau_\alpha| + |\tau_\beta|. \tag{3.13}$$

In order to get an overview of the robustness of our crank turning approaches against variable crank positions, we positioned the crank center at different distances from the manipulator base. According to Schneider et al., 2005a; Schneider et al., 2005d, the minimum distance was chosen to be $\text{dist}_{\text{crank,min}} = 0.12\,\text{m}$ and the maximum distance $\text{dist}_{\text{crank,max}} = 0.27\,\text{m}$. In each crank position the joint torque consumption according to (3.13) was calculated for each time step of the dynamics simulation. The resulting curve was plotted over the crank angle for three rotations (1080°). Fig. 3.6(a) shows the result for the minimum crank distance of 0.12 m. The black line indicates the absolute torque of both elastic joints if these joints are controlled by Power Controlled Continuous Relaxation LPVF with a relaxation constant $c = 21$ (3.9). The dotted line shows the absolute torque for the Normal Force Relaxation LPVF controller. The first rotation exhibits a transient behavior until the system has accelerated to the desired cranking velocity. The torque generation for both controller types is approximately the same. If the distance of the crank from the manipulator base is increased, the Normal Force Relaxation LPVF controller shows larger absolute torques than the Power Controlled Continuous Relaxation LPVF controller. Fig. 3.6(b) shows this result for $\text{dist}_{\text{crank}} = 0.21\,\text{m}$ and Fig. 3.6(c) for $\text{dist}_{\text{crank}} = 0.27\,\text{m}$.

In the course of two crank rotations ($d = 0.16\,\text{m}$) the weight ($m_{\text{load}} = 0.1\,\text{kg}$) is lifted 1 m. For each crank distance $\text{dist}_{\text{crank}}$ from the manipulator base we integrated the joint torque consumption

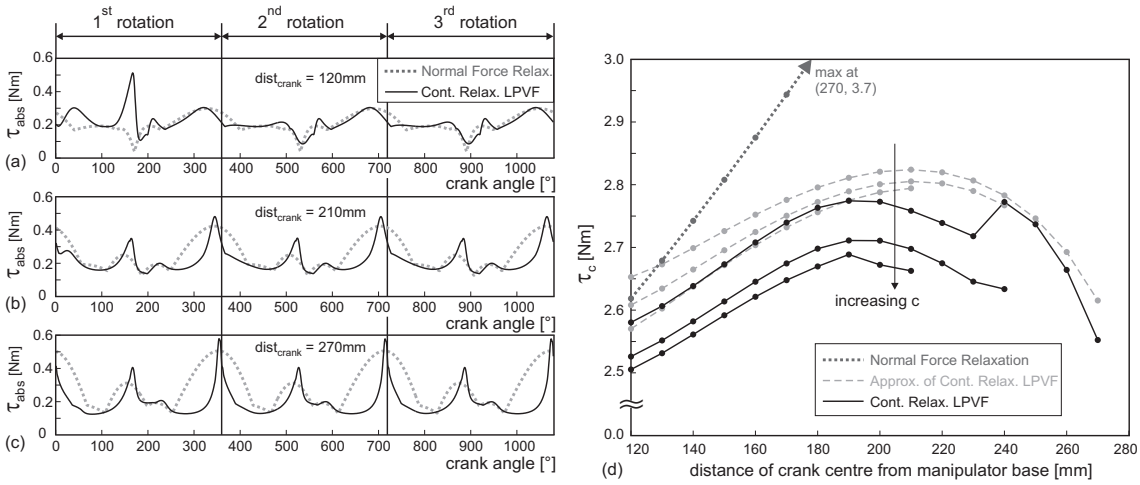

Figure 3.6: Torque consumption for three different crank distances (a-c) and the cumulative torque for two crank rotations (d).

(3.13) of the second and third rotation in order to get the cumulated torque consumption for lifting the weight by 1 m:

$$\tau_c(\mathrm{dist_{crank}}) = \int_{T360^\circ}^{T1080^\circ} (|\tau_\alpha| + |\tau_\beta|)\, dt. \tag{3.14}$$

The first rotation was omitted to avoid starting effects. Fig. 3.6(d) depicts the results of (3.14) for the manipulator operated by Normal Force Relaxation LPVF controllers (dotted line), the Power Controlled Continuous Relaxation LPVF controllers (solid black line) and their approximation (dashed line).

We have shown that the manipulator equipped with Normal Force Relaxation LPVF joint controllers generated the lowest hand forces in the loaded crank turning task [Fig. 3.5(g)]. However, it can be seen in Fig. 3.6(d) (dotted line) that the cumulative torque consumption is increasing with increasing distance of the crank from the manipulator base. In fact, its cumulative torque consumption is almost always higher than that of the other approaches.

The second highest cumulative torque consumption is exhibited by the Approximation of the Power Controlled Continuous Relaxation approach [Fig. 3.6(d), dashed lines]. The three different dashed lines indicate simulations with three different c-values (3.11). It can be seen that a higher relaxation constant c leads to a lower cumulative torque consumption. However, if c is chosen too high, the operating range of the planar manipulator decreases. In other words, the loaded crank cannot be operated if the arm has to adopt outstretched postures during cranking.

Crank turning with Power Controlled Continuous Relaxation LPVF controllers [Fig. 3.6(d), solid black lines] displays the lowest cumulative torque consumption. It is possible to increase the relaxation constant c even more than in the approximated version before the operating range degenerates. Power Controlled Continuous Relaxation allows for a local joint control of an elastic manipulator in loaded crank turning with the lowest energy consumption of all competing controllers discussed in the present chapter.

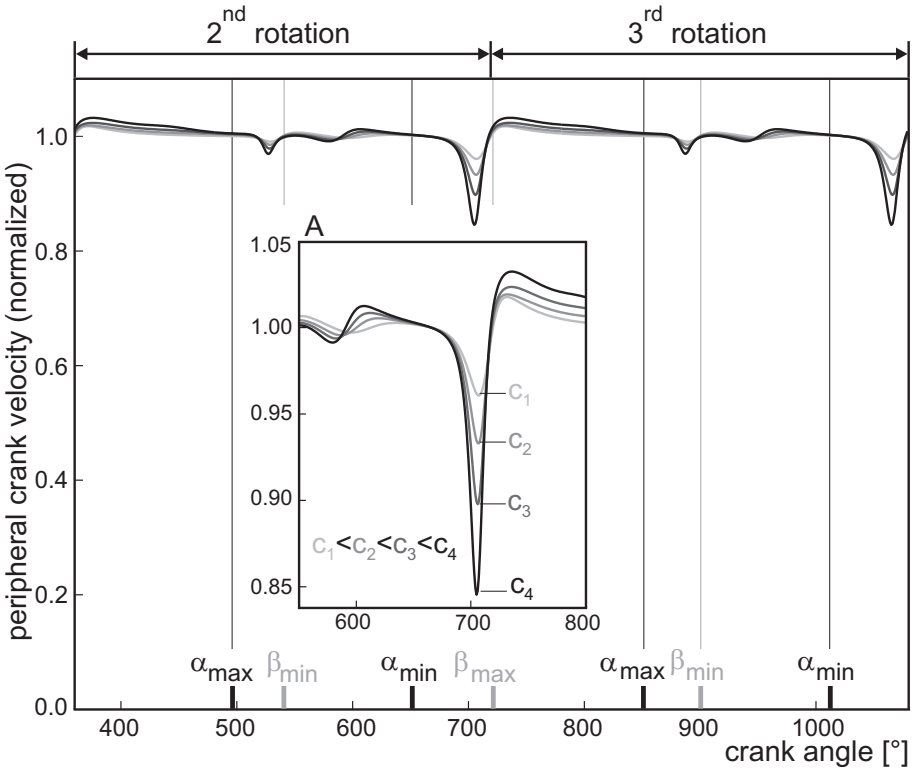

Figure 3.7: Peripheral crank velocity and the influence of the relaxation constant c.

3.4.4 Different cranking velocities

In the loaded crank-turning case it has been shown that LPVF with Power-Controlled Continuous-Relaxation solves the task of winching up a weight with a crank. However, an important aspect is the ability of the local joint controllers to move a closed kinematic chain with a desired velocity. Fig. 3.7 shows the normalized peripheral crank velocity of the loaded crank operated by an elastic manipulator with Power-Controlled Continuous-Relaxation LPVF. The crank velocity is controlled by means of the central velocity controller (ω-controller) as depicted in Fig. 3.2. The desired cranking velocity in Fig. 3.7 is 1 (normalized). The deviation from the desired velocity depends on the choice of the relaxation constant c. The occurrences of extreme values of the manipulator joint angles (joint reversals) are plotted along the abscissa in Fig. 3.7 in black for the α-joint ($\alpha_{\min}$ and $\alpha_{\max}$) and in gray for the β-joint ($\beta_{\min}$ and $\beta_{\max}$). It can be seen that the extreme values of both joints appear between the maxima and minima of the crank velocity curves.

Inset A in Fig. 3.7 shows an enlarged section of the crank velocity curve. A larger c (for example c_4) increases the difference between the desired and the actual cranking velocity. A smaller c (for example c_1) decreases the velocity deviation. Therefore, the relaxation constant c can be regarded as a mediator between energy consumption and accuracy of the achieved cranking (task) velocity.

3.4.5 Spring constants of the joints

LPVF operate on elastic joints in closed kinematic chains. For the design of the elastic joints of the manipulator the joint stiffness (spring constant) has to be chosen. For the given system with a weight of 0.1 kg attached to the crank a value of $k_{\alpha,\beta} = 10\,\mathrm{Nm/rad}$ turned out to be a sensible choice. With this spring constant the joint stiffness lies in the same order of magnitude as it is found in humans (Franklin and Milner, 2003). We varied the weight from 10% to 100% of its original value without impairing the cranking movement. If the weight is increased above the original value, the spring constants have to be increased proportionally.

3.5 Discussion

Power-Controlled Relaxation LPVF comprises an important extension of the LPVF approach (Schneider et al., 2005a) to control elastic joints in constrained kinematic chains. This extension enables a manipulator to follow an unknown contour even if a strong force acts along the intrinsically unconstrained direction of the manipulator tool.

A variety of different control approaches has been introduced for compliant motion control. In technical applications many central controllers are based on *hybrid control* (Raibert and Craig, 1981) or *impedance control* (Hogan, 1985). In hybrid control the manipulator contact is partitioned into force/torque and position/velocity vector spaces. A tool for the specification of this partitioning was provided by Mason in the form of the *compliance frame* or *task frame formalism* (Mason, 1981; Bruyninckx and De Schutter, 1996). In impedance control mechanical impedance parameters (i.e. inertia, viscosity, stiffness) of the manipulator which is in contact with an object are regulated. Both methods require central controllers with global knowledge about the setup.

In contrast nature has invented local control strategies based on positive feedback (also called *reflex reversal*) that could be used for the generation of compliant motions for example in legs during the stance phase of walking (Bässler, 1976; Schmitz et al., 1995; Cruse et al., 1995; Kindermann, 2002). Based on this biological paragon, Local Positive Velocity Feedback (LPVF) controllers have been developed (Schneider et al., 2005a). It has been shown that these decentral controllers are able to move closed kinematic chains in contour following tasks like walking (Schneider et al., 2006a) or crank turning (Schneider et al., 2005a; Schneider et al., 2005d).

This chapter introduced a crucial extension of LPVF named *LPVF with Power Controlled Relaxation*. This extension enables each single joint controller to decide how much of the joint bending has to be relaxed and how much bending must be maintained in order to enable global contour tracking and at the same time generate positive mechanical power. Positive mechanical power means that motor action and joint movement have the same direction. For a closed kinematic chain this in turn means that it is possible to work against a load force that acts into the free direction of the otherwise constrained movement.

In the case of loaded crank turning, which was chosen as a benchmark in this work, joints equipped with Power Controlled Relaxation LPVF were able to winch up arbitrary weights. In addition, all LPVF approaches solve the problem of arm posture redundancy automatically because these approaches are purely local by nature. This is because they neither have to calculate forward nor inverse kinematics or dynamics. Thus, global knowledge about the geometry of the manipulator is dispensable. Furthermore, LPVF also makes the controller nearly insensitive to changes of segment lengths. The core idea of LPVF with Power Controlled Relaxation is the introduction of a bending-dependent relaxation module. The approximation of Power Controlled Continuous Relaxation represents a special case of a *relaxation polynomial* of the form:

$$\rho_{\alpha,K} = \sum_{k=1}^{K} \sum_{i=1}^{I} c_i \, \alpha_{b,k}^{i}, \tag{3.15}$$

with c_i being the relaxation coefficients and $\alpha_{b,k}^{i}$ the bending signal to the power of i in time step k. It is conceivable that other relaxation modules which use a larger portion of the polynomial (3.15) can be used to adapt the system to different desired force/torque trajectories.

Some properties of the control strategy described here can be compared to constrained human arm movements, which have been studied intensively. Franklin and Milner (Franklin and Milner, 2003) used a manipulandum in order to generate arbitrary constraints while the manipulandum was moved by a human subject. Other studies used a physical crank and performed force measurements in the handle while the human subject turned the crank (Ohta et al., 2004; Russel and Hogan, 1989). As the human arm has redundant degrees of freedom (Bernstein, 1967), the experiments were designed such that the movement complexity was reduced to that of a planar manipulator where shoulder and elbow joint were regarded as the first and second hinge joint. During crank turning the arm adopts postures in which joint reversals occur. Russel and Hogan termed these positions *elbow and shoulder singularities* (Russel and Hogan, 1989). In the singularity of one joint the motion of the crank can only be generated by the motion of the other joint. Humans show no hesitation in moving the joint during zero-crossing of the joint angular velocity. This can also be found in the behavior of the system presented here.

Russel and Hogan also reported that all subjects generated non-zero normal forces which indicates that humans may take advantage of the existence of the crank contour in order to guide the arm motion. Ito et al. argued that hand forces in normal directions to the crank contour also contribute to an increase of robustness of the arm posture against external disturbances (Ito et al., 1991).

The control approach proposed here uses the normal forces in a similar way. Only normal forces reveal the existence of the movement constrained to the arm controllers. In the case of elastic joints this information is distributed to each joint mechanically in which it is expressed as bending. This allows local task performance without having a central controller with an internal world model.

In order to understand how humans solve the problem of forming unique arm trajectories from a reservoir of infinitely many possibilities, several optimization approaches have been proposed.

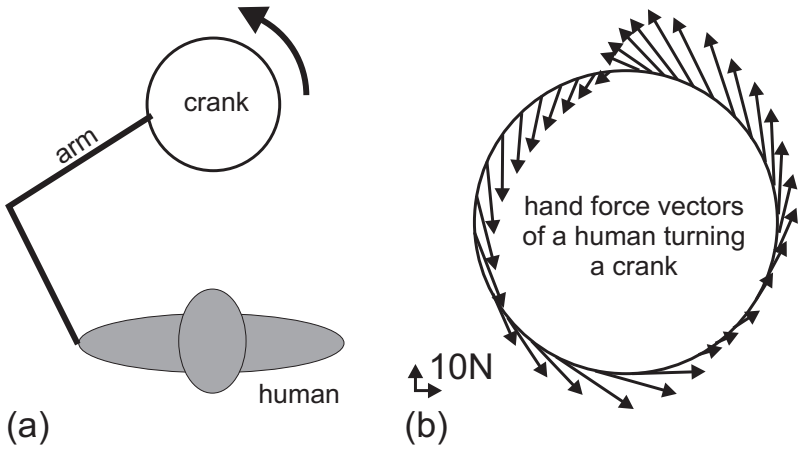

Figure 3.8: Experimental setup (a) and hand force vectors (b) of a human subject turning a crank. (Adopted from Ohta et al., 2004)

Flash and Hogan proposed the *minimum hand jerk criterion* implying movement planning in the task space (Flash and Hogan, 1985). The *minimum joint torque change criterion* (Uno et al., 1989) suggests movement planning in joint space. However, both approaches require the existence of a mental, central planer.

Ohta measured the hand force vectors of humans turning a crank and proposed a combined criterion which minimizes *hand contact force change* and *actuating force change* (on the muscular level) concurrently in order to explain their results (Ohta et al., 2004). Fig. 3.8(a) and Fig. 3.8(b) show an adoption of the setup and the course of the hand force vectors during a crank rotation as measured by Ohta. The hand force vectors generated by the control approach in this study [Fig. 3.5(c,e)] are similar to those generated by humans. This shows that, at least in closed kinematic chains, it is possible to generate a cranking behavior analog to that of humans with a decentral control strategy in joint space and may indicate that this solution is also adopted by humans.

The results of the presented study show the applicability of Power Controlled Relaxation LPVF for the loaded crank turning case only. But in principle, it can also be used for arbitrary contours.

3.6 Conclusion

This chapter introduced a crucial extension of the Local Positive Velocity Feedback (LPVF) control strategy which enables decentral control of elastic joints in closed kinematic chains. The extension, termed Power Controlled Relaxation, allows the use of LPVF control even if heavy loads have to be moved along the unconstrained direction of movement. The coordinated movement of the closed

kinematic chain is still achieved via mechanical coupling although the load to be moved obscures this coordination information.

Future work will include coupling of different closed kinematic chains in a six-legged walker while maintaining the decentral control structure. First results have already been obtained on a 3DoF test leg (Schneider et al., 2006a). Furthermore, the implementation of elastic joints with controllable stiffness would allow building a system that accommodates to a wide range of loads.

Chapter 4

Generation of powerful stance movements for walking with LPVF

The generation of movements in closed kinematic chains as opposed to open kinematic chains is a challenging task because all participating joints have to be moved in a highly coordinated manner in order to avoid destructive tensions in the limb. In this chapter a new decentral joint controller is presented which uses low-level interactions between a moving joint and its environment consisting of neighboring joints, the body and the surroundings the agent is placed in. This local joint controller is based on a **L**ocal **P**ositive **V**elocity **F**eedback (LPVF) mechanism which exploits the elastic properties of the joint. The control strategy is inspired by biological findings in the walking system of stick insects. It will become clear that a closed kinematic chain consisting of several LPVF controlled joints, though lacking a central controller, can solve tasks which need a high level of inter-joint coordination. As an example, a planar manipulator turning a crank is presented. In a further step, the LPVF algorithm will be extended to switched LPVF in order to improve the mechanical power conversion. The extended capabilities are proven in a second experiment in which a 3DoF test leg generates powerful stance movements.

4.1 Introduction

The movement of limbs can be studied under different aspects. In general one can always differentiate movements by the type of constraints which limit the freedom of a particular movement in the task or joint space. Unconstrained or free movements can be found in limbs which have no contact with other objects. In such cases the limbs form *open kinematic chains*. A movement of a joint in an open kinematic chain changes the position of the end point of the chain. However, its influence on other joints in the chain can be neglected if the limb is inelastic enough and if the movements are not too fast. This is the case for example in classical setups as can be found in industrial

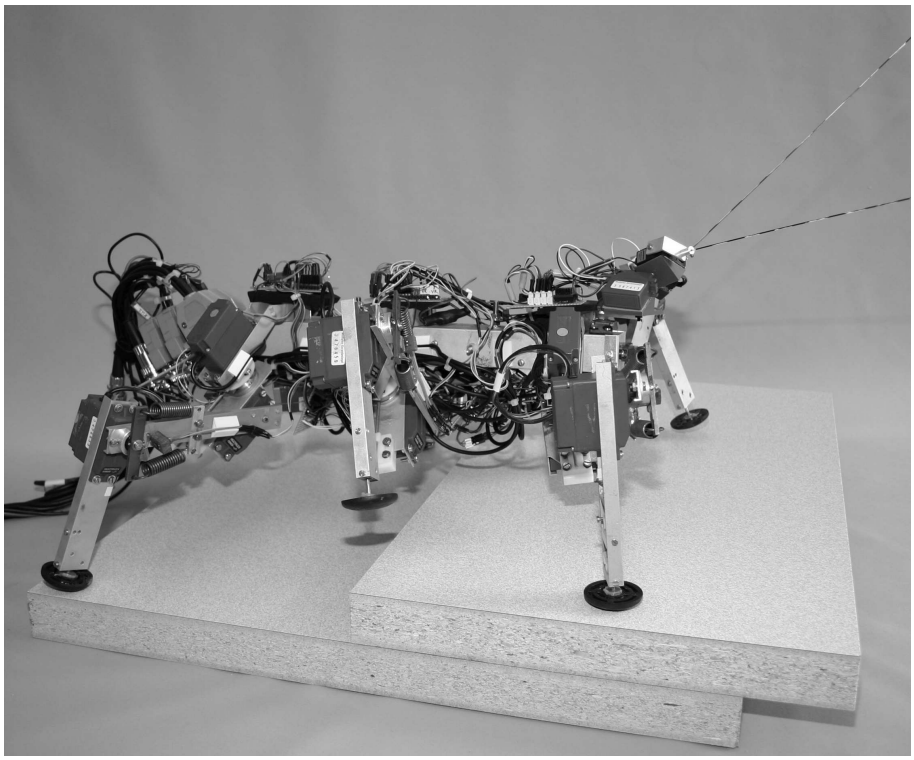

Figure 4.1: Side view of the hexapod robot Tarry IIb equipped with elastic joints.

robotics. In such cases, pure position or trajectory control on the basis of the kinematics of a limb is sufficient. The torques generated by the joint drives are not considered as long as they remain in the normal range of operation. Open kinematic chains can also be found in biological systems, for example during the swing movements of walking legs. During these movements, the foot of a leg travels from a posterior extreme position (PEP) to an anterior extreme position (AEP) normally without hitting any objects in its path. The situation is quite different if a limb movement is constrained by a mechanical connection from the end of the kinematic chain to its base. Limbs that encounter such a movement constraint are called *closed kinematic chains*. In those cases, the joints of the chain cannot be moved independently anymore. The concerted movements of all joints have to be controlled in such a way that the end point of the chain follows those directions which are left unconstrained in the task space (for example along the edge of an obstacle). At the same time additional uncoordinated movements of some joints lead to increasing forces in constrained directions and thus to mechanical tensions in the limb. This type of problem belongs to the class of so-called *compliant motion* tasks. In technical applications, these situations are found in robots performing cooperative manipulations, peg-in-hole, bead-on-wire or turning-a-crank operations. But also in walking systems we encounter closed kinematic chains during simultaneous stance movements of at least two legs. Here, the closed kinematic chain starts from the body, continues along the leg, foot, substrate and other legs on ground and meets the body again. The generation of movements in closed kinematic chains as opposed to open kinematic chains is a challenging task because all

participating joints have to be moved in a highly coordinated manner in order to avoid destructive tensions in the limb and the body. As a solution for this kind of compliant motion problems one can basically choose between two different classes of control paradigms. The first class contains all explicit approaches using central controllers, which are mostly based on the concept of *hybrid control* (Raibert and Craig, 1981) or *impedance control* (Hogan, 1985). These controllers have access to the whole body. They know the complete geometrical setup and use calculations for the kinematics and dynamics of all limbs. The second class is closer to the idea of embodiment. It consists of decentral or local controllers which make use of low level interactions between the moving joints and their environment consisting of neighboring joints, the body and the surroundings the agent is placed in.

This chapter deals with the latter of the two classes. We introduce different versions of a **L**ocal **P**ositive **V**elocity **F**eedback (LPVF) mechanism controlling an elastic joint which is able to decide on the next movement just by measuring local joint parameters (Schneider et al., 2005a). The existence of elastic features in the joint is a prerequisite for our approach to work. Two different mechanical implementations of elastic hinge joints are introduced which are used in the robot Tarry IIb as depicted in Fig. 4.1. The idea of using positive velocity feedback for elastic joints is based on findings in the walking system of stick insects (Bässler, 1976; Schmitz et al., 1995). It will be shown that, being part of a closed kinematic chain, positive velocity feedback controlled joints can accomplish tasks that require a high level of coordination. After the derivation of their function, LPVF will be tested in a crank turning task. Next, the function of LPVF will be expanded by a switched version (SLPVF), which additionally exerts strong forces during motion while maintaining the ability of coordination at the same time. In a second experiment, it will be proven that our control strategy generates powerful stance movements in a 3DoF test leg.

4.2 Biological motivation for active compliant motion

Biological research on the physiology of the walking system of the stick insect *Carausius morosus* revealed different reactions to external perturbations of legs depending on the insect being in an inactive or active state.

The inactive (standing) insect shows *resistance reflexes* in the leg joints. These reflexes counteract external forces which would cause a leg to be moved. The resistance reflexes can be explained by negative feedback position controllers acting on the joints (Bässler, 1972; Cruse et al., 2004).

In the active (walking) insect, however, the above-mentioned reflex is reversed (*reflex reversal*) (Bässler, 1976), if the acceleration of the imposed movement is below a certain threshold (Bartling and Schmitz, 2000). In the active state, the insect reacts to a perturbation force with an activation of those muscles which assist the externally induced movement of the leg instead of correcting the position deviation (Schmitz et al., 1995). This effect could be explained in different ways. First, the animal might have a **mental body model** (Cruse et al., 1998b;

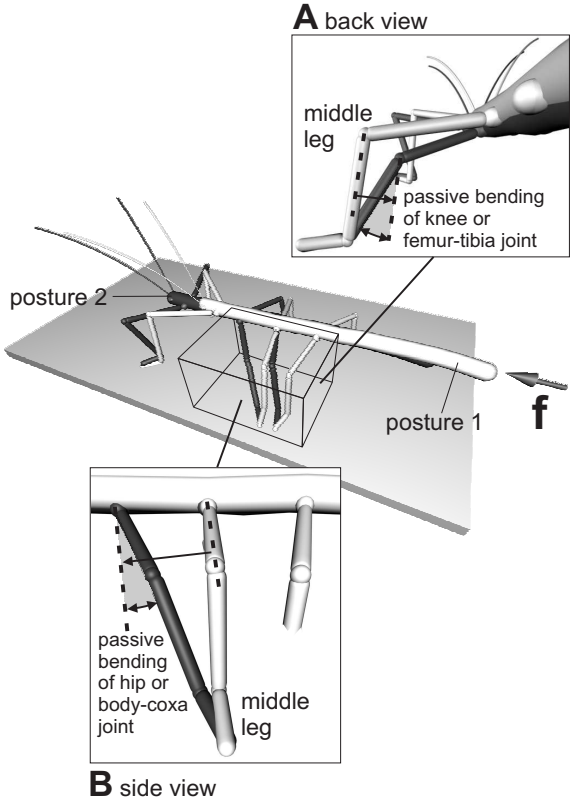

Figure 4.2: One insect in two different postures while the foot positions remain the same. In posture 1 (light gray) the elastic joints are assumed to be relaxed. When a force $\vec{f}$ acts on the body, the animal is moved to posture 2 (dark gray) without actively using its actuators (muscles). The new posture is adopted only due to the elastic properties. Inset A shows the back view of the left middle leg. The passive bending of the femur-tibia joint is depicted. Inset B shows the side view. The passive bending of the body-coxa joint of the left middle leg can be seen.

Kühn and Cruse, 2005) and possess the planning ability to actively shift the desired value for a negative feedback position controller according to the externally imposed movement. Second, a **positive position feedback** controller continues the induced joint movement. Third, a **positive velocity feedback** controller adopts the role of continuing the movement. Investigations suggest that positive feedback is responsible for reflex reversals (Bässler, 1986b; Bässler, 1986a; Bässler, 1988; Bässler, 1993). This argues against the first proposition but leaves it open which feedback characteristic, positive position or positive velocity feedback, is responsible for the reflex reversal. Cruse, Schmitz and co-workers (Cruse et al., 1995; Schmitz et al., 1995; Kindermann, 2002) showed in kinematic simulations that positive feedback in the body-coxa ("hip") and femur-tibia ("knee") joint is sufficient to produce realistic stance movements in a virtual walker.

As a first approximation we simply assume that the neuromuscular system, containing slow invertebrate muscles acting on a highly damped joint, behaves like an integrator. It converts input signals proportional to joint velocities into current angular positions of the attached joint as long

as the movement of the joint is not blocked (Zakotnik et al., 2006; Tryba and Ritzmann, 2000; Garcia et al., 2000). Positive position feedback acting on such a joint would show a continuous increase of the joint velocity after an initial excitation. This behavior was not found in biological experiments. Because of that, positive position feedback can be ruled out as an explanation for reflex reversal. The remaining positive velocity feedback exhibits a constant joint velocity after being activated by an initial force impulse. Therefore, positive velocity feedback appears to be a good candidate for modelling reflex reversal.

An important prerequisite for positive feedback to function in a multi-segment system is the existence of elastic components in the muscles and tendons actuating a joint. This is because a feedback circuit with positive velocity feedback must be able to experience passive movements it can adapt to. Using the combination of positive velocity feedback and elastic joints, we can formulate an idea how these two components can be used for the control of the stance movement in six-legged walking. Figure 4.2 shows an insect standing in two different postures with the same foot positions. In posture 1 (light gray animal) the insect stands relaxed, i.e. with no external force acting on it. The application of an external force $\vec{f}$ (arrow on the right) moves the insect's body forward to posture 2 (dark gray animal). The passive adoption of the new posture is only possible because of the elastic features of the joint actuators. Observing this externally applied motion on the single joint level provides the joints with the following information. First, each joint controller "knows" the amount of bending that has to be relaxed by an active muscle movement in order to adopt the new posture even when the external force has vanished. Second, the joint controller "knows" what would have to be done in order to repeat the same movement actively or to go on with this passively induced movement by feeding back the locally measured joint velocity (positive velocity feedback). Once excited, such a system maintains the stance movement that was imposed passively in the first place. This is achieved without any knowledge about the leg and body geometry and whether or not it is part of a complex kinematic chain.

In the following sections two different technical implementations of an elastic joint are developed and the positive velocity feedback is described in more detail.

4.3 Elastic limbs

This section is devoted to the design of two simple mechanical mechanisms which can be used in limbs to add elastic properties. These properties are essential for the biologically inspired approach to walking derived in this section.

The first step in the development of a compliant limb is the decision whether elastic elements are integrated into the segments or rather into the joints of the kinematic chain. Both approaches have their own originalities to cope with when setting up a system. For details concerning *elastic joints* see De Luca and Tomei, 1996 and for *flexible limbs* see De Luca and Siciliano, 1996. Lightweight robots designed for large working ranges, for instance in space robotics, exhibit an immanent

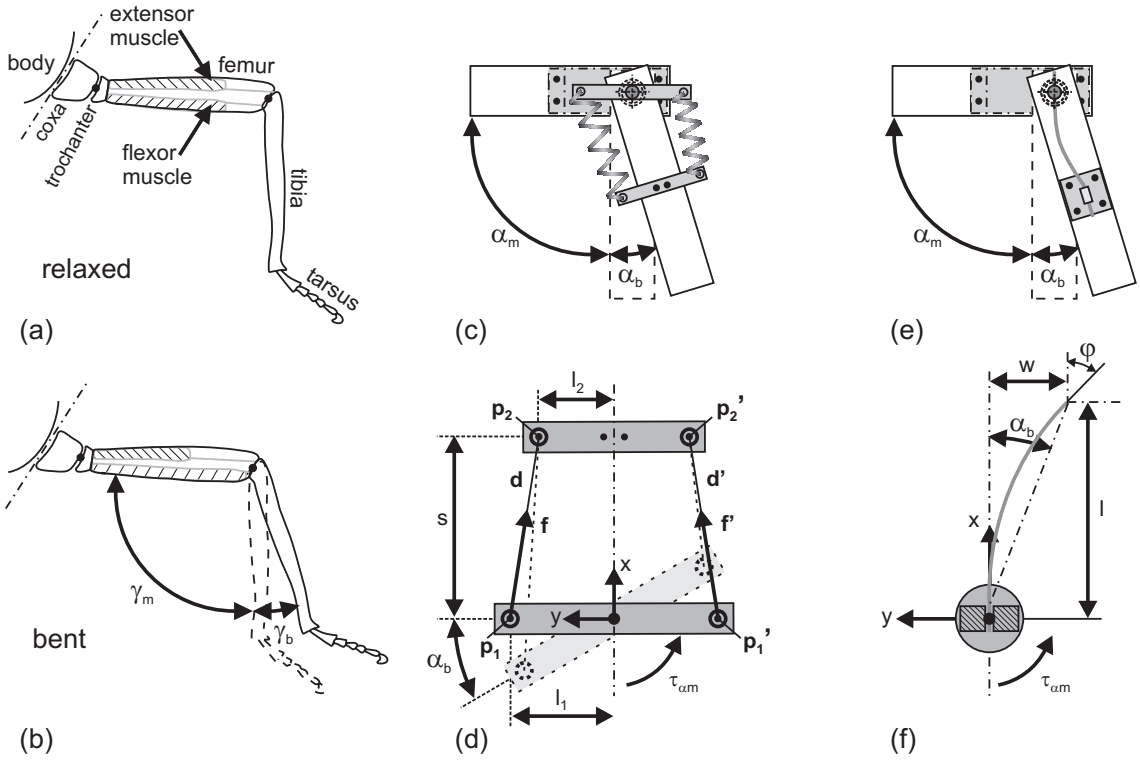

Figure 4.3: An insect leg with the femur-tibia joint in a relaxed (a) and in a bent state (b) due to an external force. Technical implementations of an elastic joint with a servo-motor and extension springs (c,d) and with a flexible beam (e,f).

flexibility of their limb segments. In this case here, we want to model a flexible mechanical leg on a biological example, the leg of the stick insect *Carausius morosus*. For this purpose it has to be figured out which are the most prominent elastic parts in such an insect leg. The candidates are the muscles and tendons which drive the joints and the elasticities of the exoskeleton. Biological studies on the cuticle of insects have shown that the stiffness of the cuticle of the tibia with a Young's modulus of $E \approx 10\,\mathrm{GPa}$ lies at least one order of magnitude higher than that of tendons ($E \approx 0.5\,\mathrm{GPa}$) (Vincent and Wegst, 2004), not to mention the elastic properties of the muscles. Thus, we focussed on the elastic properties of the joints. Figure 4.3(a) shows a simplified sketch of a stick insect's leg. It consists of three segments (coxa, femur and tibia) and three joints (body-coxa or α-joint, coxa-trochanter or β-joint and femur-tibia or γ-joint). The first joint generates the protraction and retraction, the second the levation and depression and the third the flexion and extension movement of the leg. The figure also shows the driving muscles of the femur-tibia joint (extensor and flexor muscle) as an example. In Fig. 4.3(a) the γ-joint is relaxed, i.e. without passive bending due to external forces. Both muscles are pre-stretched. In Fig. 4.3(b) the tibia is exposed to an external force and thus bent counterclockwise. Owing to their elastic properties, the extensor muscle is relaxed and the flexor muscle is stretched passively. Transformed into the angular domain, the femur-tibia joint has a default angle because of the muscle activity in the

unloaded condition, in our case termed α_m (m = muscle or motor). When bending occurs, an additional angle α_b (b = bending) can be measured. In other words, the biological joint can be approximated by a motor whose driving torque is transmitted to the actual joint via a torsion spring. Such a setup is used for example in *Whegs robots* (Ritzmann et al., 2004) or in the M_3L leg (Wadden et al., 1998). In Sec. 4.3.1 and 4.3.2 two other different mechanical designs for flexible joints are derived. The first design uses extension springs and the second one a flexible beam. The first design is used in the femur-tibia ("knee") joint and the second one in the body-coxa ("hip") joint of the robot Tarry IIb [Fig. 4.1 and Fig. 4.4(a) and (b)].

4.3.1 Elastic joint with extension springs

Figure 4.3(c) shows a technical implementation of an elastic joint constructed of a servo-motor and extension springs. The joint is formed of two segments connected by a ball bearing. The servo-motor is mounted on the upper segment. The motor's shaft protrudes through the ball bearing with its end attached to a bracket. This bracket is connected to a counter bracket on the lower limb segment via two extension springs. If one segment is fixed, a motor shaft rotation of α_m results in a rotation of the other, free segment. In a fixed motor shaft position, however, the extension springs allow for passive bending α_b of the joint by external forces. Therefore, the actual joint angle α_j is:

$$\alpha_j = \alpha_m + \alpha_b. \tag{4.1}$$

Due to the antagonistic design, the springs are mounted pre-stretched and therefore are able to compensate slackness at zero-crossing. As a result, they react with a distinct restoring force even to small deflections. This technical joint is equipped with a linear hall sensor and a magnet which together serve as an angle transducer monitoring the angle of bending α_b. Details of this construction are shown in the photograph in Fig. 4.4(a). This setup is chosen to function like a resilient joint with a torsion spring which generates a linear counter torque opposing a twist around the joint axis in the form:

$$\tau = k_b \alpha_b. \tag{4.2}$$

With τ being the counter torque, k_b is the torsional stiffness or bending stiffness and α_b the bending angle which is equal to the angle of torsion. The constant k_b describes how the bending torque changes according to the amount of bending:

$$k_b = \frac{\Delta\tau}{\Delta\alpha_b}. \tag{4.3}$$

Figure 4.3(d) depicts the geometrical details of the construction in Fig. 4.3(c). This is used in order to calculate the corresponding torsional stiffness k_b of the mechanism. The two brackets have the lengths $2l_1$ and $2l_2$. The points $\vec{p_1}$, $\vec{p_2}$ and $\vec{p_1'}$, $\vec{p_2'}$ are attachment points of the extension springs on the brackets. Both brackets are mounted at a distance s from each other. The vector

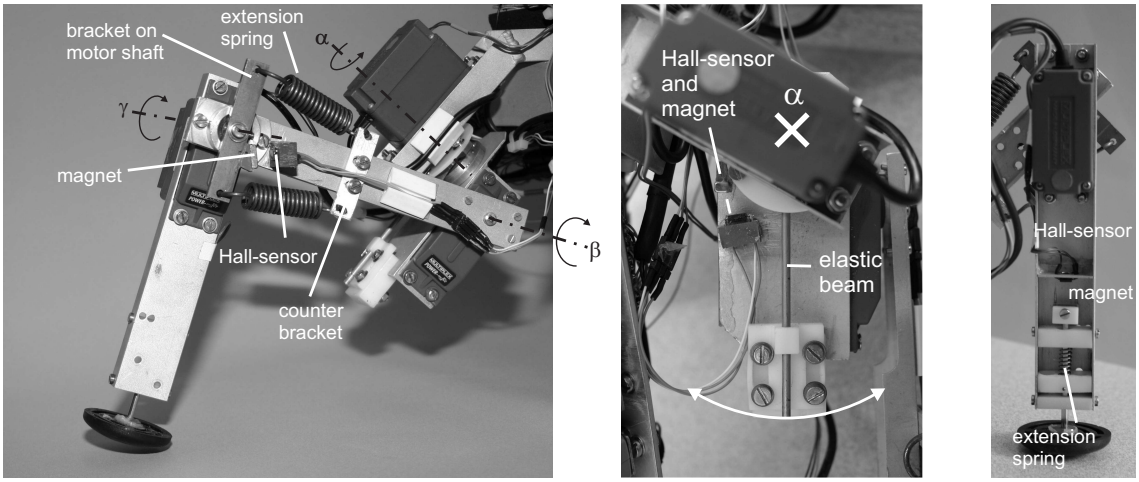

Figure 4.4: Elastic knee joint (γ-joint) with extension springs (a), elastic hip joint (α-joint) with flexible beam (b) and an elastic foot plate (c) of the Tarry IIb robot. The cross in (b) marks the rotational axis of the α-joint.

$\vec{d}$ connects $\vec{p_1}$ and $\vec{p_2}$ and $\vec{d'}$ connects $\vec{p_1'}$ and $\vec{p_2'}$. Both vectors $\vec{d}$ and $\vec{d'}$ indicate the orientation of their respective extension spring in the setup. Given the aforementioned assumptions, $\vec{p_i}$ are:

$$\begin{aligned} \vec{p_1} &= \begin{pmatrix} -s_{\alpha_b} l_1 \\ c_{\alpha_b} l_1 \end{pmatrix} \quad \vec{p_2} = \begin{pmatrix} s \\ l_2 \end{pmatrix} \\ \vec{p_1'} &= \begin{pmatrix} s_{\alpha_b} l_1 \\ -c_{\alpha_b} l_1 \end{pmatrix} \quad \vec{p_2'} = \begin{pmatrix} s \\ -l_2 \end{pmatrix} \end{aligned}, \tag{4.4}$$

with s_{α_b} denoting $\sin \alpha_b$ and c_{α_b} denoting $\cos \alpha_b$. According to (4.4) the distance vectors $\vec{d}$ are:

$$\begin{aligned} \vec{d} &= \vec{p_2} - \vec{p_1} = \begin{pmatrix} s + s_{\alpha_b} l_1 \\ l_2 - c_{\alpha_b} l_1 \end{pmatrix} \\ \vec{d'} &= \vec{p_2'} - \vec{p_1'} = \begin{pmatrix} s - s_{\alpha_b} l_1 \\ -l_2 + c_{\alpha_b} l_1 \end{pmatrix}. \end{aligned} \tag{4.5}$$

The lengths of the $\vec{d}$s are:

$$\begin{aligned} \left|\vec{d}\right| &= \sqrt{(s + s_{\alpha_b} l_1)^2 + (l_2 - c_{\alpha_b} l_1)^2} \\ \left|\vec{d'}\right| &= \sqrt{(s - s_{\alpha_b} l_1)^2 + (c_{\alpha_b} l_1 - l_2)^2}. \end{aligned} \tag{4.6}$$

The unit vectors of the restoring forces of the extension springs exerted in the direction of the $\vec{d}$s can be written as:

$$\hat{\vec{f}} = \frac{\vec{d}}{\left|\vec{d}\right|}, \; \hat{\vec{f}'} = \frac{\vec{d'}}{\left|\vec{d'}\right|}. \tag{4.7}$$

With the above preparations, the restoring forces result in:

$$\begin{aligned}\vec{f} &= \hat{\vec{f}}(\left|\vec{d}\right| - l_0)k_s = \left|\vec{d}\right| k_s - l_0 k_s \begin{pmatrix} \frac{s+s_{\alpha_b} l_1}{|\vec{d}|} \\ \frac{l_2 - c_{\alpha_b} l_1}{|\vec{d}|} \end{pmatrix} \\ \vec{f}' &= \hat{\vec{f}}'(\left|\vec{d}'\right| - l_0)k_s = \left|\vec{d}'\right| k_s - l_0 k_s \begin{pmatrix} \frac{s-s_{\alpha_b} l_1}{|\vec{d}'|} \\ \frac{c_{\alpha_b} l_1 - l_2}{|\vec{d}'|} \end{pmatrix}.\end{aligned} \tag{4.8}$$

The constant l_0 denotes the natural length of the extension springs and k_s is their spring constant. We can now calculate the torques exerted on the joints by using the cross products $\vec{\tau} = \vec{p_1} \times \vec{f}$ and $\vec{\tau'} = \vec{p_1'} \times \vec{f}'$. As it is reasonable to expect only small angular deviations α_b, we chose $c_{\alpha_b} = 1$. Additionally we assume the two brackets being of equal length ($l_1 = l_2$). These simplifications lead to the following expressions for the torques generated in the joint:

$$\begin{aligned}\tau &= -l_1 k_s(s + s_{\alpha_b} l_1 - l_0) \\ \tau' &= l_1 k_s(s - s_{\alpha_b} l_1 - l_0).\end{aligned} \tag{4.9}$$

We set up the equation for the torque balance in the joint and approximate s_{α_b} by α_b. The motor torque $\tau_{\alpha_m} = \tau_{\alpha_b}$ has to withstand the external bending:

$$\begin{aligned}\tau_{\alpha_m} &+ \tau + \tau' = 0 \\ \tau_{\alpha_m} &= 2k_s l_1^2 \alpha_b.\end{aligned} \tag{4.10}$$

From (4.10) an expression for the spring constant k_b of an equivalent torsion spring which would replace the setup in Fig. 4.3(c) and (d) can be derived as:

$$k_b = \frac{\Delta\tau_{\alpha_m}}{\Delta\alpha_b} = 2k_s l_1^2. \tag{4.11}$$

Equation (4.11) shows that the spring constant k_b depends quadratically on the length of the brackets. This is a result of the antagonistic setup of this joint mechanism. The extension springs chosen for the robot Tarry IIb have a spring constant k_s of 14200 N/m and the length of the lever arms l_1 is 20 mm. The resulting spring constant of the γ-joint according to (4.11) is $k_b \approx 11$ Nm/rad.

4.3.2 Elastic joint with a flexible beam

The second design of an elastic joint is shown in Fig. 4.3(e). Instead of extension springs a single flexible spring steel wire (flexible beam) is fixed to a fit which is mounted on the motor shaft's head. Its other end is connected with a sliding-contact bearing on a counter bracket sitting on the lower segment. This version of a compliant joint is space-saving and can therefore be used for joints very close to the body. Like in Sect. 4.3.1 this joint is chosen to function like a resilient joint with a torsion spring. Again, we want to find the equivalent spring constant k_b. For this purpose we extract the basic features of the setup as shown in Fig. 4.3(f). The motor rotates the beam

clamp. The beam is assumed to be bent by a torque τ_{α_m} because it is supported at a distance l by the counter bracket on the neighboring limb. Starting from the *Euler-Bernoulli beam equation*:

$$EI\frac{d^2w(x)}{dx^2} = -\tau(x) \tag{4.12}$$

both the out-of-plane displacement $w(x)$ which describes the shape of the bent beam and the angle of bending $\varphi(x)$ can be calculated. *Young's modulus* E and the *moment of inertia of the cross-section* I are assumed to be constant. Double integration of (4.12) results in:

$$w(x) = \frac{1}{EI}\left(\frac{-\tau(x)x^2}{2} + c_1x + c_2\right) \tag{4.13}$$

Since the slope of the line of bending is zero at the restraint ($w'(0) = 0$), the constant c_1 is zero. The same applies for the out-of-plane displacement of the beam for $x = 0$, which is $w(0) = 0$. Thus, the constant c_2 is also zero. For the torque we assume $\tau(x) = -\tau_{\alpha_m} = \text{const}$. With these assumptions the function of the out-of-plane displacement of the beam is:

$$w(x) = \frac{\tau_{\alpha_m}x^2}{2EI} = \frac{\tau_{\alpha_m}l^2}{2EI} \text{ (for } x = l). \tag{4.14}$$

In order to calculate the angle of bending at the end of the beam, (4.12) has to be integrated once, because the first derivative of the out-of-plane displacement $w'(x)$ is equal to $\tan\varphi(x)$. For small angles we assume $w'(x) \approx \varphi(x)$. The same side conditions as above apply. From this we get an expression for $\varphi(x)$:

$$\begin{aligned} w'(x) &= \tan\varphi(x) = \frac{\tau_{\alpha_m}x}{EI} \approx \varphi(x) \\ &= \frac{\tau_{\alpha_m}l}{EI} \text{ (for } x = l). \end{aligned} \tag{4.15}$$

According to Fig. 4.3(f) the displacement angle α_b can be determined as follows:

$$\tan\alpha_b = \frac{w(l)}{l} = \frac{\tau_{\alpha_m}l}{2EI} = \frac{\varphi(l)}{2} \approx \alpha_b. \tag{4.16}$$

Note the relationship between the bending of the joint and the bending of the beam.
In the next step the moment of inertia of the cross-section I has to be inserted into (4.16). In our setups we use stainless spring steel wire with a round cross-section. The moment of inertia of its cross-section is $I = (\pi/4)r^4$. Using this in (4.16) results in:

$$\alpha_b = \frac{2l\tau_{\alpha_m}}{E\pi r^4}.$$

Finally, we get an expression for the spring constant k_b of the equivalent torsion spring:

$$k_b = \frac{\Delta\tau_{\alpha_m}}{\Delta\alpha_b} = \frac{E\pi r^4}{2l}. \tag{4.17}$$

The spring steel wire used for the α-joints of the robot Tarry IIb has a radius r of 1 mm, the length l is 30 mm and Young's modulus E is $185000\,N/mm^2$. The spring constant of the elastic beam setup according to (4.17) is $k_b \approx 9.7\,\text{Nm/rad}$.

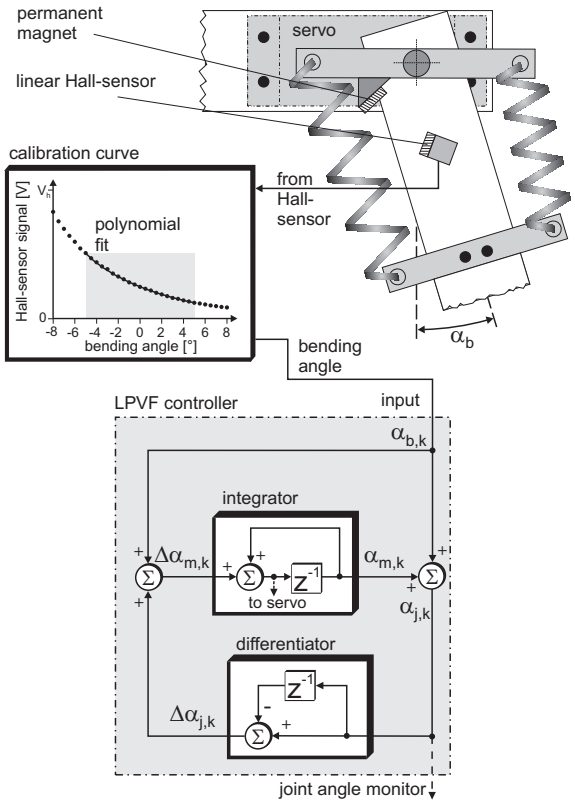

Figure 4.5: Setup of a discrete LPVF controller. The controller input is the bending angle of the joint measured with a transducer consisting of a permanent magnet and a linear Hall-sensor.

4.4 Discrete LPVF controller

In Sect. 4.2 we have introduced the function principle of local positive velocity feedback loops, which exploit the properties of elastic joints. Now, the setup of a discrete LPVF controller is derived accordingly as shown in Fig. 4.5. The LPVF controller receives information on the bending angle of the joint (input). The bending signal originates from a linear Hall-sensor (mounted on the second segment) of the joint. This Hall-sensor is excited by a permanent magnet which is mounted on the bracket on top of the servo-motor axis. When bending occurs, the Hall-sensor changes its relative position to the magnet and therefore also its output signal. The Hall-signal (a voltage) is transformed into an angular signal (working range within $\pm 5°$ during normal operation) via a prerecorded calibration curve (represented by a fitted polynomial).

The LPVF controller also sends motor commands to the servo-motor (output). The angular position signal for the servo is generated in the integrator box as depicted. Since the servo-motor has an integrated position controller (not shown) we assume that it adopts the new angular position within one cycle of the LPVF controller. This means that the maximum time constant of the servo-motor should be in the range of the LPVF controller's sample time. The servo-motors in this study were chosen to meet this criterion. Otherwise a part of the bending signal was only due to the

lag of a slowly moving servo-motor. The bending angle would not represent the joint's interaction with the environment correctly.

For the following derivations the LPVF controller is described in the discrete time domain ($\mathcal{Z}$-domain) with the subscript k denoting the k^{th} time step. The angular position $\alpha_{m,k}$ is emitted at the output of the integrator box with the appropriate time delay. The joint angle monitor output at the lower side of the overall circuit is not needed for control but is used for setting up transfer functions and for the interpretation of the behavior. On the right side of the figure, the sum formulated in (4.1) is indicated. It represents the angular joint position $\alpha_{j,k}$ which is fed into the differentiator on the lower side of the circuit to obtain the angular velocity $\Delta\alpha_{j,k}$ of the joint. As mentioned in Sect. 4.2, the joint actuation (muscle, servo) is assumed to behave like an integrator. Therefore, the actuator is modelled as an integrator in our setup as well. Its input $\Delta\alpha_{m,k}$ is the desired angular velocity of the motor. It consists of the sum of the joint velocity (Which effective joint rotation has occurred in the last time step?) and the bending signal $\alpha_{b,k}$. By adding this additional bending share to the angular velocity of the motor, the controller is able to resolve the bending which has been achieved in the last time step. The output of the integrator delivers the new angular position of the motor shaft $\alpha_{m,k}$. The system equations look as follows:

$$\alpha_{m,k} = \alpha_{m,k-1} + \Delta\alpha_{m,k-1} \tag{4.18a}$$

$$\alpha_{j,k} = \alpha_{m,k} + \alpha_{b,k} \tag{4.18b}$$

$$\Delta\alpha_{m,k} = \Delta\alpha_{j,k} + \alpha_{b,k} \tag{4.18c}$$

$$\Delta\alpha_{j,k} = \alpha_{j,k} - \alpha_{j,k-1}. \tag{4.18d}$$

In order to investigate the function of the control circuit only when it is excited by an input bending pulse, it is advisable to derive the discrete transfer function for the circuit in Fig. 4.5. Inserting (4.18d) into (4.18c) and the result into (4.18a) yields:

$$\alpha_{m,k} = \alpha_{m,k-1} + \alpha_{j,k-1} - \alpha_{j,k-2} + \alpha_{b,k-1} \tag{4.19}$$

By replacing $\alpha_{m,k}$ and $\alpha_{m,k-1}$ by (4.18b) the expression only comprises α_j and α_b:

$$\alpha_{j,k} = 2\alpha_{j,k-1} - \alpha_{j,k-2} + \alpha_{b,k}. \tag{4.20}$$

The $\mathcal{Z}$-transform of (4.20) is:

$$G(z) = \frac{\alpha_j(z)}{\alpha_b(z)} = \frac{z^2}{z^2 - 2z + 1} = \frac{z^2}{(z-1)^2}. \tag{4.21}$$

The transfer function in (4.21) is expanded into partial fractions:

$$G(z) = \frac{z}{z-1} + \frac{z}{(z-1)^2}. \tag{4.22}$$

The first term of (4.22) represents a unit step function and the second term a ramp function. The superposition of both results in the behavior that was demanded in Sect. 4.2. A force which is

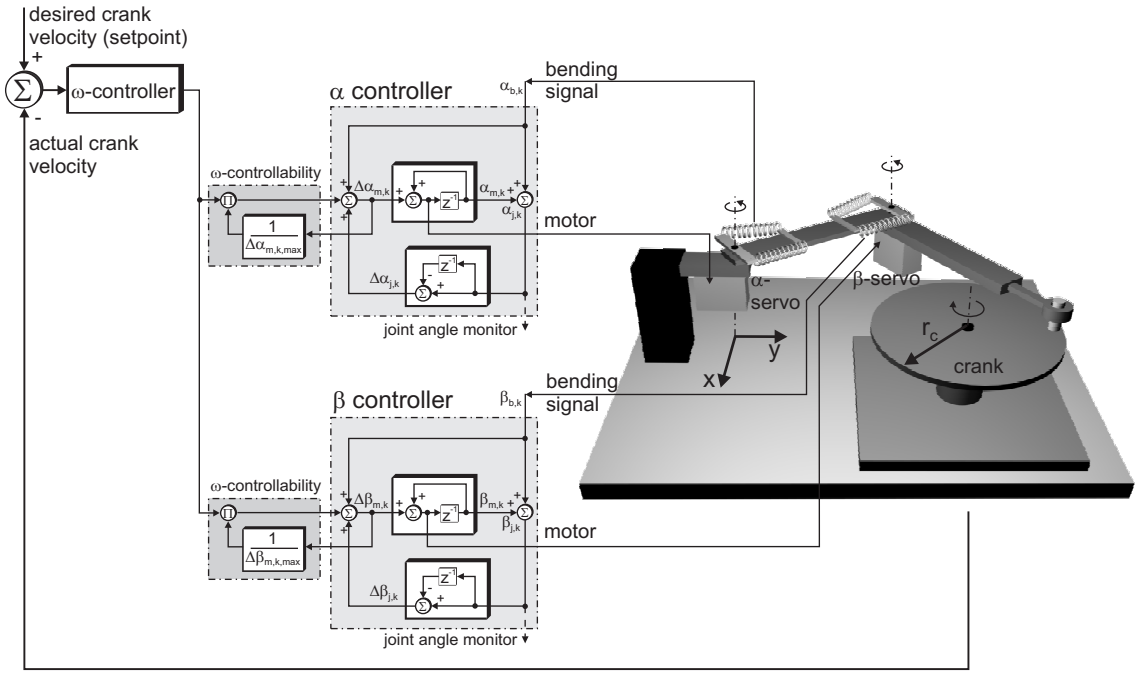

Figure 4.6: The overall setup for the crank turning experiment. On the right side the flexible two-joint planar manipulator which is connected to a crank can be seen. In the centre the two independent discrete LPVF joint controllers are shown. The left side shows the crank velocity controller and the ω-controllability measures which scale the crank velocity controller's output and connect it with the two-joint controllers.

propagated through the (closed) kinematic chain indicates an enforced movement of the limb. This external excitation is converted into an internally maintained movement of the controlled elastic joint. Without further excitation, the joint resolves the additional bending (unit step) and picks up the desired velocity (ramp). With this technique, all locally controlled joints in a limb perform movements which in their sum result in a limb motion into the unconstrained direction of the closed chain's end point. The coordination is a consequence of the mechanical coupling only.

4.4.1 Turning a crank with a planar manipulator

For the evaluation of our LPVF control approach, we chose crank turning with a two-joint planar manipulator as a test setup. Crank turning was favored over other compliant motion tasks like shifting a bead on a wire because it is a cyclic movement which allows long trials without interruptions. Apart from that, it has similarities to the generation of periodic walking movements, our long-term objective. The cranking setup is shown on the right side of Fig. 4.6. The planar manipulator has two segments ($l_1 = 197\,\text{mm}$, $l_2 = 174\,\text{mm}$) and two elastic joints (α, β). The gripper ($l_g = 50\,\text{mm}$) at the end of the second segment is attached to the handle of a crank (radius: $r_c = 80\,\text{mm}$). The base of the crank (default crank position: $x_c = 77\,\text{mm}$, $y_c = 197\,\text{mm}$) is attached to the same base as the manipulator itself (ground plate).

4.4.2 Central velocity control

As the crank turning task is implemented by means of local joint controllers, the question arises how a global variable like the rotational velocity of the crank can be controlled? One solution is depicted in Fig. 4.6. A central negative feedback velocity p-controller (top left) is introduced to the system. Its output cannot be fed directly into the inputs of the local joint controllers since it contains global information. The ω-*controllability* box (on the left side of the α and β controller) represents a measure which alters the sensitivity of the input of the LPVF controllers depending on their current joint velocity. Thus, the central velocity controller gains in importance for a particular joint input when this joint contributes a large amount to the total velocity of the whole limb. The central controller is faded out when the joint changes from a clockwise to a counterclockwise direction of rotation and vice versa because in that particular situation the angular joint velocity and, therefore, its contribution to the total limb velocity is zero.

4.4.3 Results of the crank turning experiment

The kinematics and a dynamics simulation of the crank turning experiment which have been developed are shown in Fig. 4.6. Finally, the experiment is applied to a real, custom-made robotic setup. The kinematics simulation is the first approach to the problem. The virtual posture of the planar manipulator resulting from the pure motor commands (α_m, β_m) can be determined from the forward kinematics. Whenever this virtual posture lies outside the crank perimeter it is projected back onto the crank. The inverse kinematics of the projected posture delivers the joint angles (α_j, β_j). The angular differences of these two postures according to (4.1) results in the bending angles (α_b, β_b).

The dynamics simulation is the second approach to the use of LPVF controllers in the crank setup. This has been done to prove that even under the influence of the dynamic effects of a second-order system with low damping the controllers do not develop destructive oscillatory behavior. The dynamics simulation contains details like the friction of the joint bearings, the spring constants and damping of the serial elastic elements, the characteristics of the actuators (two position-controlled servo motors) and all masses and lengths of the arm segments and the crank. In order to implement a modular simulation, all elements, like the servo-motors including their position controller and gear box, were designed and tested separately. Especially the setup of the elastic joints was modelled according to the mechanisms described in Sect. 4.3. Both the kinematics simulation and the dynamics simulation were implemented using Matlab with Simulink 6.1 and SimMechanics 2.2.1 (The MathWorks Inc., Natick, MA). In a final step, the whole control architecture was transferred to a real custom-made robot. The experimental outline for the simulations as well as the robot experiment were basically the same. The arm was initialized in a posture in which its gripper holds the crank handle in a 0° starting position [see small insets in Fig. 4.7(b),(d) and (f)]. For each of the three setups described above, three tests were performed with the desired velocities for the

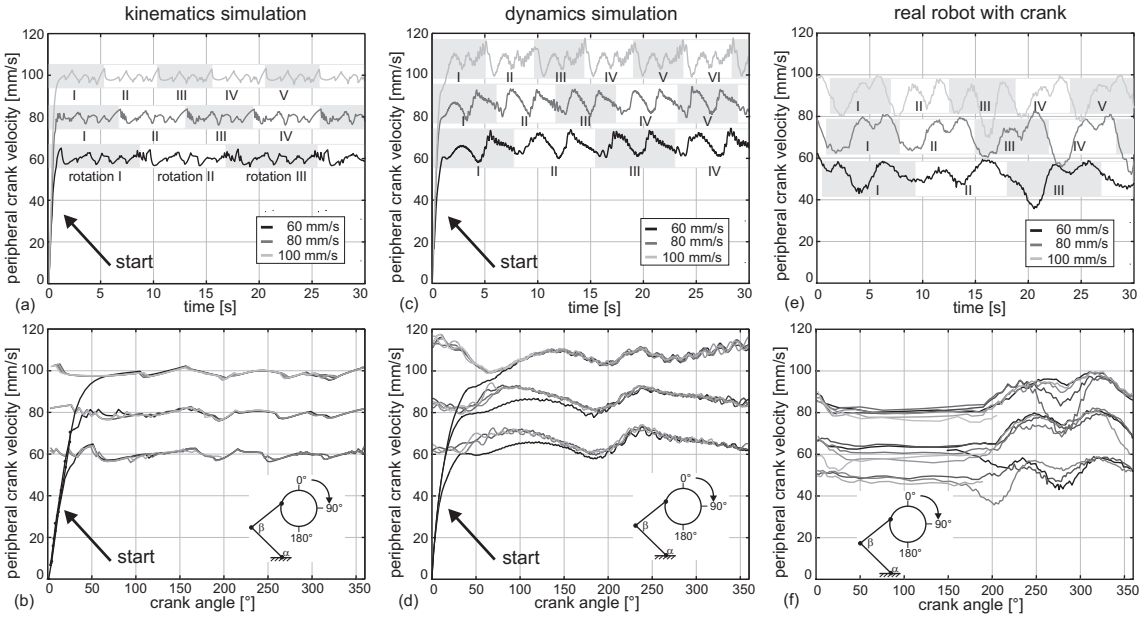

Figure 4.7: Tangential crank velocities plotted over time (a,c,e) and over crank angle (b,d,f) respectively. The gray and white bars in the top row indicate consecutive crank rotations which are counted by the roman numbers.

crank turning either being 60, 80 or 100 mm/s. At the beginning of each experiment, the particular crank was given a starting push. In the kinematics simulation this was reached by applying small offsets to the servo-motor angles. In the dynamics simulation a small torque was applied to the crank for 0.3 s. The real robot was excited manually by applying a weak push to the crank handle. After a short transient phase the planar manipulator turned the crank with the desired velocities in all cases. All experimental runs lasted 30 s. Figure 4.7(a) and (b) display the results of the kinematics simulation for the crank velocity plotted over time and over crank angle respectively. In Fig. 4.7(c), (d) and (e),(f) the same is shown for the dynamics simulation and the real robot experiment respectively. Table 4.1 summarizes the actual velocities and their deviations from the desired values. In the kinematics simulation the desired values are reached with a very good accuracy which is reflected by a mean deviation of 0.3% to 1.3%. This is due to the fact that there is no inertia which disturbs the system. In the dynamics simulation, however, the bodies involved tend to maintain their states of motion owing to their inertia. Therefore the mean deviation from the desired velocities lies between 7.4% and 9.0% and is always higher than the desired values. In the real robot experiment the whole course of the crank velocities is shifted towards lower velocities because the friction effects in the real system seem to be higher than modelled in the dynamics simulation. The mean deviation ranged from 10.4% to 14.0%. An increase of the velocity controller gain could decrease the mean deviation. However, a conservative setting for the gain was chosen to avoid oscillations of the system.

Table 4.1: Desired and actual values of the crank velocities reached in the simulations and in the real robot experiment (actual velocities given with mean value ± 1 standard deviation)

	des. velocity [mm/s]	act. velocity [mm/s]
kin. sim.	60	59.84±1.77
	80	79.57±1.71
	100	98.71±1.47
dyn. sim.	60	65.38±3.59
	80	86.20±3.60
	100	107.35±3.95
real robot	60	51.61±5.11
	80	70.95±7.14
	100	89.56±6.68

4.4.4 Efficiency, stability and operating range

In order to investigate the robustness of the LPVF control strategy, five parameters of the crank turning setup are varied in the dynamics simulation. Figure 4.8 shows the results. For the different experiments in this section, the basic setup and starting conditions have been used as chosen previously. In the first experiment, the crank radius was varied in 5 mm steps from 5 mm to 135 mm (default value was $r_c = 80\,\text{mm}$). During the experiment, the crank velocity was integrated in order to get the overall crank angle. The result was divided by 30 s, the duration of each experiment. A deterioration of the system before the end of the experiment therefore resulted in a low cranking velocity. The result is depicted in Fig. 4.8(a). A variation of about ±50% around the default crank radius still results in proper cranking.

The second experiment was concerned with the spring constant of the springs used in the elastic joints. The standard value, which lay near 10 Nm/rad (see Sect. 4.3), was multiplied by different factors from 0.1 to 2.0 (step size 0.01) in different runs. Figure 4.8(b) shows the results. Again, in a range of ±50% around the default value the system behaved docile.

Since the LPVF controller was described in the discrete time domain and implemented as a discrete algorithm, its reactions to different input frequencies depend on the sample time T_s of the controller. Therefore, the sample time was varied in the third experiment from 0.05 s to 0.11 s (step size 0.002 s). Figure 4.8(c) shows the effect of this variation. The default sample time for all controllers was $T_s = 0.08\,\text{s}$. The desired velocity was achieved for values between 0.052 s and 0.098 s.

In the next experiment, the influence of the central velocity p-controller was varied by changing its p-value (default value 0.06). The result is shown in Fig. 4.8(d). For a decreasing p-value the controller's influence on the process of cranking is also decreasing. At a value of 0 the central

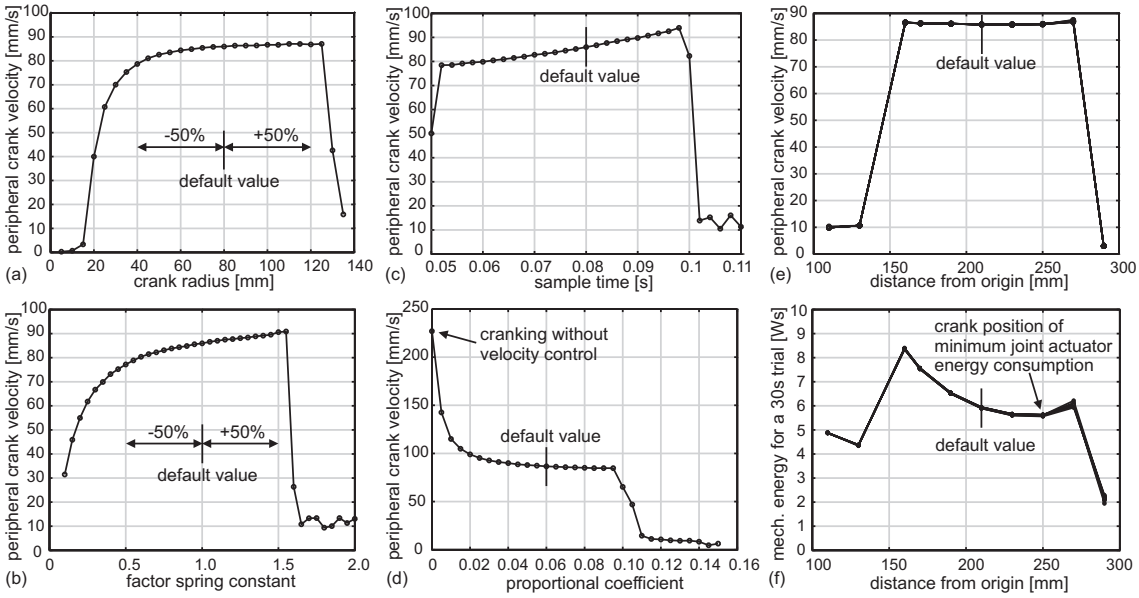

Figure 4.8: Variation of different parameters of the cranking setup in the dynamics simulation.

velocity controller is switched off. The cranking is only controlled by the local LPVF controllers. The free cranking velocity lay around 225 mm/s.

In the last experiment, the distance of the crank center from the origin of the manipulator arm was varied. The default position of the crank center was at a distance of 210 mm from the α-joint. The arm had to be kept within its operating range during a crank rotation. Owing to this fact, the position of the crank could be shifted on a straight line from 110 mm to 290 mm distance from the α-joint. Figure 4.8(e) indicates that distances from 160 mm to 270 mm were tolerated by the system without any problems. Figure 4.8(f) shows the mechanical energy which was converted by the joints during a 30 s trial. The energy consumption varies together with the distance of the crank center. The lowest energy consumption is reached at a distance of about 230 mm to 250 mm.

4.5 Power-controlled discrete SLPVF controller

So far it has been shown that joints controlled by LPVF succeed in the cooperative accomplishment of tasks in closed kinematic chains. If, however, in addition to the coordination a noteworthy joint torque has to be exerted, for example if a weight has to be lifted with the crank or if an LPVF-controlled leg has to thrust a body forward, the situation becomes more complicated. Up to now, each LPVF controller has decided on the next motor command according to the amount of mechanical bending occurring in its elastic joint. However, in the loaded situation the scalar value of bending α_b consists of two fractions. One fraction is due to the tension that occurs because the movement of the limb is not completely targeted into an unconstrained direction. The second fraction is due to the loading of the limb during the task. If the second fraction becomes too

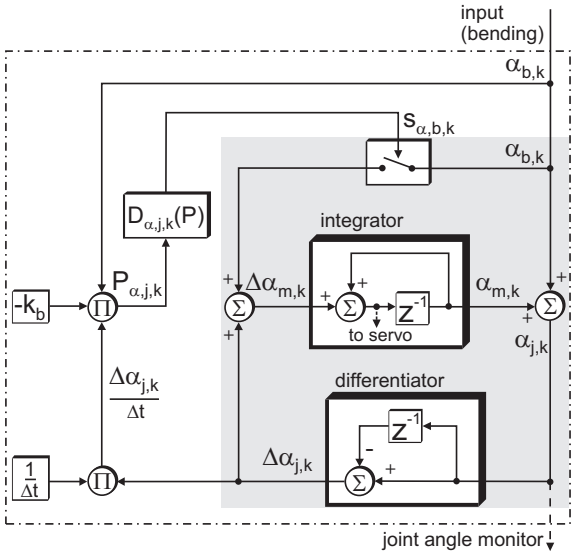

Figure 4.9: Diagram of a switched local positive velocity feedback (SLPVF) controller. Gray background highlights the core circuit. White background distinguishes the power control.

big, it obscures too much of the information needed for coordination. The performance of the limb degenerates. This dilemma can still be solved locally by incorporating the mechanical joint power into the decision process of the joint controller. For this purpose, the LPVF circuit as shown in Fig. 4.5 has to be changed into the one shown in Fig. 4.9. The gray box indicates the core LPVF circuit with a switch $s_{\alpha,b,k}$ included into the upper branch of the bending signal $\alpha_{b,k}$. With this switch the mode of operation of the circuit can be changed. At the end of this section the mechanical power is introduced as a basis for the decision whether the switch is opened (less compliance) or closed (more compliance). Before that, the system equations have to be adapted accordingly in order to incorporate the switch. Equation (4.18c) has to be changed into

$$\Delta\alpha_{m,k} = \Delta\alpha_{j,k} + s_{\alpha,b,k}\,\alpha_{b,k} \tag{4.23}$$

with $s_{\alpha,b,k} \in \{0, 1\}$. The new circuit is called **S**witched **L**ocal **P**ositive **V**elocity **F**eedback (SLPVF). As in the LPVF circuit, the bending signal is still the only input of the system. Therefore, an equation for the angular joint velocity, which solely depends on the bending is set up. Inserting (4.18b) into (4.18d) yields:

$$\begin{aligned} \Delta\alpha_{j,k} &= \alpha_{m,k} + \alpha_{b,k} - \alpha_{m,k-1} - \alpha_{b,k-1} \\ &= \Delta\alpha_{m,k-1} + \Delta\alpha_{b,k}. \end{aligned} \tag{4.24}$$

The replacement of the motor expression $\Delta\alpha_{m,k-1}$ in (4.24) by (4.23) results in:

$$\Delta\alpha_{j,k} = \Delta\alpha_{j,k-1} + s_{\alpha,b,k-1}\,\alpha_{b,k-1} + \Delta\alpha_{b,k}. \tag{4.25}$$

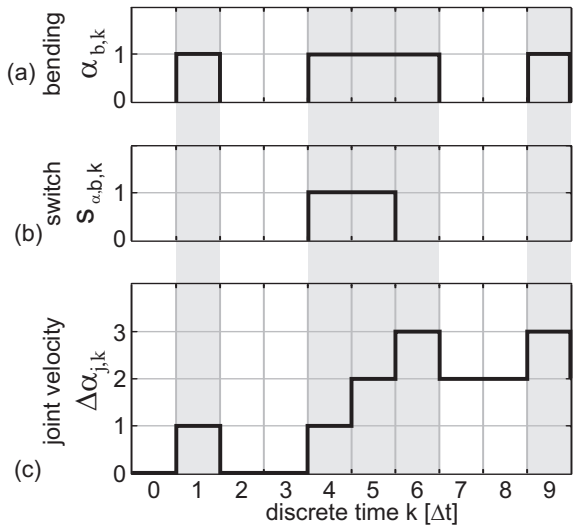

Figure 4.10: Time course of the angular velocity of the α-joint (c) depending on the bending (a) and the switch position (b) of the circuit in Fig. 4.9.

The rearrangement of (4.25) defines the angular acceleration of the joint:

$$\begin{aligned} & \Delta\alpha_{j,k} - \Delta\alpha_{j,k-1} = s_{\alpha,b,k-1}\,\alpha_{b,k-1} + \Delta\alpha_{b,k} \\ \Leftrightarrow \quad & \Delta^2\alpha_{j,k} = s_{\alpha,b,k-1}\,\alpha_{b,k-1} + \Delta\alpha_{b,k}. \end{aligned} \tag{4.26}$$

Finally, the expression for the angular joint velocity is obtained by integration of (4.26). This expression depends on the history of all angular displacements (bendings) that have occurred up to the current time step:

$$\Delta\alpha_{j,K} = \underbrace{\sum_{n=0}^{K-1} s_{\alpha,b,n}\,\alpha_{b,n}}_{\text{base angular velocity } \Delta\alpha_{j,\text{base},K}} + \alpha_{b,K} + c. \tag{4.27}$$

The joint velocity in (4.27) consists of a base angular velocity which has been accumulated by the joint in former time steps and of a part which only depends on the current elastic bending of the joint. Figure 4.10 shows an exemplary evolution of (4.27) in time. Figure 4.10(a) gives the course of a bending signal $\alpha_{b,k}$ plotted for ten time steps ($k = 0 \ldots 9$). Figure 4.10(b) shows the state of the switch during these ten steps. A value of 1 denotes a closed switch. The resulting angular velocity of the joint $\Delta\alpha_{j,k}$ is plotted in Fig. 4.10(c). The gray areas indicate the joint bending. In time steps $k = 0 \ldots 3$ the base joint velocity is 0. The switch is open and therefore the bending pulse at $k = 1$ changes the velocity only temporary. The joint falls back to the base velocity of 0 when the bending has vanished. If bending occurs while the switch $s_{\alpha,b,k}$ is closed like at $k = 4, 5$, the joint velocity also changes but in this case the base velocity of the joint is lifted too. The new value for the remaining time steps is $\alpha_{j,\text{base},6\ldots9} = 2$. The bending pulses at $k = 6$ and $k = 9$ only cause temporary changes of the joint velocity because the switch is open.

The function principle of the SLPVF circuit can be summarized as follows: An open switch only allows non-persistent changes of the velocity by outer forces acting on a kinematic chain and a closed switch generates a completely compliant behavior. This can be used to implicitly "store" the last desired state of the angular velocity in the SLPVF joint controller.
But how can it be decided in which situation the switch $s_{\alpha,b,k}$ is used to switch a joint from one mode of operation to the other? Assuming a joint, as part of a leg, is involved in moving a central body forward. During the stance movement, this joint can safely sustain its base angular velocity as long as it generates positive mechanical power. A positive mechanical joint power means that the actual angular velocity originates from the torque exerted by the same joint. However, a negative mechanical power represents the fact that the directions of joint torque and joint rotation are opposed to each other. In the negative power case, the joint has to behave compliantly (adjust to the overall movement) until it generates positive mechanical power again. The mechanical power of the joint can be calculated as:

$$P_{\alpha,j,k} = \frac{\Delta\alpha_{j,k}}{\Delta t}\tau_{\alpha,k} = -\frac{\Delta\alpha_{j,k}}{\Delta t}k_b(\alpha_{j,k} - \alpha_{m,k}) \tag{4.28}$$

with $\tau_{\alpha,k}$ being the joint torque, Δt the sample time T_s and k_b the spring constant of the joint. In order to operate the switch $s_{\alpha,b,k}$ the decision function $D_{\alpha,j,k}(P)$ is introduced:

$$D_{\alpha,j,k}(P) = \begin{cases} 1 & : \text{ if } P_{\alpha,j,k} < 0 \\ 0 & : \text{ if } P_{\alpha,j,k} \geq 0 \end{cases} . \tag{4.29}$$

If $D_{\alpha,j,k} = 1$ the switch is closed and it is opened if $D_{\alpha,j,k} = 0$. With the introduction of this extension, decentrally controlled joints in closed kinematic chains are able to exert strong net torques while at the same time keeping their ability to perform coordinated movements. This allows the application of these controllers in tasks like cranking up heavy loads and walking. The latter will be shown in the next section.

4.5.1 Dynamics simulation of a 3DoF test leg

The test setup depicted in Fig. 4.11 was chosen to prove that the decentral power-controlled SLPVF control structure is sufficient to operate a 3DoF test leg during the stance movement. The right side of Fig. 4.11 shows the central body with a left middle leg consisting of three joints. The configuration of the leg is similar to that of the stick insect leg as described in Sect. 4.3. Its physical dimensions were adopted from the robot Tarry IIb (see Fig. 4.1). The α-joint is mainly responsible for the forward movement of the body and the γ-joint for the excursion of the leg. However, in early and late stance phase the γ-joint is also responsible for the forward movement of the body and the α-joint has an influence on the leg excursion. Both joints are modelled as elastic hinge joints and are connected with a power-controlled SLPVF controller each. The β-joint is modelled as a rigid hinge joint which is mainly responsible for the body height during stance

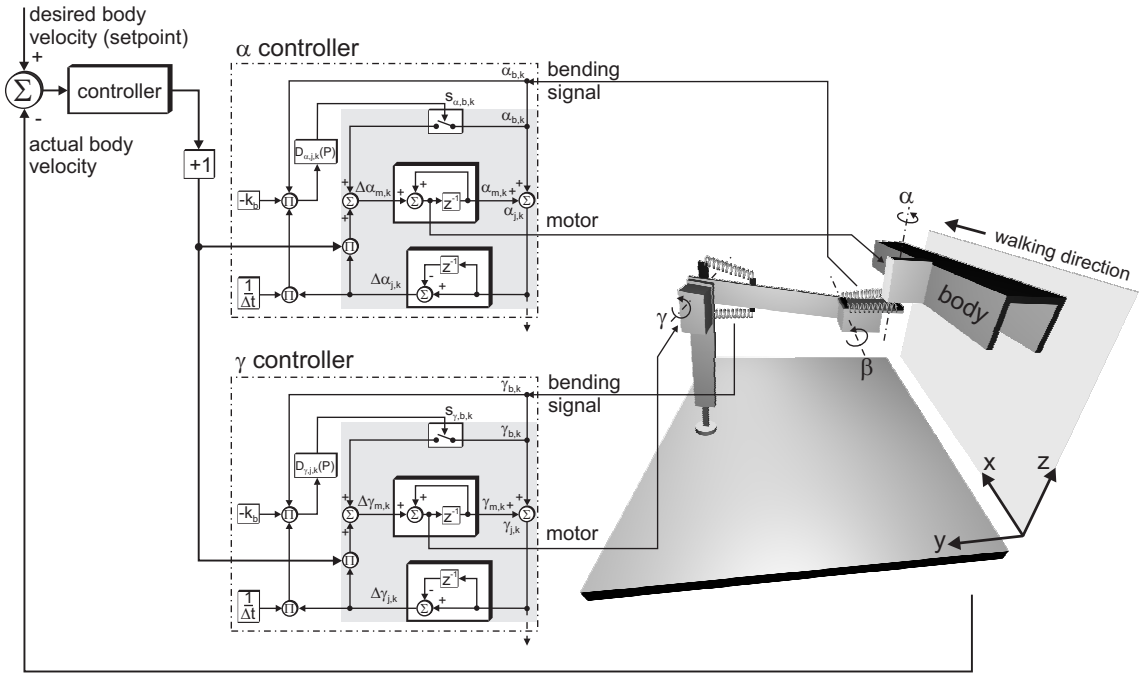

Figure 4.11: Setup of the 3DoF test leg equipped with elastic α- and γ-joints and with SLPVF controllers. The β-joint is kept under classical negative feedback position control. A central velocity controller alters the behavior of the local SLPVF controllers by modulating their loop gain.

Table 4.2: Mechanical data of the body and leg shown in Fig. 4.11.

part	length; radius [m]	weight [kg]
central body	0.32; 0.05	1.0
coxa	0.018; 0.01	0.1
femur	0.115; 0.01	0.1
tibia (incl. foot)	0.117; 0.01	0.12

movement. It is controlled by a negative feedback height controller and will not be discussed any further in this paper (for details see Cruse et al., 1998a). For the overall control of the forward velocity of the body a central velocity controller has been added on the left side of Fig. 4.11. In order to connect the central velocity controller with the SLPVF controllers, its output is used to alter the loop gain of the SLPVF circuits. This method is suggested as an alternative to the ω-controllability measure described in Sect. 4.4.2. During the swing movement, the leg moves to its anterior extreme position (AEP) on a pre-calculated sinusoidal path.

The dynamics simulation was implemented in Simulink 6.1 and SimMechanics 2.2.1. All bodies were set up as cylinders according to Table 4.2. For the simulation trials, a step length of 0.2 m (x-direction), a step width of 0.12 m (y-direction) and a body height of 0.14 m (z-direction) was chosen (coordinate system as depicted in Fig. 4.11). Within the stance movement, the ground contact of the foot is modelled as a damped spring (viscous damping 200 Ns/m, spring constant

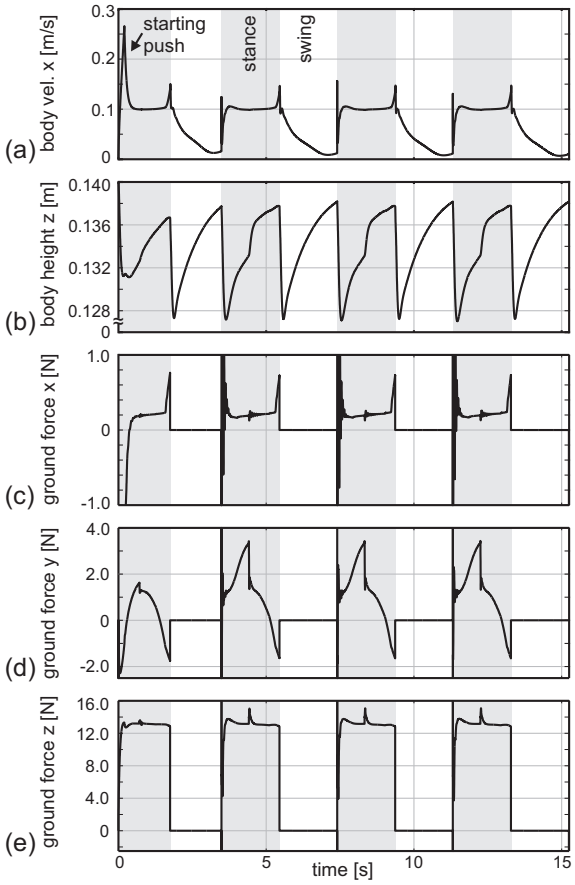

Figure 4.12: Results of the dynamics simulation of the 3DoF test leg. (a) and (b) show body velocity and height, (c), (d) and (e) show the ground reaction force of the leg. Shaded bars depict the stance intervals.

2000 N/m). During the simulation, the y-direction is locked because there are no contralateral legs to center the cross translation of the body.

4.5.2 Simulation results of the walking experiment

For the experiments with the 3 DoF test leg a walking velocity of 0.1 m/s was chosen. The simulation was started by applying an external force impulse of 3 N for 200 ms to the central body. After the transient phase, the system generated step cycles with stable stance and swing movements. In Figures 4.12 and 4.13, only four steps are shown for the sake of a detailed illustration. Figure 4.12(a) shows the body velocity in walking (x-) direction which is the control variable of the central velocity controller. During the whole simulation the body was exposed to a viscous friction. Nevertheless, the desired velocity value of 0.1 m/s was reached during stance. Owing to the influence of the β-height controller, a peak occurs at the end of each stance movement. The height controller's influence on the other joints increases in late stance because of the extreme backward position of the leg together with an outstretched tibia. In this situation the γ-controller competes directly against the β-height controller. Figure 4.12(b) depicts the body height during

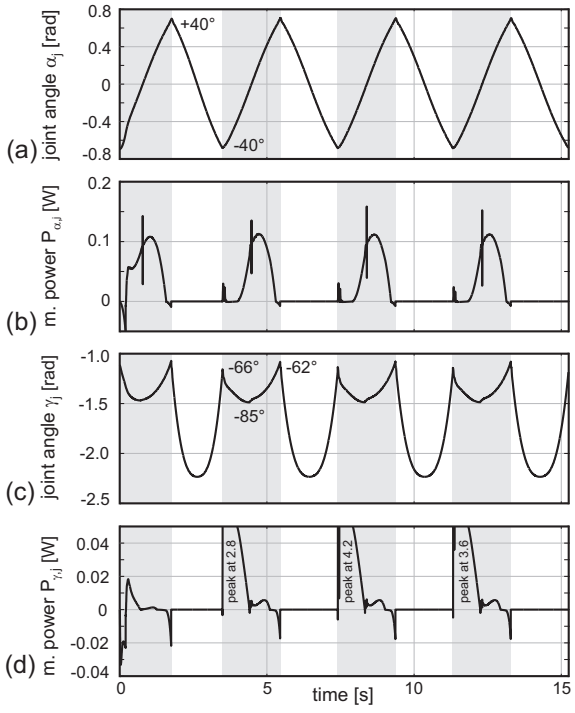

Figure 4.13: Results of the dynamics simulation of the 3DoF test leg. Joint angle and mechanical power for the α- (a,b) and γ-joint (c,d) are shown.

walking. The desired height of 0.14 m was reached with a deviation of about -0.002 m to -0.012 m. Figure 4.12(c), (d) and (e) show the x-, y- and z-components of the ground reaction force acting on the leg respectively. A positive ground reaction force in x-direction accelerates the body forward. The small peak in mid-stance indicates the change of the direction of rotation of the γ-joint. In the first half of the stance movement, the γ-joint moves inwards and in the second half outwards. The ground reaction force in y-direction indicates the share of the force that pushes the body against the "virtual wall" as depicted in Fig. 4.11. This force is also influenced by the change of rotation direction in the γ-joint. In the first half of the stance movement, the y-force is increased and in the second half decreased. The ground reaction force in z-direction supports the weight of the body. For g=9.81 m/s^2 the weight-force of the body and the leg (see Table 4.2) is approximately 13 N. The gamma-joint peak is also clearly visible in mid-stance. Figure 4.13(a) and (c) show the joint angles α_j and γ_j respectively. The angle of the α-joint increases linearly in mid-stance which accounts for the constant body velocity as shown in Fig. 4.12(a). In contrast, the γ-angle shows the characteristic behavior of changing the direction of rotation in mid-stance. Figure 4.13 (b) and (d) contain the corresponding mechanical powers $P_{\alpha,j}$ and $P_{\gamma,j}$ converted in the joints. A comparison of the mechanical powers indicates that the α-joint and γ-joint complement each other. The 3DoF leg was also tested with different nominal velocities. The absolute maximum forward velocity of the robot Tarry IIb is 0.5 m/s. The dynamics simulation of the test leg was also able to walk at that speed as shown in Fig. 4.14(a). Note that, as opposed to Fig. 4.12 and Fig. 4.13, the velocity

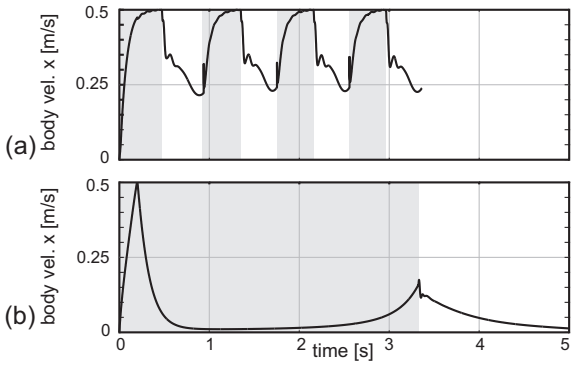

Figure 4.14: Results of the dynamics simulation of the 3DoF test leg. In contrast to the simulation presented in Fig. 4.12, here in (a) the desired body velocity is 0.5 m/s while (b) shows the behavior with no velocity control at all. Note the different scaling of the time axis as compared to Fig. 4.12 and Fig. 4.13.

is plotted over a shorter time interval of 5 s in order to show details of the fast steps. In the final experiment, the central velocity controller was switched off completely. The body was accelerated by an initial push of 5 N for 200 ms. The system was able to finish a complete stance cycle with a forward velocity of approximately 0.05 m/s. It has to be emphasized that this stance movement was generated although there was still a viscous friction acting on the body.
These tests also show that the different joints of a walking leg, whose joint axes do not lie in one plane, can be coordinated and controlled by the decentral control approach of power-controlled SLPVF.

4.6 Discussion

Compliant motion problems are common to both technical and biological systems. Tasks in which robotic limbs have mechanical contact with their own body, with other robots or with objects of their environment require setups with elastic features in order to prevent the system from damage during motion and to sense the details of the contact geometry. Important examples are opening a door (cranking), assembly tasks (peg-in-hole), contact welding (following a surface) and cooperative manipulations with several robots (Yoshikawa and Zheng, 1990; Al-Jarrah et al., 1995; Al-Jarrah and Zheng, 1998). Also in walking and climbing, all legs on the ground or on the surface of an obstacle establish closed kinematic chains (Kumar and Waldron, 1990; Gorinevsky and Schneider, 1990). Mason, 1981 formulated the *compliant frame formalism*, in which the free and constrained directions of movement are distinguished. Based on this, control strategies like *hybrid control* (Raibert and Craig, 1981) or *impedance control* (Hogan, 1985) and their derivatives have been developed. These approaches follow a central controller design which requires knowledge of global system parameters like segment dimensions, masses and inertia, which in addition have to be invariant during operation. LPVF and SLPVF control on the single joint level however are decentral control approaches which do not rely on global knowledge. They use the local angular

displacement (bending) as the sole input signal. The coordination of different joints is exclusively achieved through their mechanical interaction in the closed kinematic chain, which in turn is expressed in the local joint bending. The transfer of remote information via the mechanics is not only a simple transfer of values which renders coordinate transformations needless, but also a conversion of distant events into local information with the help of the agent's body. This aspect shows that mechanical coupling enriches the information content by additionally expressing the body features in local variables like bending. As a result the decentral control concept that has been introduced here is insensitive to changes of the mechanical setup like plastic deformations or changes of segment dimensions or even their number. Changes of the mechanical features lead to changes of local signals, which already represent the adaptation of the joint to the new situation. Therefore, there is no need for an adaptation of the local controller. The (S)LPVF approach accesses many low level mechanical interactions with just one scalar measurement per joint. It exhibits a high level of behavioral plasticity which is necessary for embodiment without explicit reasoning about the effects of low-level interactions. The agent is situated "in-the-world" rather than "on-the-world" (Smithers, 1995).

The prerequisite for the functioning of (S)LPVF is the availability of serial elastic elements in the joints. Elastic properties add inaccuracy to a system but they also comprise a lot of useful features. They can save and store mechanical energy and if they are used in compliant footplates [Fig. 4.4(c)] they can moderate impact forces (Alexander, 1990). The latter is important at the end of the swing movement when the leg touches down on the ground without prior deceleration of the movement. This mechanism is useful if walking agents on uneven substrates are uncertain about the height of the next foothold at the end of a swing movement.

Elastic elements are used in different robot setups. Agents equipped with passive compliance are less affected by control errors than stiff mechanisms.

Möhl, 2003 developed a composite drive mechanism which combines elastic behavior with powerful operation and positioning accuracy. The composite drive consists of a strong, fast and elastic and thus inaccurate force actuator and a precise but weak and slow positioning actuator which can be coupled with an electromagnetic clutch. This example shows that it is possible to achieve the goal of exact positioning while at the same time exploiting the useful properties of elastic joints.

A good example of the use of passive compliance in a walking machine is RHex, a six-legged robot developed by Koditschek, Bühler and co-workers (Saranli et al., 2001). Its legs are built from flexible beams. Owing to the elastic features of the leg, the ground contact is maintained even if the contact points lie on different ground levels, for instance in rough terrain. Elastic features in joints and limbs can also be used in constructions that combine legs and wheels like in Whegs robots developed by Quinn, Ritzmann and co-workers (Ritzmann et al., 2004). However, the results of this study show that the richness of information contained in the joint bending can be exploited

by actively using it in a control mechanism. (S)LPVF succeeds in doing that by relaxing the joint and simultaneously maintaining the externally imposed limb movement.
A promising design for elastic actuators are *McKibben* or *fluidic muscles*. A fluidic muscle is a linear actuator powered by compressed air. The compressed air represents the source of elasticity of this artificial muscle. On the one hand, the control of such a pneumatic system, especially with discretely switched valves, seems to be more complicated than an electrical servo-motor with a spring mechanism. On the other hand, the power-weight ratio of fluidic muscles as compared to that of electrical motors is much better. Dillmann, Berns and co-workers (Berns et al., 2001; Kerscher et al., 2004) developed the robots AirBug and AirInsect with fluidic muscles. The control strategies which are used on these machines again have a central rather than a decentral character. The trajectories are pre-planned and calculated by a central instance. Boblan, Bannasch and co-workers (Boblan et al., 2003) developed a human-like robot with one arm and a hand actuated by fluidic muscles. They also follow the idea of decentralization of the control structure in combination with elastic behavior. A combination of approaches like fluidic muscles and power-controlled (S)LPVF controllers might further improve the performance of such systems.

4.7 Conclusion and future work

Two simple mechanical implementations of elastic joints were introduced which have been already built in the Tarry IIb robot. Furthermore, this work proposed two closely related decentral control mechanisms for the generation and control of movements in closed kinematic chains which are equipped with elastic joints. The first algorithm is based on the idea of local positive velocity feedback (LPVF). This approach enables coordinated movements of closed kinematic chains like it was shown in the cranking experiment. Based on the LPVF control algorithm the power-controlled switched version of LPVF (power-controlled SLPVF) has been derived. This second controller fulfills the two objectives of both joint coordination and mechanical power generation at the same time without global knowledge of the underlying task and without having any information about the setup of the kinematic chain it belongs to. It has been shown in a simulation that a walking task on a 3DoF test leg can be solved by this decentral approach although the walking process requires a high level of coordination and the generation of a net mechanical power. Future work includes the use of (S)LPVF on a six-legged robot. It has to be investigated to which degree the decentral control strategy alone is sufficient for the coordination of powerful stance movements of legs while keeping the CoG within the polygon of stability.

Chapter 5

A universal joint controller for standing and walking

5.1 Introduction

The behavior of the femur-tibia joint of the stick insect *Carausius morosus* has been investigated thoroughly for many years both in standing and walking. The femur-tibia joint is actuated by the flexor and extensor tibiae muscles. The angular position, movement and acceleration of the joint angle are monitored by the femoral chordotonal organ (fCO) (Hofmann et al., 1985). The fCO is situated at the proximal part of the femur. It is connected mechanically with the upper part of the tibia by the long receptor apodeme [see Fig. 5.1(a)]. In the course of different studies two opposing control strategies have been found depending on the state of the animal.

If the animal is in an active state, i.e. walking, a positive feedback effect (reflex reversal, assistance reflex) occurs (Schmitz et al., 1995; Bässler and Büschges, 1990; Bässler, 1988; Bässler, 1976). It is assumed that the assistance reflex generates the stance movement and coordinates the joints of all legs in stance (Chapters 2-4). If the legs are disturbed during their stance movements, also a negative feedback control reaction can be observed in walking (Bartling and Schmitz, 2000; Cruse, 1981; Cruse and Pflüger, 1981). This negative feedback involves a PD-controller with a short time constant for the phasic (D-) part (Schmitz, 1985; Cruse and Schmitz, 1983).

If the animal is in a passive state, i.e. standing, the joint angle of the femur-tibia joint is controlled by a negative feedback position controller (resistance reflex) (Bässler, 1983; Wendler, 1964). This position controller also has a PD-characteristic but it has a larger time constant for the D-part than during stance (Cruse and Storrer, 1977; Storrer and Cruse, 1977). If the leg is flexed stepwise by an external force, the extensor muscle is activated in order to regain the desired angular position of the femur-tibia joint. In the case of an externally applied extension the flexor muscle corrects for the angular position. After onset of an external deflection the correcting muscle first increases

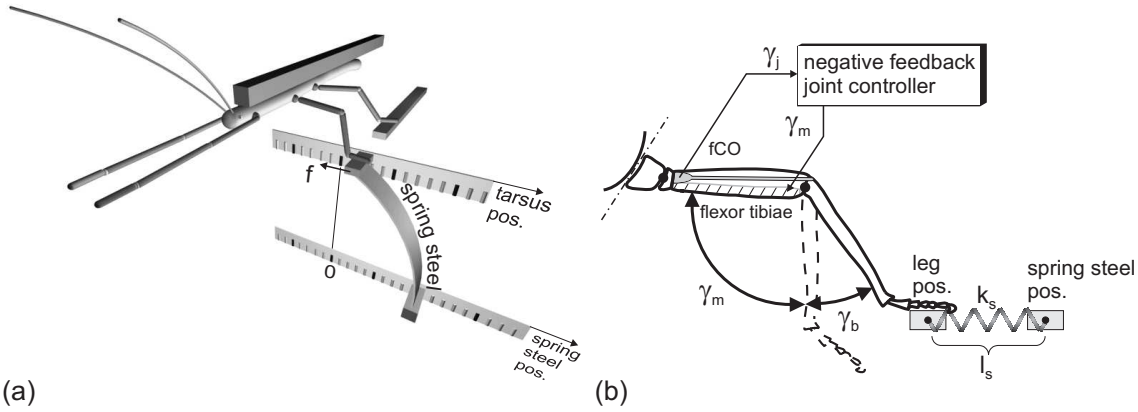

Figure 5.1: (a) Design of the biological experiment. A stick insect is tethered to a balsa wood mount. Both front legs point straight forward (*thanatosis*) and the hind legs and the right middle leg stand on fixed balsa wood supports. The left middle leg stands on a small platform that is supported by a spring steel the base of which is held by a micromanipulator. The micromanipulator moves the spring steel base away or towards the body on a perpendicular path with respect to the body axis (lower scale). At the same time the leg position is monitored (upper scale). (b) Simplified model of the experiment. Presumingly some negative feedback joint controller influences the flexor and extensor tibiae muscles in order to regulate the joint angle. The joint angle is measured by the femur chordotonal organ (fCO). If the base of the spring steel is moved, the spring is lengthened and the tarsus is pulled away from its position. This results in an additional bending of the femur-tibia joint. Depending on the elasticity k_s of the substrate, the insect is able to compensate for the enforced deviation.

its force but decreases it nearly to zero after a few seconds. This could be owing to a D-controller regulating the joint.

A recent study on the control of the femur-tibia joint of the standing stick insect changes the view on this topic drastically. It suggests that the behavior of the negative feedback joint controller depends on the compliance of the substrate the insect is standing on (Cruse et al., 2004).

On highly elastic substrate (Young's modulus is low) the negative feedback circuit behaves like an I-controller. Small deviations from the original position are compensated completely.

On a substrate with a medium elasticity the circuit behaves like a P-controller. This means that the leg attains a resting position that differs from the original position through application of a specific compensation force.

On a stiff substrate the femur-tibia joint seems to be controlled by a D-controller. The tibia end-point is forced away from the original position. In the beginning, the controller tries to compensate for this deviation by activation of the according muscle which results in a counter force. After some time the controller seems to "give up". The force decreases to zero.

Figure 5.1(a) shows the experimental setup chosen by Cruse and co-workers (Cruse et al., 2004). A stick insect is tethered to a balsa wood mount with both front legs pointing straight forward (*thanatosis*). The right middle leg and both hind legs stand on fixed supports also made from

balsa wood. The left middle leg stands on a small platform which is mounted on a spring steel. The base of the spring steel is mounted on a micromanipulator which moves the spring steel sidewards either away or towards the insect body on a line perpendicular to the body axis. Since the spring constant k_s of the spring steel is known, the force acting on the tibia endpoint of the leg in horizontal direction can be calculated by measuring the tarsus position (p_{tarsus}) and the position of the spring steel (p_s)

$$f = (p_s - p_{\text{tarsus}}) \cdot k_s. \tag{5.1}$$

Cruse and co-workers found that the position controller is able to compensate for a spring steel stiffness smaller than $k_s = 0.05\,\text{N/m}$. In this range it works as an I-controller. Up to a spring steel stiffness of about $1\,\text{N/m}$ the animal compensates for the position only partially which resembles the behavior of a P-controller. For a larger spring steel stiffness the insect tries to withstand the deviation first by building up a counter force but after some time it attains the new position which decreases the leg force to zero which corresponds to the behavior of a D-controller.
This chapter introduces a new self-regulating negative feedback joint controller that generates the described behavior of the standing animal. Moreover, an architecture for the combination of both feedback loops is proposed that would explain also the data obtained from walking animals.

5.2 Simulation of the standing experiment

Figure 5.1(b) displays the simplified setup of the experiment shown in Fig. 5.1(a). The joint angle γ_j is the only joint quantity to be measured and hence the only input of the negative feedback joint controller. It is assumed that the negative feedback joint controller issues the motor command γ_m to the muscles in order to achieve a certain angular position of the joint. This is the only output of the joint controller. If an external force acts on the tibia endpoint, there is a difference between γ_j and γ_m which is the angle of bending γ_b. This angular deviation is due to the elasticity of the muscles and the tendons and can be calculated by the controller by subtracting the efference copy of the motor command γ_m from the measured joint angle γ_j

$$\gamma_b = \gamma_j - \gamma_m. \tag{5.2}$$

The angle of bending γ_b is also a measure for the amount of torque that acts on the joint. This torque can be calculated by

$$\tau_\gamma = \gamma_b \cdot k_\gamma, \tag{5.3}$$

with k_γ being the spring constant of the passive elasticity in the femur-tibia joint. The endpoint of the tibia rests on a support. The position of this support represents the leg position. During the simulated experiment the base of the spring steel is moved horizontally. Since the coxa-trochanter joint is immobilized in the simulation, an excursion of the tibia also leads to a lift of the tibia endpoint. In order to correct for that, the vertical part of the spring steel position is always kept

on the same level as the tibia endpoint. The horizontal distance between the position of the spring steel and the position of the leg is multiplied with the spring constant k_s of the substrate in order to calculate the force that acts upon the leg. The experiment was simulated in Simulink 6.1 and SimMechanics 2.2.1 (The MathWorks Inc., Natick, MA, USA) using the kinematic data of an average stick insect as described in Table B.5 in the appendix (see also Ekeberg et al., 2004). The spring constant of the elastic femur-tibia joint was 0.1 mNm/rad. The joint controller which was applied in the simulation is introduced in the following section.

5.3 A self-regulating negative feedback joint controller

In technical systems controllers are often designed as PID-controllers. Biological systems most often employ P- or PD-controllers (Cruse, 1996). A P- or an I-part is important in order to maintain the steady state of a system. A D-controller is suitable to react to the dynamical part of changes in the error signal input. From a technical point of view the control behavior of the femur-tibia joint controller in the standing stick insect is an apparent exception because it changes the controller characteristic and the reference value of the controller according to the elasticity of the substrate which is an environmental parameter. An apparent design approach towards a controller that regulates the femur-tibia joint according to the results of Cruse and co-workers would be a PID-controller the parameters of which were changed at runtime according to the sensed substrate elasticity (Cruse et al., 2004). However, such an approach would omit an important aspect of the biological results. If the base of the spring steel is moved and the spring steel is very stiff, the leg is forced into the new position. The counter force of the leg decreases after some time (D-controller). But additionally, the joint controller seems to accept the new position as reference value because after a while a newly induced deviation from the latter position invokes the same actions of the controller as that from the first position.

The controller introduced in this chapter takes all the requirements mentioned so far into account. The block diagram is shown in Fig. 5.2. The core of the overall control circuit is an I-controller (top of Fig. 5.2) which is part of the negative feedback position control circuit that is indicated by the area shaded in dark gray. The I-controller provides the motor command γ_m and receives the difference between the actual joint angle γ_j and the reference value $\gamma_{j,\mathrm{ref}}$ as input.

The area shaded in light gray on the right side of Fig. 5.2 represents the calculation of the joint bending, the resulting torque and the measurement of the joint angle. The motor command γ_m is subtracted from the actual joint angle γ_j which results in the bending angle γ_b of the joint. The joint torque τ_γ is calculated according to (5.3). The joint torque actuates the femur-tibia joint in the SimMechanics simulation of the leg (see Sect. 5.2). At the same time the simulation provides the actual joint angle γ_j. Taken together, the two areas shaded in dark and in light gray generate a negative feedback position control behavior of the femur-tibia joint that compensates completely

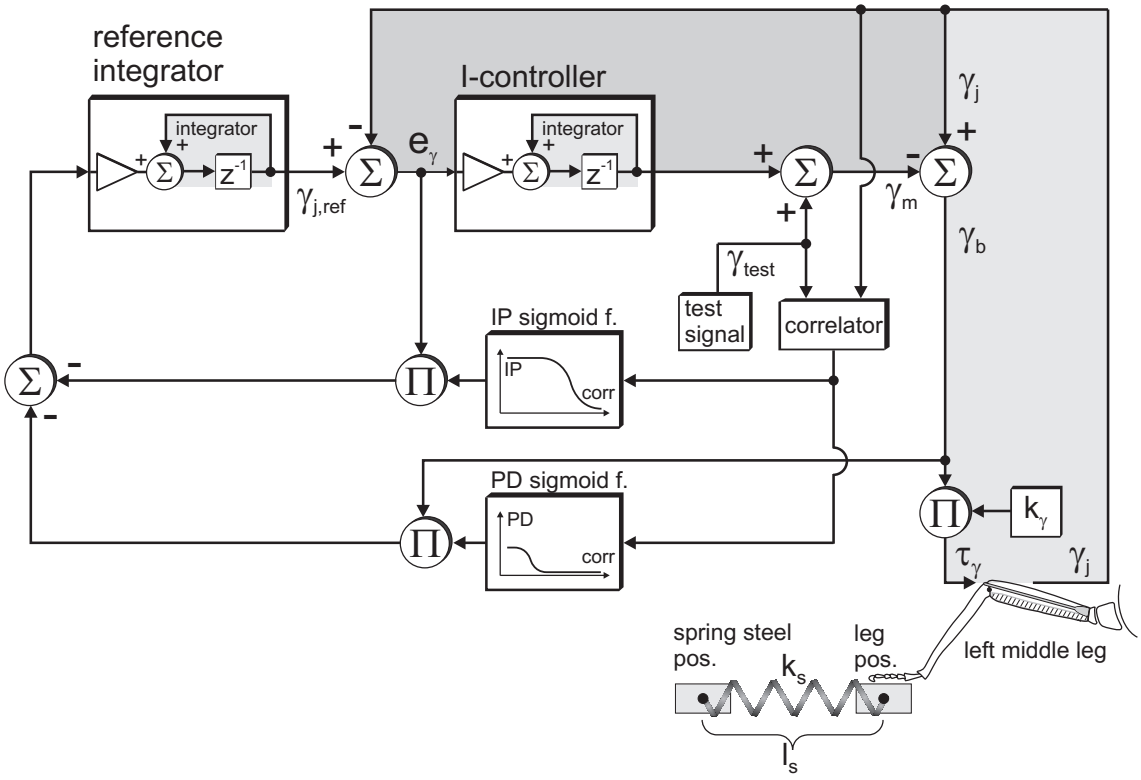

Figure 5.2: Negative feedback control circuit for the femur-tibia joint. The lower right corner shows a sketch of the left middle leg. The femur-tibia joint is driven by a joint torque τ_γ at its "input" and delivers the joint position γ_j at its "output". The femur-tibia joint possesses some elasticity due to muscles and tendons. This is simulated by a serial elastic element. The light gray area on the right indicates the joint angle and torque calculations. The dark gray area represents the negative feedback I-controller. The reference value for the I-controller is provided by the reference integrator. The current reference value is shifted by the reference integrator according to the output of the two sigmoid function which are responsible for the change from I- over P- to D-controller behavior.

for an externally enforced deviation from the desired reference position. The basic function of the circuit therefore is that of an I-controller working in the joint angle domain.

The reference value that is passed to the I-controller is produced by the reference integrator. The reference integrator is a component that acts as a memory for the current reference value $\gamma_{j,\mathrm{ref}}$ of the femur-tibia joint angle (Fischer, 2004). Any input value of the reference integrator that differs from zero shifts the reference value.

In order to sense the elasticity of the substrate, a test signal γ_{test} is generated and added to the motor command output of the I-controller. In the simulated experiments the test signal consisted of a sinusoidal function with a frequency of 70 Hz and an amplitude of 0.1 °. This test signal leads to oscillations in the joint driving torque τ_γ and thus also to periodical fluctuations in the angular position γ_j of the femur-tibia joint. However, the amplitude and the phase of the superimposed oscillations in the femur-tibia joint angle depend on the elasticity (spring constant

k_s) of the substrate. An infinitely stiff substrate would cancel out the oscillations in the joint angle completely whereas a very soft ground would allow the joint to follow the superimposed oscillations.

The correlator in Fig. 5.2 receives both the test signal and the angular position γ_j of the femur-tibia joint as inputs. It is inspired by the correlation detector introduced by Hassenstein and Reichardt (Borst and Egelhaaf, 1989; Hassenstein, 1966; Hassenstein and Reichardt, 1956). The γ_j-signal is high-pass filtered ($f_{3\mathrm{dB}} = 70\,\mathrm{Hz}$) in order to remove the low frequency portion of the signal which results from own or externally applied movements. The test signal γ_{test} is low-pass filtered first ($f_{3\mathrm{dB}} = 20\,\mathrm{Hz}$) which reflects the assumption that the real leg also causes a low-pass effect on the oscillations. Afterwards γ_{test} is also high-pass filtered. After these operations both signals are multiplied, rectified and again low-pass filtered ($f_{3\mathrm{dB}} = 10\,\mathrm{Hz}$). The output of the correlator is calibrated to deliver values between 0 ($k_s = \infty$) and 1 ($k_s = 0$).

In order to bring the control circuit from the I-control to the P-control mode, the upper of the two sigmoid functions (IP sigmoid function) is used (Fischer, 2004). If the correlator output is 1, representing a soft substrate, the output of the sigmoid function is zero. If the correlation decreases (stiffer substrate), the output of the IP sigmoid function increases. In this case, the product of the angular position error e_γ at the input of the I-controller and the output of the IP sigmoid function is not zero anymore. The product is fed as input into the reference integrator in order to move the reference value towards the actual joint angle. In this mode, the I-controller and the reference integrator are competing to make the joint angle error e_γ zero: The former by moving the actual joint and the latter by changing the reference value. As a result at a given medium elasticity of the substrate, the joint partially follows an external deflection. The behavior resembles that of a P-controller.

In order to shift the behavior further from the P-controller mode to the D-controller mode, the lower of the two sigmoid functions (PD sigmoid function) is used. If the correlation is small indicating a stiff substrate, the product of the bending angle γ_b and the output of the PD sigmoid function increases. Since this product is also fed as input into the reference integrator, it also shifts the reference value towards the actual joint angle. This is done as long as a joint bending is present that represents a joint torque. As a result, the controller "gives up" and does not produce any force after some time. This results in a D-controller behavior for a stiff substrate.

5.4 Results

The controller introduced in the last section was tested on a simulation of an insect leg as described in Sect. 5.2 and Fig. 5.1(b). After choosing the spring constant of the substrate k_s, the base of the spring steel was deflected by $1 \ldots 10\,\mathrm{mm}$ by a sigmoid ramp which was centered in the middle of a simulation cycle (5 s). For each run the behavior of the leg position was recorded.

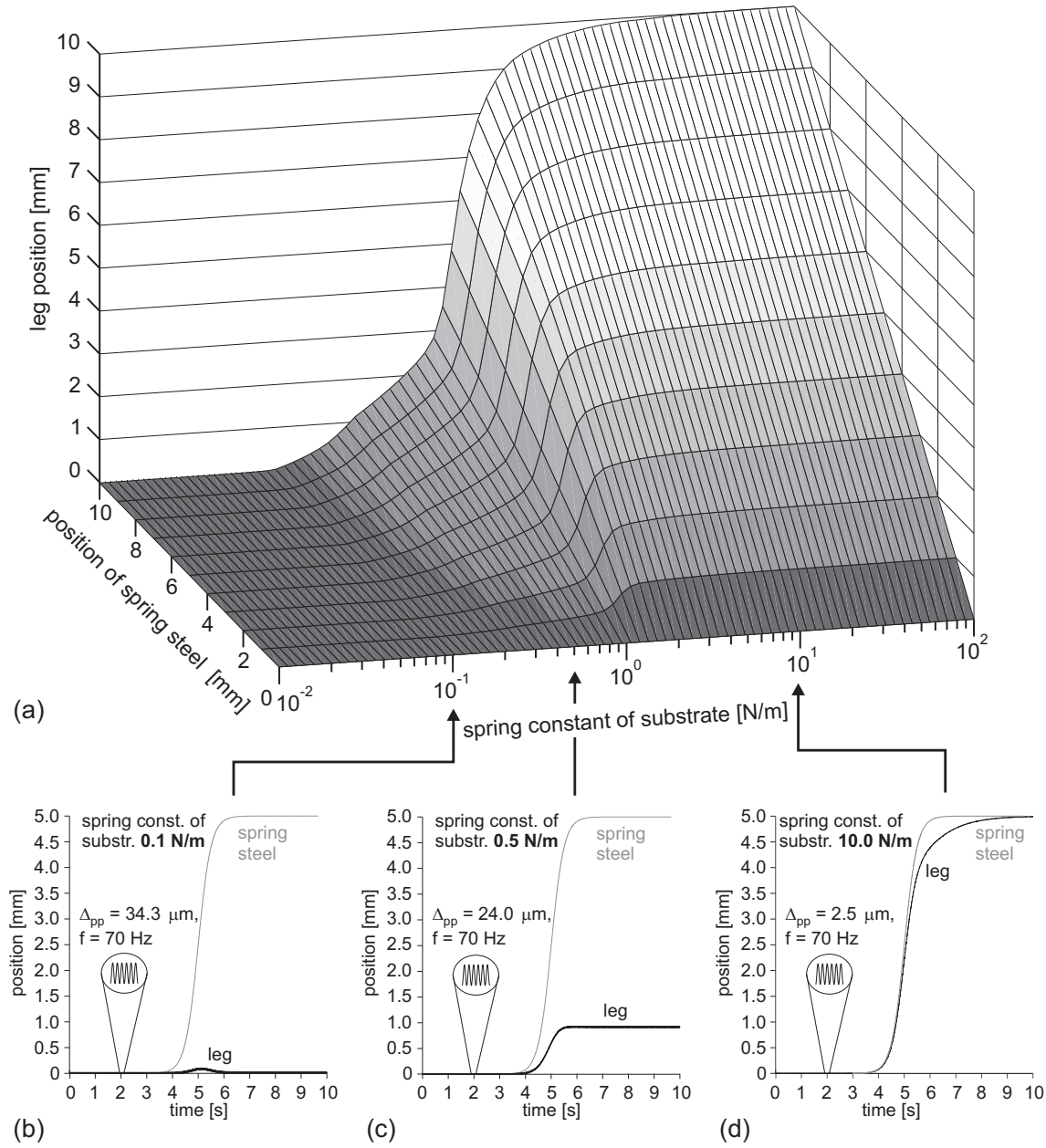

Figure 5.3: (a) Leg position plotted over different deflection amplitudes of the spring steel and over four orders of magnitude of substrate elasticity (values are taken at the end of each simulation cycle). (b,c,d) Leg and spring steel position plotted over time for three different substrate elasticities (0.1, 0.5 and 10 N/m). The controller behavior resembles that of an I-, P- and D-controller, respectively. The insets show the small oscillations superimposed on the leg position resulting from the test signal.

Fig. 5.3(a) depicts the leg position plotted over the different deflection amplitudes of the base of the spring steel and over four orders of magnitude of substrate elasticity. The data points of the 3D-surface were collected at the end of each simulation cycle when the system has reached a steady-state.

The dark gray part of the surface indicates the area in which deflections of the leg are compensated completely. In this working range the controller behaves like an I-controller. The area reaches roughly from substrate elasticities of 10^{-2} N/m to 0.2 N/m. The compensation is achieved independently of the deflection amplitude. The same holds for substrate elasticities smaller than 10^{-2} N/m (not shown here).

In the medium gray area the leg deflections are compensated only partially. The leg comes to rest between its original position and the final position of the base of the spring steel. At the same time the final resting position depends linearly on the deflection amplitude of the base of the spring steel. This indicates the behavior of a P-controller the operating range of which reaches from substrate elasticities of 0.2 N/m to 5 N/m.

In the light area the leg follows the position of the spring steel completely. It will be shown later that within this operating range the controller tries to withstand the deflection of the joint first by generation of a counter force but "gives up" after a few seconds. This area represents the D-control domain. It ranges from 5 N/m to 10^2 N/m in the simulations but the D-control behavior also occurs for all values higher than 10^2 N/m.

Figure 5.3(b) displays a plot of the spring steel position (gray) and the leg position (black) over time for a spring constant of the substrate of 0.1 N/m. The deflection function for the spring steel position has an amplitude of 5 mm. It can be seen that the leg has the tendency to follow the spring steel position at the beginning of the deflection. However, the I-controller restores the original position already during the course of the deflection. The inset indicates the oscillations which were superimposed on the leg position by the 70 Hz test signal. The peak-to-peak amplitude of this oscillation is 34.3 μm.

Figure 5.3(c) shows the spring steel and leg position over time for a spring constant of 0.5 N/m and the same deflection function for the spring steel position as in Fig. 5.3(b). The joint controller is in the P-control domain which leads to a passive movement of the leg of about 1 mm. The oscillations superimposed on the leg position have a smaller peak-to-peak amplitude (24.0 μm) for the given substrate elasticity than for the softer substrate in Fig. 5.3(b).

Figure 5.3(d) presents the same plots as in Figure 5.3(b) and (c) for a rather inelastic substrate (10.0 N/m). The joint controller is in the D-control mode. The leg follows the imposed deflection completely. The superimposed oscillations are smaller than in Fig. 5.3(c). They have a peak-to-peak amplitude of 2.5 μm.

In order to judge the controller's behavior correctly it is also important to look at the forces that act on the leg during the experiments. Figure 5.4(a) shows the leg force plotted over the different deflection amplitudes of the base of the spring steel and over four orders of magnitude of substrate elasticity. Note that the two axes for deflection amplitude and substrate elasticity are the same as in Fig. 5.3(a).

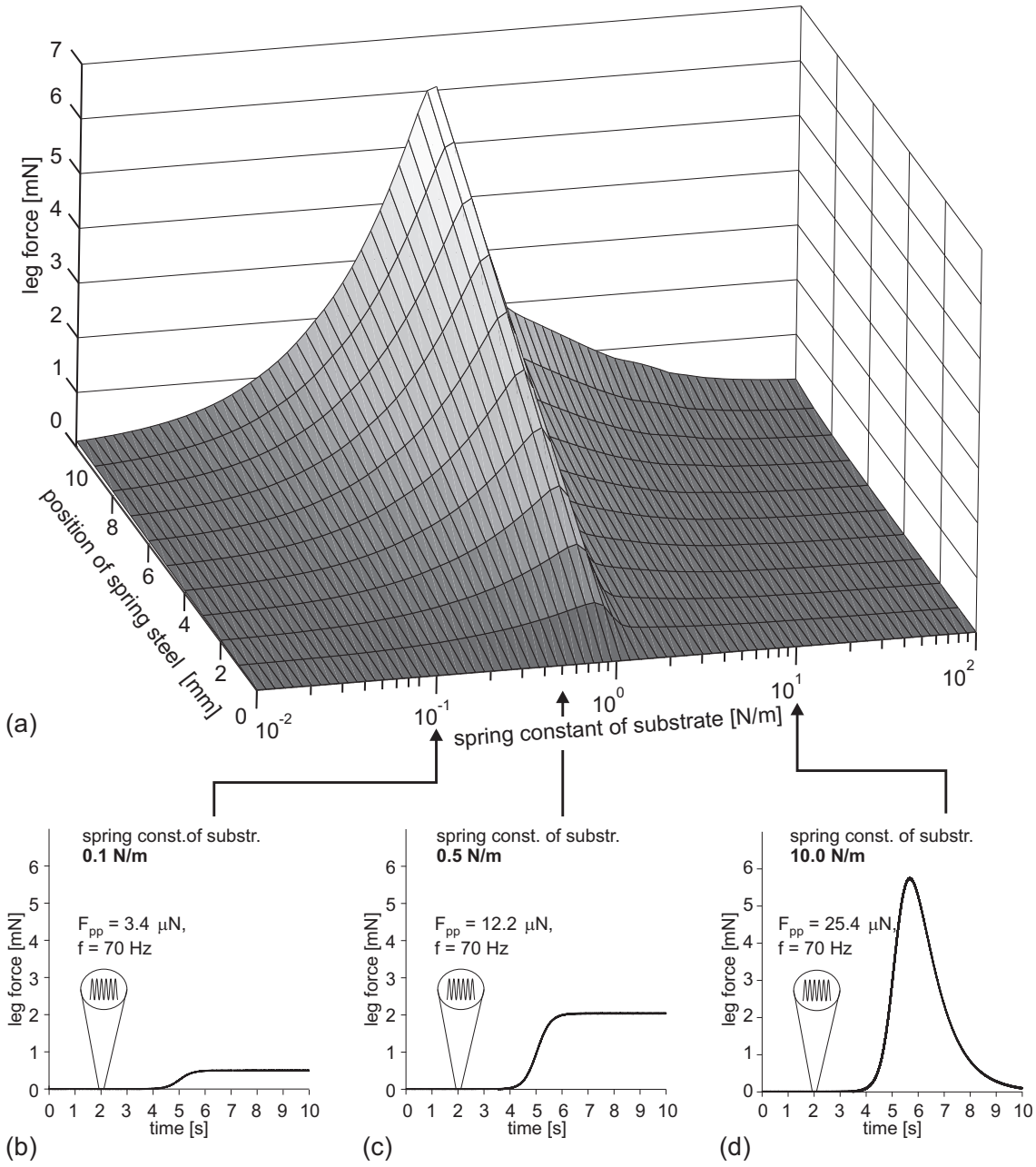

Figure 5.4: (a) Leg force plotted over different deflection amplitudes of the spring steel and over four orders of magnitude of substrate elasticity (values are taken at the end of each simulation cycle). (b,c,d) Leg forces plotted over time for three different substrate elasticities (0.1, 0.5 and 10 N/m). The controller behavior is I, P and D, respectively. The insets show the small oscillations superimposed on the leg force as a result of the test signal.

The part of the surface which is situated at the far left side of the global maximum represents the area in which deflections of the leg are compensated completely which indicates that the control circuit is in the I-control mode. As it could already be shown in Fig. 5.3(a), the I-domain reaches from substrate elasticities of 10^{-2} N/m (and smaller) to 0.2 N/m. In this range, the joint controller

produces exactly the force that is necessary to withstand the deflection. The area of transition from I-control to P-control is governed by the first sigmoid function (IP sigmoid function) that was shown in Fig. 5.2.

The part of the surface which is situated at the left side of the global maximum at substrate elasticities from 0.2 N/m to $5 \cdot 10^0$ N/m represents the P-domain of the controller circuit. The forces which are exerted onto the substrate by the leg increase due to the higher stiffness of the substrate. At the maximum force value at a substrate elasticity of 1 N/m the controller domain already ranges into the operating range of the second sigmoid function (PD sigmoid function).

Towards the D-domain of the control circuit at substrate elasticities of 5 N/m to 10^2 N/m (and larger) the force decreases again and reaches zero. This shows that the joint controller in fact "gives up" and allows the leg to adopt the new reference position. Note that those forces are shown that occur at the end of the simulation (10 s).

Figures 5.4(b), (c) and (d) show graphs of the leg force response plotted over time for the I-, P- and D-mode of the controller, respectively. The substrate elasticities are the same as in Fig. 5.3(b), (c) and (d). Note that in Fig. 5.4(d), which represents a simulation run in the D-domain, the controller generates a force at the onset of the deflection. However, this force decreases after a few seconds due to the effect of the PD sigmoid function. The insets in Fig. 5.4(b), (c) and (d) show the superimposed force oscillations which are caused by the test signal. Note that opposed to the superimposed leg oscillations in Fig. 5.3(b), (c) and (d) the force oscillation increase with rising substrate stiffness ($F_{pp} = 3.4\,\mu$N at a substrate stiffness of 0.1 N/m, $F_{pp} = 12.2\,\mu$N at a substrate stiffness of 0.5 N/m and $F_{pp} = 25.4\,\mu$N at a substrate stiffness of 10 N/m). This is due to the fact that the test signal generates oscillating motor commands that produce higher forces when the leg's freedom to move is decreased by a stiffer substrate. The amplitudes of the superimposed force oscillations are three to four orders of magnitude smaller than those forces generated during stance (Bartling and Schmitz, 2000).

Figure 5.4(d) shows that there is a force maximum at about the end of the deflection ramp at 6 s. Fig. 5.5 depicts the maximum leg force plotted over the deflection amplitude and the spring constant of the substrate. The two axes for deflection amplitude and substrate elasticity are the same as in Fig. 5.4(a) and Fig. 5.3(a). The maximum leg force increases together with the substrate stiffness and with the deflection amplitude of the base of the spring steel. At a substrate elasticity of 1 N/m the maximum force value of Fig. 5.4(a) appears as a local maximum in this graph. As opposed to Fig. 5.5, the maximum force increases further with the spring stiffness beyond this point. This shows that the PD sigmoid function, which is responsible for the decreases of the leg force, does not compensate the force immediately after onset of the external leg deflection.

Figure 5.6 combines the result of Fig. 5.4(a) and Fig. 5.3(a). It depicts the leg position plotted over the leg force as has been used by Cruse and co-workers (Cruse et al., 2004). The values were

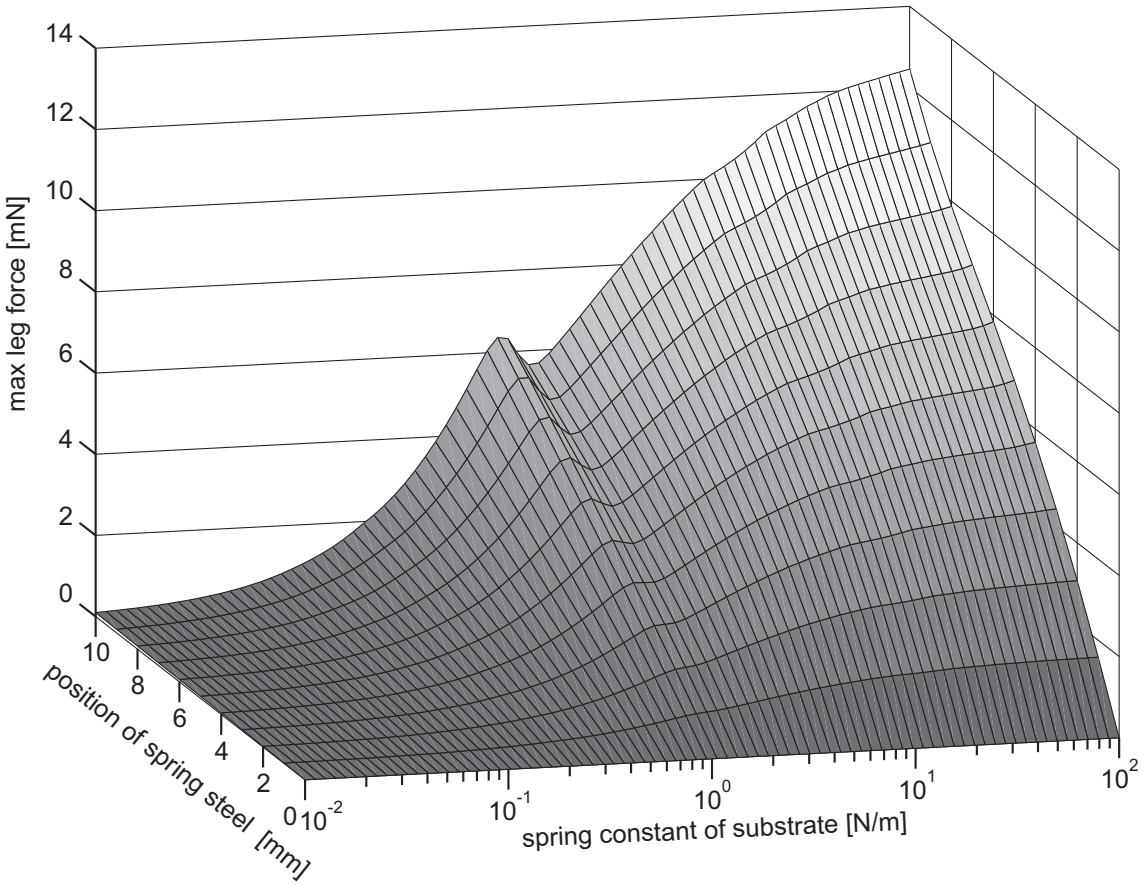

Figure 5.5: Maximum leg force plotted over different deflection amplitudes of the spring steel and over four orders of magnitude of substrate elasticity (values are taken at the end of each simulation cycle)

measured at the end of a simulation cycle for a given spring steel deflection and substrate elasticity. Data points belonging to experiments with the same substrate elasticity are connected by a line.

For a substrate elasticity of 0.1 N/m the leg force increase up to 1 mN without changing the leg position (I-control). In the P-control mode (substrate elasticities of 0.2 N/m to $\sim$ 5 N/m) the simulation shows an almost linear relationship between force and position which reflects the spring like behavior of a P-controller. The maximum force is achieved for a substrate elasticity of about 1 N/m. In the D-domain (substrate elasticities of $\sim$ 5 N/m to 100 N/m and more) the static forces decrease again until the leg follows the deflection of the base of the spring steel completely.

The prerequisite for this control approach to work is the detection of the substrate stiffness. This is done by the correlator introduced in Fig. 5.2. The output signal of this correlator is shown Fig. 5.7(a). The correlator compares the oscillations of the test signal superimposed on the motor command with those oscillations that are found in the angular position of the joint angle. A high correlation (values close to 1) signals a soft substrate and a low correlation (values close to 0) a stiff substrate. The settings of the filters in the correlator are suitable to distinguish spring constants of

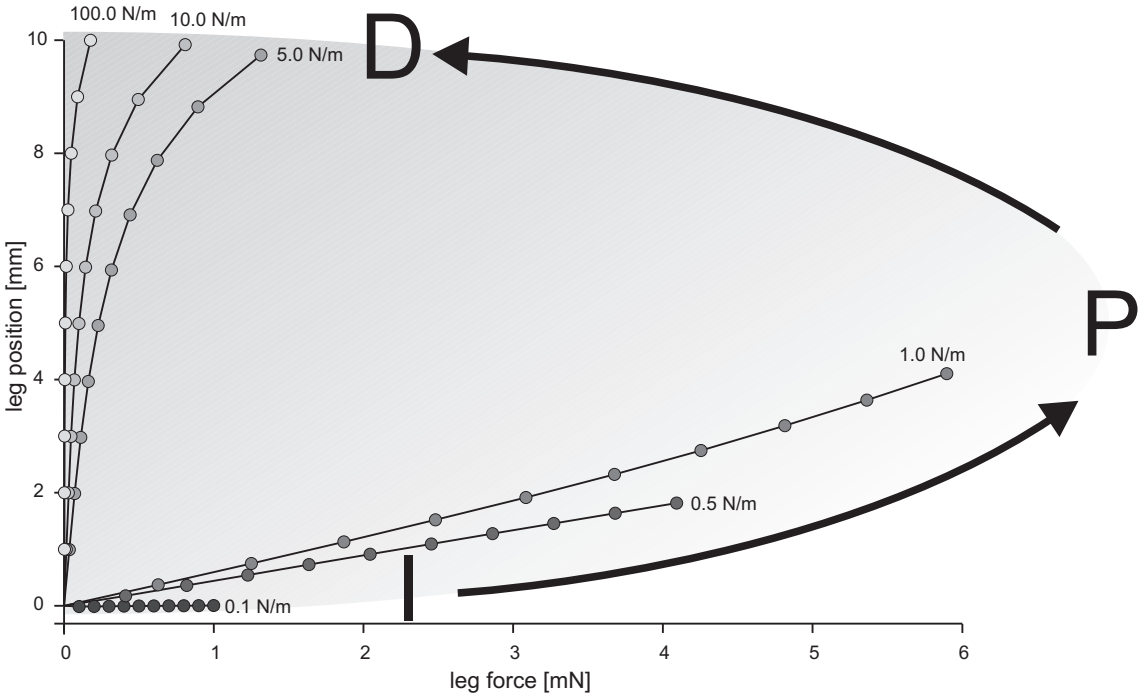

Figure 5.6: Leg position plotted over leg force. Values are taken from the end of simulation cycles when the system has reached a steady-state. The lines connect values that result from simulation experiments with the same substrate elasticity. The two arrows indicate the change of the controller mode from I over P to with an increasing substrate stiffness.

the substrate across four orders of magnitude. At the same time, there is hardly any dependance of the correlation signal on the position of the base of the spring steel during the imposed deflections. Fig. 5.7(b) shows the correlation curve plotted over time for a substrate elasticity of 0.1 N/m. The leg deflection that moves the base of the spring steel (between t=4 s and t=6 s) does not influence the correlation curve. The correlation value is ~ 0.9 during the whole simulation cycle. A corresponding result for a substrate elasticity of 0.5 N/m is displayed in Fig. 5.7(c). The correlation value is ~ 0.6 and remains constant even during the deflection of the spring steel. A substrate elasticity of 10 N/m results in a correlation plot as depicted in Fig. 5.7(d). The correlation values decreases to ~ 0.1.

5.5 Combined controller

In Chapters 2, 3 and 4 the control principle of **L**ocal **P**ositive **V**elocity **F**eedback and its derivatives were introduced. This concept is used in order to generate and maintain movements in closed kinematic chains without a central controller. Also during standing all legs touching the ground form closed kinematic chains. At the beginning of this chapter the different occurrences of positive and negative feedback in walking and standing have already been discussed. This section presents a combination of both the LPVF controller for walking and the self-regulating negative feedback

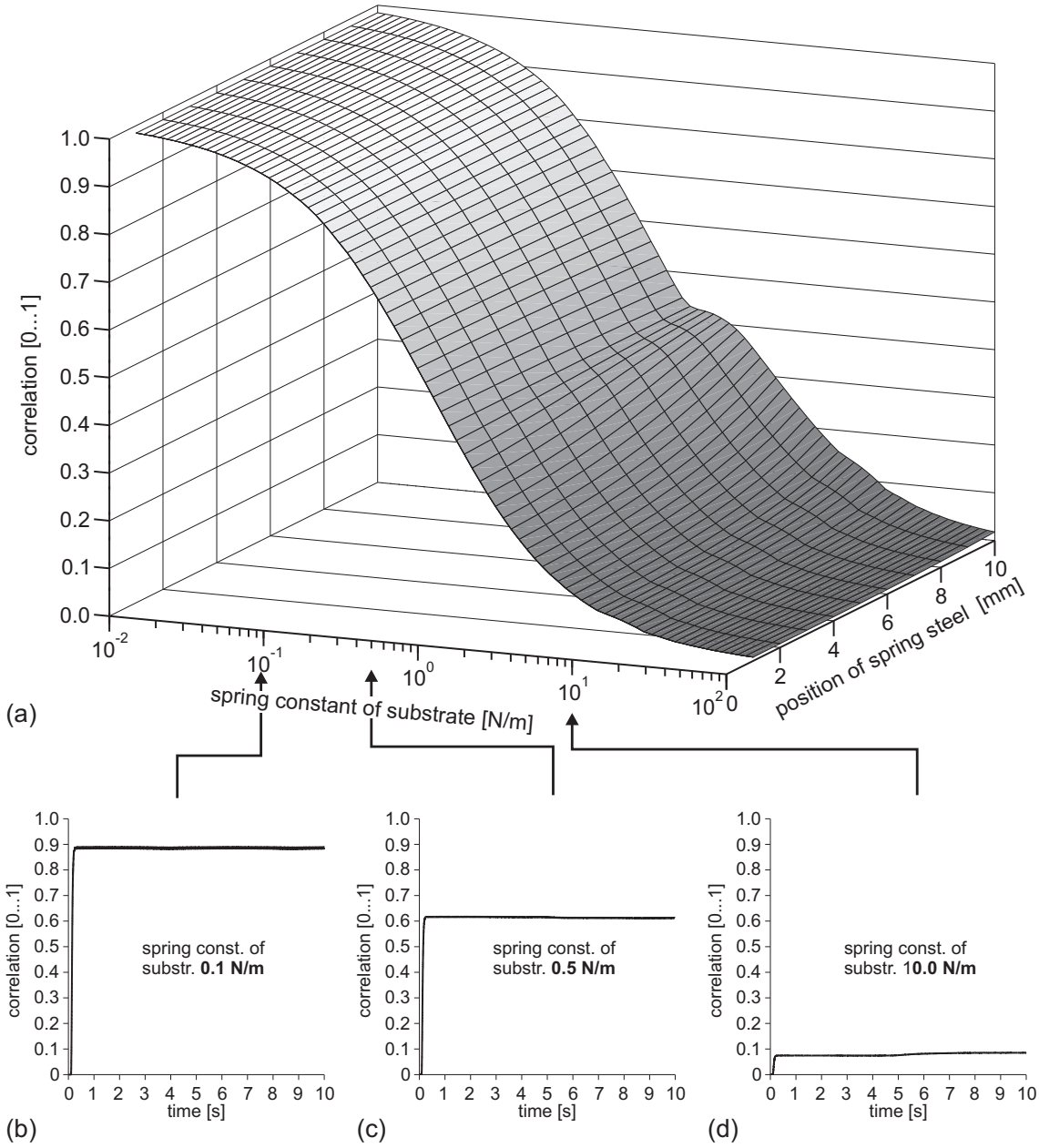

Figure 5.7: (a) Output signal of the correlator that identifies the stiffness of the substrate the leg is standing on. (b,c,d) Correlations plotted over time for three different substrate elasticities (0.1, 0.5 and 10 N/m). The controller behavior is I, P and D, respectively.

joint controller for standing. The block diagram of the combined controller is shown in Fig. 5.8. The component that is responsible for the generation of the stance movement during walking (LPVF) can be found in the upper part of the figure (light gray). The component of the controller that is active during standing is shown in the lower part. Its function was explained in Sect. 5.3. The combined controller uses the reference integrator and the I-controller [middle part of Fig. 5.8] for both modes, i.e. standing and the generation of stance movements.

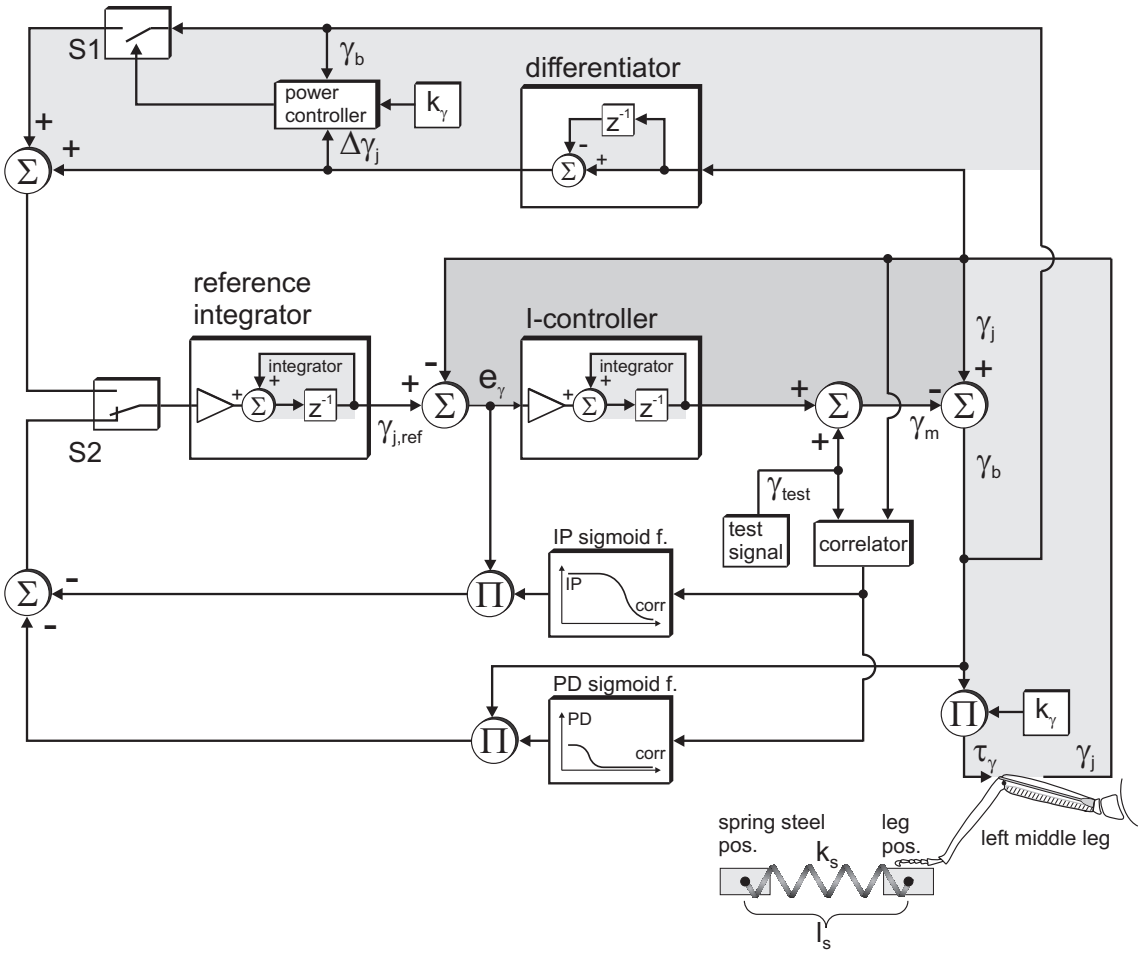

Figure 5.8: Combination of the controller for standing (lower part) as described in this chapter and a power controlled LPVF controller for walking (upper part shaded in light gray) as derived in Chapters 3 and 4.

Local Positive Velocity Feedback controllers, as introduced in this thesis, consist of a differentiator that calculates the angular joint velocity $\Delta\gamma_j$ and feeds it back into the input of an integrator that represents the muscle or motor of the joint. The differentiation of the joint angle γ_j in the combined controller is executed by the differentiator shown in Fig. 5.8. Instead of feeding the angular velocity $\Delta\gamma_j$ into the input of a motor integrator directly, it is now fed into the input of the reference integrator. In order to combine the ability of a decentral joint coordination in contour following and the ability of generating strong forces with a limb, an active relaxation strategy was introduced in Sections 3.3 and 4.5. The basis of the active relaxation is to add the joint bending γ_b on the angular joint velocity $\Delta\gamma_j$ under a certain condition. This condition depends on the mechanical power generated by the joint. In Fig. 5.8 the active relaxation is depicted in the top branch of the circuit diagram. It can be switched on and off by the switch $S1$ [switched version: Chapter 3, Fig. 3.3(b) and Chapter 4, Fig. 4.9]. The switch $S1$ is activated by a power controller that monitors the mechanical joint power that can be calculated as $P_\gamma = (\Delta\gamma_j/\Delta t) \cdot \gamma_b \cdot k_\gamma$. The

power controlled switch $S1$ can also be replaced by a continuous version [see Chapter 3, Fig. 3.3(c)]. A detailed description of the relaxation control process is given in Chapter 3.
The toggle switch $S2$ selects between the positive velocity feedback branch (top) and the negative position feedback branch (bottom). The two behaviors depend on the activation state of the animal and might be chosen by a central instance. Other possibilities will be discussed in the next section.

5.6 Discussion

During stance power controlled Local Positive Velocity Feedback provides a local control mechanism that regulates a joint movement during stance. The self-regulating negative feedback joint controller that was derived in this chapter extends the LPVF approach by adding the ability of holding a given joint angle during standing. The maintenance of a certain angular position is important in order to keep a desired posture against external disturbances. However, a recent study revealed that the joint controller of a standing stick insect does not attempt to hold a given joint angle by all means (Cruse et al., 2004). Instead, the insect is able to maintain a joint angle when standing on soft substrate and to cease if the leg is pulled away on a rigid substrate. The former might be the case if a leg is placed on a moving leaf, the latter if the leg is placed on a rigid branch moved by the wind. The new self-regulating negative feedback joint controller can explain the different behaviors.
The biological system changes the properties of the joint controller from negative to positive feedback depending on the situation given (see Sect. 5.1). In the combined controller this change is achieved by means of the toggle switch $S2$ (Fig. 5.8). It switches between positive velocity feedback and negative position feedback. There are several possibilities which type of information may be used to decide on the position of the switch. One was discussed by Bartling and Schmitz, 2000. They proposed that the controller switches from positive feedback to negative feedback if the joint is accelerated above a certain threshold. Another possibility was proposed by Cruse et al., 2004. They argued that the strength of the correlation between the motor command and the actual leg movement could be used instead of the joint acceleration. A high correlation value reflects that motor commands (intended movements) result in real joint movements in undisturbed walking. In this case, the positive velocity feedback can be activated. If a disturbance occurs during the stance cycle, the correlation value decreases which in turn leads to an activation of the negative feedback part of the controller.
During standing there is no active movement of the joint. Therefore, the correlation measure can only be determined if an additional test signal is superimposed on the motor command. During walking the correlation can be detected by using the stance movement itself as a test signal. In both cases the correlation can be used in order to toggle between positive and negative feedback.
Measurement of the correlation for estimating the spring constant of the substrate implies the following considerations.

First, in a closed kinematic chain not only the joint in question but also the other joints of the same and of other legs and the substrate are involved. Practically, this leads to a serial connection of all elastic elements in the chain. In a serial connection of springs the softest spring governs the overall behavior. Therefore, at the time of measurement all other elasticities in the chain must have a higher stiffness than that of the substrate to allow a correct measurement.

Second, more than just the controller of the femur-tibia joint of one leg may try to measure the spring constant of the substrate at the same time. In this case the interference of measurements by different legs must be prevented. Different solutions are conceivable. A mechanism might exist that distributes the measurements of different legs in time based on communication between all legs on ground. Also a local event randomization in a leg might solve the problem. A different approach was to exploit a distribution of the different measurement signals in the frequency spectrum rather than eliminating the overlap in the time domain.

A closer comparison of the results of the simulation study in this chapter with those obtained by Cruse and co-workers shows a broad principle consistency of the overall behavior but also minor differences in some details (Cruse et al., 2004). The time range of the biological experiments reached from milliseconds to 90 minutes. The intention of this chapter was to show the general control principle by means of a qualitative simulation. In the following, some considerations will be given to compare the results.

Figure 5.9(a) shows result from biological experiments in the I-controller domain (soft substrate) with the mean leg force and position plotted over time. During the first 400 ms of the induced external deflection (deflection force of 0.8 mN) the animals show considerable individual differences in the leg position as indicated by the large standard deviations. Finally, after 400 ms the I-controller prevails and the original leg position is adopted by all animals (small standard deviations). These fluctuations can not be found in the simulation result shown in Fig. 5.9(b). At a low stiffness of the substrate and a given deflection function the simulated leg always reaches its original position shortly after the end of the disturbance.

Figure 5.9(c) shows the same biological experiment as in Fig. 5.9(a) but this time with a deflection force of 1.3 mN. During the first 300 ms of the deflection the leg position has small standard deviations. After 300 ms the standard deviations of the leg position increase and remain at a high level. This indicates that some animals regain the original leg position which corresponds to an I-controller behavior and other animals accept the small deviation and leave their leg in a slightly deflected position which corresponds to a P-controller. Figure 5.9(d) shows a simulation run in the P-controller domain. At a given constant substrate stiffness the simulation always decides for the same controller domain.

In the D-controller domain the leg of the animal generates a sharp counter force peak at the beginning of the external deflection. The decay of the force towards the end of the trial has two

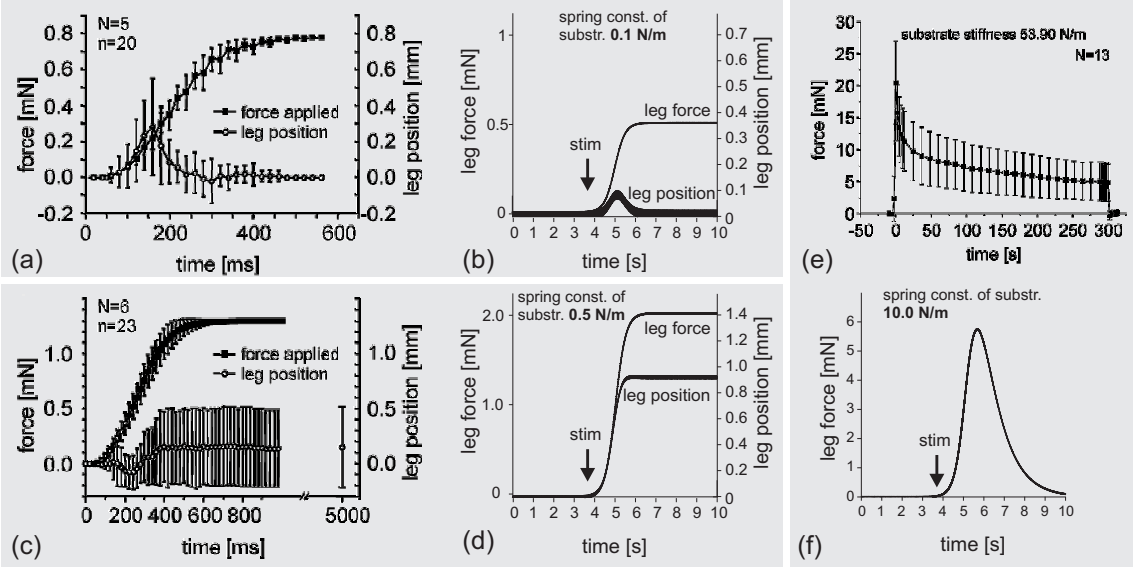

Figure 5.9: (a) Mean leg force plotted over time for an elastic substrate (0.019 N/m) as obtained from animals in deflection experiments. At the onset of the deflection the leg position shows individual differences for a deflection force of 0.8 mN (large standard deviations in the first 300 ms) but a final consolidation of the original position with only small standard deviations. (b) The simulation always shows the same principle behavior for soft substrate. The original position is regained after some time. Note, that the onset of the stimulus is marked by an arrow at ~ 4 s. (c) Same as (a) but with a deflection force of 1.3 mN. During the first 300 ms the leg position shows small standard deviations but finally some animals seem to adopt the P-controller behavior and others the I-controller behavior (large standard deviations). (d) Given a constant substrate stiffness, the simulation always decides for the same controller domain (here P-controller). (e) The biological experiment reveals two different time constants for leg deflections on stiff substrate (D-range). In the D-range the simulation shows the course of the leg force as depicted in (f) (onset of stimulus is marked by the arrow). The general behavior of "giving up" after some time is the same. [(a),(c) and (e) adopted from Cruse et al., 2004]

different time constants as shown in Fig. 5.9(e). The simulated force response of the leg in the D-controller domain resembles the biological data insofar as that no remaining forces occur. However, the simulation does not exhibit the force peak at the onset of the external deflection. Additionally, the decay shows only one time response. This is displayed in Fig. 5.9(f). The peak in the biological experiment might result from nonlinear muscle properties that depend on the velocity by which the muscle is elongated.

In general, with increasing substrate stiffness the insects show a change of the controller behavior from I over P to D. However, a closer look at the biological experiments shows that an increase of the spring constant of the substrate from 0.030 to 0.051 N/m and from 0.112 to 0.252 N/m led to smaller deviations of the leg from its original position. This represents a non-monotonic trend and as a result an unexpected more "I-like" controller behavior [Fig. 5.10(a)]. There is no obvious explanation for this observation. A possible reason could be the elasticity of the femur-tibia joint

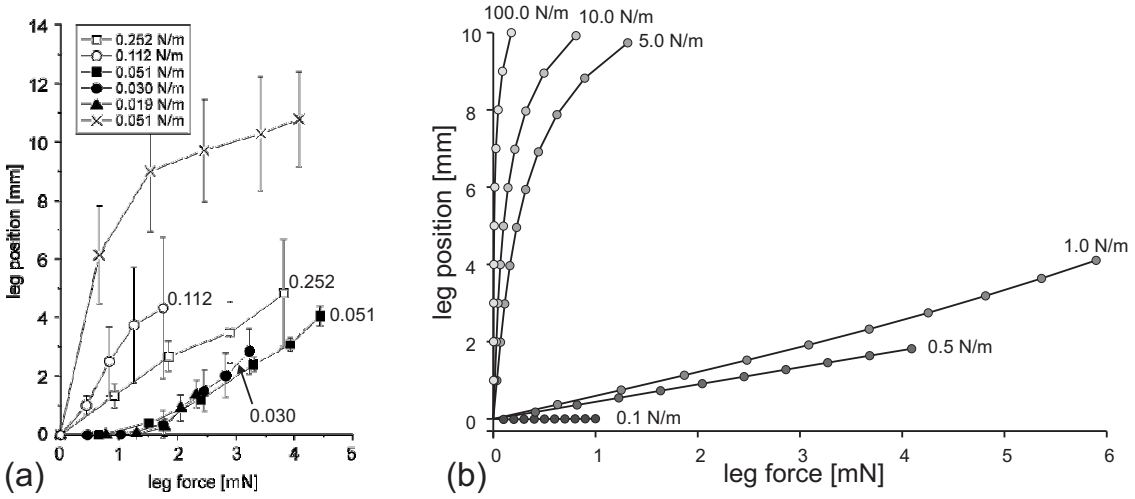

Figure 5.10: (a) The leg position plotted over leg force in the biological experiment. The curves of the different substrate elasticities show a non-monotonic order with increasing substrate stiffness. This is not found in the simulation (b). [(a) adopted from Cruse et al.,2004]

itself. If the spring constant was too low it could obscure the measurement of the substrate stiffness (see above). The non-monotonic behavior was not found in the simulations [Fig. 5.10(b)].

The reference integrator of the control circuit shown in Fig. 5.2 is used to shift the reference value of the I-controller of the joint angle. The input of the reference integrator is shifted by two different signals. The first is based on the angular error at the input of the I-controller when the control circuit changes from the I-mode to the P-mode. The second is based on the torque that is generated by the joint (represented by the angle of bending γ_b) in order to reduce the leg force in the D-mode of the control circuit. In the latter case the torque (or the force, respectively) could either be measured directly or an efference copy of the I-controller output could be used in the D-mode of the circuit. One candidate for the direct force measurement are the campaniform sensilla in the cuticle of the proximal femur that measure the mechanical strain in the exoskeleton (Pringle, 1938). They could provide the force information needed by the joint controller in order to "give up" in the D-mode. However, in a control experiment Cruse ablated these campaniform sensilla and repeated the leg deflections (Cruse et al., 2004). These experiments showed that at least the femoral campaniform sensilla do not influence the results of the experiments significantly. There could also be other proprioceptors that monitor the leg force [e.g. strain receptors at the distal part of the femoral musculature (Bässler, 1977)] but as long as direct evidence is missing it could be assumed that an efference copy of the I-controller output itself is sufficient to generate the observed behavior.

5.7 Conclusion

The combination of two controllers, the self-regulating negative feedback joint controller and the LPVF controller, results in one local controller that regulates a joint in a leg during standing and during a stance movement. The negative feedback joint controller is active during standing on various substrates and when the leg slips during walking. This controller produces a behavior similar to that shown by standing stick insects (Cruse et al., 2004). The LPVF controller regulates the joint movement as derived in Chapter 4. Toggling between the two controller types might depend on the correlation measure or on the acceleration (slipping). The correlation measure introduced here can also be used to estimate the stiffness of the substrate.

Chapter 6

Discussion

Many behavioral studies have been conducted in order to investigate how walking animals make decisions in path planning, overcome gaps or obstacles and search for footholds in rough environments. A precondition for the emergence of such complex behavior is that an animal can cope with basic requirements such as the coordinated generation of swing and stance movements of different legs. Higher order behavior depends on a reliable "low-level" control of such basic leg functions. This work investigates a hypothesis of a decentralized control scheme for elastic joints during the stance movement of walking legs. The control approach is based on the biological findings of reflex reversal.

6.1 Local positive feedback can coordinate movements

Insects like *Carausius morosus*, the model system for this study, cope with the coordination task of controlling all joints of those legs participating in a stance movement without noticeable effort. At a first glance this task might appear trivial but it is not. The stick insect has six legs each equipped with three main joints (subcoxal joint, coxa-trochanter joint, femur-tibia joint) which results in a total number of 18 joints. In the worst case, for example at the transition from standing to walking, all legs are on the ground and start to propel the body forward. This requires a cooperative movement of all 18 joints in such a way that no undesired, or even harmful, forces and moments arise in the body and the legs. A hypothetical central controller in the nervous system could be able to solve this problem. However, it would have to know the complete kinematic setup of the body in order to calculate the equations for the parallel kinematics and dynamics of the system. This also includes exact knowledge of all segment lengths and masses. These values would have to remain constant over a certain period of time in order to unequivocally solve all necessary kinematics and dynamics equations. However, this is not the case in an insect that grows and runs through different larval states or which is still able to walk on leg stumps after a predator attack. Moreover, the number of legs can decrease after autotomy.

Furthermore, stick insects have elastic segments which may bend due to external load conditions and orientation relative to the vector of gravity. All these influences may change the kinematics of the insect.

Thus, the crucial question is how to obtain the adequate movement with respect to angular position and velocity for each single joint. Cruse suggested that positive feedback on the joint level together with mechanical interaction in closed kinematic chains might solve the task without explicit computation of muscle activation (Cruse et al., 1995). The proposed strategy is the following: Assuming that an animal during stance performs a small, initial active movement in one joint while other legs have ground contact. This active joint movement leads to a passive displacement of all joints of legs on ground due to the mechanical interaction via the closed kinematic chains. In a system that comprises inelastic joints and segments, the mechanical interaction would lead to an increased torque demand in the joint drives instead of passive movements. However, in insects the joint drives consist of muscles attached to the two segments of a joint. Besides their ability to actively contract, muscles also show a passive elasticity (Zajac, 1989). Together with the elasticity of the apodemes, the muscles allow for a passive movement of a joint when an external torque is applied. This passive adaptation of angles is locally monitored by proprioceptors in each joint. In the active animal this measured passive adaptation is converted into an active joint movement in the same direction. In other words: The joint controller applies positive feedback. The result is a coordinated stance movement that is executed collectively by locally controlled joints without a need for neural communication. There is no central instance that issues a precalculated movement plan. Thus, the local positive feedback is an interpretation of the reflex reversal described earlier. The prerequisites for this local control approach to generate coordinated stance movements are elastic joints that allow for passive adaptations, appropriate sensors to measure the resulting angular displacements of the joints and positive feedback to maintain and enforce a movement. In the following each aspect of this coordination idea is discussed separately.

Passive adaptation via mechanical coupling

In closed kinematic chains, like a set of legs on ground, external forces can be measured as axial and shear stresses and twisting and bending moments everywhere in the structure. Insects have no internal skeleton but possess an exoskeleton of varying stiffness. The limbs have a high stiffness to support the body. The cuticle of the tibia, for instance, has a Young's modulus of $E \approx 10\,\mathrm{GPa}$ which lies at least one order of magnitude higher than that of muscle tendons ($E \approx 0.5\,\mathrm{GPa}$) (Vincent and Wegst, 2004). Since segments like the tibia have a higher stiffness than the more flexible joint structures, the mechanical stresses and moments have a higher impact on the joint bending than on the bending of segments. Joint elasticity also results from elastic properties of muscles which lie in series with tendons. This further decreases joint stiffness.

Proprioception of joint angles in the stick insect

The passive adaptation of joint angles is monitored by different proprioceptors. The leg of the stick insect *Carausius morosus* consists of three major joints. In the most proximal, subcoxal joint the angle of protraction and retraction is monitored by a ventral coxal hair plate (vcxHP), a dorsal hair plate and chordotonal organs which project from the thorax into the coxa (Büschges and Schmitz, 1991; Bräuning, 1982; Wendler, 1964).

The angle of levation and depression of the coxa-trochanter joint is measured by a trochanteral hair plate (trHP) and by coxo-trochanteral strand receptors (cxtrSR1, cxtrSR2) (Schmitz, 1986; Bräuning and Hustert, 1985a; Bräuning and Hustert, 1985b).

The joint angle of the femur-tibia joint is monitored by the femoral chordotonal organ (fCO) (Bässler, 1965; Bässler, 1967). It consists of a ventral scoloparium with about 80 sensory cells and a dorsal scoloparium with about 420 sensory cells (Kittmann and Schmitz, 1992). Both scoloparia are attached to the tibia via a common receptor apodeme. Only the smaller, ventral part of the fCO is involved in femur-tibia control loops (Kittmann and Schmitz, 1992). The receptor cells are direction sensitive and monitor position, velocity and acceleration of the joint angle (Hofmann et al., 1985).

Assistance reflexes

During stance, a leg has to fulfil two tasks. First, it has to move the body forward by active generation of a horizontal ground reaction force component that is directed backwards. Second, the leg has to support the weight of the animal's body by applying a vertical force component to the ground that points downwards. These two functions have to be fulfilled by the three leg joints. Within the normal range of postures during a stance cycle the forward movement of the body is accomplished by the subcoxal and the femur-tibia joint collectively. The simulations of the 3DoF insect leg (Chapter 4.5.1) successfully used **L**ocal **P**ositive **V**elocity **F**eedback for the movement generation in these two joints during stance. If the stance movement in the real stick insect was generated by a positive feedback mechanism, too, it should be present in these joints.

Heuer investigated the motor system of the subcoxal joints of stick insects in different states of activity (Heuer, 1998). She described assistance reflexes in the middle leg for imposed protraction and retraction movements when the stick insect was activated.

Schmitz and Bässler found assistance reflexes in the femur-tibia joint of activated stick insects for both passive extension and flexion movements (Schmitz et al., 1995; Bässler, 1988; Bässler, 1976).

The coxa-trochanter joint is responsible for lifting and lowering the central body. Since the body height should remain constant, positive feedback in the control of this joint is inappropriate be-

cause it makes the joint collapse under the influence of the gravitational force. In the dynamics simulation in Chapter 4 this joint was kept under negative feedback position control. Also the active stick insect should exhibit a negative feedback control behavior in this joint during stance. As expected, no reflex reversal was found for the coxa-trochanter joint in activated animals (Heuer, 1998).

Putative neural pathways for assistance reflexes

The question arises how two antagonistic reflexes like the assistance and the resistance reflex could be "wired" in a neural system?

For the subcoxal joint control loop, primary afferents from the proprioceptors which measure the joint angles project to motoneurons of protractor and retractor muscles via parallel pathways (Büschges and Schmitz, 1991). This means that afferents of those sensory cells which monitor protraction project on the retractor and protractor motoneurons, both mono- and polysynaptically. The same principle holds for the sensory cells that monitor the retraction. The net output of such a network would depend on the balance of activities of all participating pathways at the point of summation, probably at the level of the motoneurons. The balance of activities of the different pathways would enable different control loop reactions like resistance or assistance reflexes (Büschges and Schmitz, 1991). Such networks could be regarded as a neural correlate of the positive feedback loop that is used in the LPVF controller in this work. A similar organization was described for the femur-tibia control loop (Sauer et al., 1996; Driesang and Büschges, 1996). Bässler termed this organization the "parliamentary principle" (Bässler, 1993).

In LPVF controllers, the angle of bending in a joint is also an important variable. The question remains how the bending angle of the joint, representing a deviation from a desired angular joint position, could be computed neurally. Let us assume that the activity of some interneuron that projects onto a motoneuron would represent the desired joint position. Then the difference of an efference copy of this signal and the afferent activity from the joint angle encoding proprioceptor (for instance the fCO) represented the deviation which is described as bending in this thesis.

6.2 Need for model generation and hardware tests to prove hypotheses

Neuroethologists are interested to trace back an observed behavior of an animal to the activity of the underlying neuronal network. Thus, the final goal is to understand a brain by explaining it in a mechanistic way, i.e. to attribute clearly defined functions to the properties of each neuron and to the interconnections between the neurons. One qualified strategy is to quantitatively study a well defined behavior at all levels - from the macroscopic to the subcellular. However, applying methods

appropriate for each of these levels often implies - for technical reasons - that the animals have to be restrained when moving from the ethological down to the cellular level. In the investigations of such reduced and constrained systems one might easily overlook that an animal lives in a highly dynamic, physical environment. Moreover, the animal itself is an integral part of the environment and contributes - by expressing a behavior - to a change of the state of the environment. And this in turn changes the input of the animal. This loop itself may be a crucial mechanism for the expression of a behavior. A good example to illustrate this is a Braitenberg vehicle, a very simple sensori-motor machine that - when equipped with a body and placed into a real physical environment - can already show quite complex behavior (Braitenberg, 1984). Thus, one way to avoid misinterpretations of neurophysiological data is to model and to simulate the whole system including the animal and the environment. The test of such models can be performed in three different ways.

First, the model of the neural controller could be verified by a direct physiological and anatomical proof that exhibits the entire neural pathways and the cell structures which set up a controller. A direct proof would be the most desirable approach to validate a given hypothesis. In a technical sense this would be a reverse engineering approach. This is not yet feasible since it required detailed and confirmed knowledge about the fine structure of a neuronal network together with the possibility to experimentally choose (pre)defined connections and reconstruct neural "wiring".

Second, the model could be tested by software simulations of the hypothetical controller model on a virtual body that exists in a virtual world. Implementations of software simulations for physical systems can be done on different levels of abstraction. A first approach is to simulate only the kinematics of a physical body. This kind of simulation does neither include any consideration of forces acting on the body due to motion nor those forces that represent an interaction between body and virtual environment. Kinematics simulations can only verify geometrical plausibility, find singularities in the solution for a given setup or check for collisions of bodies. Kindermann presented the implementation of a positive feedback controller in a computer simulation of a stick insect (Kindermann, 2002). His simulation solely relied on kinematics calculations. Interactions of the virtual insect with its virtual environment were modeled by means of an MMC net (Cruse et al., 1998b; Steinkühler and Cruse, 1998). The insect agent performed stance movements with positive feedback and was able to walk in its, apart from gravity, forceless world. It could be shown that the positive feedback idea incorporated well within the control scheme of the overall walking controller, the Walknet (Cruse et al., 1998a). However, when this positive feedback controller was used in a dynamics simulation of a six-legged walker, it lacked the ability to generate adequate ground forces to propel the body forward (Roggendorf, 2006).

Therefore, it is also important to consider forces when movements of real physical bodies are involved in the given problem. This requires a dynamics simulation or, for slow movements of small masses, at least a simulation that includes static force-torque relationships of the setup

(see also Sect. B.5.3). However, even the most advanced software simulation neglects the infinite number of details that are part of a real world setup. When looking at every single detail alone, it may seem to be of minor importance but taken altogether they may change the behavior of a virtual agent considerably. Therefore, according to Occam's principle of scientific parsimony, it is reasonable to reduce the number of assumptions on the controller itself as far as possible without distorting the original controller hypothesis. However, at the same time the functionality of the controller should be proven in an environment that is as realistic as possible. Only then a controller hypothesis is sustainable. The experiments in this work are based on dynamics simulations with simple controller models and environments which at least provide the necessary features to examine the proposed controllers.

A third possibility is to verify a controller model by constructing a real robot. A real robot can be placed in the real world, which is according to Brooks "*its own best model*" (Brooks, 1991). A robot combines a simple construction of the "brain" and the body with the possibility to test this system in a complex environment. This goal was also followed by the construction of the hexapod robot Tarry IIb. When this robot was provided with serial elastic elements in the joints, real world walking tests revealed the minimum possible values of the spring constants that enabled stable walking. The robot is a 10:1 scale model of a stick insect. Different physical parameters scale differently with physical size. If the body and segment length increase, the friction increases quadratically, because it depends on the cross-sectional area of joints. The mass even increases cubically which also means a cubic increase of the inertia. However, only with the utilization of a physical manipulator (Chapter 2) it was possible to prove the applicability of the LPVF approach for the control of a kinematic chain of elastic joints.

6.3 Taming of positive feedback

Positive feedback is often assigned a negative meaning by associating it with terms like instability and unwanted oscillation. This thesis shows that instability can be exploited in order to facilitate a change rather than keeping a current state. LPVF positively feeds back a measured velocity in order to provoke an adaptive joint movement instead of stabilizing a fixed joint velocity with a negative feedback controller. In other words: **L**ocal **P**ositive **V**elocity **F**eedback control is desired instability. This automatically raises the question if this instability can provoke an explosive snowball effect that results in an uncontrollable behavior of the kinematic chain.

The control approach introduced in this thesis relies on the fact that the joint elasticity absorbs the angular movement of the joint drive when the overall movement of a limb leads into a mechanical constraint (e.g. an obstacle). This is the case if the arm in the cranking experiments has the tendency to move away from the crank contour or the leg in stance leaves the stance trajectory. If the active movement of the joint drive is absorbed by the elasticity, this portion is lost for the net joint movement. Since LPVF feeds back the net joint movement this also means that the overall

velocity of the joint is decreased. This directs the overall movement of the limb endpoint onto the contour which is provided by the environment. Joint elasticity therefore does not only tame LPVF passively but also actively.

A comparable finding is described by Prochazka and co-workers (Prochazka et al., 1997b; Prochazka et al., 1997a). They described positive force feedback in the feline locomotor control. There it contributes to load compensation because load-bearing muscles are excited by their own load sensors during locomotion. This process is limited amongst others by intrinsic muscle properties [i.e. force-velocity characteristic (Hill, 1938), length-tension characteristic and passive parallel stiffness]. In other words, the function of limiting the process is not necessarily done by the nervous system alone. Like in LPVF control the interplay of intrinsic properties of the joint drive and the control architecture is responsible for automatic confinement of the movement.

6.4 Comparison of a Hill-type muscle model and a spring

The functioning of the LPVF control approach requires joints that feature passive elasticities as a prerequisite (see Chapters 2-4). The passive elasticity enables the joint to be bent by external forces that act on the segments the joint is made of (passive compliance). In a closed kinematic chain the passive elasticity is the only source of information to judge the quality of the coordination between the own active movement and those of other locally controlled joints in a given task like cranking and walking. The use of a serial elastic element was inspired by biological joints which also allow for an externally applied passive movement. The elasticity of biological joints originates in the elastic features of the muscles and tendons. This raises the question to what extent a servo motor equipped with a serial elastic element can be compared to a biological muscle. Figure 6.1(a) shows a Hill-type muscle model (Zajac, 1989). In this model a muscle is divided into a sequence of two functions. The first function represents the *activation dynamics* and the second represents the *muscle contraction dynamics* (shaded in light gray).

The activation dynamics transforms activation information encoded in a sequence of spikes (neural excitation) into a continuous muscle activation. The muscle activation can be regarded as a measure of the number of active actin-myosin bridges. The normalized muscle activation is fed as input into the muscle contraction dynamics.

The contraction dynamics consists of two characteristics, a force-length characteristic (top) and a force-velocity characteristic (bottom). The former is often modeled as a Gaussian-type function and reflects the fact that a muscle produces its maximum force when the muscle length L is near to the resting length L_0. At the resting length L_0 the actin-myosin overlap in the sarcomeres is optimal without a restriction of the freedom of movement for the sliding filaments. A shorter length L results in an overlap of the opposite actin filaments. This impairs the combination of myosin with appropriate actin filaments. Additionally, the myosin filaments are squeezed as soon as they come close to the Z-disks. A higher length L decreases the overlap of actin and myosin filaments

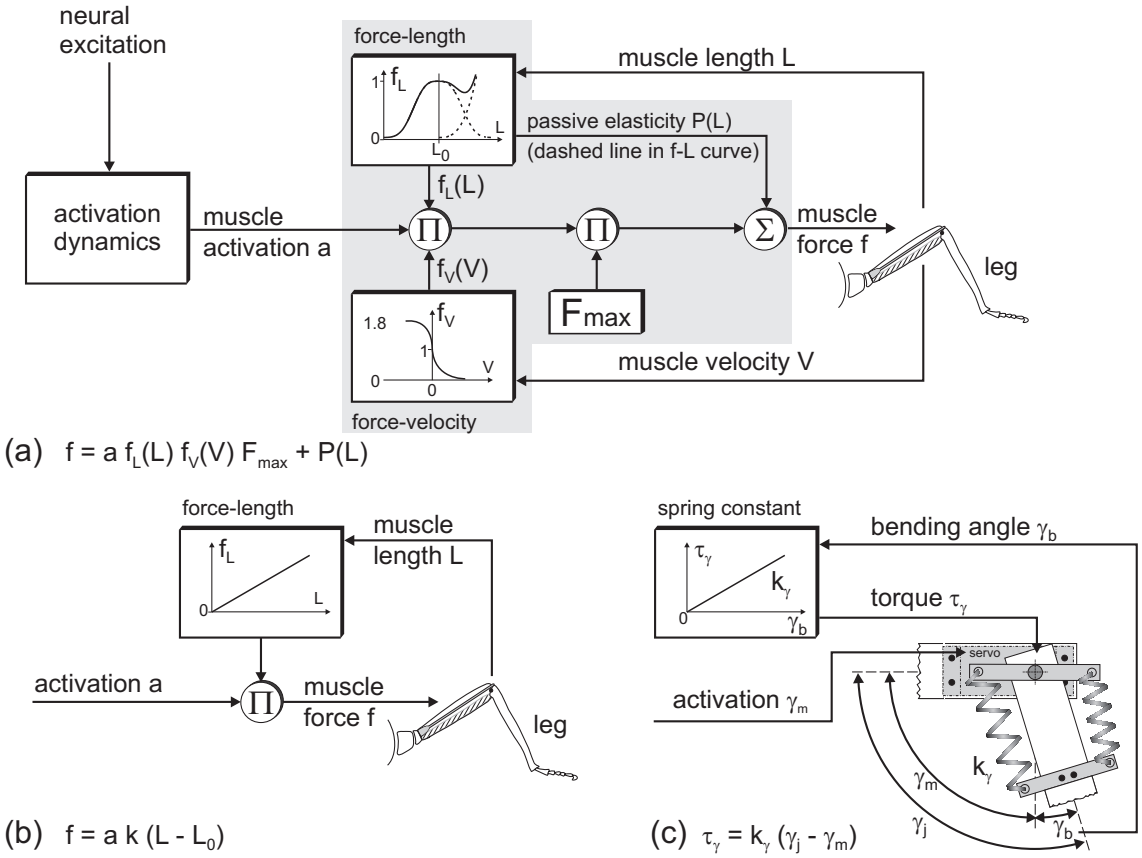

Figure 6.1: (a) Comparison of a Hill-type muscle model (muscle contraction dynamics shaded in gray), (b) a linearized version of a muscle model and (c) the elastic joint with extension springs.

linearly which decreases the number of cross bridges that can be formed. Normal muscle operation keeps the lengths of the sarcomeres in an optimal working range. The force-length characteristic takes the muscle length L as a parameter and outputs the normalized force $f_L = [0 \dots 1]$. The muscle length depends on the state of the mechanical setup the muscle is placed in.

The force-velocity characteristic is often modeled as a sigmoid function. It describes the relationship between the muscle force and the contraction/elongation velocity of the muscle. It takes the muscle velocity V as the input parameter and issues the normalized force $f_V = [0 \dots 1]$ at its output. The muscle velocity also depends on the mechanical state of the mechanical part the muscle is connected with.

The two normalized forces f_L and f_V are multiplied with each other and the normalized muscle activation a. The result is scaled with the maximum isometric force $F_{\max}$. Finally, in order to get the actual muscle force f, the passive elastic force P is added. The muscle force equation is given in Fig. 6.1(a). The muscle force f acts on the leg joint and generates the dynamic behavior of the physical segments.

Figure 6.1(b) displays a simplified and linearized version of the muscle model in Fig. 6.1(a). It leaves out the activation dynamics and omits the force-velocity characteristic completely. The

force-length characteristic is linearized. For a given activation a the muscle force f only depends on the length L of the muscle. This resembles the function of an extension spring with a spring constant k and a resting length L_0. As opposed to a mechanical spring that obeys Hooke's Law this muscular "spring" can change its spring constant and absolute force with the level of activation. In the isometric case (constant L), the activation a controls the force directly. The muscle force equation is given in Fig. 6.1(b).

Figure 6.1(c) shows the implementation of an elastic joint as it was proposed in this thesis (for example in Sect. 4.3.1). It consists of a servo motor that is mounted on one segment of a joint. The servo motor drives the second segment via a serial elastic element (here represented by a construction with two parallel extension springs). The difference between the joint angle γ_j and the motor angle γ_m represents the bending angle γ_b of the torsion of the serial elastic element. The bending angle is multiplied by the spring constant k_γ in order to calculate the torque τ_γ that acts on the joint. The angular position of the motor axis γ_m can be regarded as activation value that adjusts the pre-tension of the serial elastic element and thus regulates the overall torque at a given time.

Common to all three models is that they generate a muscle force f as a response to an activation value a. The elastic servo motor in Fig. 6.1(c) behaves similar to the activated, linearized model in Fig. 6.1(b). However, the elastic servo motor only implements a constant torque-angle characteristic whereas in the other two models the spring constants can be modified via the activation level a. The Hill-type muscle model exhibits further non-linear characteristics which are not considered in the elastic servo motor. Changes in the control scheme of the servo motor might enable it to mimic the Hill-type model (see next section).

6.5 Outlook

The work presented in this thesis contains both different biological aspects and aspects of control theory. Each of these aspects might induce further investigations in the biological field as well as in the technical utilization of the control concept.

The first aspect is the proof that positive velocity feedback on the single joint level can be used to generate powerful movements in closed kinematic chains. This gives rise to further biological investigations to consolidate details of the actual biological controller setup. Especially the finding that a net force generation can only be achieved if an active relaxation mechanism is combined with the **L**ocal **P**ositive **V**elocity **F**eedback should be investigated in the biological system. The relaxation mechanism as proposed in Sections. 3.3.2, 3.3.3 and 4.5 depends on the amount of joint bending or the mechanical power. In the biological system, the joint bending in the femur-tibia joint could for example be encoded by the difference between an efference copy of the muscle activation and the joint angle as monitored by the fCO. The campaniform sensilla monitor the

strain in the femoral cuticle. This strain should also contain some information on the bending state of the joint. The mechanical joint power is the product of the joint torque (proportional to the joint bending) and the angular velocity of the joint. The angular joint velocity for the femur-tibia joint is also monitored by the fCO.

The second aspect regards the negative feedback controller for the standing animal as derived in Chapter 5. The assumption that the substrate elasticity is monitored by superimposing small test movements on the femur-tibia joint, requires biological investigations in order to find out whether a stick insect follows a similar strategy.

A closely related aspect is that of the correlation of a desired and the actual joint movement. If a control instance had access to the information how much of the intended movement could really be accomplished by the joint, it could estimate the elasticity of the substrate. If such a correlation system is supposed to work even during animal movement, it might be necessary to know how much correlation could be expected for a normal walking situation. In any case it is important to find out if the animal is aware of successful movement generation and if there is a physiological representation of this information.

The combined controller as derived in Chapter 5 contains positive feedback and negative feedback control structures. However, it was not possible to reproduce the biological findings of Bartling and Schmitz, 2000. They found that an external deflection of a stick insect's leg during stance leads to a negative feedback reaction of the leg. This means that both signs of feedback can occur during the stance cycle. A simple switching from positive to negative feedback does not explain the results of the biological experiment. It might also be the case that the negative feedback effect observed by Bartling and Schmitz, 2000 results from the complex muscle function in the real insect. This could be verified by the introduction of a muscle model into the simulation.

An important aspect of this thesis is the introduction of a serial elastic element as the basis of a joint the movement of which is controlled by **L**ocal **P**ositive **V**elocity **F**eedback. The elastic joint consists of a servo motor and extension springs and is mechanically very robust. The concept of measuring the bending angle with a combination of a Hall sensor and a permanent magnet caused some problems in the practical use since the sensors had to be calibrated in a torque free setting to reduce offset errors. It might be more convenient to measure the joint torque directly. However, the small size of robotic joints in the Tarry IIb robot makes the use of strain gauges difficult. Potentially, the direct measurement of the electrical current of the servo's DC-motor might provide usable information on the joint torque. This in turn could be used to change the position control mechanism in the servo itself. The elasticity of the servo drive would be a result of the new controller behavior rather than that of a physical spring. In addition, a muscle model could be included into the servo controller characteristic to gain a better approximation of the biological joint movement.

Appendix A

Elastostatics of Beams

The application of **L**ocal **P**ositive **V**elocity **F**eedback control, as it is derived in this work, is confined to elastic joints. Joint elasticity in biological systems is an attribute of the muscles and tendons that drive a joint. In technical applications it is either a property of the actual drive like in McKibben or fluidic muscles (Berns et al., 2001; Kerscher et al., 2004; Boblan et al., 2003) or it is implemented with an additional passive elastic element like a spring or a rubber block. For example the robot Tarry IIb utilizes pairs of extension springs in its femur-tibia (also: γ or "knee") joints in order to add elasticity to the otherwise inelastic servo drives (Schneider et al., 2006a). Since all joints in this robot are rotational, these extension springs have to act like torsion springs. In its body-coxa (also: α or"hip") joints Tarry IIb possesses constructions that use elastic beams in order to achieve the required elasticity of torsion springs. Chapter 4 features an explanation on how the elasticity of an elastic beam construction can be calculated with the Euler-Bernoulli beam equation.

The content of this chapter covers a basic explanation of measures which are important for understanding the elastic behavior of beams and the derivative of the Euler-Bernoulli beam equation (A.31). For this purpose all necessary derivations were taken from standard text-books for engineering mechanics (Magnus and Müller, 1974; Brommundt and Sachs, 1988; Schumpich, 1980) and compiled in a suitable order.

A.1 Strain

Strain is a local deformation of a body, or more precisely, it is the relative change of the length of a body with respect to its resting length. The word "length" in this context is substitutional for length or diameter. If a force F acts on a simple rod, as shown in Fig. A.1, it generates an elongation in longitudinal direction and a contraction in cross direction. The change in length is:

$$\Delta l = l - l_0 > 0. \tag{A.1}$$

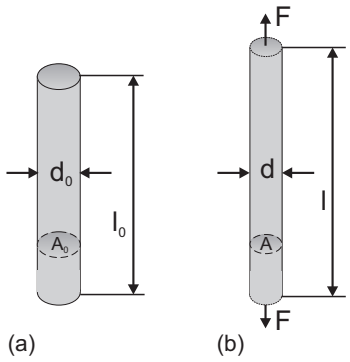

Figure A.1: Simple rod (a) with the length l_0, the diameter d_0 and the cross-sectional area A_0. (b) The same rod showing an extension under the influence of a force F.

The change in diameter is:

$$\Delta d = d - d_0 < 0. \tag{A.2}$$

Both measures can also be written with respect to their original lengths. These relative values are called *strain* in longitudinal and in cross direction. They can be written as:

$$\epsilon_l = \frac{\Delta l}{l_0} = \frac{l - l_0}{l_0} \tag{A.3a}$$

$$\epsilon_c = \frac{\Delta d}{d_0} = \frac{d - d_0}{d_0} \tag{A.3b}$$

A positive ϵ represents an *elongation* and a negative ϵ a *contraction* of the rod. The unit of strain is $[\epsilon] = 1\%$.

A.2 Stress

Mechanical stress measures the forces that appear within a body when this body is exposed to external forces. Fig. A.2 shows two examples for stress. Fig. A.2(a) shows a rod which experiences an external force F. The internal forces can be visualized when the rod is cut along the line $1-1$. In this case the normal force $N(=F)$ appears. These internal forces balance out the external forces so that the net force acting on the rod is zero (The rod does not move!). When the normal force is related to the cross-sectional area of the rod the expression for the *normal stress* reads as follows:

$$\sigma = \lim_{A_0 \to 0} \frac{\Delta N}{\Delta A_0} = \frac{N}{A_0} \tag{A.4a}$$

$$\sigma = \frac{F_N}{A_0}. \tag{A.4b}$$

ΔN can be regarded as the normal force of single fibres with the cross-sectional area ΔA_0 which together build the rod. In Fig. A.2(b) an external force acts tangentially on the cross-section of a

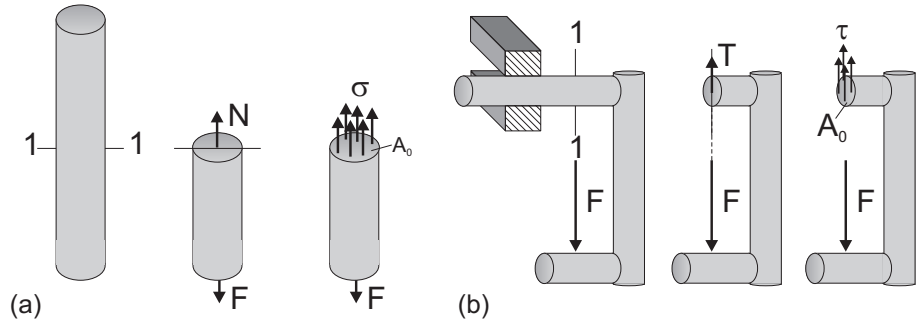

Figure A.2: (a) shows a rod which is exposed to an external force F. If the rod is cut along the line $1-1$, the normal force $N(=F)$ can be observed. The internal normal force balances the external forces. The normal stress is the normal force related to the cross-sectional area A_0. (b) shows the same for forces acting tangential on a structure. The shear stress is the tangential force related to the cross-sectional area A_0.

structure represented by the intersection line $1-1$. According to the normal stress we can define the *shear* or *tangential* stress:

$$\tau = \lim_{A_0 \to 0} \frac{\Delta T}{\Delta A_0} = \frac{T}{A_0} \tag{A.5a}$$

$$\tau = \frac{F_T}{A_0}. \tag{A.5b}$$

A.3 Young's Modulus

Young's modulus is the material property that describes the relationship between stress and strain. In other words: *How much force per cross-sectional area causes how much lengthening of the workpiece.* Fig. A.3 shows a stress strain diagram for constructional steel for an increasing force F acting on a steel rod. From $\sigma = 0$ up to a value of $\sigma = \sigma_{pl}$ the strain ϵ grows proportionally. The value σ_{pl} is the *proportional limit.* For values larger than σ_{pl} the strain shows a progressive growth until $\sigma = \sigma_{el}$. Up to this point the process is reversible. For values from $\sigma = \sigma_{el}$ to $\sigma = \sigma_{yp}$ (the *yield point*) the rod shows plastic deformations. Reaching the yield point, the strain shows a stepwise growth at approximately constant load. Above the yield point the curve increases further until just before the tensile limit σ_{tl} the rod shows a lateral contraction (constriction). Beyond this point the stress decreases until the rod disrupts.

The stress-strain diagram for uniaxial load shows that stress and strain are proportional if the load is small enough. Hooke's law can be applied:

$$\epsilon = \frac{\sigma}{E} \text{ or } \sigma = E\epsilon. \tag{A.6}$$

The proportional factor E is Young's modulus as introduced above.

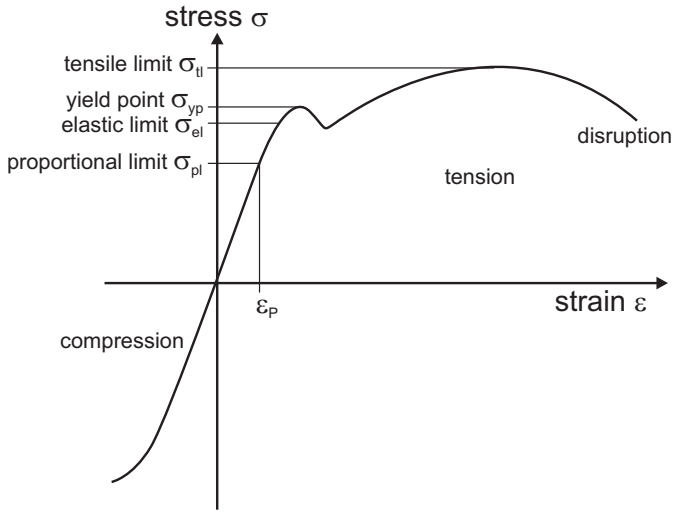

Figure A.3: Exemplary stress strain diagram for constructional steel.

A.4 Introducing load intensity, the derivative of the cross force and the bending moment

If a beam is loaded with a force distributed along its longitudinal axis we call this distributed force the *load intensity* $p(x)$. This situation is depicted in Fig. A.4(a).
If $p(x)$ is constant we call this a *uniform load*. The load intensity of a beam is defined as:

$$p(x) = \lim_{\Delta x \to 0} \frac{\Delta F}{\Delta x} = \frac{dF}{dx}. \tag{A.7}$$

In Fig. A.4(b) a small section of length Δx is cut out of the beam. The force balance is restored by adding the internal forces. The uniform load which acts on the beam segment can now be replaced by a single force $\Delta\vec{F}$ whose absolute value is:

$$\Delta F = p(\xi)\Delta x. \tag{A.8}$$

Where ξ is a coordinate between x and $x + \Delta x$. The absolute value of the single force $\Delta\vec{F}$ is equal to the hatched area in Fig. A.4(b) under the curve $p(x)$ which is equal to the area of the rectangle $p(\xi)\Delta x$. The line of action of $\Delta\vec{F}$ proceeds through the center of gravity (cog) of the hatched area. The force and moment equilibrium conditions are set up below. The coordinate $x + \Delta x$ is chosen as reference point for the moment equilibrium condition (A.9c):

$$\Sigma F_{ix} = 0 = F_n(x + \Delta x) - F_n(x) \tag{A.9a}$$

$$\Sigma F_{iz} = 0 = F_t(x + \Delta x) - F_t(x) + p(\xi)\Delta x \tag{A.9b}$$

$$\Sigma M_i = 0 = M_l(x + \Delta x) - M_l(x) \tag{A.9c}$$

$$- \quad F_t(x)\Delta x + p(\xi)\Delta x(x + \Delta x - \xi_{cog}).$$

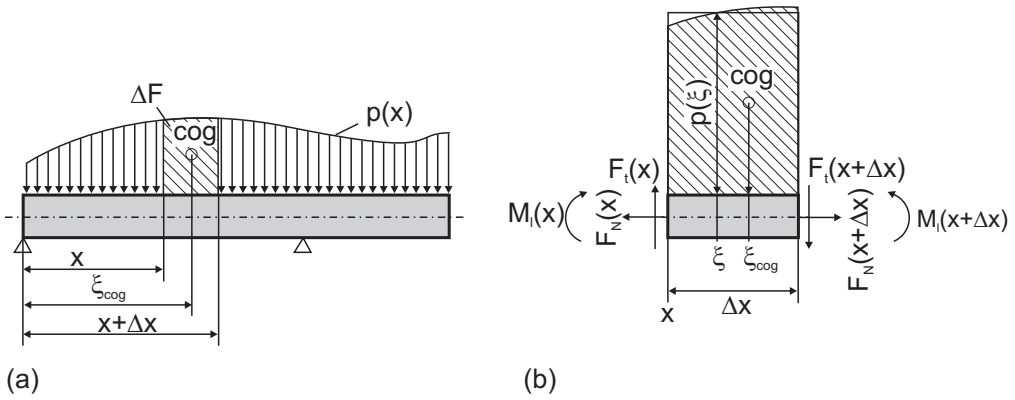

Figure A.4: Force and moment balance at a beam segment.

The first equilibrium condition in (A.9a) states that the normal force does not change with x as long as there are no outer forces present. Division of (A.9b) and (A.9c) by Δx results in:

$$0 = \frac{F_t(x+\Delta x) - F_t(x)}{\Delta x} + p(\xi) \tag{A.10a}$$

$$0 = \frac{M_l(x+\Delta x) - M_l(x)}{\Delta x} - F_t(x) + p(\xi)(x + \Delta x - \xi_{cog}). \tag{A.10b}$$

By applying the transition $\Delta x \to 0$ both coordinates ξ and ξ_{cog} move towards x and $(x+\Delta x-\xi_{cog})$ becomes zero. The limit values of the difference quotients in (A.10a) and (A.10b) are the derivatives at the coordinate x

$$\frac{dF_t}{dx} = -p(x) \tag{A.11a}$$

$$\frac{dM_l}{dx} = F_t(x). \tag{A.11b}$$

If we combine (A.11a) and (A.11b) in order to eliminate F_t we get:

$$M_l'' = -p(x). \tag{A.12}$$

This expression will be used later to derive the Euler-Bernoulli beam equation.

A.5 Moment of inertia of the cross-section

In this section the *moment of inertia of the cross-section* is introduced. Assuming a cross-sectional area A as depicted in Fig. A.5 with the coordinate system y, z. One defines the following moments of inertia for the different axes:

$$I_y = \int_A z^2 dA \text{ about y-axis} \tag{A.13a}$$

$$I_z = \int_A y^2 dA \text{ about z-axis} \tag{A.13b}$$

$$I_{yz} = \int_A yz dA \text{ product of inertia} \tag{A.13c}$$

$$I_p = \int_A r^2 dA \text{ polar moment of i.} \tag{A.13d}$$

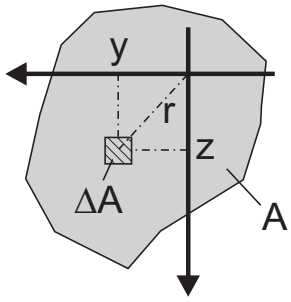

Figure A.5: Cross-section of a beam with a very small cross-sectional area ΔA

The product of inertia will not be used any further. But there is a relationship between (A.13a), (A.13b) and (A.13d) which is helpful for the calculation of the moment of inertia of some cross-sectional shapes:

$$I_y + I_z = \int_A (y^2 + z^2) dA = \int_A r^2 dA = I_p. \tag{A.14}$$

Because I_p does not change when the coordinate system is rotated, $I_y + I_z = I_p$ is rotation invariant.

A.6 Deformation of a beam segment (Kinematics)

According to the strain concept as described in Sect. A.1, the strain of a beam segment, whose endpoints are exposed to a moment M, is derived. The situation is depicted in Fig. A.6.
Before going into details, some assumptions on how beam segments rotate have to be made. For an *Euler beam* these assumptions were proposed by *Kirchhoff*. A beam can be divided into normals which are lines that are perpendicular to the neutral axis of the beam. When the beam is bent, the normals:

1. do not bend (they remain straight, also termed: Bernoulli hypothesis),
2. keep their length,
3. remain perpendicular to the neutral axis.

In Fig. A.6(a) the triangular cross-section of a symmetrical beam is depicted. The cross-section in longitudinal direction is depicted in Fig. A.6(b). When a beam is bent around the y-axis, the inner fibres become shorter and the outer fibres become longer. Somewhere within the beam there is an axis whose length is not affected by the bending. This axis is called the *neutral axis* or *neutral plane*. For all fibres which lie further outside, the bending generates a positive strain which means that the stress σ is positive and vice versa for fibres which lie further inside. This is visualized in Fig. A.6(c). For the bending we define a radius of curvature according to Fig. A.6(d) as follows:

$$\rho \Delta\alpha = \Delta x. \tag{A.15}$$

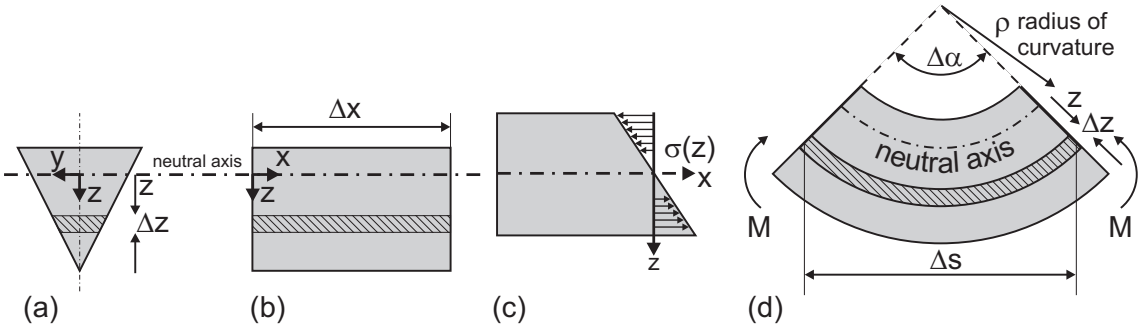

Figure A.6: In (a) the triangular cross-section of a beam can be seen. (b) The side view of a small beam segment of length Δx and the neutral axis. (c) The characteristic of the stress σ in z-direction. (d) Bending of the beam segment if a moment M is applied on both ends of the segment. The radius of curvature is ρ and the length of the hatched volume segment is Δs.

Δx is the unchanged length of the neutral axis. When we examine a fibre at the coordinate z (measured from the neutral axis) we can determine its length after bending:

$$\Delta s = (\rho + z)\Delta\alpha. \tag{A.16}$$

Now, the strain for the beam at the coordinate z can be defined:

$$\begin{aligned} \epsilon(z) &= \frac{\Delta s - \Delta x}{\Delta x} = \frac{(\rho + z)\Delta\alpha - \rho\Delta\alpha}{\rho\Delta\alpha} = \frac{z}{\rho} \\ \rho &= \frac{z}{\epsilon(z)}. \end{aligned} \tag{A.17}$$

Since the radius of curvature ρ is constant for a given cross section we have a linear equation for ϵ which is the mathematical form of the first assumption made above.
With Hooke's Law from (A.6) and the expression for the strain (A.17) an expression for the stress σ can be found:

$$\sigma(z) = E\epsilon(z) = \frac{E}{\rho}z. \tag{A.18}$$

Because of Bernoulli's hypotheses there is also a linear relationship for the strain. The result is depicted in Fig. A.6(c).

A.6.1 Equilibrium of a beam segment

A closer look on the cross-section of a beam reveals that the normal stress σ acts on each small area ΔA as shown in Fig. A.5. The course of σ can be seen in Fig. A.6(c). We demand equilibrium for the according forces and moments. In order to formulate this, all normal forces are summed up and are then called N. In a second step σ can be replaced by (A.18):

$$N = \int_A \sigma dA \tag{A.19a}$$

$$= \frac{E}{\rho}\int_A z dA. \tag{A.19b}$$

In order to gain equilibrium the integral in (A.19b) must be zero. This is the case if the point of origin lies in the center of gravity. Hence, in a beam without a net normal force the cross-sectional center of gravity defines the neutral plane.

Accordingly, the moment around the z-axis can be calculated:

$$M_z = -\int_A y(\sigma dA) \tag{A.20a}$$

$$= -\frac{E}{\rho}\int_A yz dA. \tag{A.20b}$$

For the unilateral bending only a bending moment around the y-axis is allowed. Hence, M_z has to be zero as well.

Finally, the moment around the y-axis is set up:

$$M_y = \int_A z(\sigma dA) \tag{A.21a}$$

$$= \frac{E}{\rho}\int_A z^2 dA. \tag{A.21b}$$

The integral in (A.21b) is the moment of inertia of the cross-section around the y-axis as defined in Sect. A.5. We replace the integral by (A.13a) and write

$$\rho = \frac{EI_y}{M_y} \tag{A.22}$$

instead. The term EI_y is called the *flexural rigidity*. It can be viewed as the resistance of the material against bending. We use (A.22) for the calculation of the deflection line in section A.7. By inserting (A.22) into (A.18) we get:

$$\sigma(z) = \frac{M_y}{I_y} z. \tag{A.23}$$

The expression in (A.23) can be used to calculate the stress in section A.7.

A.7 Differential equation of the deflection line

In this section it is described how the deflection line of a beam which is bent can be calculated. In Fig. A.7(a) we define some measures for the following considerations. The angle of deflection $\varphi(x)$ defines the orientation of the cross-sectional area at coordinate x. $w(x)$ is the out-of-plane displacement of the beam. From curve sketching it is known that:

$$\tan\varphi = w' \text{ and } \varphi = \arctan w' \tag{A.24a}$$

$$\frac{d}{dx}\arctan w' = \frac{w''}{1+w'^2} \tag{A.24b}$$

$$\cos\varphi = \frac{1}{\sqrt{(1+w'^2)}}. \tag{A.24c}$$

Fig. A.7(b) implies that:

$$\Delta s = \rho\Delta\alpha \tag{A.25a}$$

$$\Delta x \approx \Delta s\cos\varphi \tag{A.25b}$$

$$\Delta\alpha = \varphi(x) - \varphi(x+\Delta x) = -\Delta\varphi. \tag{A.25c}$$

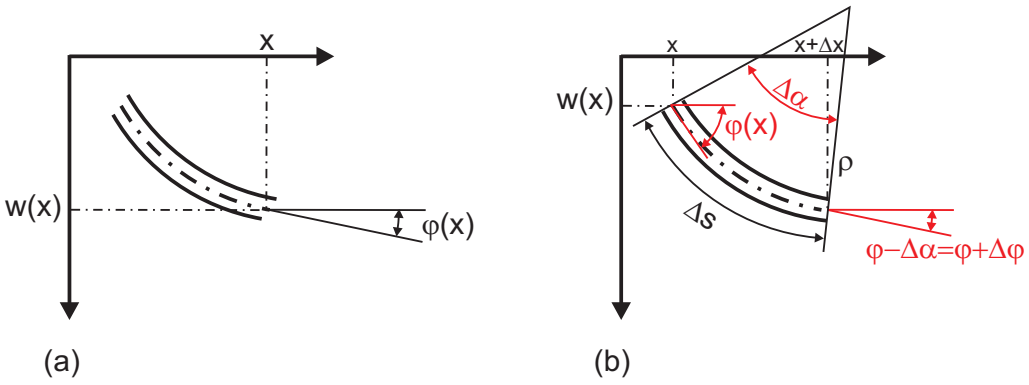

Figure A.7: Derivation of the differential equation of the deflection line.

With (A.25b) and (A.25c) we build:

$$\frac{\Delta\varphi}{\Delta x} = \frac{-\Delta\alpha}{\Delta s\cos\varphi} \quad |\text{application of (A.25a)} \tag{A.26a}$$

$$= \frac{-\Delta\alpha}{\rho\Delta\alpha\cos\varphi} \tag{A.26b}$$

$$= \frac{-1}{\rho\cos\varphi} \tag{A.26c}$$

$$\lim_{\Delta x\to 0}\frac{\Delta\varphi}{\Delta x} = \frac{d\varphi}{dx} = \varphi' = \frac{-1}{\rho\cos\varphi}. \tag{A.26d}$$

By multiplying (A.24a) by $\cos\varphi$ we can write:

$$\begin{aligned}\varphi'\cos\varphi &= \cos\varphi\frac{d}{dx}(\arctan w') \quad |\text{application of (A.24b) yields:}\\ &= \cos\varphi\frac{w''}{1+w'^2} \quad |\text{application of (A.24c) yields:}\\ &= \frac{w''}{(1+w')^{3/2}} = \underbrace{-\frac{1}{\rho}}_{\text{(see A.26c)}}.\end{aligned} \tag{A.27}$$

For small deformations (A.27) can be simplified:

$$-\frac{1}{\rho} \approx w''(x). \tag{A.28}$$

The fraction $1/\rho$ is the curvature of bending. The combination of (A.18) and (A.23) yields:

$$\sigma(z) = \frac{M_y}{I_y}z = E\epsilon(z) \tag{A.29a}$$

$$\frac{\epsilon(z)}{z} = \frac{M_y}{EI_y}. \tag{A.29b}$$

Replacing $\epsilon(z)/z$ by (A.17) delivers the *Euler-Bernoulli beam equation*:

$$\begin{aligned}\frac{1}{\rho} &= \frac{M_y}{EI_y} = -w''\\ EI_y w'' &= -M_y.\end{aligned} \tag{A.30}$$

If this equation is differentiated twice and M_y'' is replaced by (A.12), the result is another representation of the Euler-Bernoulli beam equation:

$$EI_y w''''(x) = p(x). \tag{A.31}$$

Under the assumption of a uniform load we can also write:

$$EI_y w'''(x) = \int_0^x p(\xi)d\xi = -F(x). \tag{A.32}$$

The missing derivatives of $w(x)$ can be calculated by integration:

$$EI_y w''(x) = -F(x)x + c_1 \tag{A.33a}$$

$$EI_y w'(x) = -\frac{1}{2}F(x)x^2 + c_1 x + c_2 \tag{A.33b}$$

$$EI_y w(x) = -\frac{1}{6}F(x)x^3 + \frac{1}{2}c_1 x^2 + c_2 x + c_3 \tag{A.33c}$$

The integration constants c_1, c_2 and c_3 can be determined by appropriate side conditions taken from the specific task that has to be calculated. It is always reasonable to remember that $w'''' \propto p(x)$ (load function), $w''' \propto -F_t(x)$ (cross-force), $w'' \propto M_y(x)$ (bending moment) and $w' \propto \tan\varphi$ (inclination or slope of the line of bending).

A.8 Cantilever with end moment

Given a weightless cantilever of length l with a constant flexural rigidity EI which is loaded by an end moment of M_0. We assume $M(x) = -M_0 = \text{const}$. The task is to calculate the deflection line $w(x)$, the deflection at the end of the cantilever $w(l)$ and the angle of bending $\varphi(l)$. This calculation can be started with double integration of (A.30) which yields:

$$\begin{aligned} w'(x) &= -\frac{1}{EI_y}\int M(x)dx \\ &= -\frac{1}{EI_y}M(x)x + c_1 \\ w(x) &= -\frac{1}{EI_y}\int M(x)x + c_1 dx \\ &= -\frac{1}{EI_y}\left(\frac{M(x)x^2}{2} + c_1 x + c_2\right). \end{aligned}$$

Since the slope of the line of bending is zero at the restraint ($w'(0) = 0$) the constant c_1 is zero. The same applies for the out-of-plane displacement of the beam for $x = 0$ which is $w(0) = 0$. Here the constant c_2 is also zero. With these assumptions the function of the out-of-plane displacement of the beam is:

$$w(x) = \frac{-M(x)x^2}{2EI_y}. \tag{A.34}$$

Replacing $-M(x)$ by M_0 and evaluation of $w(x)$ at the coordinate $x = l$ yields:

$$w(l) = \frac{M_0 l^2}{2EI_y}. \tag{A.35}$$

In order to calculate the angle of bending at the end of the cantilever (A.30) has to be integrated once. The same side conditions as above apply:

$$\begin{aligned} w'(x) &= -\frac{1}{EI_y}\int M(x)dx \\ &= \frac{-M(x)x}{EI_y}. \end{aligned}$$

According to (A.24a) $w' = \tan(\varphi)$. For small angles it can be safely assumed that $w' \approx \varphi$. This means that:

$$\varphi(x) = \frac{-M(x)x}{EI_y}. \tag{A.36}$$

Again replacing $-M(x)$ by M_0, the angle of bending at the end of the cantilever ($x = l$) is:

$$\varphi(l) = \frac{M_0 l}{EI_y}. \tag{A.37}$$

In order to solve the task, Young's modulus E and the shape of the cross-section of the beam for I_y is needed. Assuming a round profile with radius R we can calculate I_y. For a round profile $I_y = I_z$. Therefore $I_y = I_p/2$, according to (A.14), holds true. The polar moment of inertia is:

$$\begin{aligned} I_p &= \int_A r^2 dA = \int_0^R r^2 (2\pi r dr) \\ &= \frac{1}{4} 2\pi R^4 = \frac{\pi}{2} R^4 \end{aligned}$$

Thus, the moment of inertia around the y-axis is $I_y = \pi/4R^4$. I_y can now be inserted into (A.37).

Appendix B

Kinematics and Static Force-Torque Relationships

The focus of this study lies on the feedback mechanisms in *closed kinematic chains*. For a correct handling of the kinematics and dynamics simulations used in this work, it is important to define what a closed kinematic chain is and which parameters are used for its description. This chapter states some basic concepts of kinematics and is supposed to serve as a reference especially for the choices of the coordinate frames for the planar manipulator in Sect. B.5, the insect leg in Sect. B.7 and a whole animal in Sect. B.7.3. This chapter does not claim to cover the topic of kinematics completely on any account. Intensive studies on the most prominent topics of robotics can be found in two recommendable books by Craig and by Spong (Craig, 2005; Spong and Vidyasagar, 1989).

B.1 Introduction

The classical *kinematics* is concerned with the motion of rigid bodies regardless of forces or torques that might be responsible for an observed motion. The effects of forces and torques on the motion of rigid bodies is explained by classical *dynamics*.

In movement studies of animals and in engineering experimenters and engineers have to deal with the movement of rigid bodies that are flexibly connected with each other by *prismatic* (linear) or *revolute* (rotary) joints. These chains are termed *kinematic chains* or, more popular, arms and legs. Such concatenations introduce parent-child relationships of the bodies involved. This means that the movement of a body in a chain (parent) results in a movement of all following bodies (children) accordingly. This fact makes the calculation of all motions more complicated than for free moving single bodies. Therefore, the kinematics of a kinematic chain is more than

just applying the fundamental equations of motion. It is also bookkeeping of the geometrical relationship between the coordinate frames attached to each body.

Once the coordinate frames for a given kinematic chain have been set up, the *forward kinematics* and the *inverse kinematics* can be derived. The forward kinematics delivers the position of certain points in the chain (normally the end-effector, wrist or hand) if the relative angular (revolute) or linear (prismatic) displacements of all joints are given. The calculations for a planar manipulator and an insect leg are given in Sect. B.5.1 and B.7.1, respectively. The inverse kinematics delivers the relative displacements of all joints for a given endpoint position. See Sections B.5.2 and B.7.2 for the derivations of the inverse kinematics of the planar manipulator and the insect leg. Especially for larger kinematic chains it is useful to find a convention on how the different coordinate frames are attached to the segments of the kinematic chain and how they are numbered. In Sect. B.2 some details on the Denavit-Hartenberg convention are given. The use of this convention simplifies the kinematic analysis of kinematic chains considerably.

Finally, we also have to distinguish between *open* and *closed* kinematic chains. An open kinematic chain represents the classical case in which for example a robot arm performs free movements without contact with other objects of its environment. In walking this is the case during the swing phase of a leg. The above mentioned kinematic parent-child relationship of the chain's joints is maintained. However, if the the end-effector of a kinematic chain is in contact with an object which itself is connected to the base of the manipulator via the ground, the kinematic chain is closed. This closed loop does not allow to choose the angle of a single joint in the chain independently anymore; in fact all other joints in the chain have to be controlled accordingly in order to prevent potentially harmful tensions and twisting. The kinematic parent-child relationship of consecutive joints is lost. In order to describe the relationships in a closed kinematic chain, forces and torques can not be neglected. Therefore, the dynamics or at least the static *force-torque relationship* (see Sect. B.4) in the system should be considered.

B.2 Kinematics and the Denavit-Hartenberg convention

Denavit and Hartenberg introduced a formalism that allows the transformation between the local coordinate frames of a given kinematic chain (Denavit and Hartenberg, 1955). The formalism is based on homogeneous matrices and is referred to as the *DH-convention*. This convention reduces the number of free parameters in a given kinematic chain (see below) and thus simplifies the transformation equations clearly. In the following some important aspects of the DH-convention are explained. This section is a condensed compilation of the corresponding chapter of the robotics book by Spong (Spong and Vidyasagar, 1989).

B.2.1 Homogeneous transformations

A homogeneous transformation between coordinate systems can generally be written as a homogeneous matrix H:

$$H = \begin{bmatrix} R_{3\times3} & \vec{d}_{3\times1} \\ \vec{0}_{1\times3} & 1 \end{bmatrix}. \tag{B.1}$$

This transformation consists of a rotation matrix $R_{3\times3}$ and a translation vector $\vec{d}_{3\times1}$. The translation is given by

$$\vec{d_x} = \begin{pmatrix} d_x \\ 0 \\ 0 \end{pmatrix}; \quad \vec{d_y} = \begin{pmatrix} 0 \\ d_y \\ 0 \end{pmatrix}; \quad \vec{d_z} = \begin{pmatrix} 0 \\ 0 \\ d_z \end{pmatrix} \tag{B.2}$$

in the current coordinate system. The rotation is expressed as follows:

$$R_{x,\alpha} = \begin{bmatrix} 1 & 0 & 0 \\ 0 & \cos\alpha & -\sin\alpha \\ 0 & \sin\alpha & \cos\alpha \end{bmatrix}; \quad R_{y,\phi} = \begin{bmatrix} \cos\phi & 0 & \sin\phi \\ 0 & 1 & 0 \\ -\sin\phi & 0 & \cos\phi \end{bmatrix}; \quad R_{z,\theta} = \begin{bmatrix} \cos\theta & -\sin\theta & 0 \\ \sin\theta & \cos\theta & 0 \\ 0 & 0 & 1 \end{bmatrix}. \tag{B.3}$$

Given the homogeneous matrix H, the inverse of H is calculated as follows:

$$H = \begin{bmatrix} n_x & o_x & a_x & p_x \\ n_y & o_y & a_y & p_y \\ n_z & o_z & a_z & p_z \\ 0 & 0 & 0 & 1 \end{bmatrix}; \quad H^{-1} = \begin{bmatrix} n_x & n_y & n_z & -\vec{p}\cdot\vec{n} \\ o_x & o_y & o_z & -\vec{p}\cdot\vec{o} \\ a_x & a_y & a_z & -\vec{p}\cdot\vec{a} \\ 0 & 0 & 0 & 1 \end{bmatrix}. \tag{B.4}$$

According to (B.1), (B.2) and (B.3), any homogeneous transformation has a maximum of six free parameters $(\alpha, \phi, \theta, d_x, d_y, d_z)$.

By the use of the DH-convention the number of free parameters for a joint-link pair is reduced to only four. The four parameters are the **angle** θ, the **length** a (in most of the cases a coincides with the segment length), the **offset** d and the **twist** α. For a rotary joint, the segment length, the twist and the offset are constant and describe the geometrical setup of the joint and a segment. Only the angle θ changes with time. For a linear joint, the segment length, the twist and the angle are constant and the offset d changes with time and characterizes the function of the linear joint.

B.2.2 Choice of the coordinate frames

The reduction to a four parameter set can be achieved by a sensible choice of the coordinate frames. This is shown in Fig. B.1(a). The segments are numbered from $0-N$ whereas each segment obtains a coordinate system labelled with the same number as the segment. The coordinate system with the number 0 is the *base frame*. The joints are numbered from $1-N$ and the z-axes of the coordinate frames represent the axes of these joints. The coordinate frames for all segments are set up according to the following procedure:

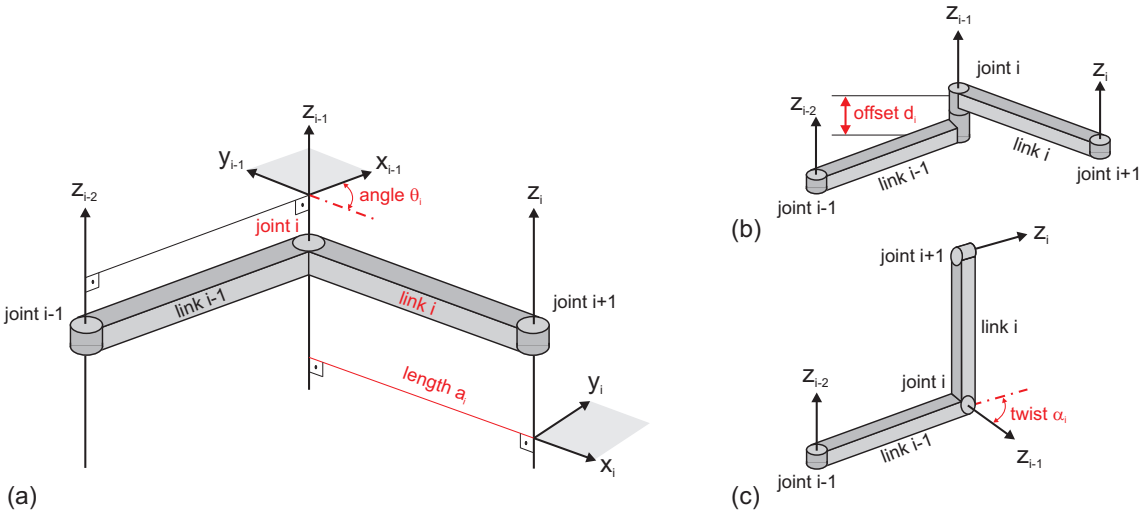

Figure B.1: Coordinate systems according to DH-convention. (a) Adjustment of the coordinate systems and the measurement of the joint angle θ_i and the segment length a_i. In this case all coordinate systems should be positioned within the joints but are shifted outwards for better visibility. The grey areas indicate the x-y planes of the coordinate frames. (b) Example for a linear offset d_i in a joint. (c) Example for two consecutive joints whose axes of rotation are twisted by an angle α_i.

1. The origin o_i of the i^{th} frame lies either
   (a) where the common normal shared by the axes z_i and z_{i-1} intersects with z_i
   (b) or at the point of intersection if z_i and z_{i-1} intersect
   (c) or within the joint if z_i and z_{i-1} represent parallel axes.
2. The x_i-axis of the i^{th} frame starts in the origin o_i and lies either
   (a) on the common normal shared by axes z_i and z_{i-1} pointing away from z_{i-1}
   (b) or perpendicular to the plane spanned by the the intersecting z_i and z_{i-1} axes.
3. The y_i axis of the i^{th} frame completes a right-hand frame.

The choice of the x_0- and y_0-axis is solely subject to the restriction of setting up a right-hand system for the base frame. Note that in Fig. B.1(a) the z-axes are all parallel. Therefore, the origins of all coordinate systems have to sit within the joints. In this case they are shifted outwards only for the sake of clarity. Please also note that for example for crooked links the origins of the coordinate systems could even lie outside the manipulator.

B.2.3 Identification of the DH-parameters

After setting up the coordinate frames, the four parameters angle, length, offset and twist have to be identified. These parameters are used for the DH-transformation matrix in Sect. B.2.4.

1. The **angle** θ_i is the angle between x_{i-1} and x_i measured about the z_{i-1}-axis [see Fig. B.1(a)].

2. The **length** a_i is the distance between the origin o_i and the intersection of x_i and z_{i-1} along the x_i-axis [see Fig. B.1(a)].

3. If two consecutive segments are connected by a linear joint, they exhibit a **linear offset** d which describes the linear displacement and thus is a function of time. This offset can also be found if for example the x-y planes of two coordinate frames are not the same. In this case the offset is a fixed geometrical parameter of the kinematic setup. The latter case is depicted in Fig. B.1(b). Formally, d_i is the distance between the origin o_{i-1} and the intersection of the x_i-axis with the z_{i-1}-axis.

4. The **twist** α_i describes the angle between the axes z_i and z_{i-1} measured about the x_i-axis. An example for the twist angle is displayed in Fig. B.1(c).

B.2.4 Setting up the DH transformation matrix

Once all segments of the kinematic chain have been assigned coordinate frames and the DH-parameters have been identified, the transformation A_i from one coordinate frame to the next can be created. A transformation matrix T_j^k for the transformation from a coordinate frame j into a coordinate frame k is the product of all intermediate transformations A_i

$$T_j^k = \begin{cases} \prod_{i=j+1}^{k} A_i & : \text{ if j<k} \\ I & : \text{ if j=k} \\ \left(T_j^k\right)^{-1} & : \text{ if j>k} \end{cases} . \tag{B.5}$$

According to the DH-convention introduced above, the transformation matrix A_i, which represents a transformation from coordinate frame $i-1$ into a coordinate frame i, is calculated as a product of four transformations:

$$\begin{aligned} A_i &= R_{z_{i-1},\theta_i} \cdot T_{z_{i-1},d_i} \cdot T_{x_i,a_i} \cdot R_{x_i,\alpha_i} \\ &= \begin{bmatrix} \cos\theta_i & -\sin\theta_i & 0 & 0 \\ \sin\theta_i & \cos\theta_i & 0 & 0 \\ 0 & 0 & 1 & 0 \\ 0 & 0 & 0 & 1 \end{bmatrix} \cdot \begin{bmatrix} 1 & 0 & 0 & 0 \\ 0 & 1 & 0 & 0 \\ 0 & 0 & 1 & d_i \\ 0 & 0 & 0 & 1 \end{bmatrix} \cdot \begin{bmatrix} 1 & 0 & 0 & a_i \\ 0 & 1 & 0 & 0 \\ 0 & 0 & 1 & 0 \\ 0 & 0 & 0 & 1 \end{bmatrix} \cdot \begin{bmatrix} 1 & 0 & 0 & 0 \\ 0 & \cos\alpha_i & -\sin\alpha_i & 0 \\ 0 & \sin\alpha_i & \cos\alpha_i & 0 \\ 0 & 0 & 0 & 1 \end{bmatrix} \\ &= \begin{bmatrix} \cos\theta_i & -\sin\theta_i\cos\alpha_i & \sin\theta_i\sin\alpha_i & a_i\cos\theta_i \\ \sin\theta_i & \cos\theta_i\cos\alpha_i & -\cos\theta_i\sin\alpha_i & a_i\sin\theta_i \\ 0 & \sin\alpha_i & \cos\alpha_i & d_i \\ 0 & 0 & 0 & 1 \end{bmatrix} \end{aligned} \tag{B.6}$$

The *forward kinematics* of a manipulator can be found in the the fourth column of $T_0^N = A_1 \cdot A_2 \ldots A_N$.

B.3 Velocity kinematics

In order to relate infinitesimal translations $d\vec{p}_{(3\times1)}$ and rotations $d\vec{\phi}_{(3\times1)}$ of the manipulator endpoint to infinitesimal joint displacements $d\vec{q}_{(N\times1)}$ (linear or rotational), the *manipulator Jacobian* J is introduced:

$$d\vec{u} = \begin{pmatrix} d\vec{p} \\ d\vec{\phi} \end{pmatrix}_{(6\times1)} = J(q)d\vec{q}_{(N\times1)}. \tag{B.7}$$

Here, $d\vec{u}$ denotes the infinitesimal (endpoint) displacement vector. Division of (B.7) by dt yields an expression that relates the linear velocity ($d\vec{p}/dt = \vec{v}_{(3\times1)}$) and the angular velocity ($d\vec{\phi}/dt = \vec{\omega}_{(3\times1)}$) of the manipulator endpoint to the displacement velocities of the joints ($\dot{\vec{q}}_{(N\times1)}$):

$$\begin{pmatrix} \vec{v}_0^N \\ \vec{\omega}_0^N \end{pmatrix}_{(6\times1)} = \begin{bmatrix} J_{\vec{v}_{(3\times N)}} \\ --- \\ J_{\vec{\omega}_{(3\times N)}} \end{bmatrix}_{(6\times N)} \dot{\vec{q}}_{(N\times1)} = J_0^N \dot{\vec{q}}_{(N\times1)}. \tag{B.8}$$

The manipulator Jacobian matrix J_0^N consists of two parts. $J_{\vec{v}}$ represents the part of the matrix which is responsible for the transformation of the joint displacements into the linear velocity of the endpoint. $J_{\vec{\omega}}$ transforms the joint displacements into the angular velocity of the endpoint. J_0^N can be calculated geometrically with the help of vector cross products (Spong and Vidyasagar, 1989, pp. 112-116) which yields:

$$J_0^N = [\vec{J}_1 \dots \vec{J}_i \dots \vec{J}_N]; \quad \vec{J}_i = \underbrace{\begin{bmatrix} \vec{z}_{i-1} \times (\vec{o}_N - \vec{o}_{i-1}) \\ --- \\ \vec{z}_{i-1} \end{bmatrix}}_{\text{joint } i \text{ is revolute}}; \quad \vec{J}_i = \underbrace{\begin{bmatrix} \vec{z}_{i-1} \\ --- \\ \vec{0} \end{bmatrix}}_{\text{joint } i \text{ is prismatic}}, \tag{B.9}$$

or it can be calculated analytically by differentiation of the forward kinematics transform (Sciavicco and Siciliano, 2000, pp. 100-102):

$$J_0^N = [\vec{J}_1 \dots \vec{J}_i \dots \vec{J}_N]; \quad \vec{J}_i = \underbrace{\begin{bmatrix} \frac{\partial \vec{d}_o^N}{\partial q_i} \\ --- \\ \vec{z}_{i-1} \end{bmatrix}}_{\text{joint } i \text{ is revolute}}; \quad \vec{J}_i = \underbrace{\begin{bmatrix} \vec{z}_{i-1} \\ --- \\ \vec{0} \end{bmatrix}}_{\text{joint } i \text{ is prismatic}}. \tag{B.10}$$

Note that the rotational part of $\vec{J}_i$ in (B.10) could also be generated through differentiation in the form $\partial\vec{\phi}_o^N/\partial q_i$ but $\phi(q)$ is usually not available directly [see Sciavicco and Siciliano for a discussion of this topic (Sciavicco and Siciliano, 2000, p. 101)]. Because of that we keep the formulation for $J_{\vec{\omega}}$ as it is shown in (B.8) for (B.10).

If the linear velocity of the manipulator endpoint is needed, only the upper 3 rows of the Jacobian are used. We write:

$$\vec{v} = \underbrace{\begin{bmatrix} \frac{\partial d_x}{\partial \theta_1} & \frac{\partial d_x}{\partial \theta_2} & \cdots & \frac{\partial d_x}{\partial \theta_N} \\ \frac{\partial d_y}{\partial \theta_1} & \frac{\partial d_y}{\partial \theta_2} & \cdots & \frac{\partial d_y}{\partial \theta_N} \\ \frac{\partial d_z}{\partial \theta_1} & \frac{\partial d_z}{\partial \theta_2} & \cdots & \frac{\partial d_z}{\partial \theta_N} \end{bmatrix}}_{J_v} \dot{\vec{q}}. \tag{B.11}$$

J_v can be obtained by differentiation of the forward kinematics (last column) of the homogeneous transformation matrix T_0^N:

$$T_0^N = \begin{bmatrix} R_0^N & \vec{d}_0^N \\ \vec{0}_{1\times 3} & 1 \end{bmatrix}. \tag{B.12}$$

B.4 Static force-torque relationship

The manipulator Jacobian, as derived in Sect. B.3, can also be used in order to relate external forces and torques, represented by $\vec{f}_{\text{ext}}$ (measured in the base frame), that act on the endpoint of the manipulator to the internal torques and forces generated in the joints (represented by $\vec{\tau}_{\text{int}}$). In order to create an expression for this purpose we have to remember how the mechanical work of a linear and a rotational movement is calculated:

$$\underbrace{W_{\text{trans}}(A \to B) = \int_A^B \vec{F}(\vec{s}) d\vec{s} = \vec{F} \cdot \vec{s};}_{\text{translation}} \quad \underbrace{W_{\text{rot}} = \vec{\tau} \cdot \vec{\phi}}_{\text{rotation}}.$$

An infinitesimal displacement $d\vec{u}$ of the manipulator endpoint which is exposed to a force $\vec{f}_{\text{ext}}$ results in a virtual work dW:

$$dW = \vec{f}_{\text{ext}} \cdot d\vec{u}. \tag{B.13}$$

The corresponding infinitesimal joint displacement $d\vec{q}$ under given torques and forces $\vec{\tau}_{\text{int}}$ of the joint drives also results in a virtual work dW:

$$dW = \vec{\tau}_{\text{int}} \cdot d\vec{q}. \tag{B.14}$$

The two different formulations in (B.13) and (B.14) are equal because they describe the same amount of virtual work:

$$\vec{f}_{\text{ext}}^T \cdot d\vec{u} = \vec{\tau}_{\text{int}}^T \cdot d\vec{q}. \tag{B.15}$$

The scalar products in the virtual work expressions are represented by the transpose operation in (B.15). Replacing $d\vec{u}$ by the manipulator Jacobian (B.7) yields:

$$\vec{f}_{\text{ext}}^T \cdot J(q) d\vec{q} = \vec{\tau}_{\text{int}}^T \cdot d\vec{q}. \tag{B.16}$$

This holds for all infinitesimal joint displacements $d\vec{q}$. Therefore, we eliminate $d\vec{q}$ from (B.16) and transpose both sides. This results in:

$$\vec{\tau}_{\text{int}} = J^T(q) \cdot \vec{f}_{\text{ext}}. \tag{B.17}$$

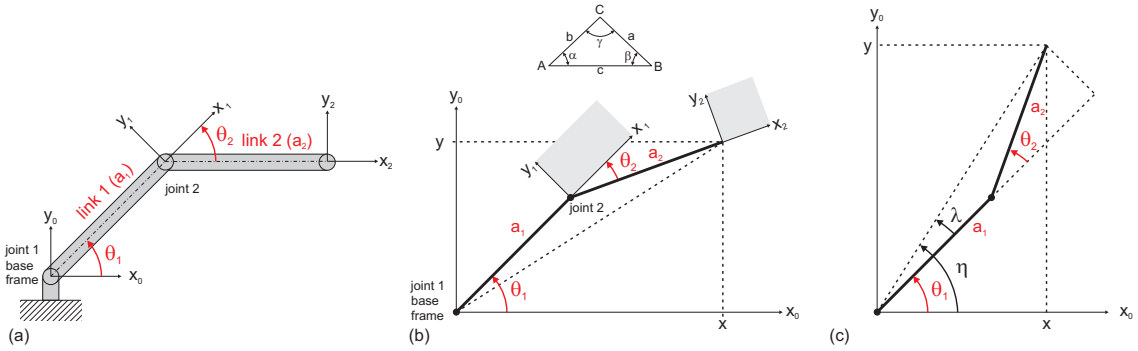

Figure B.2: (a) Coordinate systems and setup of a planar manipulator consisting of two joints and two links. (b) Line drawing of the planar manipulator in an elbow up posture. The grey areas indicate the $x-y$-planes of the coordinate frames. (c) Line drawing and auxiliary angles η and λ of the planar manipulator in elbow down posture. The auxiliary angles are needed for the derivation of the inverse kinematics in Sect. B.5.2.

Equation (B.17) can also be solved for $\vec{f}_{\text{ext}}$:

$$\vec{f}_{\text{ext}} = J^{-T}(q) \cdot \vec{\tau}_{\text{int}}. \tag{B.18}$$

Equations (B.17) and (B.18) can be used to transform contact forces at the manipulator endpoint into joint torques (forces) and vice versa. Note that since the Jacobian is not orthogonal its transposed is not equal to its inverse.

B.5 Two link planar manipulator

In this section we derive the kinematic relationships for a two link planar manipulator as depicted in Fig. B.2(a). This kind of manipulator was used for all crank turning experiments in this study.

B.5.1 Forward kinematics

The sketch in Fig. B.2(a) shows the manipulator with all three coordinate frames attached to the appropriate links. Since both joint axes of the manipulator are parallel to each other, the offsets (d_1, d_2) and twists (α_1, α_2) are zero. The labelling is chosen in accordance with the convention introduced in Sect. B.2. We set up the DH transformation matrices for the joints one and two:

$$A_1 = \begin{bmatrix} \cos\theta_1 & -\sin\theta_1 & 0 & a_1\cos\theta_1 \\ \sin\theta_1 & \cos\theta_1 & 0 & a_1\sin\theta_1 \\ 0 & 0 & 1 & 0 \\ 0 & 0 & 0 & 1 \end{bmatrix}; \quad A_2 = \begin{bmatrix} \cos\theta_2 & -\sin\theta_2 & 0 & a_2\cos\theta_2 \\ \sin\theta_2 & \cos\theta_2 & 0 & a_2\sin\theta_2 \\ 0 & 0 & 1 & 0 \\ 0 & 0 & 0 & 1 \end{bmatrix}.$$

It can be seen that these two matrices contain rotations about the parallel z-axes according to a z-rotation matrix as introduced in (B.3) and a translation vector which is composed of an x- and

y-component according to (B.2). The transformation from the base frame (coordinate frame 0 = joint 1) to frame 2 can now be calculated with the help of (B.5):

$$\begin{aligned} T_0^2 &= A_1 A_2 \\ &= \begin{bmatrix} c\theta_1 c\theta_2 - s\theta_1 s\theta_2 & -c\theta_1 s\theta_2 - s\theta_1 c\theta_2 & 0 & c\theta_1 c\theta_2 a_2 - s\theta_1 s\theta_2 a_2 + c\theta_1 a_1 \\ s\theta_1 c\theta_2 + c\theta_1 s\theta_2 & -s\theta_1 s\theta_2 + c\theta_1 c\theta_2 & 0 & s\theta_1 c\theta_2 a_2 + c\theta_1 s\theta_2 a_2 + s\theta_1 a_1 \\ 0 & 0 & 1 & 0 \\ 0 & 0 & 0 & 1 \end{bmatrix}. \end{aligned} \tag{B.19}$$

Application of the addition theorems

$$\sin(x \pm y) = \sin x \cos y \pm \cos x \sin y \tag{B.20a}$$

$$\cos(x \pm y) = \cos x \cos y \mp \sin x \sin y \tag{B.20b}$$

on (B.19) yields:

$$T_0^2 = \begin{bmatrix} R_0^2(\vec{\theta}) & \vec{p}(\vec{\theta}) \\ \vec{0}_{1\times 3} & 1 \end{bmatrix} = \begin{bmatrix} \cos(\theta_1+\theta_2) & -\sin(\theta_1+\theta_2) & 0 & a_1\cos\theta_1 + a_2\cos(\theta_1+\theta_2) \\ \sin(\theta_1+\theta_2) & \cos(\theta_1+\theta_2) & 0 & a_1\sin\theta_1 + a_2\sin(\theta_1+\theta_2) \\ 0 & 0 & 1 & 0 \\ 0 & 0 & 0 & 1 \end{bmatrix}. \tag{B.21}$$

The last column of (B.21) contains the cartesian coordinates of the manipulator endpoint (o_2), and the rotational part of the matrix contains the orientation of the coordinate frame of the endpoint.

B.5.2 Inverse kinematics

In this section we derive the inverse kinematics of the planar manipulator in Fig. B.2(a). For this purpose, the line drawing of the manipulator in Fig. B.2(b) is used. The drawing shows the arm in an elbow-up posture. We start with the law of cosines for an arbitrary triangle [illustrated in the small inset in Fig. B.2(b)]:

$$c^2 = a^2 + b^2 - 2ab\cos\gamma.$$

Thus, for the manipulator setup in Fig. B.2(b) follows:

$$x^2 + y^2 = a_1^2 + a_2^2 - 2a_1a_2\cos(\pi - \theta_2). \tag{B.22}$$

Note, that the θ_2-angle is negative in the drawing (right-hand frame). Reorganization of (B.22) yields:

$$\cos(\pi - \theta_2) = \frac{x^2+y^2-a_1^2-a_2^2}{-2a_1a_2} \quad |\text{with } \cos(\pi-\theta_2) = -\cos\theta_2 \text{ follows}$$

$$\cos(\theta_2) = \frac{x^2+y^2-a_1^2-a_2^2}{2a_1a_2}. \tag{B.23}$$

The angle θ_2 could now be calculated easily by applying the $\cos^{-1}$ function to (B.23). In this case we would only find one solution for the manipulator angles for a given endpoint. But there are

two possible solutions for the inverse kinematics of a two link planar manipulator, the *elbow up* and the *elbow down* posture. In order to find an expression for θ_2 that maintains two solutions we have to look on the formulas for half angles in geometry. We apply the following equation for the half of an angle θ_2:

$$\tan^2\left(\frac{\theta_2}{2}\right) = \frac{1-\cos\theta_2}{1+\cos\theta_2}. \tag{B.24}$$

Insertion of (B.23) into (B.24) yields:

$$\begin{aligned}\tan^2\left(\frac{\theta_2}{2}\right) &= \frac{2a_1a_2 - x^2 - y^2 + a_1^2 + a_2^2}{2a_1a_2 + x^2 + y^2 - a_1^2 - a_2^2} \\ &= \frac{(a_1+a_2)^2 - (x^2+y^2)}{(x^2+y^2) - (a_1-a_2)^2}.\end{aligned} \tag{B.25}$$

For θ_2 we get:

$$\theta_2 = 2\tan^{-1}\left(\pm\sqrt{\tfrac{(a_1+a_2)^2-(x^2+y^2)}{(x^2+y^2)-(a_1-a_2)^2}}\right) \quad |\text{with } \tan^{-1}(-x) = -tan^{-1}(x) \text{ follows}$$

$$\theta_2 = \pm 2\tan^{-1}\left(\sqrt{\tfrac{(a_1+a_2)^2-(x^2+y^2)}{(x^2+y^2)-(a_1-a_2)^2}}\right). \tag{B.26}$$

By choosing the plus or minus sign in (B.26), the elbow up or elbow down posture can be set.

In the next step the angle θ_1 has to be determined. In order to do so, it will turn out to be useful to introduce two auxiliary variables η and λ as depicted in Fig. B.2(c). θ_1 is the difference between η and λ:

$$\theta_1 = \eta - \lambda,$$

with

$$\eta = \tan^{-1}\left(\frac{y}{x}\right); \quad \lambda = \tan^{-1}\left(\frac{a_2\sin\theta_2}{a_1 + a_2\cos\theta_2}\right). \tag{B.27}$$

Therefore, the expression for the angle θ_1 results in:

$$\theta_1 = \tan^{-1}\left(\frac{y}{x}\right) - \tan^{-1}\left(\frac{a_2\sin\theta_2}{a_1 + a_2\cos\theta_2}\right). \tag{B.28}$$

This completes the derivation of the inverse kinematics of the planar manipulator.

B.5.3 Velocity kinematics and static force-torque relationship

In this section the Jacobian of the planar manipulator is set up. For calculation of the contact forces in the crank turning task, the transposed Jacobian and the inverse of the transposed Jacobian are required.

Application of (B.10) to the last column of (B.21) yields the Jacobian of the planar manipulator:

$$J = \begin{bmatrix} \frac{\partial d_x}{\partial\theta_1} & \frac{\partial d_x}{\partial\theta_2} \\ \frac{\partial d_y}{\partial\theta_1} & \frac{\partial d_y}{\partial\theta_2} \end{bmatrix} = \begin{bmatrix} -\sin(\theta_1+\theta_2)a_2 - \sin\theta_1 a_1 & -\sin(\theta_1+\theta_2)a_2 \\ \cos(\theta_1+\theta_2)a_2 + \cos\theta_1 a_1 & \cos(\theta_1+\theta_2)a_2 \end{bmatrix}.$$

The transposed of the Jacobian of the planar manipulator is:

$$J^T = \begin{bmatrix} -\sin(\theta_1+\theta_2)a_2 - \sin\theta_1 a_1 & \cos(\theta_1+\theta_2)a_2 + \cos\theta_1 a_1 \\ -\sin(\theta_1+\theta_2)a_2 & \cos(\theta_1+\theta_2)a_2 \end{bmatrix}. \tag{B.29}$$

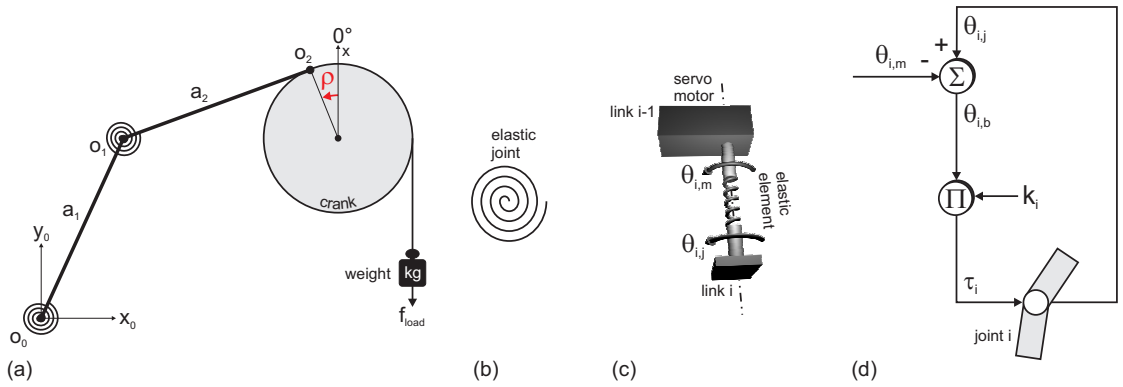

Figure B.3: (a) Setup of a crank turning task with a planar manipulator equipped with elastic joints. The positive cranking direction is counterclockwise. The crank is loaded with a counter force f_{load}. (b) Symbol for an elastic rotational joint. (c) 3D example of a joint with an elastic element that acts as a torsion spring. (d) Model of a servo-motor that drives a joint via a torsion spring.

The inverse of (B.29) is:

$$J^{-T} = \begin{bmatrix} \frac{\cos(\theta_1+\theta_2)}{a_1(-\cos(\theta_1+\theta_2)\sin\theta_1+\sin(\theta_1+\theta_2)\cos\theta_1)} & \frac{-(\cos(\theta_1+\theta_2)a_2+\cos\theta_1 a_1)}{a_1 a_2(-\cos(\theta_1+\theta_2)\sin\theta_1+\sin(\theta_1+\theta_2)\cos\theta_1)} \\ \frac{\sin(\theta_1+\theta_2)}{a_1(-\cos(\theta_1+\theta_2)\sin\theta_1+\sin(\theta_1+\theta_2)\cos\theta_1)} & \frac{-(\sin(\theta_1+\theta_2)a_2+\sin\theta_1 a_1)}{a_1 a_2(-\cos(\theta_1+\theta_2)\sin\theta_1+\sin(\theta_1+\theta_2)\cos\theta_1)} \end{bmatrix}. \quad \text{(B.30)}$$

Application of the addition theorems (B.20a) and (B.20b) on (B.30) leads to the following simplification:

$$J^{-T} = \begin{bmatrix} \frac{\cos(\theta_1+\theta_2)}{a_1\sin\theta_2} & \frac{-(\cos(\theta_1+\theta_2)a_2+\cos\theta_1 a_1)}{a_1 a_2\sin\theta_2} \\ \frac{\sin(\theta_1+\theta_2)}{a_1\sin\theta_2} & \frac{-(\sin(\theta_1+\theta_2)a_2+\sin\theta_1 a_1)}{a_1 a_2\sin\theta_2} \end{bmatrix}. \quad \text{(B.31)}$$

Insertion of (B.29) into (B.17) and (B.31) into (B.18) allows the calculation of the two joint torques of the planar manipulator from the contact force vector at the endpoint and vice versa.

B.6 Simulation of a crank turning experiment

In this section a simple method for the simulation of the closed kinematic chain in a crank turning task is introduced. The cranking setup is similar to that in Chapter 3; the crank is loaded with a weight that applies a force f_{load} onto the crank. In contrast to classical crank turning tasks, the manipulator used elastic joints. A sketch of it is depicted in Fig. B.3(a). The manipulator is provided with servo-drives that use serial elastic elements which are indicated by the symbol in Fig. B.3(b). The straight forward way to introduce elasticity in a rotational joint is the use of a torsion spring which is placed between the drive axis and the next link in the chain as sketched in Fig. B.3(c). For a servo-drive it can be assumed that the bending angle $\theta_{i,b}$ in the i^{th} joint is the difference between the joint angle $\theta_{i,j}$ and the angle of the motor axis $\theta_{i,m}$

$$\theta_{i,b} = \theta_{i,j} - \theta_{i,m}.$$

This geometrical relationship is shown in Fig. B.3(d). If the spring constant of the torsion spring $k_{s,i}$ is known, the torque in the joint can be calculated as:

$$\tau_i = \theta_{b,i} \cdot k_{s,i}.$$

The torque acts on joint i and can be used within the equations for the dynamics of a kinematic chain or it can be used to calculate the endpoint force according to (B.18). This causes the whole system to move in accordance to the dynamics equations which in turn results in a new joint angle $\theta_{i,j}$.

In order to constitute a detailed description of the crank turning setup, the forward kinematics of the crank itself has to be defined in the base frame of the manipulator. The crank is represented by a lever with the length r_c. The center of the crank is positioned at $(x_c, y_c)^T$. The origin $\vec{o}_2$ of the endpoint frame of the manipulator coincides with the crank handle. Therefore, the position of the crank handle which depends on the crank angle ρ can be written as:

$$\vec{o}_2 = \begin{pmatrix} x \\ y \end{pmatrix} = \begin{pmatrix} x_c - \sin\rho \cdot r_c \\ y_c + \cos\rho \cdot r_c \end{pmatrix} \tag{B.32}$$

Note, that the x-axis of the crank frame points upwards which results in a 0° starting position as indicated in Fig. B.3(a). The tangent to the contour of the crank at the crank handle position is the derivative of (B.32) with respect to the crank angle ρ:

$$\frac{d\vec{o}_2}{d\rho} = \begin{pmatrix} -\cos\rho \cdot r_c \\ -\sin\rho \cdot r_c \end{pmatrix}. \tag{B.33}$$

Equipped with these formulas we arrange a graphical representation of the simulation of the crank turning experiment as depicted in Fig. B.4. In order to investigate the coordination of the joint controllers under the condition that a heavy weight is attached to the crank we make the following assumptions:

- The weight attached to the crank generates the force f_{load}.
- The segments of the manipulator have a very small mass compared to the attached weight.
- The crank has a small mass.
- The cranking velocity is slow.

These assumptions were made in order to extract the coordination behaviors of the **L**ocal **P**ositive **V**elocity **F**eedback joint controllers, moving a heavy weight, without the influence of the inertias of the arm segments and the crank.

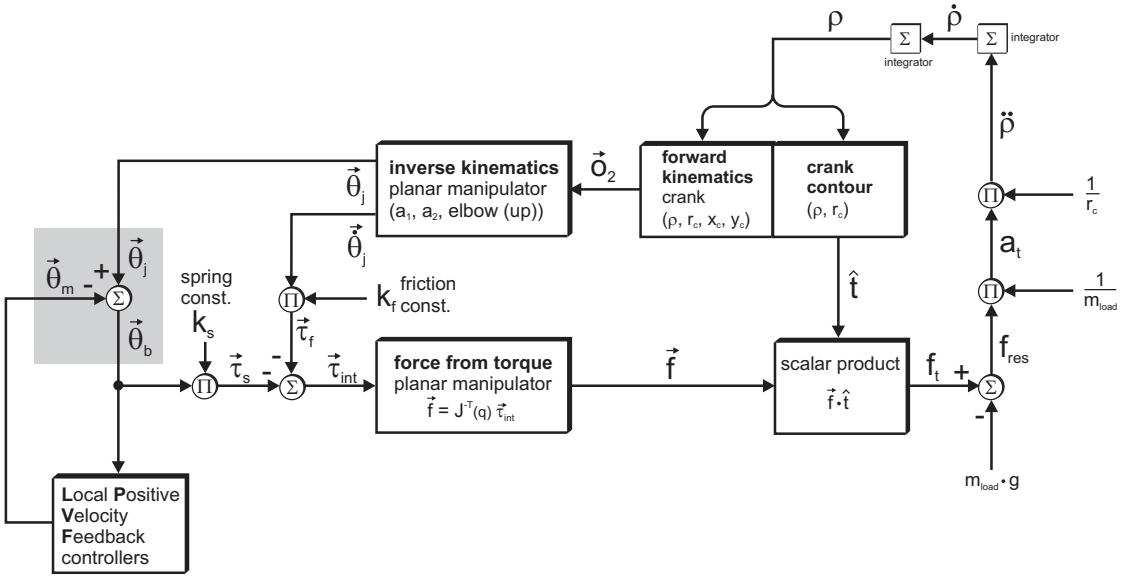

Figure B.4: Graphical representation of the simulation of the loaded crank turning task.

We start our examination on the left side of Fig. B.4 and proceed counterclockwise through the circuit. The grey box indicates the elastic joint as shown in Fig. B.3(d). The vector of both bending angles $\vec{\theta_b} = (\theta_{1,b}, \theta_{2,b})^T$ serves as input for the **L**ocal **P**ositive **V**elocity **F**eedback controllers which calculate the next angular position of the motor axes $\vec{\theta_m} = (\theta_{1,m}, \theta_{2,m})^T$ for each joint independently. Furthermore, the multiplication of the bending angles with the spring constants k_s delivers the drive torques $\vec{\tau}_s = (\tau_{1,s}, \tau_{2,s})^T$ which are reduced by torques $\vec{\tau}_f = (\tau_{1,f}, \tau_{2,f})^T$ due to viscous friction in the joints. The resulting torque $\vec{\tau}_{\text{int}}$ is used to calculate the force $\vec{f}$ at the endpoint $\vec{o}_2$ of the manipulator according to (B.18) and (B.31). Since only the tangential share of the handle's force is used to lift the weight attached to the crank, we build the scalar product of $\vec{f}$ and a unit vector $\hat{t} = \vec{t}/\|\vec{t}\|$ that lies tangential to the contour of the crank. The tangent to the crank contour on which the unit vector is based is calculated with (B.33). The result of the scalar product is the tangential force f_t which counteracts the weight force $f_{\text{load}} = m_{\text{load}} \cdot g$. The difference f_{res} of these two forces accelerates the weight. The linear acceleration value is a_t. Division of a_t by the crank radius r_c yields the angular acceleration $\ddot{\rho}$ of the crank. Double integration of $\ddot{\rho}$ results in the crank angle ρ which is converted into the current crank handle position $\vec{o}_2$ by means of the crank kinematics (B.32). With the help of the inverse kinematics of the manipulator [(B.26) and (B.28)] the manipulator joint angles can be calculated. With this last step the simulation loop is closed.

B.7 Simplified insect leg

Despite the ability of joint coordination in loaded and unloaded crank turning tasks, chapter 4 also shows that LPVF joint controllers are well suited for the joint control in a walking leg. The

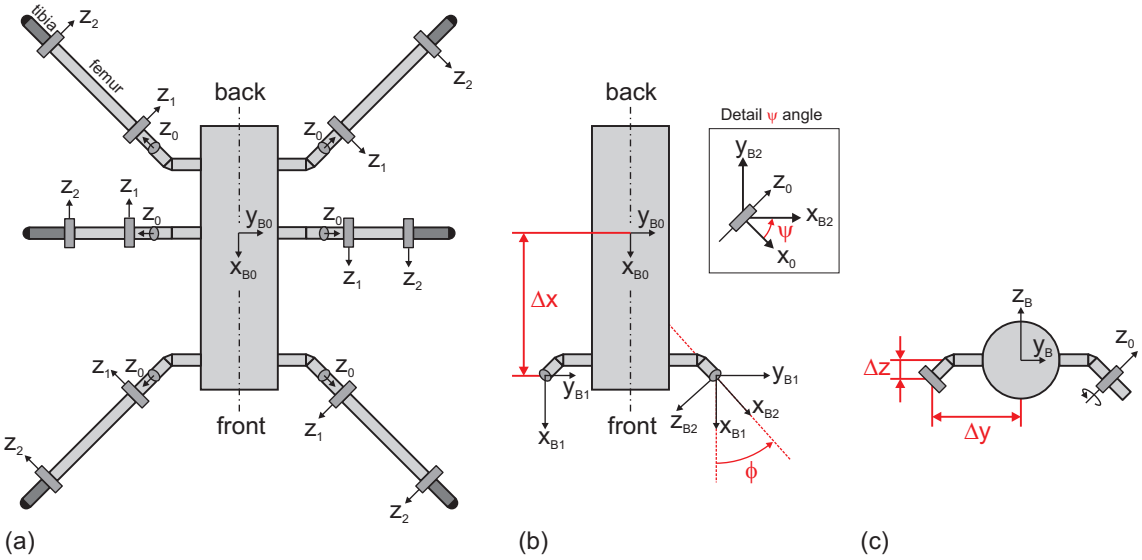

Figure B.5: Graphical representation of the coordinate frames for a six-legged walker. (a) Configuration of the six legs in top view. The body coordinate frame $B0$ and all axes of rotation (z-axes) are given. (b) The Δx-distance from a coxa to the body coordinate frame and the convention for the ϕ-angle is visualized in top view. The ψ-angle is depicted in the small inset. (c) The Δy- and Δz-distances from a coxa to the body coordinate frame are shown in a front view.

theory of Local Positive Velocity Feedback in this work is based on the concept of reflex reversal that occurs in the leg joints of activated stick insects (Bässler, 1976). The simulations that are described in chapter 4 use a leg kinematic that is based on the anatomical shape of a stick insect's leg. The robot Tarry IIB is also modelled on the stick insect *Carausius morosus* on a 1:10 scale. A kinematic model which is suitable for both, the robot and the insect, is derived in this section.

B.7.1 Forward kinematics

Before the kinematics of the leg itself is described, the geometrical arrangement of the six legs of a stick insect has to be defined. Fig. B.5(a) shows a top view of a six-legged walker. The body base frame $B0$ can be chosen freely. For the robot it is placed between the coxae of the middle legs (Also positions between the front or hind leg coxae are possible). Another choice could be the *center of gravity* (COG) of the robot. But the position of the COG is subject to changes according to the payload that is carried by the robot. Fig. B.5(b) and Fig. B.5(c) show how the distances $(\Delta x, \Delta y, \Delta_z)$ for the parallel translation from the body base frame $B0$ to the coxa frame $B1$ are measured. The DH-parameters for this parallel translation are collected in Table B.1.

Table B.1: DH parameters for the parallel translation from the body base frame $B0$ to the coxa frame $B1$.

link i	a_i	α_i	d_i	θ_i
I	Δx	0	Δz	0
II	Δy	0	0	$\frac{\pi}{2}$
III	0	0	0	$-\frac{\pi}{2}$

By using the information from Table B.1 and the setup template (B.6), the three transformation matrices are set up as follows:

$$A_I = \begin{bmatrix} \cos 0 & -\sin 0 \cos 0 & \sin 0 \sin 0 & \Delta x \cdot \cos 0 \\ \sin 0 & \cos 0 \cos 0 & -\cos 0 \sin 0 & \Delta x \cdot \sin 0 \\ 0 & \sin 0 & \cos 0 & \Delta z \\ 0 & 0 & 0 & 1 \end{bmatrix} = \begin{bmatrix} 1 & 0 & 0 & \Delta x \\ 0 & 1 & 0 & 0 \\ 0 & 0 & 1 & \Delta z \\ 0 & 0 & 0 & 1 \end{bmatrix}.$$

A_I contains the the forward (or backward) and the up (or down) shift.

$$A_{II} = \begin{bmatrix} \cos \frac{\pi}{2} & -\sin \frac{\pi}{2} \cos 0 & \sin \frac{\pi}{2} \sin 0 & \Delta y \cdot \cos \frac{\pi}{2} \\ \sin \frac{\pi}{2} & \cos \frac{\pi}{2} \cos 0 & -\cos \frac{\pi}{2} \sin 0 & \Delta y \cdot \sin \frac{\pi}{2} \\ 0 & \sin 0 & \cos 0 & 0 \\ 0 & 0 & 0 & 1 \end{bmatrix} = \begin{bmatrix} 0 & -1 & 0 & 0 \\ 1 & 0 & 0 & \Delta y \\ 0 & 0 & 1 & 0 \\ 0 & 0 & 0 & 1 \end{bmatrix}$$

A_{II} contains the sideward shift.

$$A_{III} = \begin{bmatrix} \cos\left(-\frac{\pi}{2}\right) & -\sin\left(-\frac{\pi}{2}\right) \cos 0 & \sin\left(-\frac{\pi}{2}\right) \sin 0 & 0 \\ \sin\left(-\frac{\pi}{2}\right) & \cos\left(-\frac{\pi}{2}\right) \cos 0 & -\cos\left(-\frac{\pi}{2}\right) \sin 0 & 0 \\ 0 & \sin 0 & \cos 0 & 0 \\ 0 & 0 & 0 & 1 \end{bmatrix} = \begin{bmatrix} 0 & 1 & 0 & 0 \\ -1 & 0 & 0 & 0 \\ 0 & 0 & 1 & 0 \\ 0 & 0 & 0 & 1 \end{bmatrix}$$

A_{III} rotates the coordinate frame into the desired orientation of the goal frame $B1$. The overall transformation for the parallel translation from the body frame to the coxa frame T_{B0}^{B1} and its inverse $\left(T_{B0}^{B1}\right)^{-1}$ can now be written as:

$$T_{B0}^{B1} = A_1 \cdot A_{II} \cdot A_{III} = \begin{bmatrix} 1 & 0 & 0 & \Delta x \\ 0 & 1 & 0 & \Delta y \\ 0 & 0 & 1 & \Delta z \\ 0 & 0 & 0 & 1 \end{bmatrix}; \quad \left(T_{B0}^{B1}\right)^{-1} = \begin{bmatrix} 1 & 0 & 0 & -\Delta x \\ 0 & 1 & 0 & -\Delta y \\ 0 & 0 & 1 & -\Delta z \\ 0 & 0 & 0 & 1 \end{bmatrix}. \tag{B.34}$$

The parallel translation T_{B0}^{B1} shifts the body base coordinate frame into the coxa position.

It is known that the z_0-axis of the protaction/retraction joint (α-joint or θ_1-joint) is arranged in an inclined orientation with respect to the z_{B0}-axis of the body (Cruse, 1976). This inclination is described by two angles ϕ and ψ. First, the coxa coordinate frame $B1$ is rotated about the z_{B1}-axis by the angle ϕ followed by a rotation of $\pi/2$ about the x-axis in order to prepare the z_{B2}-axis for the ψ-rotation. The coordinate frame in this new position is labelled $B2$. Second, the

coordinate frame $B2$ is rotated about its z_{B2}-axis by the angle ψ followed by a rotation of $-\pi/2$ about the x-axis to bring the z_0-axis into the desired orientation. The DH-parameter set for the ϕ- and ψ-rotation is given in Table B.2.

Table B.2: DH-parameters for the ϕ- and ψ-rotation.

link i	a_i	α_i	d_i	θ_i
ϕ	0	$\frac{\pi}{2}$	0	ϕ
ψ	0	$-\frac{\pi}{2}$	0	ψ

The transformation matrices A_ϕ and A_ψ are:

$$A_\phi = \begin{bmatrix} \cos\phi & -\sin\phi\cos\frac{\pi}{2} & \sin\phi\sin\frac{\pi}{2} & 0 \\ \sin\phi & \cos\phi\cos\frac{\pi}{2} & -\cos\phi\sin\frac{\pi}{2} & 0 \\ 0 & \sin\frac{\pi}{2} & \cos\frac{\pi}{2} & 0 \\ 0 & 0 & 0 & 1 \end{bmatrix} = \begin{bmatrix} \cos\phi & 0 & \sin\phi & 0 \\ \sin\phi & 0 & -\cos\phi & 0 \\ 0 & 1 & 0 & 0 \\ 0 & 0 & 0 & 1 \end{bmatrix};$$

$$A_\psi = \begin{bmatrix} \cos\psi & -\sin\psi\cos\left(-\frac{\pi}{2}\right) & \sin\psi\sin\left(-\frac{\pi}{2}\right) & 0 \\ \sin\psi & \cos\psi\cos\left(-\frac{\pi}{2}\right) & -\cos\psi\sin\left(-\frac{\pi}{2}\right) & 0 \\ 0 & \sin\left(-\frac{\pi}{2}\right) & \cos\left(-\frac{\pi}{2}\right) & 0 \\ 0 & 0 & 0 & 1 \end{bmatrix} = \begin{bmatrix} \cos\psi & 0 & -\sin\psi & 0 \\ \sin\psi & 0 & \cos\psi & 0 \\ 0 & -1 & 0 & 0 \\ 0 & 0 & 0 & 1 \end{bmatrix}.$$

For a given leg, the $\Delta x, \Delta y$ and Δz parallel translation and the ϕ- and ψ-angle for the inclination of the z_0-axis are fixed, although in real animals especially the inclinations of the hind legs change noticeably during the stance phase (Cruse and Bartling, 1995). The variable angles of an actual leg are the protraction/retraction joint (θ_1- or α-angle), the levation/depression joint (θ_2- or β-angle) and the extension/flexion joint (θ_3- or γ-angle) for the sidewards movement of the endpoint of the leg. The coordinate frames for these three angles are shown in Fig. B.6(a) and Fig. B.6(b).

The segments or links that lie in between the joints are labelled a_1, a_2 and a_3. The segment $a_1 = l_c$ represents the coxa, $a_2 = l_f$ the femur and $a_3 = l_t$ the tibia of the leg. The DH-parameters for the three transformations are given in Table B.3.

Table B.3: DH-parameters for the α-, $\beta-$ and γ-rotation.

link i	a_i	α_i	d_i	θ_i
1	$a_1 = l_c$	$\frac{\pi}{2}$	0	α
2	$a_2 = l_f$	0	0	β
3	$a_3 = l_t$	0	0	γ

The transformation matrices A_1, A_2 and A_3 are thus given as:

$$A_1 = A_\alpha = \begin{bmatrix} \cos\alpha & -\sin\alpha\cos\frac{\pi}{2} & \sin\alpha\sin\frac{\pi}{2} & l_c\cos\alpha \\ \sin\alpha & \cos\alpha\cos\frac{\pi}{2} & -\cos\alpha\sin\frac{\pi}{2} & l_c\sin\alpha \\ 0 & \sin\frac{\pi}{2} & \cos\frac{\pi}{2} & 0 \\ 0 & 0 & 0 & 1 \end{bmatrix} = \begin{bmatrix} \cos\alpha & 0 & \sin\alpha & l_c\cos\alpha \\ \sin\alpha & 0 & -\cos\alpha & l_c\sin\alpha \\ 0 & 1 & 0 & 0 \\ 0 & 0 & 0 & 1 \end{bmatrix};$$

$$A_2 = A_\beta = \begin{bmatrix} \cos\beta & -\sin\beta\cos 0 & \sin\beta\sin 0 & l_f\cos\beta \\ \sin\beta & \cos\beta\cos 0 & -\cos\beta\sin 0 & l_f\sin\beta \\ 0 & \sin 0 & \cos 0 & 0 \\ 0 & 0 & 0 & 1 \end{bmatrix} = \begin{bmatrix} \cos\beta & -\sin\beta & 0 & l_f\cos\beta \\ \sin\beta & \cos\beta & 0 & l_f\sin\beta \\ 0 & 0 & 1 & 0 \\ 0 & 0 & 0 & 1 \end{bmatrix};$$

$$A_3 = A_\gamma = \begin{bmatrix} \cos\gamma & -\sin\gamma\cos 0 & \sin\gamma\sin 0 & l_t\cos\gamma \\ \sin\gamma & \cos\gamma\cos 0 & -\cos\gamma\sin 0 & l_t\sin\gamma \\ 0 & \sin 0 & \cos 0 & 0 \\ 0 & 0 & 0 & 1 \end{bmatrix} = \begin{bmatrix} \cos\gamma & -\sin\gamma & 0 & l_t\cos\gamma \\ \sin\gamma & \cos\gamma & 0 & l_t\sin\gamma \\ 0 & 0 & 1 & 0 \\ 0 & 0 & 0 & 1 \end{bmatrix}.$$

Given A_1, A_2 and A_3, the forward transformation T_0^3 can be set up. It is useful to do this in two steps. First, we set up the transformation T_2^3:

$$\begin{aligned} T_2^3 &= A_2 \cdot A_3 \\ &= \begin{bmatrix} \cos\beta\cos\gamma - \sin\beta\sin\gamma & -\cos\beta\sin\gamma - \sin\beta\cos\gamma & 0 & l_t\cos\beta\cos\gamma - l_t\sin\beta\sin\gamma + l_f\cos\beta \\ \sin\beta\cos\gamma + \cos\beta\sin\gamma & -\sin\beta\sin\gamma + \cos\beta\cos\gamma & 0 & l_t\sin\beta\cos\gamma + l_t\cos\beta\sin\gamma + l_f\sin\beta \\ 0 & 0 & 1 & 0 \\ 0 & 0 & 0 & 1 \end{bmatrix} \\ &= \begin{bmatrix} \cos(\beta+\gamma) & -\sin(\beta+\gamma) & 0 & l_t\cos(\beta+\gamma) + l_f\cos\beta \\ \sin(\beta+\gamma) & \cos(\beta+\gamma) & 0 & l_t\sin(\beta+\gamma) + l_f\sin\beta \\ 0 & 0 & 1 & 0 \\ 0 & 0 & 0 & 1 \end{bmatrix}. \end{aligned}$$

The simplification in the rotational part of T_2^3 is achieved by using the addition theorems (B.20a) and (B.20b). The complete forward kinematics T_0^3 for the leg is then calculated as follows:

$$\begin{aligned} T_0^3 &= A_1 \cdot T_2^3 \\ &= \begin{bmatrix} \cos\alpha\cos(\beta+\gamma) & -\cos\alpha\sin(\beta+\gamma) & \sin\alpha & \cos\alpha\underbrace{(l_t\cos(\beta+\gamma) + l_f\cos\beta + l_c)}_{x \text{ in the leg plane}} \\ \sin\alpha\cos(\beta+\gamma) & -\sin\alpha\sin(\beta+\gamma) & -\cos\alpha & \sin\alpha\underbrace{(l_t\cos(\beta+\gamma) + l_f\cos\beta + l_c)}_{x \text{ in the leg plane}} \\ \sin(\beta+\gamma) & \cos(\beta+\gamma) & 0 & \underbrace{l_t\sin(\beta+\gamma) + l_f\sin\beta}_{y \text{ in the leg plane}} \\ 0 & 0 & 0 & 1 \end{bmatrix}. \end{aligned}$$

The position of the tibia endpoint in the base frame o_0 of the leg is given in the last column of T_0^3.

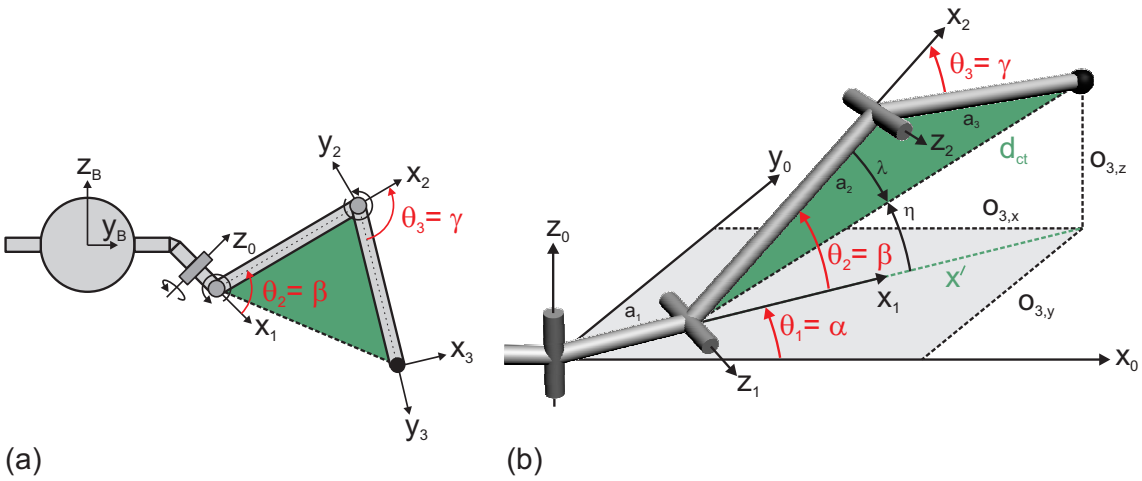

Figure B.6: Graphical representation of the coordinate frames of a leg. The colored triangle is used in the derivation of the inverse kinematics in Sect. B.7.2. (a) Front view of left front leg attached to a body. The leg coordinate frames are visualized. (b) 3D representation of a left front leg with all three variable joint angles $(\theta_1, \theta_2, \theta_3)$.

B.7.2 Inverse kinematics

In this section the inverse kinematics will be calculated for the three leg angles $\theta_1 = \alpha$, $\theta_2 = \beta$ and $\theta_3 = \gamma$. The inclination of the z_0-axis with respect to the z_{B0}-axis of the body base frame $B0$ is kept fixed. The derivation is closely related to that of the inverse kinematics of the planar manipulator in Sect. B.5.2. We use the drawing in Fig. B.6(b) for a closer inspection of the geometry. The α-angle can be calculated on the basis of the x- and y-coordinate of the tarsus point $\vec{o}_3 = (o_{3,x}, o_{3,y}, o_{3,z})^T$:

$$\alpha = \tan^{-1}\left(\frac{o_{3,y}}{o_{3,x}}\right). \tag{B.35}$$

The γ-angle is determined with the help of the law of cosines (B.22) applied to the colored triangle in Fig. B.6(b). The longest side of the triangle is the distance between the coxa and the tarsus d_{ct}. As preparation, the projection x' of d_{ct} on the x_0-y_0 plane is calculated:

$$x' = \sqrt{o_{3,x}^2 + o_{3,y}^2} - l_c. \tag{B.36}$$

The square of d_{ct} can be written as:

$$d_{ct}^2 = x'^2 + o_{3,z}^2. \tag{B.37}$$

According to the law of cosines d_{ct}^2 can also be calculated as:

$$\begin{aligned} d_{ct}^2 &= l_f^2 + l_t^2 - 2 l_f l_t \cos(\pi - \gamma) \quad |\text{with } \cos(\pi - x) = -\cos(x) \text{ follows} \\ &= l_f^2 + l_t^2 + 2 l_f l_t \cos(\gamma). \end{aligned} \tag{B.38}$$

Reorganization of (B.38) yields:

$$\cos\gamma = \frac{d_{ct}^2 - l_f^2 - l_t^2}{2 l_f l_t}. \tag{B.39}$$

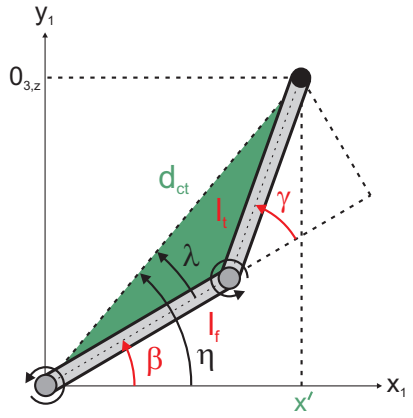

Figure B.7: The auxiliary angles η and λ are shown. The leg is in a *knee-down* posture which a real stick insect is not able to do.

This is an expression that is similar to (B.23). Following the same argument as for (B.23) we apply the equation for half angles (B.24) on (B.39) and rearrange the result as in (B.25):

$$\gamma = \pm 2 \tan^{-1} \sqrt{\frac{(l_f + l_t)^2 - d_{ct}^2}{d_{ct}^2 - (l_f - l_t)^2}}. \tag{B.40}$$

(B.40) represents the γ-angle we sought for. The parameter d_{ct}^2 can be calculated with (B.37) and (B.36).

The last angle to complete the inverse kinematics of the insect leg is the levation/depression angle β. As for the calculation of the θ_1-angle in the inverse kinematics of the planar manipulator, we introduce two auxiliary angles η and λ as shown in Fig. B.6(b). For the sake of simplicity Fig. B.7 shows a view onto the x_1-y_1 plane for the construction of η, λ and β. The angle η represents the elevation of the line d_{ct} from the x_0-y_0 plane. It is calculated by:

$$\eta = \tan^{-1} \left(\frac{o_{3,z}}{x'} \right). \tag{B.41}$$

The second auxiliary angle λ is the angle between the femur and the line d_{ct}. It is calculated just as the angle λ in (B.27):

$$\lambda = \tan^{-1} \left(\frac{l_t \sin \gamma}{l_f + l_t \cos \gamma} \right). \tag{B.42}$$

The β-angle is the difference between η and λ:

$$\beta = \eta - \lambda = \tan^{-1} \left(\frac{o_{3,z}}{x'} \right) - \tan^{-1} \left(\frac{l_t \sin \gamma}{l_f + l_t \cos \gamma} \right). \tag{B.43}$$

B.7.3 Coordinate transformation for the whole animal

So far the frame conventions were given for a leg on the left side of the central body. Fig. B.8 shows the transformation tree for legs on the left and on the right side of the central body. The grey box in the middle represents the central body. The grey boxes on the left and right side of the middle box contain the transformations for the inclination of the z_0-axis with respect to the

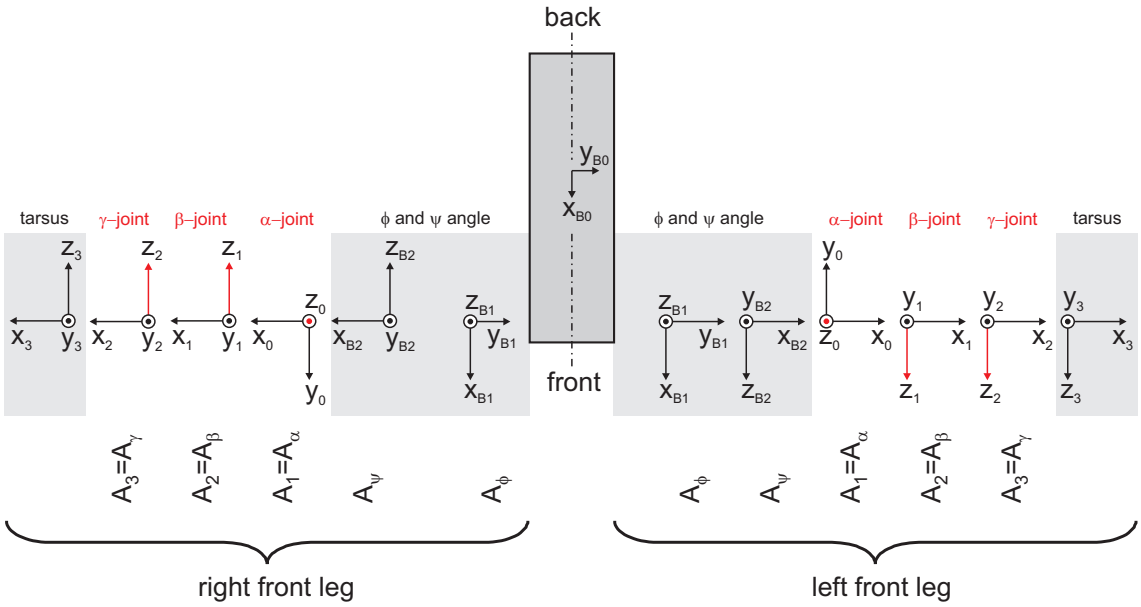

Figure B.8: Diagram of the tree of coordinate frames for a left and right front leg.

z_{B0}-axis. The uncolored areas depict the transformations of the α-, β- and γ-joint. A positive rotation of the α-joint on the left body side results in a retraction of the leg, whereas on the right body side a positive α-rotation causes a protraction of the leg. A positive rotation of the β-joint causes a levation of the leg on both sides of the body. A positive rotation of the γ-joint results in a sidewards excursion of the tibia on both sides.

For the sake of completeness we give a list of body dimensions for the robot Tarry IIb in Table B.4 and the same list for an average stick insect in Table B.5. The dimensions and masses for the segments of the stick insect were taken from Ekeberg and co-authors (Ekeberg et al., 2004). Whenever measures were needed for simulations in this work, they were taken from these two lists.
The geometrical dimensions of the box-shaped central body of Tarry IIb are 320 mm x 50 mm x 30 mm (length x width x height). The mass of the body is $\sim$ 1 kg. The width and the height of all leg segments are 25 mm x 10 mm.
In the simulations the central body of the stick insect is assumed to be box-shaped. Its dimensions are 40 mm x 5 mm x 5 mm (length x width x height). The mass of the body is 600 mg. The legs are assumed to have a round cross section with a diameter of 1 mm.

Table B.4: Body parameters for the robot Tarry IIb (fl = left front leg, ml = left middle leg, hl = left hind leg, fr = right front leg, mr = right middle leg, hr = right hind leg, m_c = mass coxa, m_f = mass femur, m_t= mass tibia). The segment masses were estimated for the use in simulations.

measure	fl	ml	hl	fr	mr	hr
Δx [mm]	148	0	-123	148	0	-123
Δy [mm]	35	35	35	-35	-35	-35
Δz [mm]	0	0	0	0	0	0
ϕ [°]	85	100	115	-85	-100	-115
ψ [°]	-45	-45	-45	-45	-45	-45
l_c [mm]	18	18	18	18	18	18
l_f [mm]	145	115	125	145	115	125
l_t [mm]	140	117	130	140	117	130
m_c [kg]	0.08	0.08	0.08	0.08	0.08	0.08
m_f [kg]	0.10	0.10	0.10	0.10	0.10	0.10
m_t [kg]	0.12	0.12	0.12	0.12	0.12	0.12

Table B.5: Body parameters for an average stick insect (fl = left front leg, ml = left middle leg, hl = left hind leg, fr = right front leg, mr = right middle leg, hr = right hind leg, m_c = mass coxa, m_f = mass femur, m_t= mass tibia).

measure	fl	ml	hl	fr	mr	hr
Δx [mm]	18	0	-12	18	0	-12
Δy [mm]	4	4	4	-4	-4	-4
Δz [mm]	0	0	0	0	0	0
ϕ [°]	85	100	115	-85	-100	-115
ψ [°]	-45	-45	-45	-45	-45	-45
l_c [mm]	1.61	1.57	1.39	1.61	1.57	1.39
l_f [mm]	17.85	13.47	15.51	17.85	13.47	15.51
l_t [mm]	17.10	13.20	16.51	17.10	13.20	16.51
m_c [mg]	0.43	1.0	1.0	0.43	1.0	1.0
m_f [mg]	10.30	8.05	8.60	10.30	8.05	8.60
m_t [mg]	3.30	1.70	2.70	3.30	1.70	2.70

Bibliography

Abdallah, C., Dorato, P., Benitez-Read, J., and Byrne, R. (1993). Delayed positive feedback can stabilize oscillatory systems. In *Proc. of the IEEE American Control Conf., San Fransisco, CA*, volume 3, pages 3106–3107.

Al-Jarrah, O. and Zheng, Y. (1998). Intelligent compliant motion control. *IEEE Transactions on Systems, Man and Cybernetics - Part B*, 28(1):116–122.

Al-Jarrah, O., Zheng, Y., and Yi, K. (1995). Trajectory planning for two manipulators to deform flexible materials using compliant motion. *Proc. 1995 IEEE Int. Conf. Robotics Automation, Nagoya, Japan*, pages 1517–1522.

Alexander, R. M. (1990). Three uses for springs in legged locomotion. *The International Journal of Robotics Research*, 9(2):53–61.

Barkhausen, H. (1932). *Einführung in die Schwingungslehre nebst Anwendgungen auf mechanische und elektrische Schwingungen*. Hirzel, Leipzig.

Bartling, C. and Schmitz, J. (2000). Reactions to disturbances of a walking leg during stance. *J. Exp. Biol.*, 203:1211–1223.

Bässler, U. (1965). Propriorezeptoren am Subcoxal- und Femur-Tibia-Gelenk der Stabheuschrecke *Carausius morosus* und ihre Rolle bei der Wahrnehmung der Schwerkraftrichtung. *Kybernetik*, 2:168–193.

Bässler, U. (1967). Zur Regelung der Stellung des Femur-Tibia-Gelenkes bei der Stabheuschrecke *Carausius morosus* in der Ruhe und im Lauf. *Kybernetik*, 4:18–26.

Bässler, U. (1972). Der Regelkreis des Kniesehnenreflexes bei der Stabheuschrecke *Carausius morosus*: Reaktionen auf passive Bewegungen der Tibia. *Kybernetik*, 12:8–20.

Bässler, U. (1976). Reversal of a reflex to a single motoneuron in the stick insect *Carausius morosus*. *Biol. Cybern.*, 24:47–49.

Bässler, U. (1977). Sense organs in the femur of the stick insect and their relevance to the control of position of the femur-tibia joint. *J. Comp. Physiol.*, 121:99–113.

Bässler, U. (1983). *Neural Basis of Elementary Behavior in Stick Insects*, volume 10 of *Studies of Brain Function*. Springer, Berlin, London, New York.

Bässler, U. (1986a). Afferent control of walking movements in the stick insect *Cuniculina impigra* II. Reflex reversal and the release of the swing phase in the restrained foreleg. *J. Comp. Physiol.*, 158:351–362.

Bässler, U. (1986b). On the definition of central pattern generator and its sensory control. *Biol. Cybern.*, 54:65–69.

Bässler, U. (1988). Functional principles of pattern generation for walking movements of stick insect forelegs: The role of the femoral chordotonal organ afferences. *J. Exp. Biol.*, 136:125–147.

Bässler, U. (1993). The femur-tibia control system of stick insects - a model system for the study of the neural basis of joint control. *Brain Res. Rev.*, 18:207–226.

Bässler, U. and Büschges, A. (1990). Interneurones participating in the "active reaction" in stick insects. *Biol. Cybern.*, 62:529–538.

Baz, A. and Poh, S. (1996). Optimal vibration control with modal positive position feedback. *Optimal Control Applications and Methods*, 17(2):141–149.

Baz, A., Poh, S., and Fedor, J. (1992). Independent modal space control with positive position feedback. *ASHE J. Dyn. Syst., Meas. Control*, 114:96–103.

Beckers, R., Deneubourg, J., and Goss, S. (1992). Trails and u-turns in the selection of the shortest path by the ant *Lasius niger*. *Journal of Theoretical Biology*, 159:397–415.

Beckers, R., Holland, O., and Deneubourg, J. (1994). From local actions to global tasks: Stigmergy and collective robotics. In Brooks, R. and Maes, P., editors, *ARTIFICIAL LIFE IV, Proceedings of the Fourth International Workshop on the Synthesis and Simulation of Living Systems*, pages 181–189, Cambridge, MA. MIT Press.

Bell, J. and Kashani, A. (1995). Structure-borne noise reduction by active damping of a radiating panel. In *Proc. of the SAE Noise and Vibration Conf., Traverse City, MI.*

Berns, K., Albiez, J., Kepplin, V., and Hillenbrand, C. (2001). Control of a six-legged robot using fluidic muscle. *ICAR 2001, 10th Int. Conference on Advanced Robotics, Budapest, Hungary.*

Bernstein, N. (1967). *The Co-ordination and Regulation of Movements.* Pergamon Press Ltd.

Bertalanffy, L. v. (1968). *General System Theory: Foundations, Development, Applications.* Braziller, New York.

Boblan, I., Bannasch, R., Schwenk, H., Miertsch, L., and Schulz, A. (2003). A human like robot hand and arm with fluidic muscles: Biologically inspired construction and functionality. In *Embodied Artificial Intelligence, Dagstuhl Event 03281*, pages 160–179, New York. Springer.

Bonabeau, E., Theraulaz, G., Deneubourg, J., Aron, S., and Camazine, S. (1997). Self-organization in social insects. *Trends in Ecology and Evolution*, 12(5):188–192.

Borst, A. and Egelhaaf, M. (1989). Principles of visual motion detection. *TINS*, 12(8):297–306.

Boucher, D., James, S., and Keeler, K. (1982). The ecology of mutualism. *Ann. Rev. Ecol. Syst.*, 13:315–347.

Braitenberg, V. (1984). *Vehicles: Experiments in synthetic psychology.* MIT press, Cambridge, MA.

Bräuning, P. (1982). Strand receptors with central cell bodies in the proximal leg joints of orthopterous insects. *Cell Tiss. Res.*, 222:647–654.

Bräuning, P. and Hustert, R. (1985a). Actions and interactions of proprioceptors of the locust hind leg coxo-trochanteral joint. I. Afferent responses in relation to joint position and movement. *J. Comp. Physiol.*, 157:73–82.

Bräuning, P. and Hustert, R. (1985b). Actions and interactions of proprioceptors of the locust hind leg coxo-trochanteral joint. II. Influence on the motor system. *J. Comp. Physiol.*, 157:83–89.

Brommundt, E. and Sachs, G. (1988). *Technische Mechanik: Eine Einführung.* Springer, Berlin, Heidelberg, New York, London, Paris.

Brooks, R. A. (1991). Intelligence without reason. In Myopoulos, R. and Reiter, J., editors, *Proceedings of the* 12^{th} *International Joint Conference on Artificial Intelligence*, pages 569–595, Sydney, Australia. Morgan Kaufmann.

Brown, T. (1911). The intrinsic factors in the act of progression in the mammal. *Proceedings of the Royal Society B*, 84:308–319.

Bruyninckx, H. and De Schutter, J. (1996). Specification of force-controlled actions in the "task frame formalism" - a synthesis. *IEEE Transactions on Robotics and Automation*, 12(4):581–589.

Büchi, A. (1922). Diesel-Motoren : Eine Untersuchung über ihre wirtschaftliche Verwendung. *Schweizer Bauzeitung*, 79.

Büchi, A. (1953). *Turbocharging of internal combustion engines: its origin, evolution, present state of development and future potentialities.* Journal of the Franklin Inst. : Monograph ; 1. Franklin-Inst., Philadelphia, Pa.

Burrows, M. and Pflüger, H. (1988). Positive feedback loops from proprioceptors involved in leg movements of the locust. *J. Comp. Physiol. A*, 163:425–440.

Büschges, A. (1994). The physiology of sensory cells in the ventral scoloparium of the stick insect femoral chordotonal organ. *J. Exp. Biol.*, 189:285–292.

Büschges, A. and Schmitz, J. (1991). Nonspiking pathways antagonize the resistance reflex in the thoraco-coxal joint of stick insects. *J. Neurosci.*, 22(3):224–237.

Craig, J. J. (2005). *Introduction to Robotics: Mechanics and Control.* Pearson Prentice Hall, Upper Saddle River, NJ, 3^{rd} edition.

Cruse, H. (1976). On the function of the legs in the free walking stick insect *Carausius morosus. J. Comp. Physiol.*, 112:235–262.

Cruse, H. (1981). Is the position of the femur-tibia joint under feedback control in the walking stick insect? I. Force measurements. *J. Exp. Biol.*, 92:87–95.

Cruse, H. (1996). *Neural Networks as Cybernetic Systems.* Thieme, Stuttgart/ New York.

Cruse, H. (2003). The evolution of cognition - a hypothesis. *Cognitive Sci.*, 27:135–155.

Cruse, H. and Bartling, C. (1995). Movement of joint angles in the legs of a walking insect, *Carausius morosus. J. Insect Physiol.*, 41:761–771.

Cruse, H., Bartling, C., and Kindermann, T. (1995). High-pass filtered positive feedback for decentralized control of cooperation. In Moran, F., Moreno, A., Merelo, J., and Chacon, P., editors, *Advances in Artificial Life*, pages 668–678, Berlin, London, New York. Springer.

Cruse, H., Kindermann, T., Schumm, M., Dean, J., and Schmitz, J. (1998a). Walknet - a biologically inspired network to control six-legged walking. *Neural Networks*, 11:1435–1447.

Cruse, H., Kühn, S., Park, S., and Schmitz, J. (2004). Adaptive control for insect leg position: Controller properties depend on substrate compliance. *J. Comp. Physiol.*, 190:983–991.

Cruse, H. and Pflüger, H.-J. (1981). Is the position of the femur-tibia joint under feedback control in the walking stick insect? II. Electrophysiological recordings. *J. Exp. Biol.*, 92:97–107.

Cruse, H. and Schmitz, J. (1983). The control system of the femur-tibia joint in the standing leg of a walking stick insect *Carausius morosus. J. Exp. Biol.*, 102:175–185.

Cruse, H. and Steinkühler, U. (1993). Solution of the direct and inverse kinematic problem by a unique algorithm using the mean of multiple computation method. *Biol. Cybern.*, 69:345–351.

Cruse, H., Steinkühler, U., and Burkamp, C. (1998b). MMC-a recurrent neural network which can be used as manipulable body model. In *Proceedings of the* 5^{th} *International Conference on Simulation of Adaptive Behavior*, pages 381–389, Cambridge, MA. MIT Press.

Cruse, H. and Storrer, J. (1977). Open loop analysis of a feedback mechanism controlling the leg position in the stick insect *Carausius morosus*: Comparison between experiment and simulation. *Biol. Cybern.*, 25:143–153.

De Luca, A. and Siciliano, B. (1996). Flexible links. In Canudas de Wit, C., Siciliano, B., and Bastin, G., editors, *Theory of Robot Control*, pages 219–256, Berlin, London, New York. Springer.

De Luca, A. and Tomei, P. (1996). Elastic joints. In Canudas de Wit, C., Siciliano, B., and Bastin, G., editors, *Theory of Robot Control*, pages 179–217, Berlin, London, New York. Springer.

DeAngelis, D., Post, W., and Travis, C. (1986). *Positive Feedback in Natural Systems*. Springer, London, Berlin, Heidelberg.

Delcomyn, F. (1991). Activity and directional sensitivity of leg campaniform sensilla in a stick insect. *J. Comp. Physiol.*, 168:113–119.

Denavit, J. and Hartenberg, R. (1955). A kinematic notation for lower-pair mechanisms based on matrices. *Journal of Applied Mechanics*, 77:215–221.

Deneubourg, J., Aron, S., Goss, S., and Pasteels, J. (1993). The self-organizating exploratory pattern of the argentine ant. *Journal of Insect Behavior*, 6:751–759.

Deneubourg, J., Goss, S., Franks N, R., Sendova-Franks, A., Detrain, C., and Chretien, L. (1990). The dynamics of collective sorting: robot-like ants and ant-like robots. In Meyer, J. and Wilson, S., editors, *Simulation of Adaptive Behaviour: from animals to animats*, pages 356–365, Cambridge, MA. MIT Press.

DiCaprio, R. and Clarac, F. (1981). Reversal of a walking leg reflex elicited by a muscle receptor. *J. Exp. Biol.*, 90:197–203.

Dorigo, M., Maniezzo, V., and Colorni, A. (1991). Positive feedback as a search strategy. Technical Report 91016, Dipartimento di Elettronica e Informatica, Politecnico di Milano, Milano, IT.

Driesang, R. and Büschges, A. (1996). Physiological changes in central neuronal pathways contributing to the generation of a reflex reversal. *J. Comp. Physiol.*, 179:45–57.

Dürr, V., Schmitz, J., and Cruse, H. (2004). Behaviour-based modelling of hexapod locomotion: Linking biology and technical application. *Arthropod Struct. Devel.*, 33(3):237–250.

Ekeberg, Ö., Blümel, M., and Büschges, A. (2004). Dynamic simulation of insect walking. *Arthropod Struct. Devel.*, 33(3):287–300.

Fanson, J. and Caughey, T. (1990). Positive position feedback control for large space structures. *AIAA Journal*, 28(4):717–724.

Fischer, B. (2004). *Implementierung eines aktiven Reglers modelliert nach dem Verhalten des Femur-Tibia-Gelenks der Stabheuschrecke*. Diploma Thesis, Dept. of Biological Cybernetics, University of Bielefeld, Germany.

Flash, T. and Hogan, N. (1985). The coordination of arm movement: a confirmed mathematical model. *J. Neurosci.*, 5:1688–1703.

Forssberg, H., Grillner, S., and Rossignol, S. (1975). Phase dependent reflex reversal during walking in chronic spinal cats. *Brain Research*, 85:103–107.

Franklin, D. and Milner, T. (2003). Adaptive control of stiffness to stabilize hand position with large loads. *Exp. Brain Res.*, 152(2):211–220.

Garcia, M., Kuo, A., Peattie, A., Wang, P., and Full, R. (2000). Damping and size: Insights and biological inspiration. In *Proceedings of the First International Symposium on Adaptive Motion of Animals and Machines*, Montreal, Canada.

Girod, B., Rabenstein, R., and Stenger, A. (2001). *Signals and Systems*. Wiley, Chichester.

Goh, C. and Caughey, T. (1985). On the stability problem caused by finite actuator dynamics in the collocated control of large space structures. *Int. J. Control*, 41(3):787–802.

Gorinevsky, S. and Schneider, A. (1990). Force control in locomotion of legged vehicles over rigid and soft surfaces. *The International Journal of Robotics Research*, 9(2):4–22.

Grassé, P. (1959). La reconstruction du nid et les coordinates inter-individuelles chez *Bellicositermes natalensis* et *Cubitermes sp.* la théorie de la stigmergie: Essai d'interprétation des termites constructeurs. *Insect Soc.*, 6:41–83.

Gurfinkel, V., Devjanin, E., Anischenko, S., Lensky, A., Mozhzhevelov, S., and Schneider, A. (1983). An adaptive manipulator with force sensors. *Mechanism and Machine Theory*, 18(4):267–270.

Hassenstein, B. (1966). *Kybernetik und Biologische Forschung.* Handbuch der Biologie I/2. Akademische Verlagsgesellschaft ATHENAION, Frankfurt.

Hassenstein, B. and Reichardt, W. (1956). Systemtheoretische Analyse der Zeit-, Reihenfolgen- und Vorzeichenauswertung bei der Bewegungsperzeption des Rüsselkäfers *Clorophanus. Z. Naturforsch.*, B11:513–524.

Heuer, A. (1998). *Untersuchung zur Funktion des thorakalen Depressor trochanteris im Höhenkontrollsystem aktivierter und laufender Stabheuschrecken.* PhD Thesis, Dept. of Biological Cybernetics, University of Bielefeld, Germany.

Hill, A. (1938). The heat of shortening and the dynamic constants of muscle. *Proc. R. Soc. Lond. B Biol. Sci.*, 126:136–195.

Hoeksema, J. and Bruna, E. (2000). Pursuing the big question about interspecific mutualism: a review of theoretical approaches. *Oecologia*, 125:321–330.

Hofmann, T., Koch, U., and Bässler, U. (1985). Physiology of the femoral chordotonal organ in the stick insect, *Cuniculina impigra. J. Exp. Biol.*, 114:207–223.

Hogan, N. (1985). Impedance control: An approach to manipulation: Part I - Theory, Part II - Implementation, Part III - Applications. *ASME J. Dynam. Syst., Meas., Contr.*, 107:1–23.

Ito, K., Tsuji, T., and Sugino, M. (1991). Impedance regulation in human movements during a rotation task. *Journal of Robotics and Mechatronics*, 3(6):455–462.

Kawato, M., Maeda, Y., Uno, Y., and Suzuki, R. (1990). Trajectory formation of arm movement by cascade neural network model based on minimum torque-change criterion. *Biol. Cybern.*, 62(4):275–288.

Kerscher, T., Albiez, J., Zöllner, J., and Dillmann, R. (2004). Airinsect - a new innovative biological inspired six-legged walking machine driven by fluidic muscles. *Proceedings of IAS 8, The* 8^{th} *Conference on Intelligent Autonomous Systems, Amsterdam, The Netherlands.*

Kindermann, T. (2002). Behavior and adaptability of a six-legged walking system with highly distributed control. *Adapt. Behav.*, 9(1):16–41.

Kittmann, R. and Schmitz, J. (1992). Functional specialization of the scoloparia of the femoral chordotonal organ in stick insects. *J. Exp. Biol.*, 173:91–108.

Klein, C. and Kittivatcharapong, S. (1990). Optimal force distribution for the legs of a walking machine with friction cone constraint. *IEEE Transactions on Robotics and Automation*, 6(1):73–85.

Kühn, S. and Cruse, H. (2005). Static mental representations in recurrent neural networks for the control of dynamic behavioural sequences. *Connection Science*, 17:343–360.

Kumar, V. and Waldron, K. (1988). Force distribution in closed kinematic chains. *IEEE Journal of Robotics and Automation*, 4(6):657–664.

Kumar, V. and Waldron, K. (1990). Force distribution in walking vehicles. *Transactions of the ASME*, 112:90–99.

Lutz, H. and Wendt, W. (2003). *Taschenbuch der Regelungstechnik.* Harri Deutsch, Frankfurt am Main, 5^{th} edition.

Magnus, K. and Müller, H. (1974). *Grundlagen der Technischen Mechanik*, volume 22 of *Leitfäden der angewandten Mathematik und Mechanik LAMM*. B. G. Teubner, Stuttgart.

Mason, M. (1981). Compliance and force control for computer controlled manipulators. *IEEE Transactions on Systems, Man and Cybernetics*, SMC-11(6):418–432.

Maxwell, J. (1868). On governors. In *Proceedings of the Royal Society*, volume 16, pages 270–283, London. Royal Society.

Möhl, B. (2003). A composite drive with separate control of force and position. In *Proc. of the* 11^{th} *International Conference on Advanced Robotics*.

Mussa Ivaldi, F., Morasso, P., and Zaccaria, R. (1988). Kinematic networks - a distributed model for representing and regularizing motor redundancy. *Biol. Cybern.*, 60:1–16.

Ohta, K., Svinin, M., Luo, Z., Hosoe, S., and Laboissière, R. (2004). Optimal trajectory formation of constrained human arm movements. *Biol. Cybern.*, 91(1):23–36.

Porta, J. and Celaya, E. (2001). Efficient gait generation using reinforcement learning. In Berns, K. and Dillmann, R., editors, *Proceedings of the* 4^{th} *International Conference on Climbing and Walking Robots (CLAWAR 2001)*, pages 411–418, London. Professional Engineering Publishing.

Press, W., Teukolsky, S., Vetterling, W., and Flannery, B. (1992). *Numerical Recipes in C: The Art of Scientific Computing*. Cambridge University Press, New York, NY, USA, 2^{nd} edition.

Pringle, J. (1938). Proprioception in insects. II. The action of the campaniform sensilla on the legs. *J. Exp. Biol.*, 15:114–131.

Prochazka, A. (1989). Sensorimotor gain control: a basic strategy of motor systems? *Prog. Neurobiol.*, 33:281–307.

Prochazka, A., Gillard, D., and Bennett, D. (1997a). Implications of positive feedback in the control of movement. *J. Neurophysiol.*, 77:3237–3251.

Prochazka, A., Gillard, D., and Bennett, D. (1997b). Positive force feedback control of muscles. *J. Neurophysiol.*, 77:3226–3236.

Raibert, M. and Craig, J. (1981). Hybrid position/force control of manipulators. *Transactions of the ASME*, 102:126–133.

Rew, K.-H., Han, J.-H., and Lee, I. (2002). Multi-modal vibration control using adaptive positive position feedback. *Journal of Intelligent Material Systems and Structures*, 13:13–22.

Riener, R., Ferrarin, M., Esteban, E., and Carlo, A. (2000). Patient-driven control of FES-supported standing up and sitting down: Experimental results. *IEEE Transactions on Rehabilitation Engineering*, 8(4):523–529.

Ritzmann, R., Quinn, R., and Fischer, M. (2004). Convergent evolution and locomotion through complex terrain by insects, vertebrates and robots. *Arthropod Struct. Devel.*, 33:361–379.

Roggendorf, T. (2005). Comparing different controllers for the coordination of a six-legged walker. *Biol. Cybern.*, 92:261–274.

Roggendorf, T. (2006). *Development of a planning system for the Walknet*. PhD Thesis, Dept. of Biological Cybernetics, University of Bielefeld, Germany.

Routledge, R. (1900). *Discoveries and Inventions of the Nineteenth Century*. G. Routledge and Sons, Ltd., London, New York, 13^{th} edition.

Russel, D. and Hogan, N. (1989). Dealing with constraints: A biomechanical approach. In *Proceedings of the IEEE Engineering in Medicine and Biology Society 11th Annual Conference*, pages 892–893.

Saranli, U., Buehler, M., and Koditschek, D. (2001). Rhex: A simple and highly mobile hexapod robot. *The International Journal of Robotics Research*, 20(7):616–631.

Sauer, A., Driesang, R., Büschges, A., and Bässler, U. (1996). Distributed processing on the basis of parallel and antagonistic pathways. Simulation of the femur-tibia control system in the stick insect. *J. Comp. Neurosci.*, 3:179–198.

Schmidt, R. (1982). *Motor control and learning : a behavioral emphasis*. Human Kinetics Publ., Champaign, Ill.

Schmitz, J. (1985). Control of the leg joints in stick insects: Differences in the reflex properties between the standing and the walking states. In Gewecke, M. and Wendler, G., editors, *Insect Locomotion*, pages 27–32, Berlin, Hamburg. Paul Parey.

Schmitz, J. (1986). Properties of the feedback system controlling the coxa-trochanter joint in the stick insect *Carausius morosus*. *Biol. Cybern.*, 55:35–42.

Schmitz, J., Bartling, C., Brunn, D., Cruse, H., Dean, J., Kindermann, T., Schumm, M., and Wagner, H. (1995). Adaptive properties of "hard-wired" neuronal systems. *Verh. Dtsch. Zool. Ges.*, 88(2):165–179.

Schneider, A., Cruse, H., and Schmitz, J. (2005a). A biologically inspired active compliant joint using Local Positive Velocity Feedback (LPVF). *IEEE Transactions on Systems, Man, and Cybernetics - Part B: Cybernetics*, 35(6):1120–1130.

Schneider, A., Cruse, H., and Schmitz, J. (2005b). Local Positive Velocity Feedback (LPVF): Generating compliant motions in a multi-joint limb. In Armada, M. and Gonzalez de Santos, M., editors, *Proceedings of the 7^{th} International Conference on Climbing and Walking Robots (CLAWAR 2004)*, pages 143–151, New York. Springer.

Schneider, A., Cruse, H., and Schmitz, J. (2005c). Switched local positive velocity feedback controllers: Local generation of retraction forces and inter-joint coordination in walking. In *Proceedings of the 3^{rd} International Symposium on Adaptive Motion of Animals and Machines*, Ilmenau, Germany, on CD.

Schneider, A., Cruse, H., and Schmitz, J. (2006a). Decentralized control of elastic limbs in closed kinematic chains. *The International Journal of Robotics Research (in press)*.

Schneider, A., Cruse, H., and Schmitz, J. (2006b). Winching up heavy loads with a compliant manipulator - a new decentral control approach. *IEEE Transactions on Systems, Man, and Cybernetics - Part B: Cybernetics (under revision)*.

Schneider, A., Schmitz, J., and Cruse, H. (2005d). A bio-inspired joint controller for the decentral control of a closed kinematic chain consisting of elastic joints. In *Proceedings of the 44^{th} IEEE Conference on Decision and Control and European Control Conference (CDC-ECC'05), on CD*, pages 233–238.

Schumpich, G. (1980). *Technische Mechanik, Teil 1 Statik*. B. G. Teubner, Stuttgart, 5^{th} edition.

Sciavicco, L. and Siciliano, B. (2000). *Modelling and Control of Robot Manipulators*. Advanced Textbooks in Control and Signal Processing. Springer, London, Berlin, Heidelberg, 2^{nd} edition.

Skorupski, P. and Sillar, K. (1986). Phase-dependent reversal of reflexes mediated by the thoracocoxal muscle receptor organ in the crayfish *pacifastacus leniusculus*. *J. Neurophysiol.*, 55(4):689–695.

Smithers, T. (1995). On quantitative performance measures of robot behaviour. *Robots and Autonomous Systems*, 15(1-2):107–133.

Soest, A. v. and Bobbert, M. (1993). The contribution of muscle properties in the control of explosive movements. *Biol. Cybern.*, 69:195–204.

Song, G., Schmidt, S., and Agrawal, B. (2001). Experimental robustness study of positive position feedback control for active vibration suppression. *J. Guidance: Engineering Notes*, 25(1):179–182.

Spong, M. W. (1987). Modeling and control of elastic joint robots. *Transactions of the ASME*, 109:310–319.

Spong, M. W. and Vidyasagar, M. (1989). *Robot Dynamics And Control*. John Wiley & Sons, New York, 1^{st} edition.

Steinkühler, U. and Cruse, H. (1998). A holistic model for an internal representation to control movement of a manipulator with redundant degrees of freedom. *Biol. Cybern.*, 79:457–466.

Storrer, J. and Cruse, H. (1977). Systemanalytische Untersuchung eines aufgeschnittenen Regelkreises, der die Beinstellung der Stabheuschrecke Carausius morosus kontrolliert: Kraftmessung an den Antagonisten Flexor and Extensor tibiae. *Biol. Cybern.*, 25:131–142.

Tryba, A. and Ritzmann, R. (2000). Multi-joint coordination during walking and foothold searching in the *Blaberus* cockroach. I. Kinematics and electromyograms. *J. Neurophysiol.*, 83:3323–3336.

Unbehauen, H. (1997). *Regelungstechnik I: Klassische Verfahren zur Analyse und Synthese linearer kontinuierlicher Regelsysteme*. Vieweg, Wiesbaden, Braunschweig, 9^{th} edition.

Uno, Y., Kawato, M., and Suzuki, R. (1989). Formation and control of optimal trajectory in human multijoint arm movement. Minimum torque-change model. *Biol. Cybern.*, 61(2):89–101.

Van Vorhis Key, S. and Baker, T. (1986). Observations on the trail deposition and recruitment behaviors of the argentine ant, *Iridomyrmex humilis* (*Hymenoptera: Formicidae*). *Ann. Entomol. Soc. Am.*, 79:283–288.

Vedel, J.-P. (1980). The antennal motor system of the rock lobster: Competitive occurence of resistance and assistance reflex patterns originating from the same proprioceptor. *J. Exp. Biol.*, 87:1–22.

Vincent, J. and Wegst, U. (2004). Design and mechanical properties of insect cuticle. *Arthropod Struct. Devel.*, 33:187–199.

Wadden, T., Benjellount, K., Hardarson, F., Wikander, J., and Ekeberg, O. (1998). Biologically inspired design of a leg for dynamic walking. In Pfeiffer, F. and Cruse, H., editors, *Biology and Technology of Walking*, European Mechanics Colloquium Euromech 375, pages 228–235.

Wendler, G. (1964). Laufen und Stehen der Stabheuschrecke *Carausius morosus*: Sinnesborstenfelder in den Beingelenken als Glieder von Regelkreisen. *Z. Vergl. Physiol.*, 48:198–250.

Wiener, N. (1948). *Cybernetics or control and communication in the animal and the machine*. Hermann, Paris.

Williamson, M. M. (2003). Oscillators and crank-turning: Exploiting natural dynamics with a humanoid robot arm. *Philosophical Transactions: Mathematical, Physical and Engineering Sciences*, 361(1811):2207–2223.

Wilson, D. (1961). The central nervous control of locust flight. *J. Exp. Biol.*, 38:471–490.

Wilson, D. and Waldron, I. (1968). Models for the generation of the motor output pattern in flying locusts. *Proceedings of the IEEE*, 56(6):1058–1064.

Yoshikawa, T. and Zheng, X. (1990). Coordinated dynamic hybrid position/force control for multiple robot manipulators handling one constrained object. *Proc. 1990 IEEE Int. Conf. Robotics Automation, Cincinnati, OH*, pages 1178–1183.

Zajac, F. (1989). Muscle and tendon: Properties, models, scaling, and application to biomechanics and motor control. *Critical Reviews in Biomedical Engineering*, 17(4):359–411.

Zakotnik, J., Matheson, T., and Dürr, V. (2006). Co-contraction and passive forces facilitate load compensation of aimed limb movements. *J. Neurosci.*, 26(19):4995–5007.

Zill, S. (1985). Plasticity and proprioception in insects: II Modes of reflex action of the locust metathoric femoral chordotonal organ. *J. Exp. Biol.*, 116:463–480.

Zill, S. and Moran, D. (1981). The exoskeleton and insect proprioception. I. Responses of tibial campaniform sensilla to external and muscle-generated forces in the American cockroach *Periplaneta americana*. *J. Exp. Biol.*, 91:1–24.